

Acoustofluidics
2020

Table of Contents

Welcome Letter	3
Conference Officials	4
Conference Sponsors	5
Invited Speakers	6
Program Schedule	7
Session 1: Acoustic Devices	7
Session 2: Bio-Acoustic Systems	9
Session 3: Physical Acoustic	12
Session 4: Acoustic Manipulation	14
Abstract-Only Presentations	16
Abstracts	19

Welcome Letter

It is a great pleasure and honor to welcome you to Acoustofluidics 2020. After running this annual conference regularly for 17 years, first as the USWNet Annual Meeting from 2003 to 2012, and since 2013 as the Acoustofluidics Conference, we were facing special challenges this year due to the COVID-19 pandemic.

In the spring of 2020, the USWNet Board in charge of running the Acoustofluidics Conference, decided to shift Acoustofluidics 2020 to be held in Glasgow, and Acoustofluidics 2021 to be held in Hangzhou, by one year. At the same time, it was decided to run the Acoustofluidics 2020 Conference as a virtual online conference, a first for all of us involved. We felt that it was particularly important for the students, postdocs, and young researchers in the field, to meet and exchange research news from the field without suffering a full one-year gap in the conference cycle.

We very much appreciate the broad support and helpful feedback from so many colleagues of the acoustofluidics community that eventually rendered this year's conference possible. It was not difficult to engage our senior colleagues in the Organizing Committee and the Scientific Committee, and to have them volunteer as session chairs. We are very grateful for their help. Moreover, we got rapid positive feedback and acceptances from the invited speakers to present at our virtual conference. Finally, we appreciate support from our sponsors at CBMS, USWNet, and the Royal Society of Chemistry, as well as the good and very constructive collaboration we have had with Sara Stearns and Shirley Galloway from PMMI Global, who have helped setting up the conference website and dealing with the abstract submission and registration of the participants under these unusual circumstances.

It has been very gratifying for us to see the positive response in the whole acoustofluidics community to our call for papers in the beginning of June 2020 under the four topical sessions decided by the Organizing Committee: Acoustic Devices, Bio-Acoustic Systems, Physical Acoustics, and Acoustic Manipulation. We have received a total of 72 abstracts from five continents and 19 different countries (among the presenting authors). Given the strong manning of the Organizing Committee and the Scientific Committee, each abstract was reviewed by five leading experts in their respective fields. Because of the large number of submissions, and to give particularly young researchers the chance to present their work, we decided to allow as many speakers as possible. We eventually selected 24 abstracts for contributed talks and 28 abstracts for flash talks. Since the scientific quality of the abstracts were very high this year, the selection was not easy.

Taking a look at the final Acoustofluidics 2020 Abstract Book, we feel confident that this year's meeting will continue to summarize the state-of-the-art in acoustofluidics research, including the newest scientific discoveries, cutting-edge acoustofluidics technologies, and innovative industrial applications as was the case for the preceding annual Acoustofluidics Conferences.

We wish you all an inspiring, stimulating, and fruitful virtual conference on 26 - 27 August 2020!



Henrik Bruus



Thomas Franke

Henrik Bruus
Chair Acoustofluidics 2020
President of USWNet

Thomas Franke
Chair Acoustofluidics 2020

Conference Officials

Conference Chairs

Thomas Franke *University of Glasgow, UK*
Henrik Bruus *Technical University of Denmark, DENMARK*

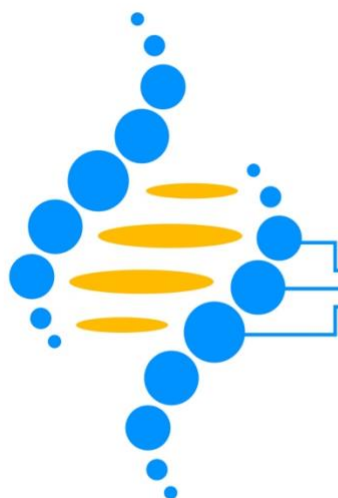
Organizing Committee

Jürg Dual *ETH Zürich, SWITZERLAND*
James Friend *University of California, San Diego, USA*
Richard Fu *Northumbria University, UK*
Peter Glynn-Jones *University of Southampton, UK*
Adrian Neild *Monash University, AUSTRALIA*
Jikui Luo *Zhejiang University, CHINA*

Scientific Committee

Per Augustsson *Lund University, SWEDEN*
Rune Barnkob *Technical University München, GERMANY*
Michaël Baudoin *Université de Lille, FRANCE*
Philippe Brunet *Université Paris Diderot, FRANCE*
Bruce Drinkwater *University of Bristol, UK*
Xuexin Duan *Tianjin University, CHINA*
Itziar Gonzales Gomez *ITEFI-CSIC, Madrid, SPAIN*
Xiasheng Guo *Nanjing University, CHINA*
Martyn Hill *University of Southampton, GREAT BRITAIN*
Tony Jun Huang *Duke University, USA*
Thomas Laurell *Lund University, SWEDEN*
Andreas Lenshof *Lund University, SWEDEN*
Kian-Meng Lim *National University of Singapore, SINGAPORE*
Philippe Marmottant *Université Grenoble Alpes, FRANCE*
Stefan Radel *TU Wien, AUSTRIA*
Hagen Schmidt *IFW Dresden, GERMANY*
Glauber T. Silva *Universidade Federal de Alagoas, BRAZIL*
Hyung Jin Sung *Korea Advanced Institute of Science and Technology (KAIST), KOREA*
Michel Versluis *University of Twente, NETHERLANDS*
Martin Wiklund *KTH Stockholm, SWEDEN*

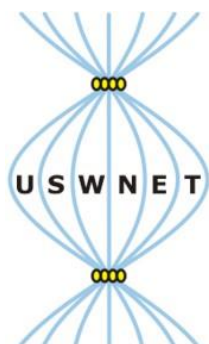
Conference Sponsors



CBMS

Chemical and Biological
Microsystems Society

Chemical and Biological Microsystems Society (CBMS)
www.cbmsociety.org



USWNet
Ultrasonic Standing Wave Network

Ultrasonic Standing Wave Network (USWNet)
www.uswnet.org

Media Benefactor



LabonaChip

Lab on a Chip / Royal Society of Chemistry
www.rsc.org

Invited Speakers

Session 1: Acoustic Devices

ACOUSTOFLUIDICS: MANIPULATING OBJECTS ACROSS 7 ORDERS OF MAGNITUDE

[Tony Jun Huang](#)

Duke University, USA



Session 2 - Bio-Acoustic Systems

SIMPLICITY OR COMPLEXITY: TRANSDUCERS AND INSTRUMENTATION STRATEGIES FOR ACOUSTOFLUIDIC MANIPULATION OF CELLS AND BIOFUNCTIONALIZED BEADS

[Martin Wiklund](#)

KTH Royal Institute of Technology, SWEDEN



Session 3: Physical Acoustic

ACOUSTIC RADIATION FORCE AND TORQUE ON NONSPHERICAL SMALL PARTICLES

[Glauber T. Silva](#)

Universidade Federal de Alagoas, BRAZIL



Session 4: Acoustic Manipulation

THE ACOUSTIC HOLOGRAM AND ITS APPLICATION FACILITATED BY THE SPATIAL MODULATION OF ULTRASOUND

[Peer Fischer](#)

Max Planck Institute, GERMANY



Wednesday, 26 August

All times are US Eastern Daylight Time (EDT) - UTC/GMT -4 hours

08:00 - 08:05 **Opening Remarks**
Thomas Franke, *University of Glasgow, UK*
Henrik Bruus, *Technical University of Denmark, DENMARK*

Session 1 - Acoustic Devices

08:05 - 08:10 **Session Introduction by Session Chairs**
Richard Fu, *Northumbria University, UK*
Jürg Dual, *ETH Zürich, SWITZERLAND*

Invited Speaker

08:10 - 08:40 **ACOUSTOFLUIDICS: MANIPULATING OBJECTS ACROSS 7 ORDERS OF MAGNITUDE**
[Tony Jun Huang](#)
Duke University, USA

Contributed Talks

08:40 - 08:50 **MICROSWIMMERS AS LIVING PROBES TO MEASURE THE ACOUSTIC ENERGY DENSITY IN ACOUSTOFLUIDIC DEVICES**
[Minji Kim](#)¹, Rune Barnkob², and J. Mark Meacham¹
¹*Washington University, St. Louis, USA and*
²*Technical University of Munich, GERMANY*

08:50 - 09:00 **A MULTINODAL ACOUSTIC TRAPPING UNIT WITH INCREASED CAPACITY AND THROUGHPUT FOR CAPTURE OF EXTRACELLULAR VESICLES**
[Axel Broman](#), Andreas Lenshof, Mikael Evander, Anson Ku, Yvonne Ceder, Johan Malmström, and Thomas Laurell
Lund University, SWEDEN

09:00 - 09:10 **MODELING AND EXPERIMENTAL EVALUATION OF A POLYMER-BASED ACOUSTOPHORESIS CHIP**
[Fabian Lickert](#)¹, Mathias Ohlin², Henrik Bruus¹, and Pelle Ohlsson²
¹*Technical University of Denmark, DENMARK and*
²*AcouSort AB, SWEDEN*

09:10 - 09:20 **CAPILLARY BRIDGE ACOUSTOFLUIDICS**
[Jeremy J. Hawkes](#)¹, Sadaf Maramizonouz¹, Changfeng Jia², Mohammad Rahmati¹, Tengfei Zheng², Martin B. McDonnell³, and Yong Qing Fu¹
¹*Northumbria University, UK,* ²*Xian Jiaotong University, CHINA, and*
³*Dstl Porton Down, UK*

09:20 - 09:30 **DROPLET GENERATION FROM STANDING SURFACE ACOUSTIC WAVE (SSAW) STABILIZED FLUIDIC MICROPATTERN**
Mehrzad Roudini¹, Dennis Niedermeier², Frank Stratmann²,
and Andreas Winkler¹
¹SAWLab Saxony, GERMANY and
²Leibniz Institute for Tropospheric Research, GERMANY

09:30 - 09:40 **MICROFLUIDICS PLATFORM FOR PROTOCOL DEVELOPMENT VIA CAPACITIVE FLUID LEVEL MONITORING AND ACOUSTIC MIXING**
Yaqi Zhang¹, Muhsincan Sesen^{1,2}, Alex de Marco¹, and Adrian Neild¹
Monash University, AUSTRALIA and ²Heriot-Watt University, UK

Flash Talks

09:40 - 09:44 **FABRICATION OF SURFACE ACOUSTIC WAVE (SAW) DEVICES USING DETACHABLE ELECTRODES BASED ON A FLEXIBLE PRINTED CIRCUIT BOARD (PCB)**
Roman Mikhaylov, Zhihua Xie, Aled Clayton, and Xin Yang
Cardiff University, UK

09:44 - 09:48 **GALLIUM NITRIDE THIN FILM FOR ACOUSTIC TWEEZER**
Chao Sun¹, Huaixing Cang¹, and Xin Yang²
¹Northwestern Polytechnical University, CHINA and
²Cardiff University, UK

09:48 - 09:52 **ACOUSTICALLY DRIVEN MENISCUS MODES IN INKJET PRINTING**
Martin van den Broek¹, Maaïke Rump¹, Roger Jeurissen²,
Hans Reinten³, Detlef Lohse¹, Michel Versluis¹, Guillaume Lajoinie¹,
and Tim Segers¹
¹University of Twente, NETHERLANDS,
²Eindhoven University of Technology, NETHERLANDS, and
³Canon Production Printing Netherlands B.V., NETHERLANDS

09:52 - 09:56 **DROPLET DEMULSIFICATION AT PARALLEL FLOW INTERFACE USING SOUND WAVES**
E. Hemachandran and Ashis Kumar Sen
Indian Institute of Technology, Madras, INDIA

09:56 -10:00 **DROPLET IMPACT CONTROL BY SURFACE ACOUSTIC WAVES**
Mehdi H. Biroun¹, Mohammad Rahmati¹, Glen McHale¹, Mehdi Jangiz²,
Hamdi Torun¹, and Richard YongQing Fu¹
¹Northumbria University, UK and ²University of Birmingham, UK

10:00 -10:04 **DROPLET MERGING IN A PDMS MICRO-WELL DRIVEN BY SURFACE ACOUSTIC WAVES**
Sudeepthi Aremanda¹, Lelie Yeo², and Ashis Kumar Sen¹
¹Indian Institute of Technology, Madras, INDIA and
²RMIT University, AUSTRALIA

10:04 -10:08 **HIGH-THROUGHPUT TRIGGERED MERGING OF DROPLETS USING TRAVELLING SURFACE ACOUSTIC WAVES**
Vincent Bussiere¹, Aurélie Vigne^{1,2}, Andreas Link¹, John McGrath¹,
Aparna Srivastav¹, Esther Richter¹, Ziyun Wang¹,
Mustafa Zaimagaoglu¹, Jean-Christophe Baret², and Thomas Franke¹
¹University of Glasgow, UK and ²Université de Bordeaux, FRANCE

10:08 – 10:25 **Break (offline)**

Session 2 - Bio-Acoustic Systems

10:25 - 10:30 **Session Introduction by Session Chairs**
Peter Glynne-Jones, *University of Southampton, UK*
Thomas Franke, *University of Glasgow, UK*

Invited Speaker

10:30 -11:00 **SIMPLICITY OR COMPLEXITY: TRANSDUCERS AND INSTRUMENTATION STRATEGIES FOR ACOUSTOFLUIDIC MANIPULATION OF CELLS AND BIOFUNCTIONALIZED BEADS**
Martin Wiklund, Karl Olofsson, and Björn Hammarström
Royal Institute of Technology, SWEDEN

Contributed Talks

11:00 -11:10 **CELL ADHESION, MORPHOLOGY, AND METABOLISM VARIATION VIA ACOUSTIC EXPOSURE WITHIN MICROFLUIDIC CELL HANDLING SYSTEMS**
Citsabehsan Devendran, James Carthew, Jessica E. Frith,
and Adrian Neild
Monash University, AUSTRALIA

11:10 -11:20 **TWO-DIMENSIONAL PATTERNING OF SWIMMING CELLS USING HYBRID ACOUSTIC WAVE DEVICES**
Mingyang Cui¹, Philip V. Bayly¹, Susan K. Dutcher²,
and J. Mark Meacham¹
¹Washington University, St. Louis, USA and
²Washington University School of Medicine, St. Louis, USA

11:20 -11:30 **ACOUSTIC SEPARATION OF VIABLE AND DEAD CELLS USING HIGH-DENSITY MEDIUM**
Karl Olofsson, Björn Hammarström, and Martin Wiklund
KTH Royal Institute of Technology, SWEDEN

11:30 -11:40 **MOTILITY-BASED SPERM SELECTION USING SURFACE ACOUSTIC WAVES**
Junyang Gai, Reza Nosrati, and Adrian Neild
Monash University, AUSTRALIA

11:40 -11:50 **ADVANCED CELL MANIPULATION WITH VORTEX-BASED ACOUSTICAL TWEEZERS**
Michael Baudoin^{1,2}, Jean-Louis Thomas³, Roudy Al Sahely¹, Jean-Claude Gerbedoen¹, Zhixiong Gong¹, Aude Sivery¹, Olivier Bou Matar¹, Nikolay Smagin¹, and Alexis Vlandas¹
¹Université de Lille, FRANCE, ²Institut Universitaire de Franc, FRANCE, and ³Sorbonne Université, FRANCE

11:50 -12:00 **A MICROFLUIDIC PLATFORM FOR ACOUSTIC PARTICLE FOCUSING IN HYDROGEL DROPLETS**
Maria Tenje, Hannah Pohlit, and Anna Fornell
Uppsala University, SWEDEN

Flash Talks

12:00 -12:04 **GENERATING ORDERED CARDIAC TISSUE MODELS USING ACOUSTIC CELL PATTERNING**
Ekaterina Pchelintseva¹, Ilona Sunyovzsky¹, James P.K. Armstrong¹, Alice Agliano¹, Bruce W. Drinkwater², Cesare Terracciano¹, and Molly M. Stevens¹
¹Imperial College London, UK and ²University of Bristol, UK

12:04 -12:08 **A PORTABLE ACOUSTOFLUIDIC BASED CHEMILUMINESCENCE BIOSENSOR**
Xian Chen, Bohua Liu, Wei Pang, and Xuexin Duan
Tianjin University, CHINA

12:08 -12:12 **HIGHLY EFFICIENT ACOUSTOPHORETIC SINGLE CELL-SUPERNATANT SEPARATION INSIDE NANOLITER DROPLETS**
Michael Gerlt¹, Dominik Haidas², Alexandre Ratschat¹, Philipp Suter¹, Petra Dittrich², and Jürg Dual¹
¹ETH Zürich, SWITZERLAND and ²ETH Zürich, Basel, SWITZERLAND

12:12 -12:16 **CHARTING CELL PROPERTIES THROUGH THEIR ACOUSTOPHORETIC MIGRATION IN A GRADIENT OF DENSITY AND COMPRESSIBILITY**
Mahdi Rezayati Charan and Per Augustsson
Lund University, SWEDEN

12:16 -12:20 **REFRACTION OF ACOUSTIC VORTEX BEAMS IN AN INHOMOGENEOUS MEDIUM**
Xudong Fan and Likun Zhang
University of Mississippi, USA

12:20 -12:24 **STREAMING IN A KUNDT'S TUBE OF AN ARBITRARY DIAMETER**
Alen Pavlic and Jürg Dual
ETH Zürich, SWITZERLAND

12:24 -12:28

**REVERSAL OF INTERPARTICLE RADIATION FORCES ACTING ON
MICRO PARTICLES INDUCED BY BULK ACOUSTIC STANDING
WAVES IN A MICROCHANNEL**

Sazid Zamal Hoque and Ashis Kumar Sen
Indian Institute of Technology, Madras, INDIA

12:28

Adjourn for the Day

Thursday, 27 August

08:00 - 08:05 **Opening Remarks**
Thomas Franke, *University of Glasgow, UK*
Henrik Bruus, *Technical University of Denmark, DENMARK*

Session 3 - Physical Acoustics

08:05 - 08:10 **Session Introduction by Session Chairs**
Per Augustsson, *Lund University, SWEDEN*
Henrik Bruus, *Technical University of Denmark, DENMARK*

Invited Speaker

08:10 - 08:40 **ACOUSTIC RADIATION FORCE AND TORQUE ON
NONSPHERICAL SMALL PARTICLES**
Glauber T. Silva
Universidade Federal de Alagoas, BRAZIL

Contributed Talks

08:40 - 08:50 **REPELLER AND ATTRACTOR VORTICES GENERATED IN
SESSILE DROPLETS BY SWIRLING SURFACE ACOUSTIC WAVES**
Shuren Song, Jia Zhou, and Antoine Riaud
Fudan University, CHINA

08:50 - 09:00 **FLEXIBLE/BENDABLE ACOUSTOFLUIDICS BASED ON ZnO/Al
SHEET SURFACE ACOUSTIC WAVES**
Yong Wang^{1,2}, Ran Tao^{2,3}, Qian Zhang¹, Jin Xie¹, and Yong Qing Fu²
¹Zhejiang University, CHINA, ²Northumbria University, UK, and ³Shenzhen University, CHINA

09:00 - 09:10 **THERMAL-GRADIENT-INDUCED FAST CONVECTION IN
ACOUSTOFLUIDIC DEVICES**
Wei Qiu¹, Jonas H. Jørgensen², Enrico Corato¹, Henrik Bruus²,
and Per Augustsson¹
¹Lund University, SWEDEN and ²Technical University of Denmark, DENMARK

09:10 - 09:20 **THEORY OF TEMPERATURE-DEPENDENT EFFECTS IN
ACOUSTOFLUIDICS INCLUDING THERMOVISCOUS BOUNDARY
LAYERS**
Jonas Helboe Jørgensen and Henrik Bruus
Technical University of Denmark, DENMARK

09:20 - 09:30 **THEORY OF ACOUSTIC STREAMING AND ACOUSTIC RADIATION FORCE OF A SOLID PARTICLE IN A VISCOELASTIC FLUID**
Jonas Fankhauser, Alexander A. Doinikov, and Jürg Dual
ETH Zürich, SWITZERLAND

09:30 - 09:40 **MICROSTREAMING INDUCED BY AN ACOUSTICALLY EXCITED GAS BUBBLE - EXPERIMENTS AND COMPARISON TO THEORY**
Sarah Cleve, Gabriel Regnault, Alexander A. Doinikov, Cyril Mauger, Philippe Blanc-Benon, and Claude Inserra
University of Lyon, FRANCE

Flash Talks

09:40 - 09:44 **POLY(N-ISOPROPYLACRYLAMIDE) MICROGELS AS SOLUBLE MARKERS FOR VISUALIZATION OF ACOUSTIC ENERGY ABSORPTION IN AQUEOUS SOLUTIONS**
Amin Rahimzadeh and Regine von Klitzing
Technische Universität Darmstadt, GERMANY

09:44 - 09:48 **ACOUSTIC CHARACTERIZATION OF POLYDIMETHYLSILOXANE (PDMS) FOR MICROSCALE ACOUSTOFLUIDICS**
Guangyao Xu and Xiasheng Guo
Nanjing University, CHINA

09:48 - 09:52 **A NUMERICAL STUDY OF THE COUPLING LAYER BETWEEN A PIEZOELECTRIC BULK TRANSDUCER AND A GLASS DEVICE**
William N. Bodé and Henrik Bruus
Technical University of Denmark, DENMARK

09:52 - 09:56 **ALGEBRAIC RADIATION FORCE EXPANSIONS BEYOND KING, YOSIOKA AND KAWASIMA, AND GOR'KOV, AND RELATED INVESTIGATIONS OF SHAPE DYNAMICS**
Philip L. Marston
Washington State University, USA

09:56 -10:00 **ANALYTICAL PREDICTION OF ACOUSTIC RADIATION FORCES IN SOFT-WALLED MICROCHANNELS DRIVEN BY STANDING SURFACE ACOUSTIC WAVES**
Nitesh Nama¹ and Rune Barnkob²
¹*University of Michigan, USA and*
²*Technical University of Munich, GERMANY*

10:00 -10:04 **AN ANGULAR SPECTRUM BASED FORMULA OF THE 3D ACOUSTIC RADIATION TORQUE APPLIED ON A PARTICLE OF ARBITRARY SIZE AND SHAPE BY AN ARBITRARY ACOUSTIC FIELD**
Zhixiong Gong¹ and Michael Baudoin^{1,2}
¹*University of Lille, FRANCE and*
²*Institut Universitaire de France, FRANCE*

10:04 -10:08 **CLUSTER STRUCTURATION OF PARTICLE MIXTURE IN MULTI-NODE ACOUSTIC LEVITATION WITH OPTICAL EXCLUSION**
Nathan Jeger-Madiot, Mauricio Hoyos, and Jean-Luc Aider
ESPCI, FRANCE

10:08 – 10:25 **Break (offline)**

Session 4 - Acoustic Manipulation

10:25 – 10:30 **Session Introduction by Session Chairs**
Citsabehsan “Saab” Devendran, *Monash University, AUSTRALIA*
Rune Barnkob, *Technical University München, GERMANY*

Invited Speaker

10:30 -11:00 **THE ACOUSTIC HOLOGRAM AND ITS APPLICATION FACILITATED BY THE SPATIAL MODULATION OF ULTRASOUND**
[Peer Fischer](#)^{1,2}, Zhichao Ma¹, Kai Melde¹,
Athanasios G. Athanassiadis¹, and Tian Qiu^{1,2}
¹Max Planck Institute for Intelligent Systems, *GERMANY* and
²University of Stuttgart, *GERMANY*

Contributed Talks

11:00 -11:10 **LONG-DISTANCE MICROPARTICLE STEERING USING GIGAHERTZ ACOUSTIC STREAMING**
Xinyi Guo^{1,2,3}, Zhichao Ma³, Rahul Goyal³, Moonkwang Jeong¹,
Wei Pang², Peer Fischer³, Xuexin Duan², and Tian Qiu¹
¹University of Stuttgart, *GERMANY*, ²Tianjin University, *CHINA*, and
³Max Planck Institute for Intelligent Systems, *GERMANY*

11:10 -11:20 **NUMERICAL SIMULATION OF ACOUSTIC STREAMING GENERATED BY GHz AIN-THIN-FILM TRANSDUCERS ON AIN-SiO₂-BRAGG-REFLECTOR SUBSTRATES**
André G. Steckel and Henrik Bruus
Technical University of Denmark, DENMARK

11:20 -11:30 **EFFECTS OF PARTICLE SHAPE ON ACOUSTOPHORETIC MANIPULATION OF NON-SPHERICAL MICROPARTICLES IN ULTRASONIC STANDING WAVES**
Amir Tahmasebipour, Matthew R. Begley, and Carl D. Meinhart
University of California, Santa Barbara, USA

- 11:30 -11:40** **ACOUSTIC CELL PATTERNING FOR MUSCULOSKELETAL TISSUE ENGINEERING**
 James P.K. Armstrong¹, Sirli Treumuth¹, Bruce W. Drinkwater², and Molly M. Stevens¹
¹Imperial College London, UK and ²University of Bristol, UK
- 11:40 -11:50** **THREE-DIMENSIONAL MANIPULATION OF PARTICLE BY ACOUSTIC TWISTED FOCUSING BEAM**
 Xiangxiang Xia, Feiyan Cai, and Hairong Zheng
Chinese Academy of Sciences, CHINA
- 11:50 -12:00** **SIMULATED AND EXPERIMENTAL DEMONSTRATIONS OF ACOUSTIC HOLOGRAM ENHANCED PHASED ARRAYS FOR MANIPULATION**
 Luke Cox¹, Kai Melde^{2,3}, Anthony Croxford¹, Peer Fischer^{2,3}, and Bruce Drinkwater¹
¹University of Bristol, UK, ²Max Plank Institute for Intelligent Systems, GERMANY, and ³University of Stuttgart, GERMANY

Flash Talks

- 12:00 -12:04** **ACOUSTOFLUIDIC BIDIRECTIONAL MICROPUMP**
 Yuan Gao, Mengren Wu, Yang Lin, Weiqi Zhao, and Jie Xu
University of Illinois, Chicago, USA
- 12:04 -12:08** **CONTROLLED MANIPULATION AND ACTIVE SORTING OF PARTICLES INSIDE MICROFLUIDIC CHIPS USING BULK ACOUSTIC WAVES**
 Kyriacos Yiannacou and Veikko Sariola
Tampere University, FINLAND
- 12:08 -12:12** **ACOUSTIC TRAPPING AROUND OBSTACLES AND CORNERS**
 Asier Marzo¹, Marco A.B. Andrade², María A. Cuellar¹, Jaime Goñi¹, Ryuji Hirayama³, and Diego Martínez³
¹Universidad Pública de Navarra, SPAIN, ²Universidade de São Paulo, BRAZIL, and ³University College London, UK
- 12:12 -12:16** **ACOUSTIC PARTICLE TRAPPING IN A SPHERICAL MICROCHAMBER**
 Bettina Sailer, Rune Barnkob, and Oliver Hayden
Technical University of Munich, GERMANY
- 12:16 -12:20** **ACOUSTIC EXTRACTION AND TRAPPING OF A DROPLET FROM A LIQUID-LIQUID INTERFACE**
 Robert Lirette, Joel Mobley, and Likun Zhang
University of Mississippi, USA

12:20 -12:24 **MICROPARTICLE PATTERNING ON BENDABLE AND FLEXIBLE SAW DEVICES**
Sadaf MaramiZonouz, Mohammad Rahmati, and Richard Yongqing Fu
Northumbria University, UK

12:24 -12:28 **SONOLITHOGRAPHY AS A TOOL FOR IN-AIR PARTICLE MANIPULATION AND SURFACE PATTERNING USING BULK ULTRASONIC STANDING WAVES**
Jenna M. Shapiro¹, Bruce W. Drinkwater¹, Adam W. Perriman¹, and Mike Fraser²
¹University of Bristol, UK and ²University of Bath, UK

Closing Remarks and Announcement of Acoustofluidics 2021

12:28 -12:40 Thomas Franke, *University of Glasgow, UK*
Henrik Bruus, *Technical University of Denmark, DENMARK*

12:40 **Conference Adjourns**

Abstract-Only Presentations

Acoustic Devices

ACOUSTO-MECHANICALLY ENHANCED OSTEMER-GLASS POLYMER HYBRID: TOWARDS CHEAPER ACOUSTOFLUIDIC DEVICES
Karl Olofsson, Elin Forss, Björn Hammarström, and Martin Wiklund
KTH Royal Institute of Technology, SWEDEN

MICROFLUIDIC FUNCTIONALITIES AND WIRELESS SENSING USING SURFACE ACOUSTIC WAVE ACTUATOR AND METAMATERIAL-BASED RESONATOR ON A SINGLE PLATFORM
Shahzad Zahertari¹, Ran Tao^{1,2}, Hamdi Torun¹, Pep Canyelles-Pericas³, and Richard Y.Q. Fu¹
¹Northumbria University, UK, ²Shenzhen University, CHINA, and ³University of Twente, NETHERLANDS

REDUCTION OF TAYLOR-ARIS DISPERSION BY LATERAL ACOUSTIC STREAMING
Pierre Gelin, Dominique Maes, and Wim De Malsche
Vrije Universiteit Brussel, BELGIUM

TWO-DIMENSIONAL MXENES EXFOLIATED AND SPIN-COATED USING SURFACE ACOUSTIC WAVE FOR GAS SENSING
Zerong Chen, Ran Tao, and JingTing Luo
Shenzhen University, CHINA

Bio-Acoustic Systems

A BEAD-BASED ACOUSTOFLUIDIC PLATFORM FOR TIME-CONTROLLED ENZYME REACTIONS IN DROPLETS

Zhenhua Liu, Anna Fornell, and Maria Tenje
Uppsala University, SWEDEN

ACOUSTIC LEVITATION OF *LEISHMANIA* PARASITES

Abelino Vargas^{1,2}, Diana C. Ochoa¹, Marcela Camacho^{1,2}, and Itziar González³
¹*National University of Colombia, Bogotá, COLOMBIA,*
²*International Physics Center (CIF), COLOMBIA, and*
³*CSIC Spanish National Research Council, SPAIN*

ANALYSIS OF A MICROPILLAR BASED QUARTZ CRYSTAL MICROBALANCE SENSOR

Siqi Ji and Hongwei Sun
University of Massachusetts, Lowell, USA

SORTING OF SAME-SIZED CELLS IN TWO-STAGE MICROCHANNEL VIA ACOUSTOFLUIDICS: A NUMERICAL ANALYSIS

Arash Mahboubidoust, Abas Ramiar, Kurosh Sedighi, and Donya Shahani
Babol Noshirvani University of Technology, IRAN

Physical Acoustics

ANALYZING PHYSICAL FIELDS AND PARTICLE MOTIONS INFLUENCED BY DIFFERENT DESCRIPTIONS OF PDMS IN THE MODEL OF SAW-PDMS ACOUSTOFLUIDICS

Zhengyang Ni and Xiasheng Guo
Nanjing University, CHINA

DEFECTS IN A NEW PERIODIC STRUCTURE FORMED BY TWO DIFFERENT SIDE BRANCHES

Mohamed El Malki
Mohammed First University, MOROCCO

DYNAMIC COATING OF ONE LIQUID BY ANOTHER BY EMPLOYING THE ACOUSTOWETTING PHENOMENON

Avital Reizman and Ofer Manor
Technion - Israel Institute of Technology, ISRAEL

MODELING OF ACOUSTIC ENHANCED ELECTROCHEMICAL POLISHING PROCESSES

Johannes Landskron, Sabrina Tietze, Conrad Wolf, and Klaus Stefan Drese
Coburg University of Applied Sciences and Arts, GERMANY

Acoustic Manipulation

A MULTI-CHANNEL PROGRAMMABLE AMPLIFIER FOR HIGH VOLTAGE HIGH FREQUENCY TRANSDUCER EXCITATION

Hiep X. Cao^{1,2}, Han-sol Lee^{1,2}, Dae W. Jung², Byungjeon Kang², Jong-Oh Park^{1,2}, and Chang-Sei Kim^{1,2}

¹*Chonnam National University, KOREA and*

²*Korea Institute of Medical Microrobotics, KOREA*

ACOUSTOPHORETIC MANIPULATION OF PARTICLES IN IMPEDANCE MISMATCHED SYSTEMS

Amal Nath and Ashis K. Sen

Indian Institute of Technology, Madras, INDIA

CONTROL OF A BULK ACOUSTIC WAVE MICRO-CHANNEL THROUGH FREQUENCY SHIFTING AND ITS APPLICATION TO CELL RECONCENTRATION

Ludovic Bellebon^{1,2}, Déborah François², Mauricio Hoyos¹, and Jean-Luc Aider¹

¹*ESPCI Paris, FRANCE and* ²*Aenitis Technologies, FRANCE*

DISPENSING AND MANIPULATION OF FEMTOLITRE DROPLETS BY INKJET NOZZLE

Dege Li¹, Bingfang Huang¹, Yi Cao¹, Chao Zheng¹, Yonghong Liu¹, and Yanzhen Zhang^{1,2}

¹*China University of Petroleum, CHINA and*

²*Swinburne University of Technology, AUSTRALIA*

ROBOTIC MICROFINGERS: ACOUSTIC ASSEMBLY AND MAGNETIC MANIPULATION

Xiaolong Lu^{1,2}, Hui Shen¹, and Ying Wei¹

¹*Nanjing University of Aeronautics and Astronautics, CHINA and*

²*Max-Planck Institute for Intelligent Systems, GERMANY*

WASHING ELECTROPORATED CELLS USING SURFACE ACOUSTIC WAVE (SAW)

Fangda Wu¹, Mao Mao², Fan Yuan², Ming Hong Shen¹, and Xin Yang¹

¹*Cardiff University, UK and* ²*Duke University, USA*

Abstracts

Acoustofluidics
2020

A graphic consisting of three concentric red circles is positioned behind the word 'Acoustofluidics'.

Session 1 - Acoustic Devices

Invited Speaker

ACOUSTOFLUIDICS: MANIPULATING OBJECTS ACROSS 7 ORDERS OF MAGNITUDE

Tony Jun Huang

Duke University, USA

Contributed Talks

MICROSWIMMERS AS LIVING PROBES TO MEASURE THE ACOUSTIC ENERGY DENSITY IN ACOUSTOFLUIDIC DEVICES

Minji Kim¹, Rune Barnkob², and J. Mark Meacham¹

¹Washington University, St. Louis, USA and ²Technical University of Munich, GERMANY

A MULTINODAL ACOUSTIC TRAPPING UNIT WITH INCREASED CAPACITY AND THROUGHPUT FOR CAPTURE OF EXTRACELLULAR VESICLES

Axel Broman, Andreas Lenshof, Mikael Evander, Anson Ku, Yvonne Ceder, Johan Malmström, and Thomas Laurell

Lund University, SWEDEN

MODELING AND EXPERIMENTAL EVALUATION OF A POLYMER-BASED ACOUSTOPHORESIS CHIP

Fabian Lickert¹, Mathias Ohlin², Henrik Bruus¹, and Pelle Ohlsson²

¹Technical University of Denmark, DENMARK and ²AcouSort AB, SWEDEN

CAPILLARY BRIDGE ACOUSTOFLUIDICS

Jeremy J. Hawkes¹, Sadaf Maramizonouz¹, Changfeng Jia², Mohammad Rahmati¹, Tengfei Zheng², Martin B. McDonnell³, and Yong Qing Fu¹

¹Northumbria University, UK, ²Xian Jiaotong University, CHINA, and ³Dstl Porton Down, UK

DROPLET GENERATION FROM STANDING SURFACE ACOUSTIC WAVE (SSAW) STABILIZED FLUIDIC MICROPATTERN

Mehrzad Roudini¹, Dennis Niedermeier², Frank Stratmann², and Andreas Winkler¹

¹SAWLab Saxony, GERMANY and

²Leibniz Institute for Tropospheric Research, GERMANY

MICROFLUIDICS PLATFORM FOR PROTOCOL DEVELOPMENT VIA CAPACITIVE FLUID LEVEL MONITORING AND ACOUSTIC MIXING

Yaqi Zhang¹, Muhsincan Sesen^{1,2}, Alex de Marco¹, and Adrian Neild¹

¹Monash University, AUSTRALIA and ²Heriot-Watt University, UK

FABRICATION OF SURFACE ACOUSTIC WAVE (SAW) DEVICES USING DETACHABLE ELECTRODES BASED ON A FLEXIBLE PRINTED CIRCUIT BOARD (PCB)

Roman Mikhaylov, Zhihua Xie, Aled Clayton, and Xin Yang
Cardiff University, UK

GALLIUM NITRIDE THIN FILM FOR ACOUSTIC TWEEZER

Chao Sun¹, Huaixing Cang¹, and Xin Yang²
¹*Northwestern Polytechnical University, CHINA* and ²*Cardiff University, UK*

ACOUSTICALLY DRIVEN MENISCUS MODES IN INKJET PRINTING

Martin van den Broek¹, Maaïke Rump¹, Roger Jeurissen², Hans Reinten³, Detlef Lohse¹, Michel Versluis¹, Guillaume Lajoinie¹, and Tim Segers¹
¹*University of Twente, NETHERLANDS*,
²*Eindhoven University of Technology, NETHERLANDS*, and
³*Canon Production Printing Netherlands B.V., NETHERLANDS*

DROPLET DEMULSIFICATION AT PARALLEL FLOW INTERFACE USING SOUND WAVES

E. Hemachandran and Ashis Kumar Sen
Indian Institute of Technology, Madras, INDIA

DROPLET IMPACT CONTROL BY SURFACE ACOUSTIC WAVES

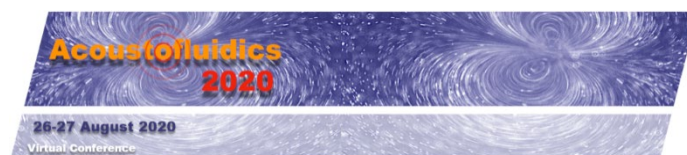
Mehdi H. Biroun¹, Mohammad Rahmati¹, Glen McHale¹, Mehdi Jangi², Hamdi Torun¹, and Richard YongQing Fu¹
¹*Northumbria University, UK* and ²*University of Birmingham, UK*

DROPLET MERGING IN A PDMS MICRO-WELL DRIVEN BY SURFACE ACOUSTIC WAVES

Sudeepthi Aremanda¹, Lelie Yeo², and Ashis Kumar Sen¹
¹*Indian Institute of Technology, Madras, INDIA* and ²*RMIT University, AUSTRALIA*

HIGH-THROUGHPUT TRIGGERED MERGING OF DROPLETS USING TRAVELLING SURFACE ACOUSTIC WAVES

Vincent Bussiere¹, Aurélie Vigne^{1,2}, Andreas Link¹, John McGrath¹, Aparna Srivastav¹, Esther Richter¹, Ziyun Wang¹, Mustafa Zaimagaoglu¹, Jean-Christophe Baret², and Thomas Franke¹
¹*University of Glasgow, UK* and ²*Université de Bordeaux, FRANCE*



Acoustofluidics: manipulating objects across 7 orders of magnitude

Tony Jun Huang

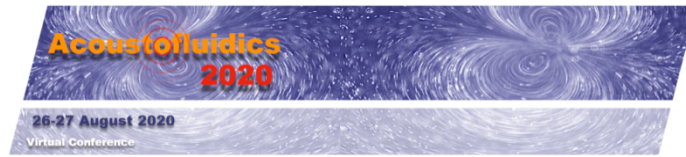
William Bevan Distinguished Professor of Mechanical Engineering and Materials Science
Pratt School of Engineering, Duke University, U.S.A.
E-mail: tony.huang@duke.edu, URL: <https://acoustofluidics.pratt.duke.edu/>

Abstract

In this talk, we summarize our recent progress on acoustofluidic devices and review their applications, with emphasis on the manipulation of cells, particles, microorganisms, and fluidic flows. These acoustofluidic devices can manipulate objects across 7 orders of magnitude (from a few nanometers to a few centimeters). Their versatility, simple device designs, non-invasive and contactless operation, and label-free nature are all characteristics that make them ideal tools for fundamental research, diagnostics, and therapeutics. For example, we have created devices to sort and separate nanosized bioparticles such as exosomes from blood for health diagnostics. We have also shown the capacity for gene delivery through acoustofluidic sonoporation of target cells to facilitate the uptake of plasmid DNA. To further expand the applications of our technology, we have developed acoustofluidic methods for the rapid mixing of reagents to synthesize nanoparticles and complex arrays of nanostructures. We have demonstrated the versatility of acoustofluidics by developing acoustic tweezers that have the ability to rotate, concentrate, and sort nanoparticles and microorganisms; we have worked with target nanoparticles such as quantum dots, and larger model organisms such as *C. elegans* and zebrafish at micro and centimeter scales. Additionally, progress has been made towards making acoustic tweezer technology more compatible with existing workflows in biomedical laboratories, such as the seamless integration of an acoustofluidic nanoscope to common microscopes and the manipulation of bioparticles in Petri dishes without the need of customized microfluidics. Improving on the resolution of our previous technology, we have also shown the capability to dynamically modulate acoustic wavefields to position and manipulate particles in multiconfigurational patterns for a variety of applications such as tissue engineering and cell-cell interaction studies. Thanks to their versatility, biocompatibility, and convenience in operation, acoustofluidic devices hold great potential to become a staple in noncontact manipulation and advance many areas of biological research and clinical applications.

Biography

Tony Jun Huang is the William Bevan Distinguished Professor of Mechanical Engineering and Materials Science at Duke University. Previously he was a professor and the Huck Distinguished Chair in Bioengineering Science and Mechanics at The Pennsylvania State University. He received his Ph.D. degree in Mechanical and Aerospace Engineering from the University of California, Los Angeles (UCLA) in 2005. His research interests are in the fields of acoustofluidics, optofluidics, and micro/nano systems for biomedical diagnostics and therapeutics. He has authored/co-authored over 230 peer-reviewed journal publications in these fields. His journal articles have been cited more than 18,000 times, as documented at Google Scholar (h-index: 73). He also has 26 issued or pending patents. He was elected a fellow of the following six professional societies: the American Association for the Advancement of Science (AAAS), the American Institute for Medical and Biological Engineering (AIMBE), the American Society of Mechanical Engineers (ASME), the Institute of Electrical and Electronics Engineers (IEEE), the Institute of Physics (IoP), and the Royal Society of Chemistry (RSC). Huang's research has gained international recognition through numerous prestigious awards and honors including a 2010 National Institutes of Health (NIH) Director's New Innovator Award, a 2012 Outstanding Young Manufacturing Engineer Award from the Society for Manufacturing Engineering, a 2013 American Asthma Foundation (AAF) Scholar Award, JALA Top Ten Breakthroughs of the Year Award in 2011, 2013, and 2016, the 2014 IEEE Sensors Council Technical Achievement Award from the Institute of Electrical and Electronics Engineers (IEEE), the 2017 Analytical Chemistry Young Innovator Award from the American Chemical Society (ACS), the 2019 Van Mow Medal from the American Society of Mechanical Engineers (ASME), and the 2019 Technical Achievement Award from the IEEE Engineering in Medicine and Biology Society (EMBS).



Microswimmers as living probes to measure the acoustic energy density in acoustofluidic devices

Minji Kim^{1*}, Rune Barnkob², and J. Mark Meacham^{1†}

¹Department of Mechanical Engineering and Materials Science, Washington University in St. Louis, St. Louis, MO 63130, USA

*E-mail: kim.minji@wustl.edu, †E-mail: meachamjm@wustl.edu, URL: <https://meachamlab.wustl.edu/>

²Heinz-Nixdorf-Chair of Biomedical Electronics, Department of Electrical and Computer Engineering, Technical University of Munich, 81675 Munich, Germany

Introduction

We propose a method for use of motile *Chlamydomonas reinhardtii* (CR) algae cells to determine the acoustic energy density E_{ac} , a primary measure of acoustic microfluidic device performance. We previously reported *qualitative* mapping of acoustic pressure fields using living microswimmers as active probes.¹ Here, we extend this approach to enable *quantitative* measurement of the acoustic energy density as an alternative to conventional passive particle tracing. First, the utility of CR cells as measurement probes is described. Acoustophysical properties were measured and combined with previously reported values for CR cell swimming capability² to allow connection of the evolving cell density distribution to the acoustic field shape and strength. The acoustic energy density within a straight microchannel driven at the first half-wavelength resonance was then calculated using the balance of swimming and acoustic radiation forces. Measurements were comparable to those obtained using acoustophoretic migration of passive particles, demonstrating the potential of the method to become a rapid and accurate experimental measurement tool in acoustofluidics.

C. reinhardtii as living measurement probes

CR is a motile unicellular alga (diameter $8.0 \pm 1.1 \mu\text{m}$, $n = 138$) that exhibits random swimming motion (speed $\sim 100 \mu\text{m/s}$)². Laboratory culture is straightforward. Wild-type cells (strain CC-125) are streaked and grown in agar plates at 25°C under constant lighting for 48 hrs. After this initial incubation period, plates can be stored on the bench for several weeks at room temperature (CR cells prefer conditions from 20–32°C); however, for the experiments reported here, new plates were made every week to ensure cell viability. Cells are scraped from agar plates and suspended in a nutrient deficient medium for three hours prior to an experiment. Density gradient centrifugation was used to obtain the mass density of deciliated cells. The speed of sound in neutrally buoyant cell suspensions was measured at various volume fractions. Average compressibility was then calculated using Wood's equation. The cell preparation steps ensure a cell suspension of a single mating type, which provides active particles of uniform size and acoustophysical properties (relative to other biological cell types).

Acoustic energy density measurement using living probes

CR cells swim within an imposed acoustic field so that the density distribution of swimming cells can be correlated to the field shape and strength throughout a device. The balance of the swimming force, acoustic radiation force, and drag dictates the extent of spread of a cell population (Fig. 1A,B). If the strength of an acoustic potential well exceeds a characteristic threshold swim force F_{swim} , the magnitude of the swimming force will equal that of the acoustic radiation force at the trap boundary. E_{ac} at the first half-wavelength resonance of a straight channel can be expressed as

$$E_{ac} = F_{swim} / [4\pi a^3 \Phi_{cell} k_y \sin(2k_y y_{bd})] \quad (1)$$

where a is the cell radius, k_y the wavenumber, and y_{bd} the location of the trap boundary. The acoustic contrast factor Φ_{cell} is a function of the density and compressibility of the cells and medium.

The cell sample concentration was adjusted to 10^6 cells per mL. The cell suspension was loaded into a silicon-glass chip with a rectangular fluidic channel ($l = 30 \text{ mm}$, $w = 375 \mu\text{m}$, $d = 50 \mu\text{m}$), with the random motion of cells naturally forming a uniform distribution. A bulk PZT-8 piezoelectric element was used to actuate the device at 1.81 MHz. The voltage was linearly increased from 0 to 10 V at discrete steps. Below a

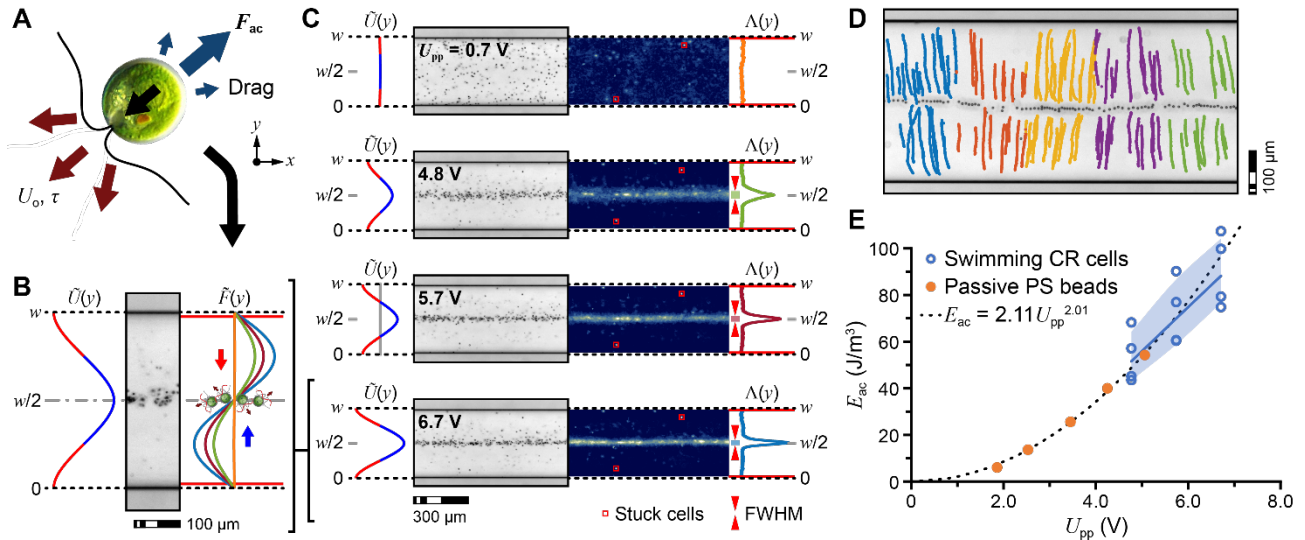


Figure 1: (A) Forces acting on an acoustically-confined swimming cell. (B) Cells trapped within the potential well of a straight channel driven at the first half-wavelength resonant frequency ($f = 1.81$ MHz). (C) Brightfield images and heat maps of CR cell distributions. (D) Brightfield images and particles trajectories of polystyrene beads. (E) E_{ac} vs. U_{pp} obtained using active CR probes and passive particle tracing.

threshold voltage (~ 3 V), the swim force overcomes the acoustic radiation force and cells explore the entire channel. The local acoustic radiation force eventually exceeds the swimming force, and cells become confined to the potential well at the channel midline (Fig. 1B,C). The acoustic trap boundary location for different input voltages was defined as the full width at half maximum (FWHM) for cell density distributions $\Lambda(y)$ averaged along a length of channel (Fig. 1C). Using FWHM to represent the trap width, E_{ac} could be calculated as a function of drive voltage (Fig. 1E, open blue circles with blue average fit line).

Method validation using passive particles

Acoustic energy density was also measured using a conventional approach (passive beads)³ to validate the newly reported method (active CR probes). Passive particle movement in an acoustic field is governed by the balance of the acoustic radiation force and viscous drag. Hence, for particles with radius R in a quiescent liquid with viscosity η , E_{ac} is

$$E_{ac} = 3\eta u_y / [2\Phi_{\text{particle}} R^2 k_y \sin(2k_y y)] \quad (2)$$

where u_y is the particle velocity. E_{ac} can be calculated from a least-squares fit in u_y and y for each trajectory.

Migration of 5 μm polystyrene (PS) beads, suspended in the algae medium, was recorded over the same voltage range. In contrast to the cell-based measurement approach, it was challenging to obtain a uniform initial distribution, and the method relied on laborious tracing of individual microbead trajectories (Fig. 1D). Velocity varied according to the input voltage enabling determination of E_{ac} from Eq. 2 (Fig. 1E, closed orange circles).

Conclusion

We have shown that the acoustic energy density of a microfluidic channel can be rapidly and accurately determined using living microswimmers as measurement probes. Dynamically-responsive CR cells overcome limitations of conventional passive particle tracing methods to produce comparable results. Though critical method development and refinement remain, by establishing this approach, we hope to improve the operational stability of acoustofluidic technologies and accelerate their adoption in emerging chemical, biological, and biomedical application areas.

Acknowledgements

This work was supported by the National Science Foundation, under Grant No. CMMI-1633971, the German Academic Exchange Service (grant 57442045), and the Spencer T. and Ann W. Olin Fellowship (MK).

References

- [1] M. Kim, E. Huff, P.V. Bayly, and J.M. Meacham, *Acoustofluidics 2019*, Enschede, Netherlands, 25-28 August 2019.
- [2] M. Kim, E. Huff, M. Bottier, S.K. Dutcher, P.V. Bayly and J.M. Meacham, *Soft Matter* **15**, 4266-4275 (2019).
- [3] R. Barnkob, P. Augustsson, T. Laurell, and H. Bruus. *Lab Chip*, **10**, 563-570 (2010).

A multinodal acoustic trapping unit with increased capacity and throughput for capture of extracellular vesicles

Axel Broman¹, Andreas Lenshof¹, Mikael Evander¹, Anson Ku², Yvonne Ceder³, Johan Malmström³ and Thomas Laurell¹

¹Department of Biomedical Engineering, Lund University, Lund, Sweden

E-mail: axel.broman@bme.lth.se

²Department of Translational Medicine, Lund University, Lund, Sweden

³Department of Clinical Sciences, Lund University, Lund, Sweden

Introduction

We report a new design of an acoustophoretic trapping device with greatly increased capacity and throughput, compared to current commercial systems. By using a larger capillary that supports an acoustic multi-node resonance, **capacity and throughput were increased 40-fold** compared to traditional single-node systems. It was possible to capture and enrich extracellular vesicles from urine samples at 30 times higher flow rate than previously reported.

Background

In acoustic trapping, a strong localised acoustic field is generated inside a channel which retains particles against flow, allowing for nanoparticle enrichment and purification. Hammarström [1] showed the first capturing of particles down to 100 nm size by pre-loading the trap with larger seed particles. Ku [2] recently showed that it was possible to enrich exosomes from urine using the AcouTrap at a modest flow rate of 15 $\mu\text{l}/\text{min}$, isolating 0.79 ng of vesicle bound mRNA from 9.75 ml urine.

Device

The new acoustic trapping unit comprises a glass capillary (2x4x50 mm³) and a piezoelectric transducer actuated at 4.4 MHz, creating 9 distinct trapping nodes stacked vertically above the transducer, figure 1. The trapping capacity of the device was assessed by trapping 12 μm polystyrene seed particles, followed by washing to remove weakly trapped particles and then collecting and counting the particles in the cluster.

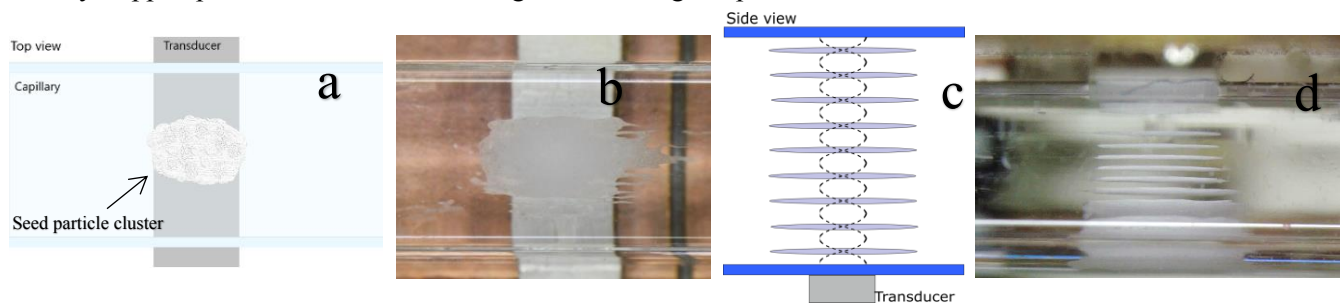


Figure 1: a) Schematic drawing of the device from a top view. b) Photograph of a trapped cluster as viewed from above. c) Schematic drawing of the device viewed from the side. A standing wave with multiple pressure nodes creates separate clusters of seed particles. d) Photograph of a trapped cluster as viewed from the side, with the transducer at the top of the picture.

The trapping efficiency of fluorescent nanoparticles at different flow rates and fixed voltage (11 V_{pp}) was investigated by loading the trap with seed particles where after a known volume of fluorescent nanoparticle suspension was aspirated and trapped. The trapping cluster was collected, and the fluorescence was compared to the original sample. Finally, urine samples of different volumes (1, 2 or 3 ml) were trapped at 500 $\mu\text{l}/\text{min}$. The trapped urine exosomes were then analysed using nanoparticle tracking (NanoSight) to determine size distribution. Following RNAase treatment to remove any free RNA, exosomal RNA was extracted from the samples and analysed in an Agilent 2100 Bioanalyzer.

Results and discussion

A maximum trapping capacity of $8.6 \cdot 10^5$ seed particles was measured, figure 2a, as compared to the AcouTrap which has a trapping capacity of around $2 \cdot 10^4$ corresponding seed particles, i.e. a 40-times increase. The trapping efficiency measurements showed that it was possible to hold a stable cluster and trap submicron particles for flow rates up to 2000 $\mu\text{l}/\text{min}$, i.e. 40 times higher than the highest recommended flow rate for the AcouTrap, figure 2b.

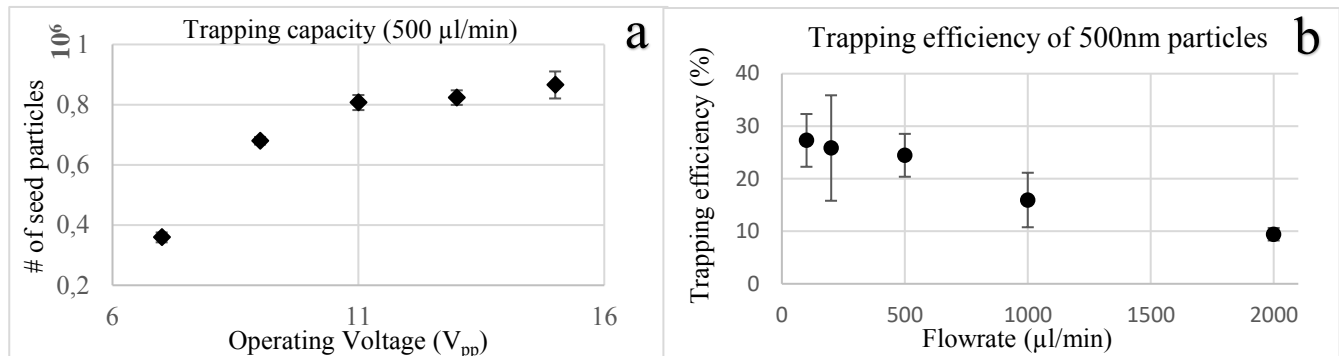


Figure 2: a) The trapping capacity of 12 μm polystyrene seed particles vs. actuator voltage. Particles were counted in a BD FACS Canto II along with a known concentration of Trucount beads to calculate the capacity. The flow rate was constant at 500 $\mu\text{l}/\text{min}$. b) Trapping efficiency of 500 nm fluorescent particles on the seed particle cluster for different flow rates. The operating voltage of the piezo was fixed at 11 V_{pp} . Trapping efficiency was obtained by measuring the fluorescence of the trapped sample using a plate reader (FLUOstar Omega) and comparing versus the 500 nm particle input sample.

The nano track analysis displayed a peak of particles at around 100 nm, figure 3a, and the corresponding Bioanalyzer data confirmed RNA around a few 100 nucleotides in size, figure 3b, both of which are to be expected from exosomes. The total recovered RNA was around 2 ng from 3 ml of urine, figure 3c. The total processing time for 3 ml of urine was approximately 10 minutes as compared to 6-7 hours using the AcouTrap [2].

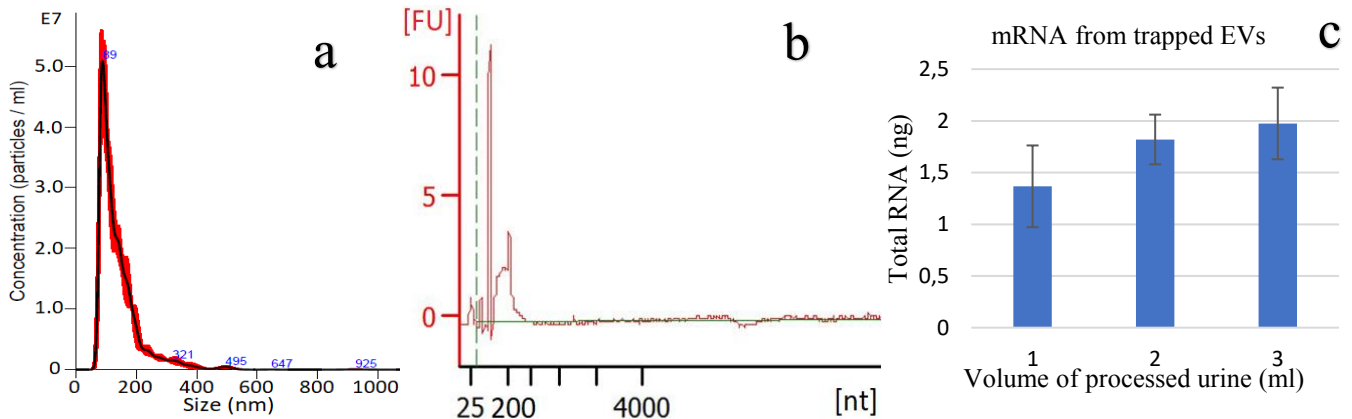


Figure 3: a) Nanoparticle tracking of 3 ml of processed urine. A clear peak of particles around 100 nm that corresponds well to the size of exosomes. b) RNA results from the bioanalyzer from 3 ml of processed urine. There is a clear peak around a few hundred nucleotides, which is typical for mRNA in exosomes. c) Quantification of average total mRNA from all samples.

Conclusion

Our multinodal trapping device shows both greatly increased capacity and throughput, allowing for rapid enrichment of extracellular vesicles and nanoparticles from millilitre sized samples.

References

- [1] B. Hammarström et al. *Lab chip*, 2012, **12**, 4296-43
- [2] A. Ku et al. *PLoS ONE*, 2019, 14(5)

Modeling and experimental evaluation of a polymer-based acoustophoresis chip

Fabian Lickert¹, Mathias Ohlin², Henrik Bruus¹ and Pelle Ohlsson^{2*}

¹Department of Physics, Technical University of Denmark, Kongens Lyngby, Denmark
E-mail: fabianl@dtu.dk, URL: www.fysik.dtu.dk/microfluidics

²AcouSort AB, Lund, Sweden,

*E-mail: pelle.ohlsson@acousort.com, URL: www.acousort.com

Introduction

In this work, we compare numerical simulations with measurements of the focusability of suspended microparticles and the acoustic energy density in a PMMA-chip using the concept of whole-system ultrasound resonances, introduced recently by Moiseyenko and Bruus [1] to explain how to obtain particle acoustophoresis in polymer-based devices. Polymer acoustophoresis devices are desirable, as they reduce cost and facilitate integration into diagnostic cartridges. However, so far it has been a challenge to reach the high throughput and separation performance of silicon-glass devices. Here, we measure an energy density of 4.1 J m^{-3} at 25 V_{pp} and good microparticle focusing in the PMMA chip.

Overview of the device

The device under study, shown in Fig. 1, is a chip made from polymethylmethacrylate (PMMA) containing a long, straight microchannel. The chip is mounted on top of a piezoelectric transducer (PZT) using an approximately $100 \text{ }\mu\text{m}$ -thick coupling layer of glycerol, modeled as 99% glycerol and 1% water. The top electrode of the transducer is split in half by cutting a groove to enable an anti-symmetric voltage actuation ($V_{pp} = 25 \text{ V}$) as described in Refs. [1,2]. Hereby, a standing pressure wave is excited in the channel with a vertical pressure node in the center.

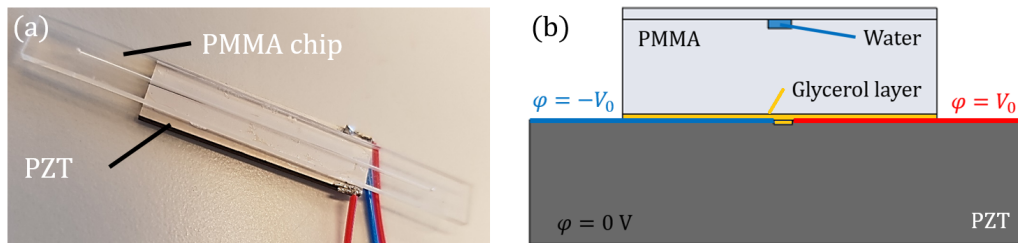


Figure 1: The device consists of a water-filled channel of length 40 mm , width $375 \text{ }\mu\text{m}$, and height $150 \text{ }\mu\text{m}$ embedded in a PMMA chip of length 50 mm , width 5 mm , and height 1.675 mm . The chip is placed on top of a piezoelectric PZT actuator with dimensions $25 \text{ mm} \times 8 \text{ mm} \times 2 \text{ mm}$, coupled through a $100 \text{ }\mu\text{m}$ -thick glycerol layer. (a) A picture of the PMMA chip mounted on top of the PZT transducer. (b) The 2D cross-section of the device used in the numerical simulations.

Numerical simulation of the 2D system

We model the device numerically using the FEM-software *COMSOL Multiphysics*, as described in detail in our previous work Refs. [1,2]. We analyze the acoustic energy density E_{ac} inside the water-filled channel in the frequency range from 0.8 to 1.5 MHz , around the nominal 1-MHz -resonance frequency of the used PZT transducer. In this frequency range three prominent resonances f_1 , f_2 , and f_3 are identified, the strongest one at $f_2 = 1.275 \text{ MHz}$ with $E_{ac} = 7.93 \text{ J m}^{-3}$, as shown in Fig. 2(a) and (b). We find numerically that the highest acoustic energy densities in the channel are obtained by placing the PMMA chip with the channel far away from the transducer. The reason is that in this configuration, a strong vibrational resonance is induced in the thin lid. As shown in Fig. 2(c), the acoustic radiation force for the resonance f_2 is nearly ideal: Its horizontal component is strong and points towards the vertical center plane, whereas its vertical component is relatively small. This leads to a focusing of particles at the pressure node at the vertical center plane of the channel. The acoustic radiation force of the other two resonances f_1 and f_3 are weaker and less ideal in shape.

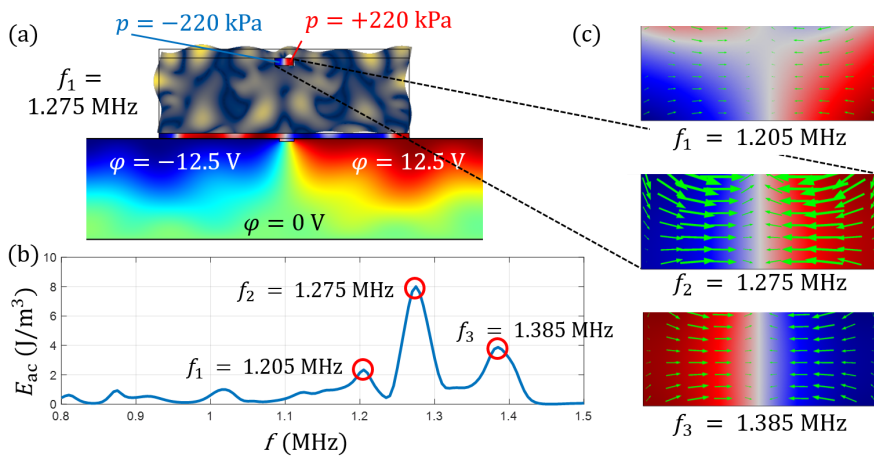


Figure 2: Simulation results. (a) Displacement u of the PMMA chip from 0 nm (blue) to 14.0 nm (yellow), pressure p_1 from -220 kPa (blue) to $+220$ kPa (red) in the water and from -250 kPa to $+250$ kPa in the glycerol, and the electric potential φ in the PZT transducer. (b) Acoustic energy density E_{ac} inside the channel versus frequency f . (c) Close-up of the fluidic channel with pressure p_1 (blue-red) and the normalized acoustic radiation force F_{rad} (green vectors).

Experimental verification

The above system is characterized experimentally by analyzing the particle focusing ability of the polymer chip. Particle focusing, using a suspension of $4.8\text{-}\mu\text{m}$ -diameter polystyrene particles in *Milli-Q* water at 37°C , was characterized by the full-width-threshold-maximum (FWTM) number: we use the width of the recorded intensity curve of the CCD images at a threshold of 10% of the maximum intensity. Sweeping the frequency from 1.0 to 1.3 MHz in steps of 0.01 MHz, the particle focusing during continuous flow operation was recorded by a CCD camera for each frequency point, see Fig. 3(a). We also characterized the focusing under stop-flow conditions in a neutrally buoyant solution (2 mL *OptiPrep*, 8 mL *Milli-Q* water) at 20°C , where the particle focusing was recorded as an image series at a fixed frequency of $f = 1.16$ MHz at different times t after turning on the acoustics, see Fig. 3(b).

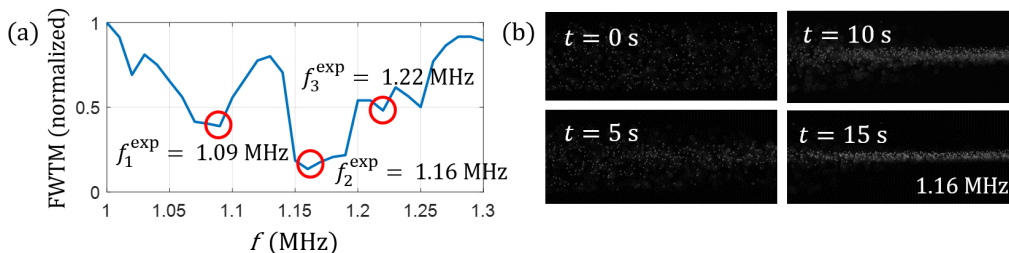


Figure 3: (a) Measured full width at threshold maximum (FWTM) vs. frequency. (b) Images of the particles in the channel at $f = 1.16$ MHz during a no-flow condition as function of time after turning on the acoustics.

Analyzing the particle intensities in the given frequency range, we found several minima in the intensity distribution over the channel width, indicating good focusing strengths. The best focusing was observed at $f_2^{\text{exp}} = 1.16$ MHz. At this resonance frequency, we used the light-intensity method [3] to measure the average acoustic energy density, and found it to be $E_{ac} = (4.1 \pm 0.1) \text{ J m}^{-3}$ (average of three repeated measurements). The simulated resonance frequency ($f_2 = 1.27$ MHz) differs about 9% from the experimentally found f_2^{exp} , while the acoustic energy density in the simulation is twice the value of the experiment. Those differences are rooted in the uncertainties of the used material parameters for the PMMA as well as additional losses through clamping and fluid connections, which have not been considered in the simulation model.

Conclusion and outlook

We have found some promising resonance frequencies in our numerical simulation in the acoustic energy density, that are suitable for acoustophoresis applications. Some guidelines for the design of polymer devices were given, such as orienting the chip with the channel away from the transducer and removing the top electrode under the channel. The existence of the simulated resonances in a purely PMMA-based chip was confirmed through experiments. Further characterization of the materials is needed to increase the accuracy of the parameters and thereby improve the overall simulation model.

Acknowledgement

This work is part of the Eureka Eurostars-2 E!113461 AcouPlast project funded by Innovation Fund Denmark, grant no. 9046-00127B, and Vinnova, Sweden's Innovation Agency, grant no. 2019-04500.

References

- [1] R.P. Moiseyenko and H. Bruus. *Physical Review Applied* **11**, 014014 (2019). [pdf]
- [2] W.N. Bodé, L. Jiang, T. Laurell, and H. Bruus. *Micromachines* **11**, 292 (2020). [pdf]
- [3] R. Barnkob, I. Iranmanesh, M. Wiklund and H. Bruus. *Lab Chip* **12**, 2337-2344 (2012). [pdf]

Capillary Bridge Acoustofluidics

Jeremy J Hawkes¹, Sadaf Maramizonouz¹, Changfeng Jia², Mohammad Rahmati¹, Tengfei Zheng², Martin B. McDonnell³, Yong Qing Fu¹

¹ Faculty of Engineering and Environment, Northumbria University, Newcastle upon Tyne, NE1 8ST, UK.
E.mail: jeremyjhawkes@gmail.com

² State Key Laboratory for Manufacturing Systems Engineering, Xian Jiaotong University, 710049, Xian, 710048, P.R. China

³ Dstl Porton Down, Salisbury, Wiltshire SP4 0JQ, UK

Introduction The capillary bridge: a liquid spanning a gap and held by surface tension (see figure 1), will be introduced as a convenient method to form acoustofluidics channels for particle and fluid manipulation. These channels are easily constructed on microscope slides using fluid guides cut from foil or thin plastic sheets. No clean room or specialized facilities are required apart from a 3D printer and a plotter cutter. The absence of side walls, simplifies cleaning, reduces retention on the walls and allows fluid paths to be reconfigured and interrogated at any location and any time. We create plate waves in the slide, using a PZT to drive the edge of the slide [1] with a glue-free pressure contact. Vibrations are transferred from PZT to the slide, and then to the liquid in the capillary bridge, where cells and other particles are driven to the nodes formed in the liquid. These nodes are often straight and parallel lines. Capillary bridges are now leading us to develop new theories of how nodes form in acoustofluidic systems:

Nodes are found to form at right angles to the microscope slide face in simulations and in experiments with bridges of $\sim\lambda/2$ (λ = wavelength) liquid depth. We propose that most of these nodes have originated from the crossing of standing leaky waves and not reflections from the liquids side walls. The node separation in the fluid is therefore dependent on the locations of the nodes in the glass.

Particle alignment in the liquid bridge is governed by the channel edge, not the PZT source direction. We propose that at the air:water interface the glass experiences a change in acoustically coupled mass which increases with water depth, and therefore the wave alignment in the glass changes at the boundary edge. The nodes in the liquid bridge follow this induced boundary alignment in the glass.

Evanescent waves formed at the foil/liquid interface are used to explain experimental observations that patterns of dot like clumps form near the liquid guide surface in systems with a liquid depth of $\sim\lambda/7$.

These capillary bridge acoustofluidics channels without side walls could be configured to generate functions for many of the flowing and static applications of their walled counterparts e.g. filtration/separation, deposition on a surface, particle agglutination, droplet creation and fluid mixing.

The Capillary Bridge

Systems were constructed with uniform gaps between the microscope slide and the fluid guide of 0.75 and 0.2 mm over a 40 mm length, as illustrated in figure 1. Fluid guides formed by a polystyrene sheet (0.05 mm thick 3 mm wide) were tightly stretched to achieve a uniformity along the gap. The sheet was cut to the required channel shape using a plotter cutter. Fluid was introduced through a hole in one end of the fluid guide and withdrawn from the other end. During the node alignment observation there was no flow.

Leaky waves align particles along narrow bridges (channels)

When the microscope slide was vibrated at a resonance near 1 MHz, yeast cells in a half wavelength deep capillary bridge align along the length direction of the bridge as in figure 2a. Simulations show that the presence of water changes the wave vibration pattern in the adjacent glass.

Figure 2: Nodes formed in capillary bridges without any flow. a) One capillary bridge 3mm wide x 0.75 mm deep Yeast aligns in 3 bands. b) Simulation of glass (above), fluid bridge and polystyrene film below).

The nodes in the water are vertical and waves in the glass are changed by the adjacent water.

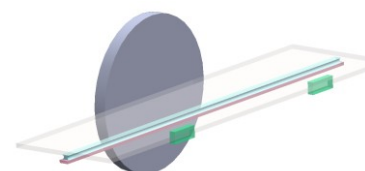
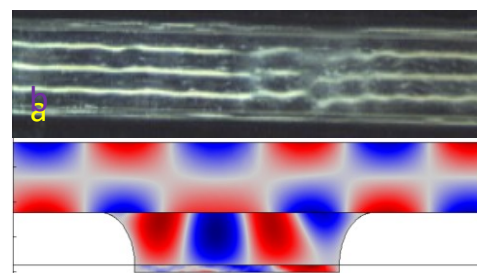
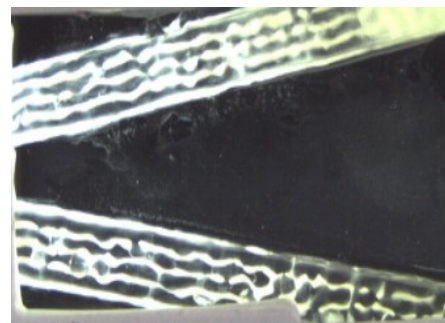


Figure 1: Simplified diagram of the microscope slide edge pushed against the PZT drive with the capillary bridge below formed between the slide face and the fluid guide (pink). A bridge can be formed above or below the slide.



Particle (node) alignment usually forms parallel to the edge of the bridge regardless of its angle compared to the PZT face (see figure 3).

Figure 3 Two bridges set at 20° angles to the PZT. Yeast clump alignment follows the bridge edge not the PZT face.



Although this node alignment suggests that standing waves are formed between the free surfaces of the fluid this is unlikely since the free fluid surfaces may be curved and are narrower than the horizontal surfaces.

We propose an alternative explanation for the nodal pattern: Antinode regions on the glass surface act as point emitters sending sound into the fluid as shown in figure 4. The circular waves spread through the fluid forming nodes and antinodes aligned at right angles to the glass surface (like Bragg diffraction). Node separation is therefore governed by the wavelength in the glass and not the water. However the glass wavelength decreases with water depth since water mass-loading is coupled to the glass. This also locally distorts waves in the glass producing a pattern aligned with the edge of the fluid. Therefore the alignment of cell clumps seen in figures 2 and 3 is following the node alignment in the glass. This is in contrast to PDMS chambers where there is no mass change at the wall and no alignment along the wall[2].

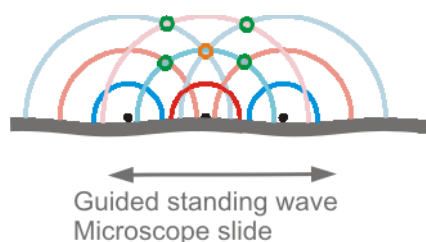


Figure 4: Circular waves in the fluid emitted by antinode regions on the glass. In the fluid nodes (green circles) and antinodes (orange circle) form along vertical lines (Diagram shows a moment in time nodes and antinodes form continuous vertical lines over one cycle).

Evanescent waves move particles onto the fluid guide surface

In channels with depths less than half of a wavelength, the cell clumps form a pattern of small dots, which appear to be on the waveguide surface.



Figure 4: Bridge depth 0.2 mm ($\sim\lambda/7$). An array of small clumps form on the polystyrene surface.

At 1 MHz the wavelength of the antisymmetric wave A0 in the polystyrene is 0.46 mm. This is shorter than the 1.5 mm wave in the water therefore the angle θ_{leak} for sound leaking into the fluid is imaginary.

$\theta_{leak} = \sin^{-1}(\lambda_{fluid}/\lambda_{plate})$ This will cause an evanescent wave (a short circuit of positive displacements in the fluid returning to negative displacements in the slow moving wave of the wall) with most energy located near the waveguide surface. The evanescent wave forms into a standing wave grid pattern where particles are accumulated in small clumps at nodes on the surface of the polystyrene wall. This has been proposed as a method for bringing cells to an antibody coated wall[3].

Conclusions

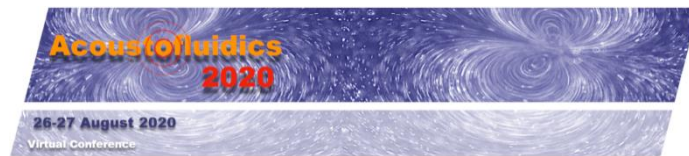
Capillary bridge channels appear to be a good contender for most acoustofluidics applications where enclosed channels are currently used.

Without walls the number of sound paths are reduced consequently the interpretation and testing of models is simplified. The following are conclusions we have obtained:

- (1) Nodes formed by crossing waves leaking at angles from a standing waves on the drive surface describe features of the observed nodes better than the regular model of nodes formed by standing-waves in the fluid reflected by the liquids side walls. (This also applies to some PDMS channels).
- (2) The water mass changes the wave patterns in the glass which in turn defines the location of nodes in the fluid.
- (3) Evanescent waves can be formed by waves induced in the fluid guide.

References

- [1] A. Haake, A. Neild, G. Radziwill, J. Dual, *Biotechnology and Bioengineering* **92**, 8-14 (2005).
- [2] I. Leibacher, S. Schatzer, J. Dual, *Lab on a chip* **14**, 463-470 (2014).
- [3] J. J. Hawkes, M. J. Long, W. T. Coakley, M. B. McDonnell, *Biosensors and Bioelectronics* **19**, 1021-1028 (2004).



Droplet generation from standing surface acoustic wave (sSAW) stabilized fluidic micropattern

Mehrzad Roudini¹, Dennis Niedermeier², and Frank Stratmann², and Andreas Winkler¹

¹IFW Dresden, SAWLab Saxony, PF 270116, 01171 Dresden, Germany

E-mail: m.roudini@ifw-dresden.de

²Leibniz Institute for Tropospheric Research, Leipzig, Germany

Introduction

Atomizers are attracting widespread interest in many technical processes due to their capability to disperse a bulk of a liquid into single droplets with different ranges in size and velocity, by means of the liquid kinetic energy or additional external forces. Small and compact Surface Acoustic Wave (SAW) aerosol generators (or nebulizers) are able to generate micrometer-sized droplets with low velocity without the need for moving parts or nozzles, and were demonstrated as possible key components for various future applications, including inhalation therapy, material deposition, liquid chromatography / spectroscopy and olfactory displays. Despite the extensive diversity of industrial applications, the further development into application-adapted devices requires both, the understanding of the yet unknown droplet generation mechanism(s) underlying SAW atomization and the estimation of the initial droplet size distribution produced by SAW aerosol generators in dependence of fluid and SAW properties.

In this work, the hydrodynamics associated with sSAW interaction will be discussed based on high-speed videomicroscopy results. Three laterally separated regions governed by different acoustofluidic effects have been identified in the atomization zone at a standing SAW (sSAW) wavefield, including acoustically stabilized liquid films (acoustowetting) and quasi-stationary liquid micropatterns.

Furthermore, the altering of the measured droplet size distribution, in relation to the original droplet size distribution at the time droplet generation, due to the humidity of the surrounding gas phase will be discussed.

Statement of the Contribution

In the current study, dedicated experiments were carried out to visualize the resultant liquid film pattern outside and inside the high-frequency acoustic wavefield. A microscopy image of the atomization chip with two interdigital transducers (IDTs) and microchannels is shown in Fig. 1(a). In the current chip layout, two IDTs (90 μm wavelength, 0.5 mm aperture) are opposing each other with a distance of 6 mm for standing SAW excitation based on superposition of two counter propagating travelling SAW. DI water was used for the aerosol generation and the liquid flow rate was varied from 30 $\mu\text{l}/\text{min}$ to 100 $\mu\text{l}/\text{min}$ during experiments.

The atomization zone was microscopically inspected using high-speed videography to visualize the droplet generation and the hydrodynamics in the acoustically generated and stabilized liquid films and pattern (up to 52 kfps video recording with 10 μs exposure time). In additions, our unique compact SAW aerosol generator was placed and investigated inside the Leipzig Aerosol Cloud Interaction Simulator (LACIS-T), a large turbulent wind tunnel, at different constant levels of air humidity to determine the initial droplet size distribution at the time of droplet generation, and to get a closer view on the underlying droplet formation mechanisms on the chip surface. LACIS-T was combined with an optical particle spectrometer with resolution down to the sub- μm scale.

Results/Discussion

Three regions have been observed in the atomization zone governed by different acoustofluidic effects, including the formation of liquid films and quasi-stationary fluidic micropattern in a standing SAW (sSAW) wavefield. A liquid film with chaotic surface fluctuations is immediately formed in front of the channel outlet and at the boundary of the acoustic wavefield due to the contributions of fluid wetting and Eckart streaming (**region 1** - See Fig. 1(b)). Within the SAW wavefield, a thin thickness-modulated film is observed advancing perpendicular to the main SAW propagation direction and into the atomization zone, i.e. towards higher amplitudes (**region 2** - See Fig. 1(b)). It was observed that droplet-shaped liquid pattern was generated locally and travelled frequently along the modulated liquid film. These interesting facts which are also reported in the literature as a soliton-like wave pulse propagation using travelling SAW [1]. However, the local source of aerosol droplets was identified to sSAW-induced quasi stable liquid droplet-shaped pattern observed at the location with highest sSAW amplitude (**region 3** - See Fig. 1(b)). The observed pattern, clearly observable in front view of the atomization zone (See Fig. 1(b)), formed periodically with a distance of the half the SAW wavelength $\lambda_{\text{SAW}}/2$. According to our investigations, SAW atomization mechanism and observed droplet size origin are different with those available in the literature in highly resonant acoustofluidic systems, especially ultrasonic atomization [2].

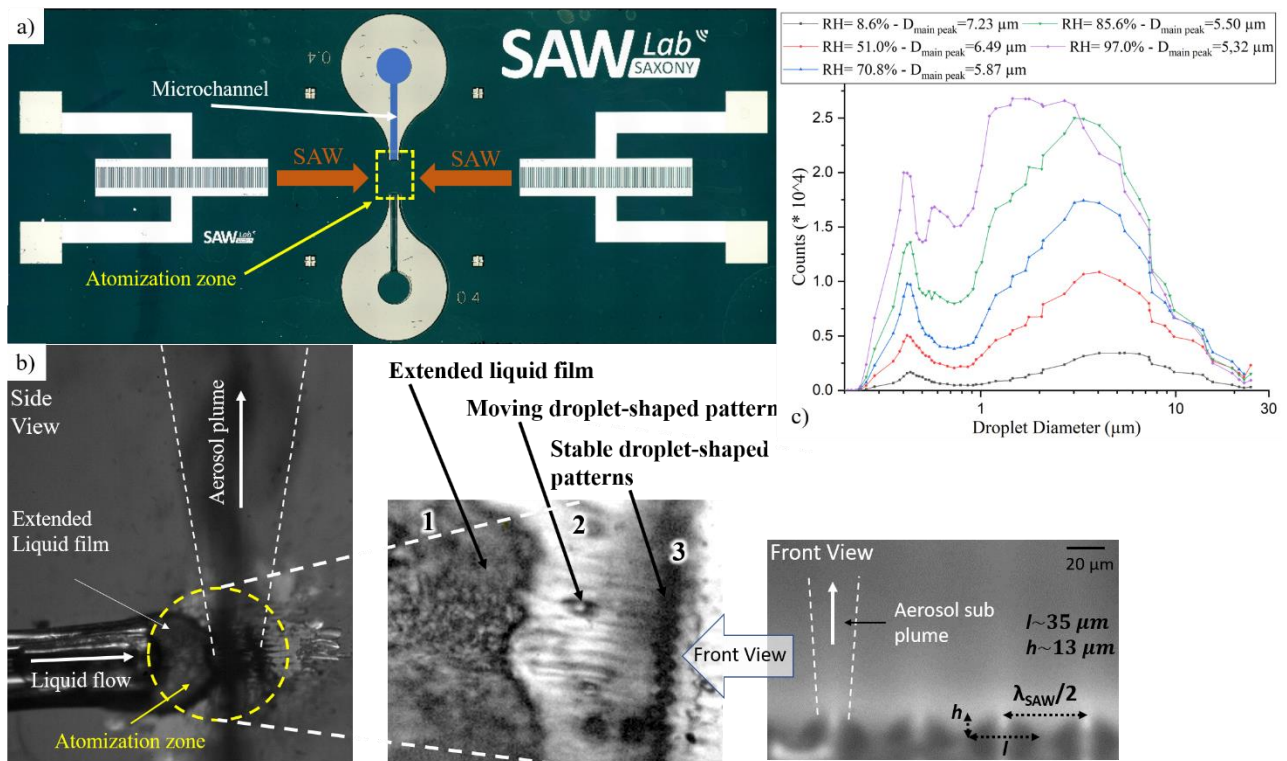


Figure 1: a) Microscopy image of SAW chip for aerosol generation with on-chip integrated microchannels. b) microscopy images of the atomization zone and of the extended thin liquid film in front of the microchannel (side view and front view). c) Particle/droplet size distributions measured by a particle spectrometer for five different inlet dew-point temperatures T_d leading to five different values of relative humidity inside the measurement section of LACIS-T (8.6%, 51.0%, 70.8%, 85.6%, and 97.0%).

Furthermore, the particle/droplet size distributions measured at five different dew-point temperatures. A bimodal log-normal droplet size distribution was obtained with droplet diameters in general below 30 μm (See Figure 1(c)). The mean diameter of the main droplet fraction decreased from 7.23 ± 0.7 μm to 5.32 ± 0.9 μm with increasing relative humidity from 8.6 % to 97 %, apparently due to evaporation of smaller droplets in unsaturated air, an effect disregarded in literature on SAW nebulization so far. A second peak corresponds to a mean diameter as small as 600 nm at high humidity conditions, which is likely to correspond to a droplet generation mechanism not reported so far and extremely difficult to measure or visualize with conventional techniques.

Conclusion

In the current study, the behavior of the so far furthest developed SAW-based aerosol generator was investigated optically and inside the LACIS-T wind tunnel at different constant levels of air humidity to get deeper insights in the underlying droplet formation mechanisms on the chip surface and to determine the initial droplet size distribution in SAW nebulization. The adverse effect of the surrounding gas phase on the measured droplet size distribution was confirmed, highlighting the importance of water-saturated gas atmosphere during droplet size measurements. Furthermore, the atomization zone was optically inspected to visualize the droplet generation and the hydrodynamics in the acoustically generated and stabilized liquid film and the liquid patterns. Thereby, the droplet source was identified to fluid micropattern, generated and stabilized by the sSAW. Furthermore, there have been some disagreements in various scenarios concerning available theoretical equations for droplet size prediction. One possible and likely explanation could be a droplet generation by high-speed microjets induced by the collapse of cavitation bubbles inside the liquid film.

References

- [1] A. R. Rezk, O. Manor, J. R. Friend, and L. Y. Yeo, Nature Communications **3**, 1167 (2012).
- [2] M. Roudini, D. Niedermeier, F. Stratmann, and A. Winkler, Physical Review Applied (2020).

Microfluidics platform for protocol development via capacitive fluid level monitoring and acoustic mixing

Yaqi Zhang¹, Muhsincan Sesen^{1,2}, Alex de Marco^{3,4} and Adrian Neild¹

¹Department of Mechanical and Aerospace Engineering, Monash University, Clayton, Victoria (Australia)

²Institute of Biological Chemistry, Biophysics and Bioengineering, Heriot-Watt University, Edinburgh, EH14 4AS, (United Kingdom)

³Department of Biochemistry and Molecular Biology, Monash University, Clayton, Victoria (Australia)

⁴ARC Centre of Excellence for Advanced Molecular Imaging (Monash University, Australia)

E-mail: yaqi.zhang@monash.edu, URL: <https://www.labformicrosystems.com/>

Introduction

Integrated microfluidic platforms are capable of conduction and automation of complex bio/chemical reactions [1, 2] by incorporating reagent dispensing, metering, detection and mixing capabilities. Typically in such systems, fluid handling was achieved via opening of microvalves allowing reagent metered into a new channel section. As the dispensed volume was controlled by channel geometry, prerequisite knowledge of the protocol was required in designing the system, directly on chip protocol development was hindered.[3] In our previous work, a versatile system was developed utilizing microvalve to regulate the flow into an initially empty reaction chamber (154 nL). The reaction chamber been progressively filled in this manner and surface acoustic wave (SAW) induced streaming aid mixing capability.[4] As dispensed volume was controlled by time that the valve opens, the dispensed volume can be tuned, on chip protocol development and refinement. Here, we incorporate capacitive sensing as a feedback mechanism to automate reagent dispensing, adding system multiplex capability and improving dispensing accuracy within 2 nL. In addition, SAW can be monitored using the capacitive sensor on temperature fluctuation and mixing progress.

System description

Figure 1 shows the schematic of the feedback control setup. The chip consist two parts, the microfluidic channel containing the single layer valve and reaction chamber is made of PDMS and the piezoelectric substrate (128° cut LiNbO₃) on which electrodes for SAW generation and capacitance sensor was patterned. In order to mix reagent over large area, 70 MHz was chosen for SAW actuation. For a given geometry, the capacitance reading change linearly with the relative permittivity of the surrounding fluid (eg, DI water or air), which is a function of temperature, fluid type and fluid conductivity. This enabled capacitive sensor monitor fluid level, temperature change and mixing progress during SAW actuation.

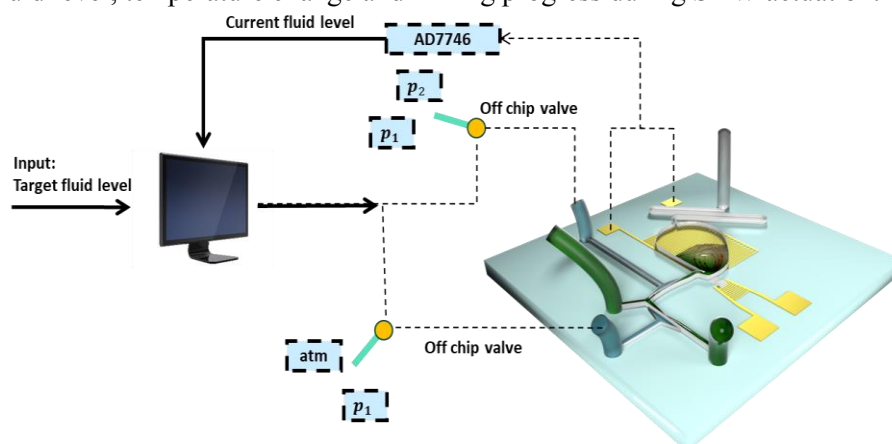


Figure 1: Overview of the system set up. The capacitive reading (measured via capacitance to digital converter AD7746) and pressure supply to the on chip valves are synchronized through a Labview interface which has a user input for dispensing volume. Off chip valve was used for rapid switch between pressure levels applied on the on chip valve. (p1=1.4 bar and p2= 0.6 bar)

Results

The accuracy of the reagent dispensing via feedback control was assessed. Firstly, a comparison of the optical and capacitive measurement of the dispensed volumes is given in Fig.2 (a), a single fluid type was added sequentially into the chamber, showing a very high level of accuracy, the error being in the range of 1 nL. This process was repeated three times to demonstrate the robustness, accuracy and response of the dispensing automation. As plotted in Fig 2 (b), the actual dispensed volume (both capacitive and optical) against the valve actuation threshold, showing the fast response of valve actuation and accuracy in fluid dispensing. In most

cases, different reagent is dispensed each time to allow reaction take place. PBS was sequentially dispensed into the chamber initially contains 25% or 50% PBS to demonstrate the accuracy in dispensing multiple reagent. The actual dispensed volume was plotted against the target level shown in Fig.2 (c), showing accuracy within 2 nL.

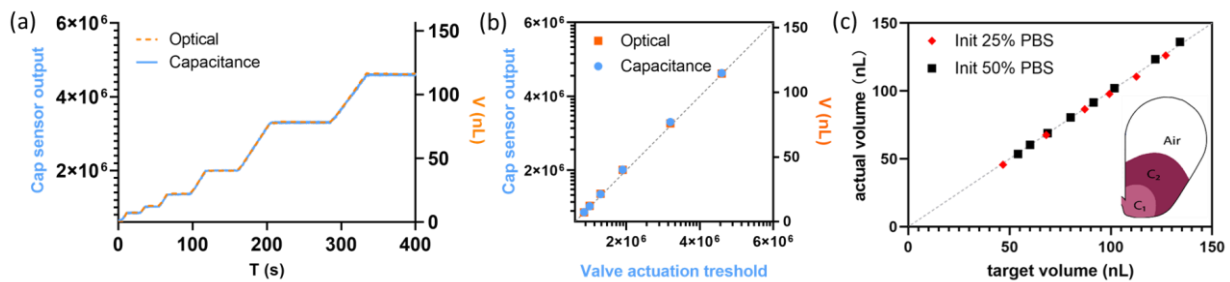


Figure 2: Fluid level dispensing capability via feedback controll. (a) Comparison between capacitance sensor readout and optical chamber reagent measurement on a single run of sequential fluid dispensing. The plot shows the agreement between the two fluid metering methods. (b) The accuracy of the dispensed versus target volume across three tests (error bar included). (c) Comparison of theoretical estimation of sequential dispensing PBS based on capacitance reading (red) with optical measurement of experimental results (black).

Capacitive sensing is capable of measure the temperature change and mixing progress when the fluid level is set, this enabled monitoring without optical access. Fig.3 (a) shows the temperature change and mixing time when power applied on SAW increased. Fig.3 (b) showing the capacitance readout in during the mixing process, the capacitance increase significantly when fresh fluorescein been added in, then dispensing valve shut and SAW actuated, the second increase was observed, this was due to the temperature change. As shown in Fig.3 (d) for a given fluid level, capacitance valve varies with fluid conductivity. As such, mixing progress between fluid with different conductivity can be monitored as plotted in Fig.3 (c).

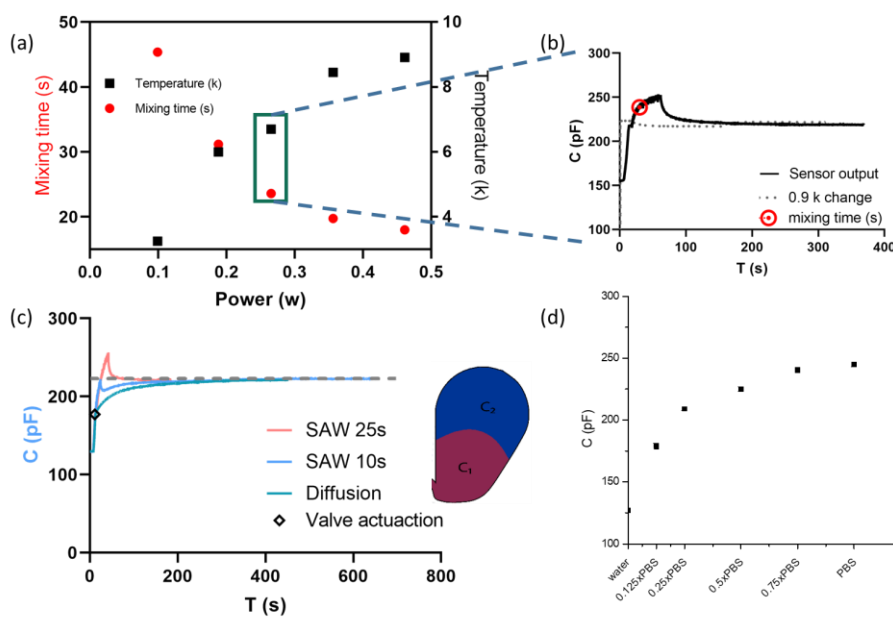


Figure 3: Chamber monitoring. (a) Mixing time (red) as well as temperature (black) change against power. (b) Capacitance change during one mixing case, fresh fluorescein was added in, feeding channel shut. SAW was actuated for mixing, after visualize mixing process complete, the SAW was turned off. (c) Comparison of capacitance readout for mixing fluid with different conductivity (PBS and 50% diluted PBS), when it is fully mixed (SAW actuation=25 s), under mixed (SAW actuation=10s) and passive control (diffusion) (d) Capacitance reading as function of PBS concentration at fluid level at 154 nL.

Conclusion

An automated system has been developed with multiplexing potential for performing protocols on-chip with nanolitre dispensing flexibility, SAW aided rapid mixing and capacitive sensing for fluid level, temperature and mixing progress monitoring.

References

- [1] S.S. Dey, L. Kester, B. Spanjaard, M. Bienko, A. Van Oudenaarden, Integrated genome and transcriptome sequencing of the same cell, *Nature biotechnology*, 33 (2015) 285-289.
- [2] I. Lignos, S. Stavrakis, G. Nedelcu, L. Protesescu, A.J. deMello, M.V. Kovalenko, Synthesis of Cesium Lead Halide Perovskite Nanocrystals in a Droplet-Based Microfluidic Platform: Fast Parametric Space Mapping, *Nano Letters*, 16 (2016) 1869-1877.
- [3] T. Thorsen, S.J. Maerkl, S.R. Quake, Microfluidic large-scale integration, *Science*, 298 (2002) 580-584.
- [4] Y. Zhang, C. Devendran, C. Lupton, A. de Marco, A. Neild, Versatile platform for performing protocols on a chip utilizing surface acoustic wave (SAW) driven mixing, *Lab on a Chip*, 19 (2019) 262-271.

Fabrication of Surface Acoustic Wave (SAW) Devices Using Detachable Electrodes Based on a Flexible Printed Circuit Board (PCB)

Roman Mikhaylov¹, Zhihua Xie², Aled Clayton³ and Xin Yang¹

¹Department of Electrical and Electronic Engineering, School of Engineering, Cardiff University, Cardiff CF24 3AA, UK

²Department of Civil Engineering, School of Engineering, Cardiff University, Cardiff, CF24 3AA, UK

³Tissue Micro-Environment Group, Division of Cancer & Genetics, School of Medicine, Cardiff University, Cardiff CF14 4XN, UK

E-mail: MikhaylovR@cardiff.ac.uk,

URL: <https://www.cardiff.ac.uk/people/research-students/view/1427027-mikhaylov-roman>

Introduction

Surface acoustic wave (SAW) based devices have been widely used in acoustofluidics for application such as separation of micro-/ nano-cells [1,2], droplet actuation [3] and 3D manipulation of cells [4]. The common method for fabricating SAW based devices is to pattern a metal interdigital transducer (IDT) onto a piezoelectric substrate, e.g. LiNbO₃, which requires both clean room facilities and careful operation, as the bulk LiNbO₃ substrate is very fragile and any damage to the substrate is unlikely to be repaired. This study further developed upon our recent work on an alternative manufacture technique for developing SAW based devices [5]. By replacing the rigid PCB used in the previous study, a flexible PCB was applied to allow more uniform contact between the IDT and the piezoelectric substrate. This device was combined with a microfluidic channel to test actuation on nanoparticles with flow. The preliminary results showed the flexible PCB-based SAW (PCB-SAW) device was able to effectively produce standing SAW (SSAW) when a pair of IDTs was used and could actuate nanoparticles.

Development and characterisation of the PCB-based SAW device

The working principle of the PCB-SAW device is demonstrated in Fig. 1a, where the PCB IDTs are clamped onto a piezoelectric substrate (LiNbO₃) to generate SAWs. The IDTs were manufactured on a PCB with a pitch size of 200 μm. The PCB and LiNbO₃ substrate are held together by a 3D printed clamping jig, Fig. 1b. The PCB-SAW device was benchmarked against a conventional SAW device with the same parameters through a droplet transportation experiment. A 1-μL droplet was used to measure the relationship between the droplet pumping velocity and input power, Fig. 1c, where it was observed that the PCB-SAW device starts to drive the droplet when the input power achieves ~0.5W. When the input power is 1 W, the conventional SAW device produces a droplet velocity of ~40 mm/s while the PCB-SAW device achieves ~10 mm/s. To test the PCB-SAW device for biological application human non-small-cell lung carcinoma (NSCLC) cells were introduced to a microfluidic channel (200 μm (W) × 60 μm (H)) bonded to the LiNbO₃ substrate (Fig. 1d, left image). When the input power is applied, the NSCLC cells are attracted to the pressure nodes and three cell traces are created (Fig. 1d, middle image). When the signal phase of one of the IDTs is shifted by 180°, the pressure nodes are redistributed inside the microchannel which attract the NSCLC cells to move to the new positions (Fig. 1d, right image). The NSCLC cells were also used to test the biocompatibility of the PCB-SAW device. After flushing them through the microchannel at a flow rate of 20 μL/ min, a viability test was performed and resulted in the viability of the cells remained high (~97%).

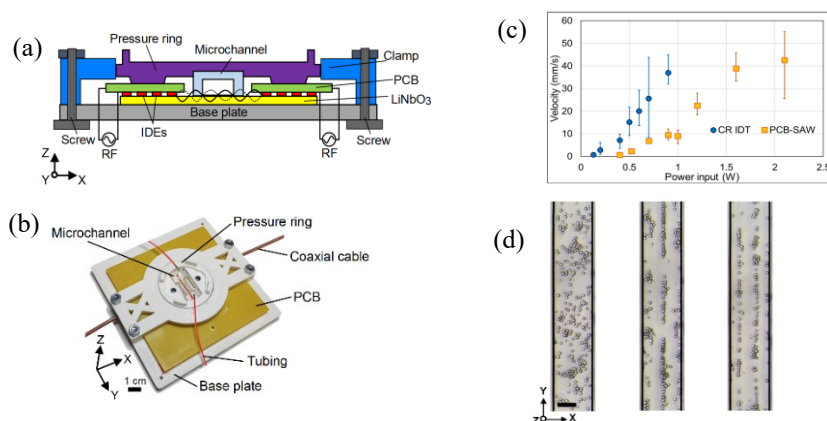


Figure 1: PCB-SAW device. **a)** 2D schematic of the working principle of the PCB-SAW device and **b)** the real-life model of the PCB-SAW device. **c)** Comparison of 1 μL droplet actuation using standard IDTs and the PCB-SAW device at different input powers. **d)** Alignment of NSCLC cells within the microchannel before and after the SSAW is applied, with and without a 180° phase shift.

Nanoparticle tests using the flexible PCB-based SAW device

The PCB-SAW device was further developed by using a thin-film flexible PCB, which was patterned with the IDT (FPIDT) as shown in Fig. 2a. The use of the FPIDT can overcome the restriction caused by the shape and rigidity of the rigid PCB. To demonstrate the PCB-SAW technique was able to manipulate nanoparticles, the FPIDT pitch size was reduced to 120 μm to produce a higher frequency SAWs of 33.17 MHz. The jig for holding the FPIDT and a microchannel is shown in Fig. 2b, which was optimized from the previous one by reducing the size of the 3D printed components with separating the PCB IDTs to individual electrodes. The new design also adopted a tilt-angle IDT design [2] with two different angles, 5° and 15°. Fluorescence microscopic images were collected showing the 700 nm nanoparticles distribution at the 5° and 15° devices at the input power of 3.16 W, Fig 2c and 2d, respectively. The illuminance profile was collected from the area where the purple box is displayed. It can be observed that in both cases the particles were actuated and the distribution profile changed and distinct trace line peaks appeared. For the case of the 5° channel more trace lines appeared and the particles traveled further across the channel, $\sim 600 \mu\text{m}$, compared to the 15°, $\sim 525 \mu\text{m}$. Fig 2e and 2f show the actuation of 100 nm nanoparticles at 5° and 15° respectively, at the same power input as 700 nm. Similar as the 700 nm, the 100 nm particles at the 5° had more trace lines and reached $\sim 600 \mu\text{m}$ while the 15° reached about $\sim 525 \mu\text{m}$. From this qualitative study it can be observed that the FPIDT can actuate nanoparticle and that the particles are capable of being actuated further when a lesser tilt angle channel is used.

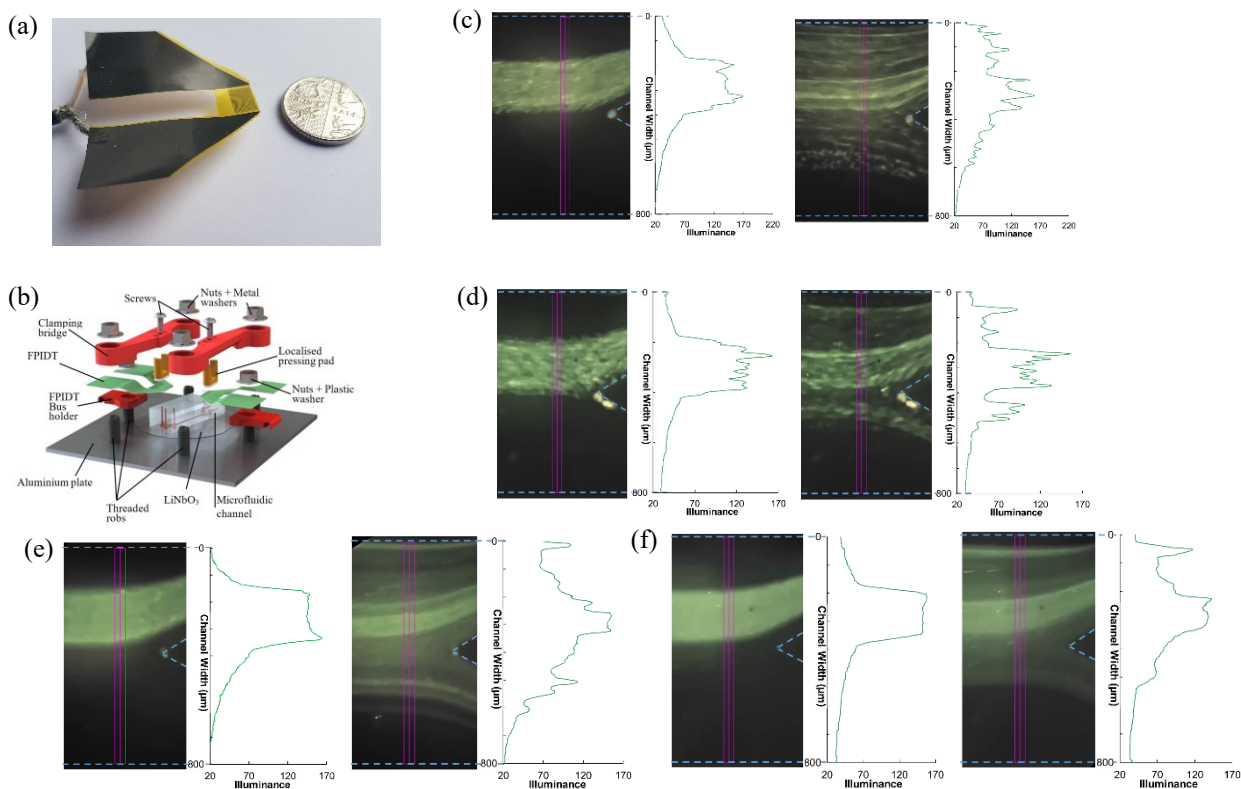


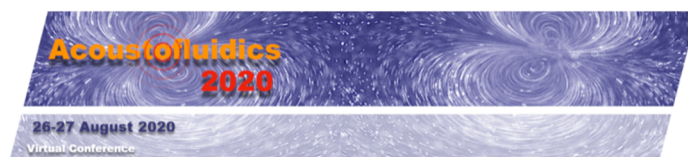
Figure 2: The flexible PCB-based SAW device and the application. **a)** Photo of the flexible PCB IDT (FPIDT). **b)** 3D assembly of the FPIDT SAW device. **c)** Fluorescence images of the 700 nm nanoparticles actuated by the FPIDT SAW device with a 5-degree tilted channel. **d)** Fluorescence images of the 700 nm nanoparticles actuated with a 15-degree tilted channel. **e)** Fluorescence images of the 100 nm nanoparticles actuated device with a 5-degree tilted channel. **f)** Fluorescence images of the 100 nm nanoparticles actuated with a 15-degree tilted channel.

Conclusion

The PCB-SAW device has been proven to be able to produce effective SAW for actuation of micro- and nanoparticle as the SAW device made by conventional photolithography technique. The assembling of the PCB-SAW device can be used as an alternative manufacturing method to lower the entry requirement of acoustofluidic applications to benefit wider researchers.

References

- [1] P. Li *et al.*, PNAS **112** (16), 4970-4975 (2015)
- [2] Z. Wang *et al.*, The Journal of Molecular Diagnostics **22** (1), 50-59 (2020)
- [3] S. P. Zhang *et al.*, Nature communication **9** (1), 2928-2938 (2018)
- [4] I. Bernard *et al.*, Lab on the Chip **17** (14), 2470-2480 (2017)
- [5] R. Mikhaylov *et al.*, Lab on the Chip **20** (10), 1807-1814 (2020)



Gallium Nitride Thin Film for Acoustic Tweezer

Chao Sun¹, Huaixing Cang¹, Xin Yang²

¹ School of Life Sciences, Northwestern Polytechnical University, 710072, P.R. China

E-mail: chaosun@nwpu.edu.cn, hxcang@nwpu.edu.cn

² Department of Electrical and Electronic Engineering, School of Engineering, Cardiff University, UK CF24 3AA, E-mail: YangX26@cardiff.ac.uk

Introduction

Gallium nitride (GaN) is a compound semiconductor which has advantages to generate new functionalities and applications due to its piezoelectric, pyroelectric, and piezo-resistive properties [1]. Recently, surface acoustic wave (SAW) based acoustic tweezers were developed as an efficient and versatile tool to manipulate nano- and micro-particles aiming for patterning, separating and mixing biological and chemical components [2]. Conventional piezoelectric materials to fabricate SAW devices such as lithium niobate suffers from its low thermal conductivity and incapability of fabricating multiphysical and integrated devices. This work piloted the development of a GaN-based Acoustic Tweezer (GaNAT) and its application in manipulating micro-particles and biological cells. The GaNAT demonstrated its ability to work on high power (up to 10W) with minimal cooling requirement while maintaining the device temperature below 32°C. Acoustofluidic modelling was successfully applied to numerically study and predict acoustic pressure field within the GaNAT, which agree well with the experimental results on patterning polystyrene microspheres and two types of biological cells including fibroblast and renal tumour cells. The GaNAT allowed both cell types to maintain high viabilities of 84.5% and 92.1%, respectively.

Material and methods

A photo of the fabricated GaNAT comprising a polydimethylsiloxane (PDMS) microchannel and a GaN-based SAW device is shown in Fig. 1a. The SAW device was made by a GaN/sapphire wafer patterned with a pair of interdigital transducers (IDTs), between which the microchannel was bonded to form the GaNAT. The GaN thin film was grown on a sapphire substrate in [0001] direction, and Fig. 1b shows its cross-section image obtained using a scanning electron microscope. The GaN and sapphire layers are measured to be ~4.5 μm and ~600 μm thick, respectively. The GaN surface was patterned by bilayers of chromium/gold (30 nm/150 nm-thick) as electrodes. Both the width and pitch of the finger electrodes are 70 μm, which produce SAWs with a wavelength of 280 μm. Each IDT contains 40 pairs of finger electrodes with an aperture size of 7 mm. A vector network analyser (VNA, E5061B ENA, Keysight) was used to measure the transfer functions of the GaN SAW device, S_{11} (reflection coefficient) and S_{21} (transmission coefficient). The IDT's surface temperature was measured using an infrared thermal camera. A numerical model was applied to investigate the acoustofluidic conditions of the GaNAT using COMSOL Multiphysics® version 5.4.

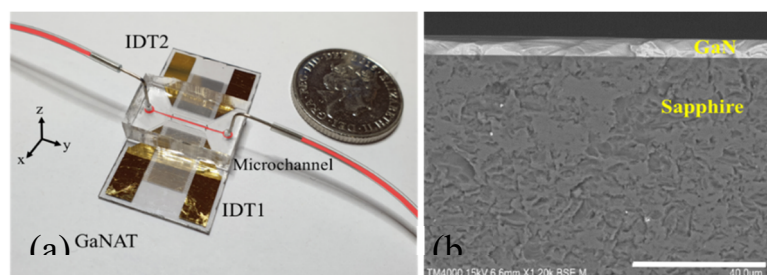


Figure 1: GaNAT. (a) Photo of the GaNAT device. (b) The scanning electron microscopic image of the undoped GaN film on a sapphire substrate. The scale bar is 40 μm.

A microparticle sample was prepared using 10 μm polystyrene microspheres mixed with phosphate-buffered saline to verify the numerical results and the GaNAT performance. Biological cells were used to explore the potential of manipulation cells using the GaNAT and to test whether the GaNAT was able to maintain cell viability during acoustic actuation. Two types of biological cells, e.g., mouse renal tumour cells (TSC1-associated tumour cells, Tsc1-204) and mouse fibroblast cells (MEF, Tsc1-387-2), were prepared for the test. For the viability study, both the fibroblast and renal tumour cells were divided into two groups: SSAW ON group - cells passing through the GaNAT with SSAW present, and SSAW OFF group - those without SSAW present. The two phase differences (0° and 180°) of the two RF signal was investigated against the pattern of the microparticles or cell aggregation.

Results and discussion

From the results of S_{11} and S_{21} spectra of the SAW devices, the lower frequency peaks at 19.40 MHz corresponds to the Rayleigh mode and 38.91 MHz corresponds to the Sezawa mode. At a room temperature of 24 °C, the temperature rise on the IDTs as the consequence of the increased forward power and the temperature on the IDTs was increased to ~31 °C at 10 W, which was the maximum power supplied to the GaNAT in this study. Without using any active cooling system such as Peltier cooler, the GaNAT was able to effectively convert RF powers to SAWs while keeping the device temperature below the biological limit.

The simulation results of the acoustic pressure are shown in Figs. 2a –b. Fig. 2a demonstrates the first-order acoustic pressure field with no phase difference ($\Delta\phi=0^\circ$) between the RF signals driving the two IDTs, which results in the PNs located at the middle and two sides of the microchannel. Fig. 2c and Fig. 2e show the 10 μm polystyrene microparticle and cells aggregate at three positions inside the microchannel, respectively. The width of the microchannel in this study is the same as the SSAW's wavelength ($\lambda=280 \mu\text{m}$). By shifting the phase difference to $\Delta\phi=180^\circ$, one can position the ANs to be at the middle and two sides of the microchannel (Fig. 2b), microspheres and cells were immediately shifted to five traces as the microscopic top-view images shown in Fig. 2d and Fig. 2f, respectively. The good agreement between the numerical prediction and experimental observation demonstrated the ability of GaNAT in actuating and trapping microspheres and cells in a controllable pattern. The viabilities of the renal tumour cells and fibroblast cells were 84.5% and 92.1% for the SSAW ON group, respectively. The viabilities were 88.1% and 96.9% for the SSAW OFF group, respectively. For these two groups, fibroblast cells showed higher viabilities because they are more tolerable to the changes in temperature and/or CO_2 concentration after they were removed from the incubator. Nevertheless, both the cell types showed good cell viability after acoustic manipulation using the GaNAT.

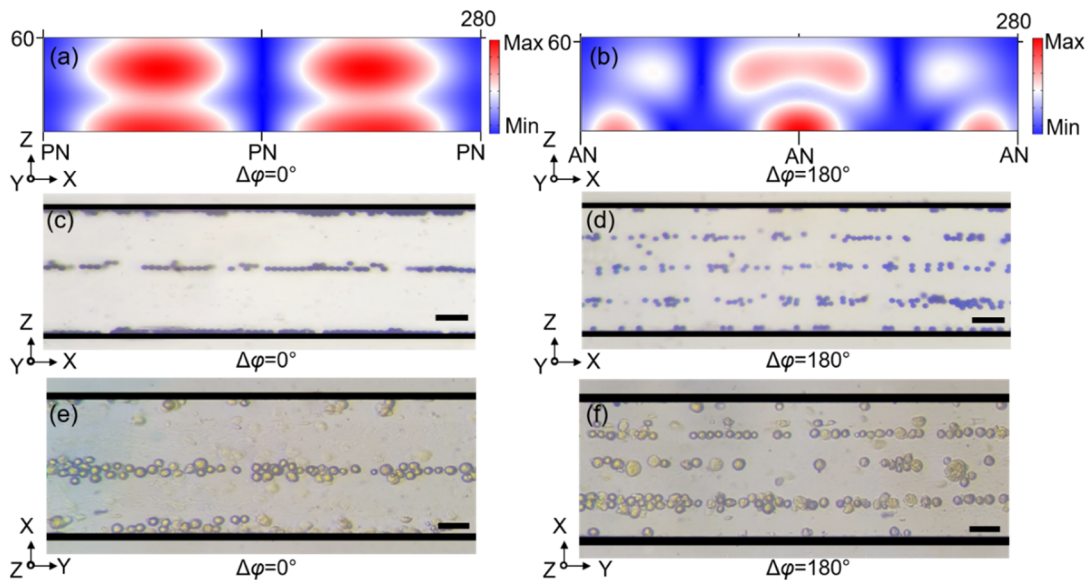


Figure 2: Numerical and experimental studies of the GaNAT. (a) and (b): acoustic pressure field inside the microchannel for the pressure node (PN) and pressure anti-node (AN) located at the middle of the channel, respectively. (c) and (d): microscope images of the 10 μm polystyrene microsphere patterned in the GaNAT actuated by the corresponding acoustic pressures in (a) and (b). (e) and (f): the cells patterning in the GaNAT for the pressure node and pressure anti-node located at the middle of the channel, respectively. The scale bar is 50 μm .

Conclusion

Despite the electromechanical coupling coefficient of GaN being lower than LiNbO_3 , the use of GaN to develop acoustic tweezers made by GaN-based IDTs working at megahertz frequencies for manipulating cells and microparticles has been demonstrated. As a novel thin-film piezoelectric material for fabricating acoustofluidic devices, GaN/sapphire structure can be used to generate Rayleigh and Sezawa waves. The thermal performance could be further improved by using Si as a substrate and this would also offer compatibility with high yield, high volume low cost semiconductor manufacturing to significantly reduce the cost of these devices. The numerical simulation results for the GaNAT were validated using the experimental results of microparticles and cell manipulation. Acoustophoresis realised by the GaNAT will open the area of exploring multiphysical application of GaN towards monolithic integration with electronics for developing biosensors and N/MEMS.

References

- [1] H. Amano, Y. Baines, E. Beam, M. Borga, T. Bouchet, P.R. Chalker, et al., The 2018 GaN power electronics roadmap, *Journal of Physics D-Applied Physics*, 51(2018).
- [2] A. Ozcelik, J. Rufó, F. Guo, Y. Gu, P. Li, J. Lata, et al., Acoustic tweezers for the life sciences, *Nature Methods*, 15(2018) 1021-8.

Acoustically driven meniscus modes in inkjet printing

Martin van den Broek¹, Maaïke Rump¹, Roger Jeurissen², Hans Reinten³, Detlef Lohse¹, Michel Versluis¹, Guillaume Lajoinie¹, and Tim Segers¹

¹Physics of Fluids group, Max-Planck Center Twente for Complex Fluid Dynamics, Department of Science and Technology, MESA+ Institute, and J. M. Burgers Centre for Fluid Dynamics, University of Twente, Netherlands

E-mail: m.rump@utwente.nl, URL: <https://pof.tnw.utwente.nl>

²Department of Applied Physics, Eindhoven University of Technology, Netherlands

³Canon Production Printing Netherlands B.V.

Introduction

Inkjet printing is a much used and well established technique for non-contact material deposition. In inkjet printing, reproducibility is key. For maximum printing accuracy, each fired droplet must be exactly the same, in volume, velocity and jetting angle[1]. Understanding reproducibility issues greatly helps in designing better printheads. Here, we address the issue of variations in the jetting angle that may arise due to higher order meniscus modes. To this end, we study both experimentally and theoretically the model landscape of a meniscus in a drop-on-demand printhead as a function of the driving frequency and amplitude.

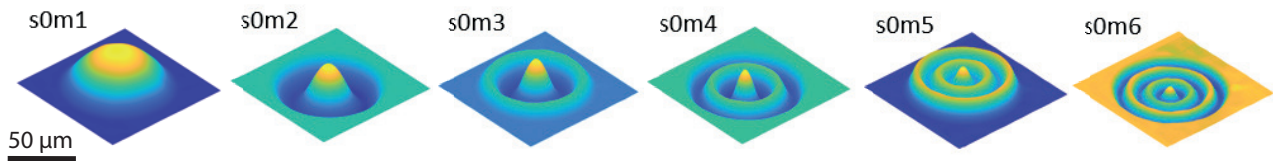


Figure 1: Measured modes of a water-air meniscus in an acoustically driven drop-on-demand printhead. s corresponds to the number of azimuthal nodes, and m corresponds to the number of radial nodes.

Experimental methods

The printhead used in the experiments was a glass capillary tube with a tapered nozzle, 70 μm in diameter (Microdrop Technologies GmbH, AD-K-501). A cylindrical piezo-electric element surrounds the capillary tube and can be driven to actuate the printhead. During actuation, first a local negative pressure wave is generated that travels through the capillary tube and pulls the meniscus inward. Second, a positive pressure wave is generated that pushes the liquid toward the tapered end. These traveling acoustic waves drive the meniscus motion. The time between these generated pressure waves is in the order of microseconds.

The time-dependent surface profile of the meniscus was characterized using a digital holographic microscope (LynceeTec DHM - R1000). In holographic imaging, the height profile of the interface is reconstructed from the phase information. Using stroboscopic imaging, we extracted the meniscus shape as a function of the driving frequency and amplitude. The meniscus was pinned at the edge of nozzle and consequently, standing wave patterns emerged. The standing waves are known as (oscillatory) normal modes. The results of the axisymmetric normal modes, measured with MilliQ-water, are shown in Fig. 1. The driving frequency at which each mode was found is indicated in Fig. 2.

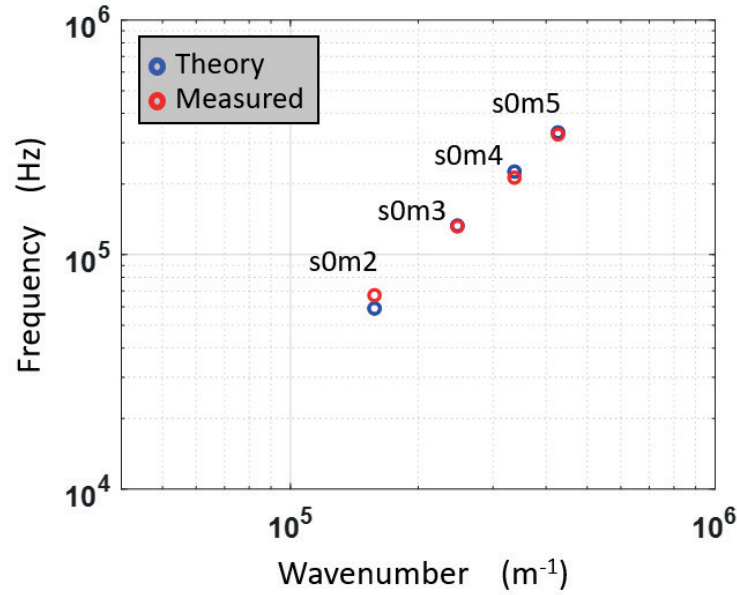


Figure 2: Theoretical and experimental mode resonance frequencies plotted versus the wave number for a water filled print head.

Modeling the meniscus modes

To predict the frequency at which each mode occurs, an inviscid model was developed. The meniscus oscillations are assumed to be harmonic. Solving the Laplace equation results in the capillary dispersion relation:

$$\omega^2 = \frac{\sigma}{\rho} k^3 \quad (1)$$

and a description of the different modes that fit in the cylindrical geometry using Bessel functions, as follows:

$$\left(\frac{1}{r} \frac{\partial}{\partial r} \left(r \frac{\partial}{\partial r} \right) + \frac{1}{r^2} \frac{\partial^2}{\partial \theta^2} + k^2 \right) S(r, \theta) = 0 \quad (2)$$

This is the same general solution as for a vibrating circular membrane[2]. The difference in the system described here is that the meniscus is continuously driven by the channel acoustics. Therefore, the flow in the bulk has to be taken into account as a boundary condition. The results of the theoretical predictions for the different modes are compared with the experimental results in fig. 2 and they show a good agreement.

Conclusion

For the first time, we have observed meniscus modes in kHz ranges. A modal landscape was mapped and the developed theory was found to be in good agreement with the experimental data. These findings not only improve understanding of oscillating menisci, but also aid in improving the design of driving conditions of inkjet printheads.

References

- [1] M.J. van der Meulen, H. Reinten, H. Wijshoff, M. Versluis, D. Lohse, and P. Steen. *Physical Review Applied* **13**, 054071 (2020).
- [2] Sen, S. N.. *Acoustics - Waves and Oscillations (3rd Edition)* New Academic Science (2014).

Droplet demulsification at parallel flow interface using sound waves

E. Hemachandran¹ and A. K. Sen¹

¹Department of Mechanical Engineering, Indian Institute of Technology Madras, Chennai, India
E-mail: me16d026@smai.iitm.ac.in, URL: <http://www.ashislab.in/>

Introduction

Coalescence of droplets in a flowing condition can be useful for on-line recovery of droplet contents (cells or molecules) that have been already processed in a droplet microfluidic system. Droplet coalescence in a flowing condition is challenging due to long drainage time compared with short residence time [1]. However, in a passive manner with the help of microchannel-geometry and droplet initial configuration, coalescence has been achieved in the same fluid in which the droplets are initially suspended [2]. Many active methods such as chemical, electrical, and magnetic field for droplet coalescence have also been attempted [3]. Here coalescence of droplets present in one stream with another co-flowing immiscible liquids using sound waves is experimentally demonstrated.

Theory

Acoustic relocation was observed for fluids of miscible nature even with 0.1% difference in impedance between the flowing fluids[4], however, in case of immiscible fluids, acoustic relocation was only observed once acoustic radiation force acting at the immiscible interface exceeds the interfacial tension between the co-flowing fluids[5]. The acoustic capillary number (C_{ac}) which characterizes the competition between interfacial tension and acoustic radiation force is defined as $C_{ac} = F_{ac}/F_{int} \sim E_{ac}\Delta\hat{z}w/\gamma$, where E_{ac} is the acoustic energy density, $\Delta\hat{z}$ is the impedance contrast between the fluids, w is the width of the microchannel, γ is the interfacial tension between the fluids.

A schematic of the acoustic demulsification device is shown in Fig. 1. Co-flowing fluids between the aqueous and oil phase were established. The acoustic standing wave is created inside the microchannel by attaching the piezoelectric transducer beneath the microchannel. Droplets generated in the oil phase are made to co-flow with the continuous aqueous phase. As shown in Fig 1a, in the absence of acoustic wave field, the droplet will follow its streamline without coalescing with the other phase. When the droplet is subjected to the influence of acoustic waves, it changes its streamline and is pushed towards the fluid-fluid interface due to acoustic forces where it gets coalesced with the continuous aqueous phase as shown in Fig 1b. As the thin film thickness reduces, van der Waals force dominates. Once the thin film is ruptured then along with van der Waals force, Laplace pressure facilitates the coalescence of droplets into continuous aqueous stream as shown Fig 1c.

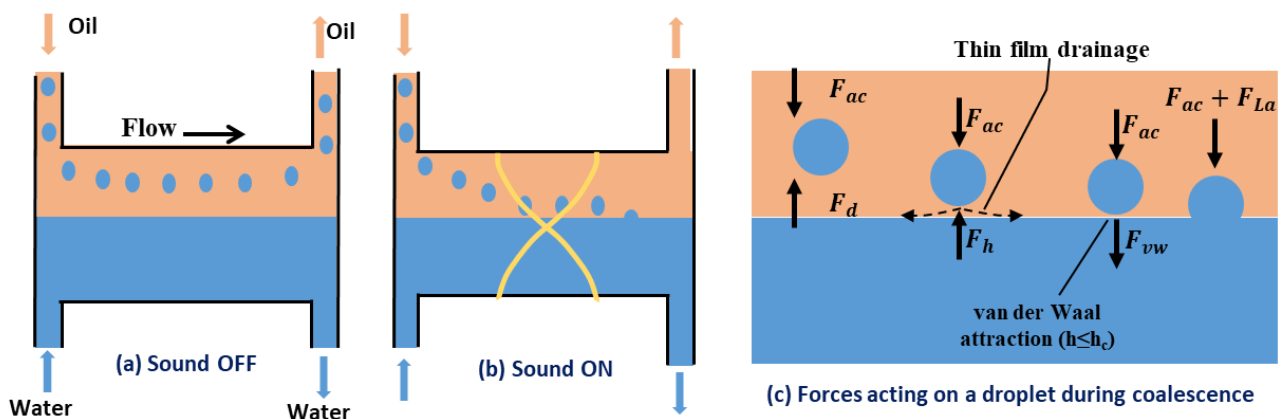


Figure 1: Schematic of acoustic demulsification at co-flowing fluid-fluid interface. Adapted from Ref. [6].

Results and discussion

In the present study, we have always maintained $Ca_{ac} < 0.9$ to prevent relocation or to maintain in non-relocation regime. The acoustic radiation force ($F_{rad} = 4\pi a^3 \phi k E_{ac} \sin(2ky)$) is employed to move the droplet towards the fluid-fluid interface to facilitate the acoustic demulsification process.

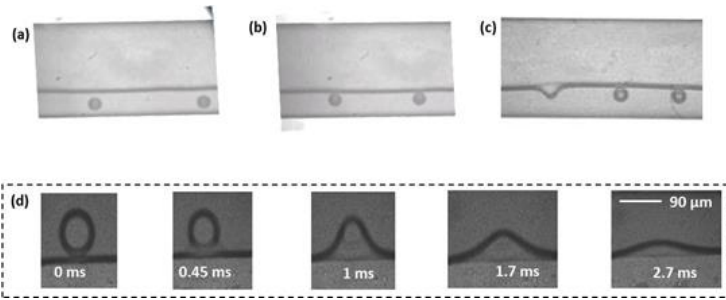


Figure 2: (a) In the absence of acoustics, droplets follow its streamline (b) Upon onset of acoustics droplets are pushed towards the interface (c) Once the thin film present between the droplet and interface drains, demulsification occurs (d) Droplet coalescence captured at interface

To achieve the coalescence of droplets from one phase to other, the following three criteria have to be satisfied. First, the co-flowing immiscible liquids stream relocation⁴ should be prevented i.e. acousto capillary number should be less than 1 ($Ca_{ac} < 1$). Second, the acoustic migration time ($T_{ac} = T_{ac1} + T_{ac2}$) should be less than advection time (T_{adv}). Third, the width of water stream should be greater than the oil stream so that the pressure node lies in water stream ($W_{aq} > W_{oil}$). The important parameters governing this phenomenon are acoustic energy density (E_{ac}), viscosity (μ), interfacial tension (γ) and flow rates (Q) of the two phases.

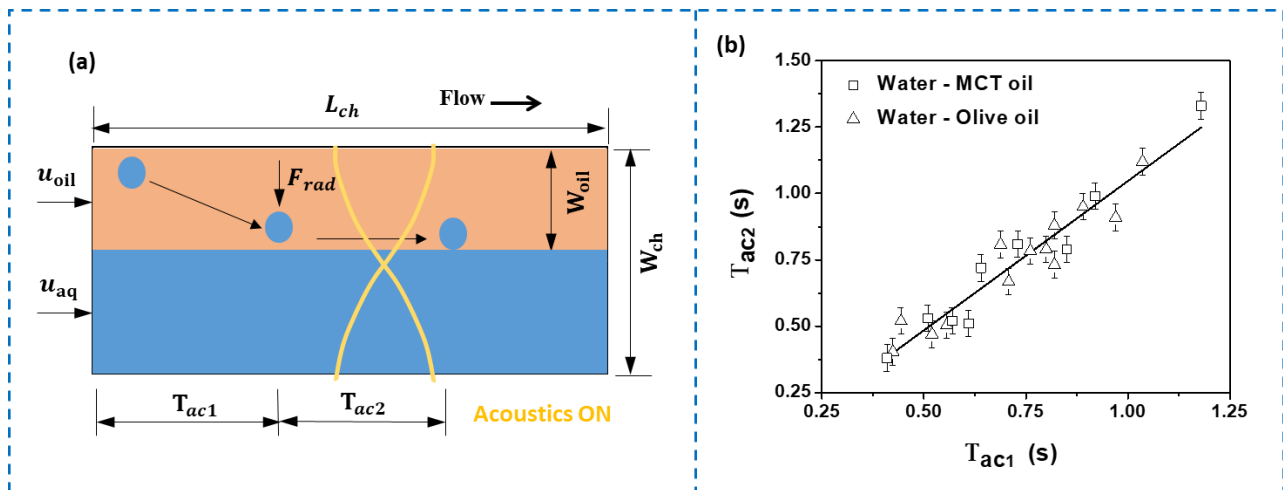


Figure 3 (a) Schematic representation of acoustic migration time and film drainage time upon onset of sound waves inside the microchannel. (b) Experimental relationship between acoustic migration time and film drainage time. Adapted from Ref. [6].

In our experiments we found that the time required to move droplet from nearby wall to interface (T_{ac1}) and from interface to drain the thin film between the droplet and interface (T_{ac2}) are of the same order of magnitude and also approximately same (from Fig.3b, $T_{ac1} \cong T_{ac2}$) for the different flow rates and energy densities. From Stoke's drag and hydrodynamic lubrication theory both T_{ac1} and T_{ac2} are proportional to viscosity. Once the thin film is drained, the coalescence is almost instantaneous where the coalescence time, $T_{col} \sim 1$ ms, as shown in Fig.2(c), which is negligible ($T_{col} \ll T_{ac}$) compared to T_{ac1} and T_{ac2} (in the order of 1 second).

Conclusion

We experimentally demonstrated droplet demulsification at co-flowing interface using bulk acoustic wave. This simple acoustic demulsification can be a useful tool for on-line recovery of droplet contents in microfluidics system.

References

- [1] D. R. Link, E. Grasland-Mongrain, A. Duri, F. Sarrazin, Z. Cheng, G. Cristobal, M. Marquez and D. A. Weitz, *Angew. Chemie - Int. Ed.*, **45**, 2556–2560 (2006)
- [2] A. Lai, N. Bremond and H. A. Stone, *J. Fluid Mech.*, **632**, 97–107 (2009)
- [3] S.-Y. Teh, R. Lin, L.-H. Hung and A. P. Lee, *Lab Chip*, **8**, 198–220 (2008)
- [4] S. Deshmukh, Z. Brzozka, T. Laurell and P. Augustsson, *Lab Chip*, **14**, 3394–3400 (2014).
- [5] E. Hemachandran, S. Karthick, T. Laurell and A. K. Sen, *EPL (Europhysics Lett.)*, **125**, 54002 1-7 (2019).
- [6] E. Hemachandran, T. Laurell and A. K. Sen, *Phys. Rev. Appl.*, **12**, 044008 1-13 (2019)

Droplet impact control by surface acoustic waves

Mehdi H. Biroun¹, Mohammad Rahmati¹, Glen McHale¹, Mehdi Jangi², Hamdi Torun¹,
Richard YongQing Fu¹

¹ Faculty of Engineering & Environment, Northumbria University, Newcastle upon Tyne, NE1 8ST, UK
E-mail: Mehdi.Hosseini@northumbria.ac.uk

² Department of Mechanical Engineering, University of Birmingham, Birmingham, B15 2TT, UK

Introduction

Minimizing the contact time of droplet impact is important for applications such as self-cleaning, anti-erosion or anti-icing [1]. Recent studies have used surface texturing to break droplets during impact or cause asymmetric spreading, but these involve specially engineered substrates that are not easily reconfigurable [2]. To reduce the droplet retraction time, many studies are focused on changing the symmetrical shape of the droplet during the impingement. Macrostructure surface designs with various post arrays have also been explored to reduce the contact time of bouncing droplets [3]. In this study, we propose a novel method to actively control the droplet impact and reduce the contact time of an impacting droplet by remotely generating surface acoustic waves (SAWs), which then propagate along a smooth and non-textured surface into the area where the droplet impact is occurring [4].

Results

A ZnO/Si SAW device with a resonant frequency of 66.10 MHz was applied to investigate the droplet impact manipulation by SAWs. Figs. 1 shows snapshots of the droplet impact images on the SAW device surface for three different cases of direct free impact (DFI) travelling surface acoustic waves (TSAWs, i.e., with waves propagating from IDTs along one side of the droplet), and standing surface acoustic waves (SSAWs, i.e., two waves propagating from two opposite sides of the droplet), respectively. For the cases of DFI and SSAW, when the droplet impinges onto the solid surface, it starts to spread into its maximum diameter before it starts to retract with a deformation pattern that is symmetric with respect to the z-axis. Whereas the TSAW case shows a more irregular and asymmetric pattern (see Fig. 1(b)), in particular during its maximum spreading and retraction/detachment periods.

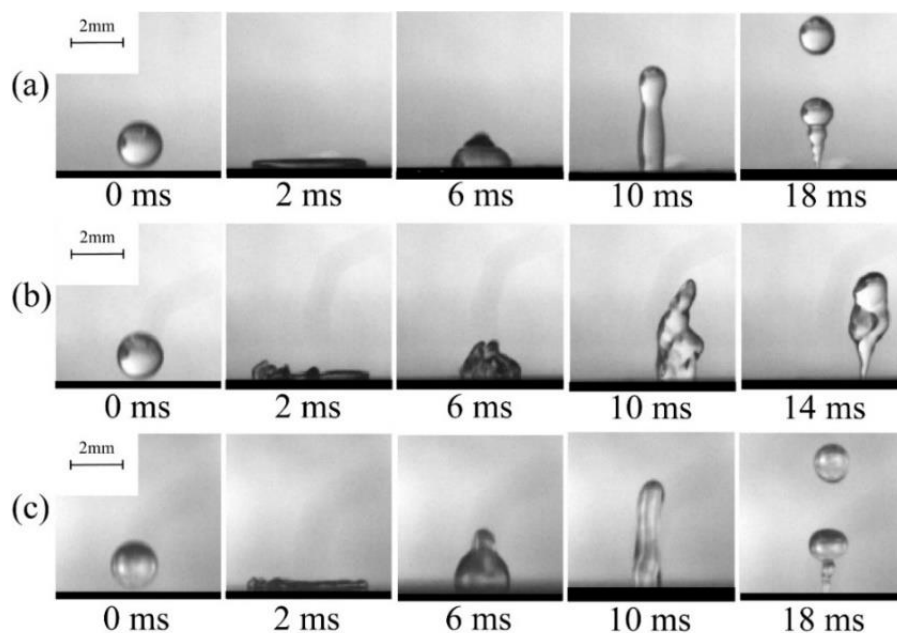


Figure 1: Experimental snapshots of a water droplet impinging on the solid surface. (a) Droplet free impact case without SAW applied, (b) impact on ZnO/Si surface with TSAW applied to propagate from left to right (c) impact on ZnO/Si surface while SSAW is applied to the surface. For all the experiments, the droplet impact velocity and volume are 1.4 m/s and 3.56 μl .

Fig. 2(a) shows the temporal evolution of the normalized contact width. During the spreading and retracting stages (e.g., $t < 6$ ms), the dynamics are comparable for these three cases. The contact time for the TSAW case is reduced by ~ 4.6 ms compared with the DFI case, mainly due to the shortening of the detachment period in this case. Fig. 2(b) shows the normalized contact time of the droplet versus applied SAW power to the IDTs. For the TSAW cases, the contact time is reduced by increasing the applied SAW power. Whereas at lower applied SAW power ($P < 15$ W), the reduction percentage of the contact time is not significant, due to the lower energy transferred from the solid surface during the impingement. By increasing applied SAW power up to 40 W, the contact time is significantly reduced by $\sim 25\%$. For the SSAW case, the evolution of the contact time can be divided into two stages. The contact time reduction is observed at applied SAW power lower than 25 W, whereas the contact time is increased at normalized applied SAW power higher than this value. The contact time for the DFI scenarios is not a function of impact velocity. Interestingly, our experimental results showed that there is a threshold of droplet impact velocity for a complete rebound from the hydrophobic and non-textured surface. As illustrated in Fig. 2(c), the initial kinetic energy of the droplet, with impact velocities below 1.26 m/s, is not sufficiently high enough to detach the entire droplet from the surface at the end of the retract step. The results presented in Fig. 2(c) illustrates that the impact regime can be efficiently modified by applying the TSAW from deposition to rebound at impact velocities below 1.26 m/s.

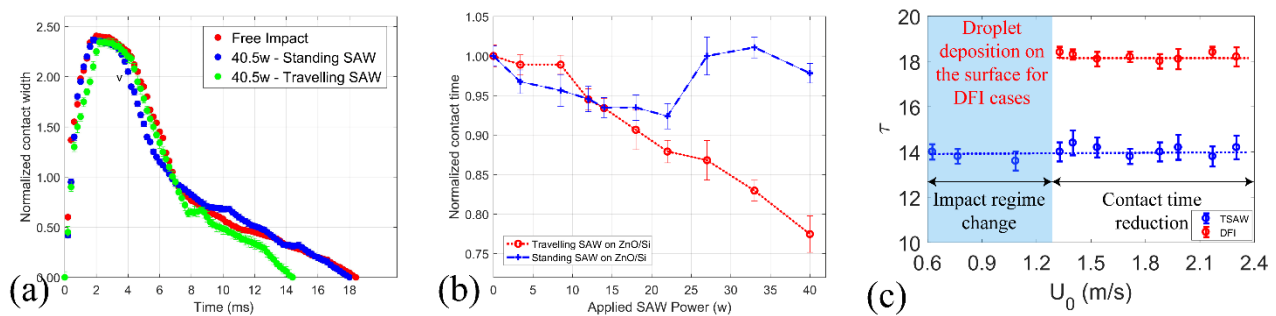


Figure 2: (a) Normalized contact width of droplet impact on SAW device for DFI, TSAW and SSAW scenarios. (b) Normalized contact time as a function of applied SAW power. Error bars represent SD of the results. (d) Contact time versus impact velocity for a droplet with a volume of $3.56 \mu\text{l}$ for DFI and TSAW scenarios. The shaded area represents droplet deposition on the surface for DFI cases.

Discussion and conclusion

We present a new method for droplet bouncing control in which the bouncing time and direction can be reduced by altering the internal flow within the spreading and retracting phase of the rebound process by surface acoustic waves. This can be done by using an acoustic wave travelling along a smooth unstructured surface to transfer energy into the liquid and thus breaking the symmetry of the internal flow during the impingement. Our experimental results, supported by numerical simulations [4], show a contact time reduction of as much as 35%.

This approach can be used effectively for applications where it is desirable to reduce the contact between solid and liquid to avoid surface erosion (for example, airplane wings or wind turbine blades). In addition, the ability to clean and remove the impacting liquid droplet allows for the manufacture of anti-contamination / anti-bacterial surfaces using this method. The ability to reduce the droplet's contact time may also be used to regulate the thermal gradient between solid and liquid, or to deicing and anti-icing applications in aircraft wings or wind turbine surfaces. In the other hand, for spray cooling applications such as spray cooling of nuclear reactors and electronic components, it is desirable to control the contact time and area of the droplet with the high-temperature surface to control the rate of heat transfer, and the method we proposed in this study could be suitable for these spray cooling applications.

References

- [1] Bird, J. C., Dhiman, R., Kwon, H. M. & Varanasi, K. K. *Nature* **503**, 385–388 (2013)
- [2] Guo, C., Zhao, D., Sun, Y., Wang, M. & Liu, Y. *Langmuir*, **34**, 43 (2018).
- [3] Liu, Y., Andrew, M., Li, J., Yeomans, J. M. & Wang, Z. *Nat. Commun.* **6**, (2015).
- [4] Mehdi H. Biroun, Jie Li, Ran Tao, Mohammad Rahmati, Glen McHale, Linxi Dong, Mehdi Jangi, Hamdi Torun, YongQing Fu, *Physical review applied*, in press (2020).

Droplet merging in a PDMS micro-well driven by surface acoustic waves

A. Sudeepthi¹, L. Yeo², and A. K. Sen¹

¹Micro Nano Bio-Fluidics Unit, Fluid Systems Laboratory, Department of Mechanical Engineering, Indian Institute of Technology Madras, Chennai-600036, India
 E-mail: sudeepthi106@gmail.com, URL: <http://ashislab.in/>

²Micro/Nanophysics Research Laboratory, School of Engineering, Royal Melbourne Institute of Technology (RMIT University), Melbourne, Victoria 3001, Australia

Introduction

Droplet merging is crucial to initiate chemical reactions that would find applications in the fields of biology and chemistry. Recently, surface acoustic waves (SAWs) are exploited to perform droplet merging in continuous flow microfluidic systems [1-3]. Slowing down droplets in an expansion chamber and subsequent trapping using traveling SAW radiation force facilitated droplet coalescence [1]. Merging of surfactant stabilized droplets is executed by destabilizing the droplet-droplet interface via acoustic streaming [2]. The method provides a safer way to manipulate biological entities within droplets, as the droplets are not directly exposed to SAWs. Further, SAW pulse actuation is synchronized with the fluorescence detection module to perform selective merging of surfactant stabilized droplets [3]. While the antecedent studies report merging of the droplets in microchannels, we experimentally demonstrate here the merging of droplets a PDMS microwell by employing SAWs. Microwell structures are long-established to carry out cell-related studies, sample preparation, and biological assays. Moreover, microwell structures provide individual well addressability to carry out multiple independent operations parallelly.

Experimental details

The schematic of the experimental setup is shown in Fig. 1a. The setup consists of a PDMS microwell bonded onto a SAW device. The device is operated at 19.76 MHz frequency in all the experiments. The PDMS microwell is of 5 mm diameter and 0.5 mm height and positioned in front of IDT such that the liquid dispensed in the microwell is subjected to symmetric SAW exposure. The microwell is filled with 12 μl of DI water and mineral oil droplets of volumes $\leq 0.1 \mu\text{l}$ are gently dispensed. Water volume is maintained constant throughout all the experiments. As the mineral oil density (850 kg/m^3) is less than water (989 kg/m^3) and possesses a negative spreading parameter, it floats on water while forming a liquid lens with finite contact angle.

Results and discussion

Upon the actuation of liquid (water) with SAWs, streaming motion is set up in the microwell, creating two equal size symmetric streaming vortices (Fig. 1b and 1c). The presence of the PDMS microwell

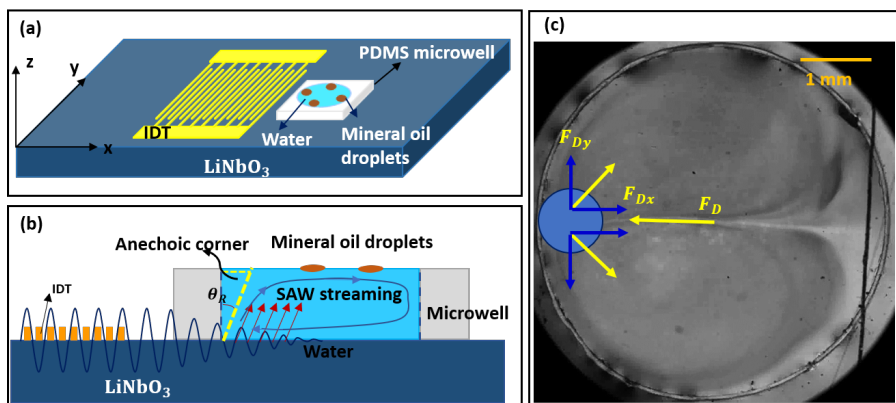


Figure 1: (a) Schematic of the experimental setup. (b) Schematic showing the acoustic streaming in the microwell. (c) Droplet trapping zone in the microwell.

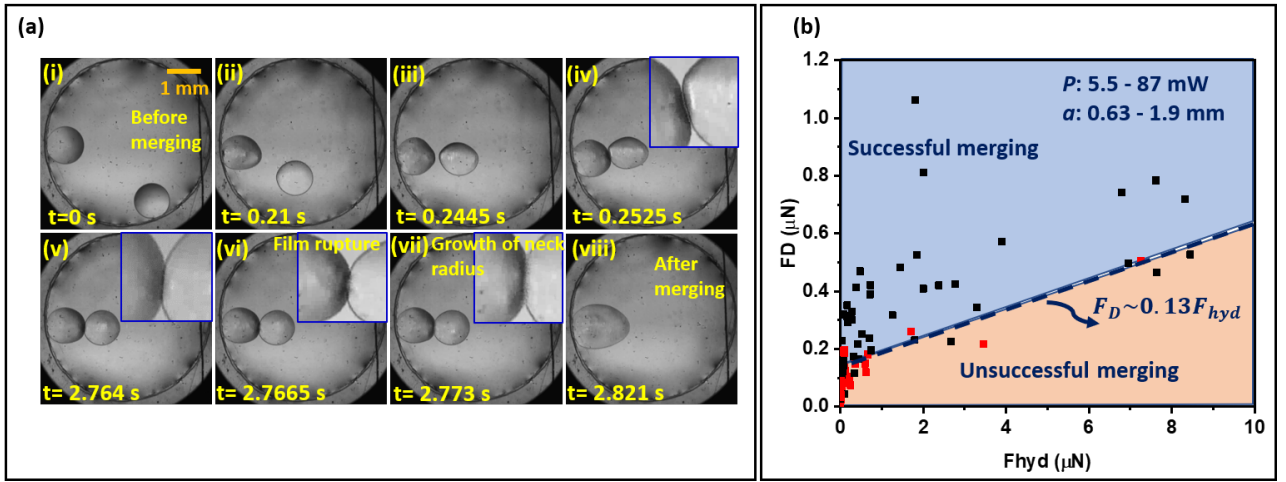


Figure 2: (a) Time-lapse image of the droplet merging in microwell under the action of SAWs. (b) Plot showing the regimes of droplet merging for the various experimental conditions.

wall together with the symmetric exposure to SAW renders a distinctive feature: formation of a droplet trapping zone in the microwell, as shown in Fig. 1c. Droplets are carried to the trapping zone and retained close to each other by the acoustic streaming induced drag force. The magnitude of the drag force can be estimated from $F_D = 6\pi\mu a u(1 + 0.15Re^{0.687})$ where μ is the viscosity of water, a is the droplet radius, Re is the particle Reynolds number and u is the relative velocity of the fluid to the particle. The magnitude of the drag force is estimated to be $\sim (10^{-7} - 10^{-6})$ N for the range of droplet diameters: 0.63-1.9 mm and input powers: 5.5-132 mW investigated in the present study. As the droplets approach close to each other, continuous phase (CP) fluid gets trapped between them, and the thickness of the CP fluid film continues to decrease as the droplets squeeze in further under the action of F_D . When the thickness of the film becomes of the order of a few micrometers, hydrodynamic pressure starts to build up in the thin film and offers hydrodynamic film drainage force given by $F_{hyd} = \frac{3\pi\mu l_i^4}{2\beta h^3} \frac{dh}{dt}$ where h is the thin film thickness, l_i is the length of the droplet interfaces in contact, $\frac{dh}{dt}$ is the film thinning rate and $\beta=4$ for mobile interfaces. The order of magnitude of F_{hyd} is estimated to be 10^{-6} N. If the drag force magnitude is sufficient to retain the droplets closer against the action of F_{hyd} , the inter droplet distance shrinks further to nanometer-scale due to the continued drainage of the CP liquid in the thin film. At this length-scale van der Waals forces of attraction (F_{vdw}) become effective and cause the film rupture leading to the droplet merging. The magnitude of van der Waals force of attraction can be estimated by $F_{vdw} = \frac{A l_i^2}{6h^3}$ where A is the Hamaker constant, which is typically $\sim 10^{-21}$ J for mineral oils; the estimated magnitude of F_{vdw} is $\sim 10^{-6}$ N at a film thickness of ~ 10 nm, which is comparable to F_{hyd} . Therefore, film rupture takes place, as shown in Fig. 2a(vi) and leads to the droplet merging. The regimes of droplet merging are demarcated for various experimental conditions (input power and droplet diameters) in terms of the ratio of the governing forces, as shown in Fig. 2b. Droplet merging is observed when the ratio $F_D/F_{hyd} \geq 0.13$.

Conclusion

We have experimentally demonstrated the merging of droplets in a PDMS microwell driven by SAW streaming. Droplet merging is realized owing to the formation of a droplet trapping zone in the PDMS microwell where the droplets are trapped and merged. Merging process is governed by the interplay between acoustic streaming induced drag force (F_D) that promotes merging and the hydrodynamic film drainage force (F_{hyd}) that develops in the thin film of the continuous phase liquid trapped between the droplets to resist the merging. The critical ratio of these forces to realize droplet merging was obtained from the experimental data as $(F_D/F_{hyd}) \geq 0.13$. The regions of successful and unsuccessful merging events are demarcated for various experimental conditions in which the input power and droplet size are varied. The device could find potential applications in the areas of on-chip mixing of reagents.

References

- [1] M. Sesen, T. Alan, and A. Neild. Lab Chip **14**(17), 3325-3333 (2014).
- [2] M. Sesen, A. Fakhfour, and A. Neild. Analytical Chemistry **91**(12), 7538-7545 (2019).
- [3] V. Bussiere, A. Vigne, A. Link, J. McGrath, A. Srivastav, J. Baret, and T. Franke. Analytical Chemistry **91**(21), 13978-13985 (2019).

High-Throughput Triggered Merging of Droplets Using Travelling Surface Acoustic Waves

Vincent Bussiere¹, Aurélie Vigne^{1,2}, Andreas Link¹, John McGrath¹, Aparna Srivastav¹, Esther Richter¹, Ziyun Wang¹, Mustafa Zaimagaoglu¹, Jean-Christophe Baret² and Thomas Franke¹.

¹ Department of Biomedical Engineering, University of Glasgow, Glasgow G12 8LT, United Kingdom
E-mail: Thomas.Franke@glasgow.ac.uk

² Université de Bordeaux, CNRS, Centre de Recherche Paul Pascal, Pessac 33600, France

Introduction

Droplet-based microfluidics enables the precise control and analysis of (bio)chemical reactions [1] and provides a powerful platform for high throughput single-cell screening in large cell populations.[2] Droplets act as picoliter sample carriers that can be systematically sorted, trapped, mixed, pipetted, and split in a user-defined process [3]. Here, we present a new acoustofluidic device that enables rapid, selective merging of individual droplet pairs, triggered by droplet fluorescence level. We characterize the acoustic droplet merger by analyzing the impact of critical operating parameters on merging efficiency and show that the main control parameters for merging droplet pairs are the pulse delay, power and duration.

Materials and Methods

We use a tapered IDT (TIDT) deposited on top of a piezoelectric substrate (polished, 128° rot, Y-cut LiNbO₃), coated with a 200 nm SiO₂ layer, to generate travelling surface acoustic waves (T-SAWs). The theoretical resonance frequency of the T-IDT is 160-167 MHz. PDMS channels are manually aligned on the T-IDT chip and mechanically pressed against the chip to create a seal before flushing channels with Aquapel to make them hydrophobic. For on-chip production of a binary emulsion, we use a double cross-junction module with all inlet widths set to 30 μm. 2% w/w Fluosurf in 3 M NOVEC 7500 fluorinated oil constitutes the continuous phase while deionized water (18.2 M) or deionized water with trypan blue and fluorescein (10 μM) are used for the dispersed phases. Volumetric flows rates between 20 and 200 μL h⁻¹ are used, depending on droplet frequencies. Continuous oil phase was added to the emulsions to space droplets in the channel.

To excite droplets, a 488 nm 200 mW DPSS laser is aligned to the droplets' path. The fluorescence signal of individual droplets can be collected through a photomultiplier tube (H10723-20, Hamamatsu) before being analyzed in real-time by a custom LabView routine (LabView 2019, National instruments) compiled on a field-programmable gate array (FPGA; NI PCIe 7841R, Virtex-5 LX30, 200 kS s⁻¹, National instruments). If a droplet's fluorescence signal exceeds a user-defined threshold a delayed 5 V TTL signal is sent from the FPGA to trigger, with μs precision, a switcher (ZX80-DR230-S+, Mini-Circuits) permanently fed with an HF signal coming from a signal generator (SMB 100A, Rohde & Schwarz). Next, the HF signal is redirected to the T-IDT and a T-SAW pulse is actuated upon the targeted droplet pair.

Results and Discussion

The droplets flow in an expanding channel section at the merging chamber entrance (Figure 1a) where fluorescence level is measured continuously using a laser-induced epifluorescence setup. The laser beam is focused upon the droplet and detects the fluorescence emission signal with a photomultiplier tube. When the

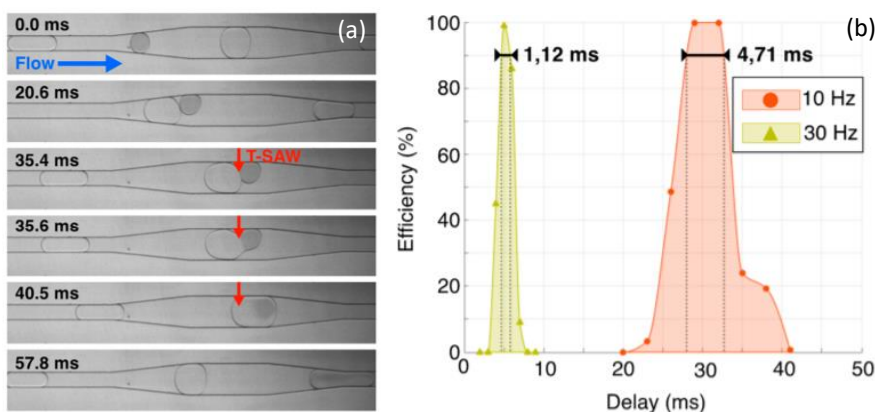


Figure 1: Timelapse image of 10 Hz (a) triggered (FT) merging. Flow direction indicated by the blue arrow. T-SAW path indicated by red arrows. No merging occurred without T-SAWs.

(b) Comparison of 10 and 30 Hz drop frequencies. Delay time intervals for highly efficient merging ($\geq 90\%$) indicated by the span between dotted lines. Data were obtained by analyzing 100 drop pairs per point. (a) and (b) adapted with permission from ref [4].

fluorescence level exceeds the threshold, a trigger actuates merging downstream. While flowing through the channel expansion, droplets with a diameter smaller than the maximum chamber width ($W_{\max} = 100 \mu\text{m}$) become slower, allowing droplets that follow and span the channel width in plug-flow to catch up. This means that smaller droplets become the front drops of droplet pairs that will eventually merge, while the larger ones become the rear drops. Merging is induced by delivering an acoustic pulse, generated by a T-IDT, that hits the droplet pair. In the newly formed drop, the daughter droplets mix quickly as the new drop exits the chamber.

Exact timing and positioning of the T-SAW, with respect to droplets position, is key to merging. When a drop exceeds the fluorescence threshold and the merging trigger is set, the SAW pulse is delayed by a user-defined delay time D . The position of the acoustic path relative to the position of targeted droplet pairs is influenced by D and by droplet frequency, as the latter affects droplet velocity. To understand how droplet frequency and signal delay time impact droplet merging, we measured merging efficiency at different combinations of production frequency and delay times. Figure 1b shows FT merging efficiency at 10 and 30 Hz fluorescein droplet production frequencies. Increasing the frequency of triggering droplets substantially reduces the D , as droplet pairs need less time to flow to the merging position. Higher droplet production frequency is also associated with a narrowing of the D range available to achieve high merging efficiency ($\geq 90\%$), meaning that that precise timing becomes essential. The D range is reduced from 4.71 to 1.12 ms when fluorescein droplet frequency increases from 10 to 30 Hz. This reduction is explained by a decrease in interaction time between the acoustic path and droplets, due to an increased averaged droplet velocity from 15 to 60 $\mu\text{m ms}^{-1}$. We found that higher merging efficiencies ($\geq 90\%$) are achieved when the front edges of rear droplets are first hit by the acoustic wave (Figure 1a; T-SAW position annotated at 35.4 ms).

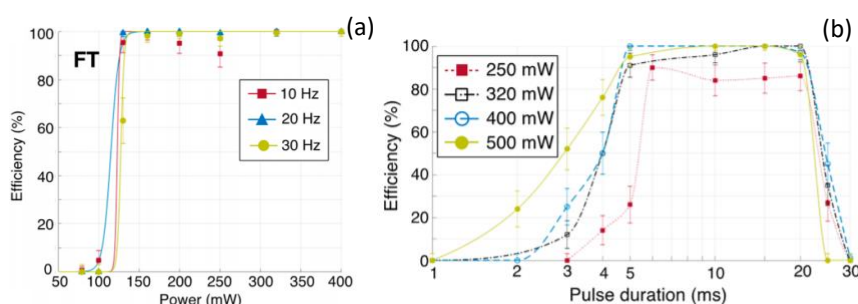


Figure 2: (a) Merging efficiency depending on electric power used for FT merging. SAW frequency = 162 MHz and PD = 10 ms.

(b) Distribution of merging efficiency as a function of pulse duration for different powers. SAW frequency = 162 MHz and delay = 29 ms. (a) and (b) adapted with permission from ref [4].

Another important parameter influencing the acoustofluidic manipulation of droplets is the amount of acoustic momentum delivered to the system. We performed FT merging at three different fluorescein droplet frequencies (10, 20, and 30 Hz) to observe merging efficiency as IDT excitation power is modulated. Our results suggest that merging efficiency critically depends on the power applied to the IDT (Figure 2a). While no merging was observed at lower signal amplitudes, efficiency rapidly increases for merging when signal power exceeds a critical level of ~ 100 mW. This trend, forcing the comparison with a switched on/switched off phenomenon, is independent of the droplet frequencies considered within our experiments.

Figure 2b shows merging efficiency for pulse durations at four different T-IDT excitation powers, ranging from 250 to 500 mW. The resulting curves, which show system behavior at four different powers, all follow a similar trend and can be divided into three consecutive intervals: a rising, a plateau, and a decreasing phase. The rising phase takes place in between 1 and 6 ms, as merging efficiency increases substantially for each power when the pulse duration (PD) is incrementally increased. Between 250 and 500 mW PD, higher powers result in higher merging efficiency, before merging efficiency stabilizes and curves enter a plateau-like phase. After 20 ms PD, merging efficiency quickly drops.

When two surfactant-stabilized droplets get closer, the drainage of the film separating them is responsible for an outward flow that leads to heterogeneous distribution of surfactant molecules along their surface. The resulting surface tension gradient leads to a Marangoni stress, which drives an inward flow counteracting film drainage, preventing droplet coalescence. We hypothesize that acoustic streaming induced by the T-SAW could disturb the Marangoni flow, enabling film drainage, and subsequent contact and merging.

Conclusion

In this work, highly specific and efficient merging was achieved within a narrow time window by triggered acoustic pulse actuation. The timing and position of the acoustic pulse was also precisely controlled relative to each detected droplet pair. Thus, we were able to ensure that the acoustic pulse initially contacted the target droplet pair at the front of the rear drop, and subsequently switched off before entry of the next droplet pair to the merging region. Our characterization of the dependency of merging efficiency on TSAW power showed a sharp onset and the existence of a critical value, above which very high merging efficiency is achieved. The device attains a merging efficiency of 100% within the range of experimental parameters tested.

References

- [1] Teh, S.-Y.; Lin, R.; Hung, L.-H.; Lee, A. P. *Lab Chip*, 2008, 8 (2), 198–220.
- [2] Weitz, D. A. *Lab Chip*, 2017, 17 (15), 2539–2539.
- [3] Sesen, M.; Alan, T.; Neild, A. *Lab Chip*, 2017, 17 (14), 2372–2394
- [4] Bussiere, V.; Vigne, A.; Link, A.; McGrath, J.S.; Srivastav, A.; Baret, J.-C.; Franke, T. *Anal Chem.* 2019, 91, 13978–85

Session 2 - Bio-Acoustic Systems

Invited Speaker

SIMPLICITY OR COMPLEXITY: TRANSDUCERS AND INSTRUMENTATION STRATEGIES FOR ACOUSTOFLUIDIC MANIPULATION OF CELLS AND BIOFUNCTIONALIZED BEADS

[Martin Wiklund](#), Karl Olofsson, and Björn Hammarström
Royal Institute of Technology, SWEDEN

Contributed Talks

CELL ADHESION, MORPHOLOGY, AND METABOLISM VARIATION VIA ACOUSTIC EXPOSURE WITHIN MICROFLUIDIC CELL HANDLING SYSTEMS

[Citsabehsan Devendran](#), James Carthew, Jessica E. Frith, and Adrian Neild
Monash University, AUSTRALIA

TWO-DIMENSIONAL PATTERNING OF SWIMMING CELLS USING HYBRID ACOUSTIC WAVE DEVICES

[Mingyang Cui](#)¹, Philip V. Bayly¹, Susan K. Dutcher², and J. Mark Meacham¹
¹Washington University, St. Louis, USA and
²Washington University School of Medicine, St. Louis, USA

ACOUSTIC SEPARATION OF VIABLE AND DEAD CELLS USING HIGH-DENSITY MEDIUM

[Karl Olofsson](#), Björn Hammarström, and Martin Wiklund
KTH Royal Institute of Technology, SWEDEN

MOTILITY-BASED SPERM SELECTION USING SURFACE ACOUSTIC WAVES

[Junyang Gai](#), Reza Nosrati, and Adrian Neild
Monash University, AUSTRALIA

ADVANCED CELL MANIPULATION WITH VORTEX-BASED ACOUSTICAL TWEEZERS

[Michael Baudoin](#)^{1,2}, Jean-Louis Thomas³, Roudy Al Sahely¹, Jean-Claude Gerbedoen¹, Zhixiong Gong¹, Aude Sivery¹, Olivier Bou Matar¹, Nikolay Smagin¹, and Alexis Vlandas¹
¹Université de Lille, FRANCE, ²Institut Universitaire de Franc, FRANCE, and
³Sorbonne Université, FRANCE

A MICROFLUIDIC PLATFORM FOR ACOUSTIC PARTICLE FOCUSING IN HYDROGEL DROPLETS

[Maria Tenje](#), Hannah Pohlit, and Anna Fornell
Uppsala University, SWEDEN

GENERATING ORDERED CARDIAC TISSUE MODELS USING ACOUSTIC CELL PATTERNING

Ekaterina Pchelintseva¹, Ilona Sunyovzsky¹, James P.K. Armstrong¹, Alice Agliano¹, Bruce W. Drinkwater², Cesare Terracciano¹, and Molly M. Stevens¹
¹Imperial College London, UK and ²University of Bristol, UK

A PORTABLE ACOUSTOFLUIDIC BASED CHEMILUMINESCENCE BIOSENSOR

Xian Chen, Bohua Liu, Wei Pang, and Xuexin Duan
Tianjin University, CHINA

HIGHLY EFFICIENT ACOUSTOPHORETIC SINGLE CELL-SUPERNATANT SEPARATION INSIDE NANOLITER DROPLETS

Michael Gerlt¹, Dominik Haidas², Alexandre Ratschat¹, Philipp Suter¹, Petra Dittrich², and Jürg Dual¹
¹ETH Zürich, SWITZERLAND and ²ETH Zürich, Basel, SWITZERLAND

CHARTING CELL PROPERTIES THROUGH THEIR ACOUSTOPHORETIC MIGRATION IN A GRADIENT OF DENSITY AND COMPRESSIBILITY

Mahdi Rezayati Charan and Per Augustsson
Lund University, SWEDEN

REFRACTION OF ACOUSTIC VORTEX BEAMS IN AN INHOMOGENEOUS MEDIUM

Xudong Fan and Likun Zhang
University of Mississippi, USA

STREAMING IN A KUNDT'S TUBE OF AN ARBITRARY DIAMETER

Alen Pavlic and Jürg Dual
ETH Zürich, SWITZERLAND

REVERSAL OF INTERPARTICLE RADIATION FORCES ACTING ON MICRO PARTICLES INDUCED BY BULK ACOUSTIC STANDING WAVES IN A MICROCHANNEL

Sazid Zamal Hoque and Ashis Kumar Sen
Indian Institute of Technology, Madras, INDIA

Simplicity or complexity: Transducers and instrumentation strategies for acoustofluidic manipulation of cells and biofunctionalized beads

Martin Wiklund¹, Karl Olofsson¹, and Björn Hammarström¹

¹Department of Applied Physics, Royal Institute of Technology, Stockholm, Sweden
 E-mail: martin@biox.kth.se, URL: <http://www.kth.se/profile/bmw>

Introduction

In this paper we review the different strategies used in the Wiklund group over two decades for transducer design and acoustofluidic instrumentation used in various bio-applications. Our strategies vary from simple to complex, and we discuss advantages and disadvantages with each implemented method. Originally the devices were used for enhancing bead-based immunoassays [1, 2], but since long the research and developed methods focus on manipulation and long-term trapping of biological cells [3-8]. We conclude that although simplicity is often favorable, complex systems also have some important advantages, in particular when handling cells.

Methods, results and discussion

In early 2000s we investigated standing-wave ultrasound for enhancing different types of bead-based immunoassays. Two types of immunoassays were studied: An agglutination-based assay (Fig. 1a) and a fluorescence-based assay (Fig. 1b). In both methods, we used focusing ultrasonic transducers and a hemispherical resonator geometry, with the original idea to implement an acoustic version of an optical tweezer. Two interesting aspects of these setup were later concluded when comparing them with more modern microscale systems: Broadbanded transducers with low Q-value have some advantages due their frequency tunability [1, 2], and lossy polymer materials may still function as acoustic reflectors under certain circumstances [2]. In particular, the latter has gained increased interest recently.

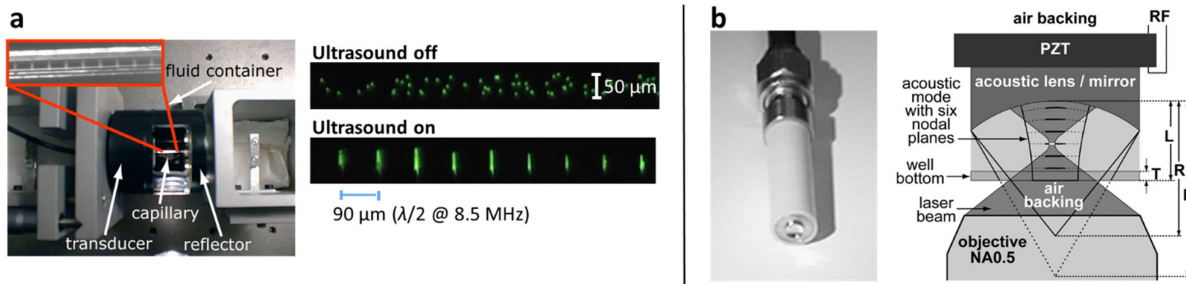


Figure 1: Experimental setups from early 2000s used in bead-based immunoassays. Both systems are based on a hemispherical resonator geometry with a focusing ultrasonic transducer and a planar reflector. The system to the left (a) [1] was integrated in a commercial capillary electrophoresis system, which allowed for driving the fluid inside the fused silica capillary with a plug-profile electro-osmotic flow. The system to the right (b) [2] shows a 5-mm-diameter focusing transducer that was combined with the polymer bottom of a disposable 96-well plate used as an acoustic reflector. This system employed ambient-analyte conditions for the ultrasensitive detection of biomolecules.

In mid and late 2000s we changed research focus and started to use glass-silicon microchannels and applications involving biological cells. Compared to most of the other groups in the acoustofluidic community, we used a different and sometimes questioned actuation strategy based on low-Q-value transducers with wedges [3] or backing layers [4] (Fig. 2). The idea with the wedges was taken from similar transducer designs used for mode conversion (bulk-to-surface waves). Although the acoustic coupling into the fluid channel did not function as we originally hypothesized, we noticed that they were efficient and flexible when tuning the transducer driving frequency matched with an intended and localized channel resonance, as well as the fact that we could use several transducers on the same chip, and an extremely useful frequency modulation method [5]. Similar functions were later found when using a planar piezoceramic with a backing layer [4], *i.e.*, a design inspired from transducers used in sonography. Both the wedge transducer and the backing layer transducer were broadband and thus, with low Q-values. Nonetheless we could in many applications actuate them by the use of a standard function generator operating at 10 V_{pp} without the need for RF amplifiers. On the other hand, in applications using high pressure amplitudes (of the order of 1 MPa), we have developed a water-

cooled transducer platform combined with a temperature regulation system and RF amplification (see Fig. 3a) [6]. With this system we are able to operate our broadbanded transducers at both high and low voltages, while retaining a safe and stable biological environment over long time periods (weeks). Here, most important is to retain a stable and constant physiological temperature in the fluid channel containing trapped cells [6].

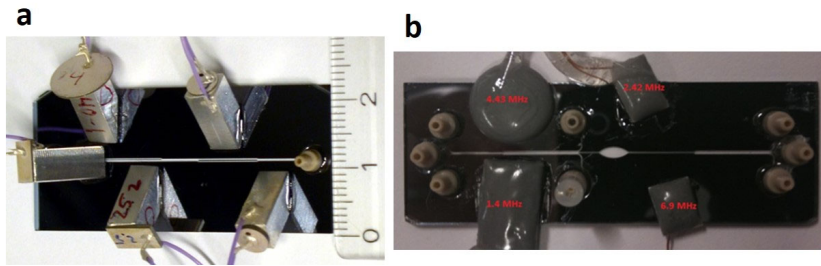


Figure 2: Glass-silicon chips used in the late 2000s. Here we used microchips with channels etched in silicon, and with glass layers on each side of the silicon layer. The system to the left (a) uses transducers where piezoceramic plates are attached to aluminum wedges. The system to the right (b) uses backing layers based on mixtures of epoxy glue and tungsten powder.

During the last decade we have primarily focused our research on acoustically formed and maintained 3D cell cultures used for immunotherapy research [7, 8]. The primary device used for this purpose is a multi-well microplate attached to a planar ring transducer (see Fig. 3b) [7]. This device uses the same temperature regulation system as discussed for the device in Fig. 3a. When designing the multi-well microchip platform we prioritized simple handling by the operator as well as compatibility with advanced live cell microscopy imaging, *i.e.*, needs from a bioapplication and user point of view. As a consequence, the final design is relatively complex with many different materials, layers and shapes, resulting in another broadbanded and low-Q-value system. However, because of the available temperature regulation and cooling system we had developed previously, our instrument turned out to be very robust, flexible and functional. We have used it almost daily for more than five years without the need for any costly service or maintenance.

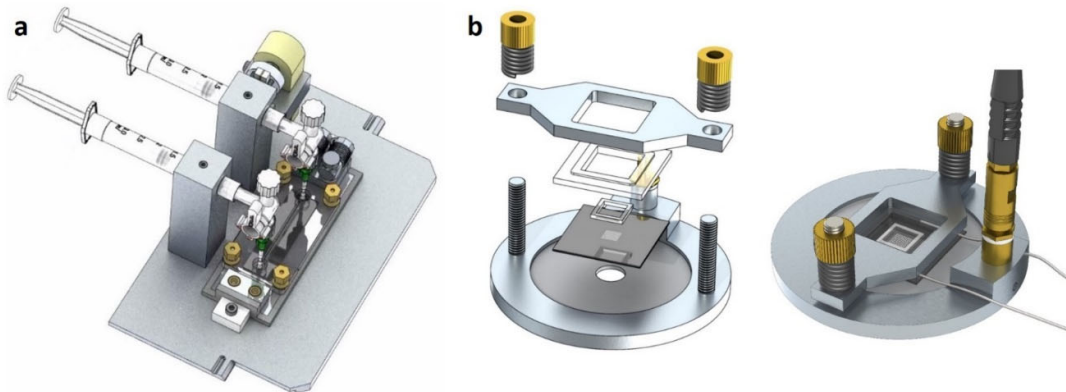


Figure 3: Complex broadbanded systems used in the 2010s with integrated water cooling and temperature control, described in detail in Refs. 6-8. They have in common that they are designed for maintaining a physiological environment for *in vitro* cell cultures, where the cell clusters are formed and shaped by ultrasonic standing wave manipulation.

Conclusion and outlook

Most of the systems developed and investigated in the Wiklund group during two decades are broadbanded with low Q-values. Despite the fact that these systems are lossy, they have some important advantages. For example, they are frequency tunable, more robust during long-time operation, and possible to actuate with various frequency modulation strategies for reducing spurious modes in ultrasound resonances. Looking forward, considering our ongoing and planned work, we will also present a completely new actuation strategy for cell manipulation where these advantages are retained but with the use of an actuation method based on surface modes in a modified piezoceramic plate similar to a miniaturized fluidic version of a Chladni plate [9].

References

- [1] M. Wiklund, S. Nilsson, H.M. Hertz, *J. Appl. Phys.* **90**, 421-426 (2001).
- [2] M. Wiklund, J. Toivonen, M. Tirri, P. Hänninen, H.M. Hertz, *J. Appl. Phys.* **96**, 1242-1248 (2004).
- [3] O. Manneberg, J. Svennebring, H.M. Hertz, M. Wiklund, *J. Micromech. Microeng.* **18**, 095025 (2008).
- [4] I.S. Iranmanesh, H. Ramachandraiah, A. Russom, M. Wiklund, *RSC Advances* **5**, 74304-74311 (2015).
- [5] O. Manneberg, B. Vanherberghen, B. Önfelt, M. Wiklund, *Lab Chip* **9**, 833-837 (2009).
- [6] M. Ohlin, I.S. Iranmanesh, A.E. Christakou, M. Wiklund, *Lab Chip* **15**, 3341-3349 (2015).
- [7] A.E. Christakou, M. Ohlin, B. Önfelt, M. Wiklund, *Lab Chip* **15**, 3222-3231 (2015).
- [8] K. Olofsson, V. Carannante, M. Ohlin, T. Frisk, K. Kushiro, M. Takai, A. Lundqvist, B. Önfelt and M. Wiklund, *Lab Chip* **18**, 2466 (2018).
- [9] B. Hammarström, N. Refstrup Skov, K. Olofsson, H. Bruus and M. Wiklund, manuscript submitted to *JASA* (2020).

Cell Adhesion, Morphology, and Metabolism Variation via Acoustic Exposure within Microfluidic Cell Handling Systems

Citsabehsan Devendran¹, James Carthew², Jessica E. Frith², and Adrian Neild¹

¹Laboratory for Micro Systems, Department of Mechanical and Aerospace Engineering, Monash University, Clayton, VIC 3800, Australia

E-mail: saab.devendran@monash.edu, URL: <https://www.labformicrosystems.com/citsabehsan>

²Department of Materials Science and Engineering, Monash University, Clayton, VIC 3800, Australia

Introduction

The manipulation of biological matter in microfluidics has become widespread in recent years. It is well established in the field of acoustofluidic cell handling, that cell viability studies are required following exposure to these systems. However, the methods used to assess this are often non-standardised and as a result vary significantly. Despite the significant fundamental advancements of acoustic manipulation techniques in terms of the underlying physics, investigations into biological effects has been underwhelming especially at higher frequency ranges (30 MHz - 600 MHz). Prevailing measures that are generally used include simple live/dead assays and less frequently, typical proliferation assays. Although biological cells are declared viable based on these measures, potential alterations in phenotypes are not indicated, which might prove undesirable, especially in clinical applications. We note significant variations in post exposure behaviour under a range of test conditions and screening techniques, for distinct cell types whilst preserving a high, comparable live/dead percentage, demonstrating the shortfall of simple live/dead assays. These post exposure alterations in phenotypes are not only frequency and amplitude dependent but are highly dependent on the cell type, as expected. Herein, we propose a range of techniques along with operational conditions appropriate for handling biological cells in a safe manner within acoustofluidics.[1]

System Principles

A major reason to use high frequency ultrasound in microfluidics, is that the wavelength is on the same order as a typical cell (i.e. 2 μm - 50 μm). This is a prerequisite for patterning of single cells[2] but has also been shown to provide the possibility of high sensitivity sorting, patterning using either standing waves or travelling waves and fluid mixing protocols enabled by surface acoustic waves (SAW).

We employ a 48.5 MHz SAW device (80 μm λ_{SAW} ; 128° YX cut LiNbO₃), that couples directly into the serpentine channel (Fig. 1a). The channel height (25 μm and 50 μm), flow rate (5 $\mu\text{L min}^{-1}$ and 10 $\mu\text{L min}^{-1}$) and excitation amplitude (400 mV and 800 mV) were altered to investigate the effects of shear, exposure times and intensity. A flow control (i.e. no acoustic exposure) and a TCP control (i.e. standard TCP protocol with no flow and acoustic exposure) were carried out as a basis for comparison. A range of post exposure assessments were conducted to gauge any phenotypical alterations of the exposed cells as denoted in Fig. 1b.

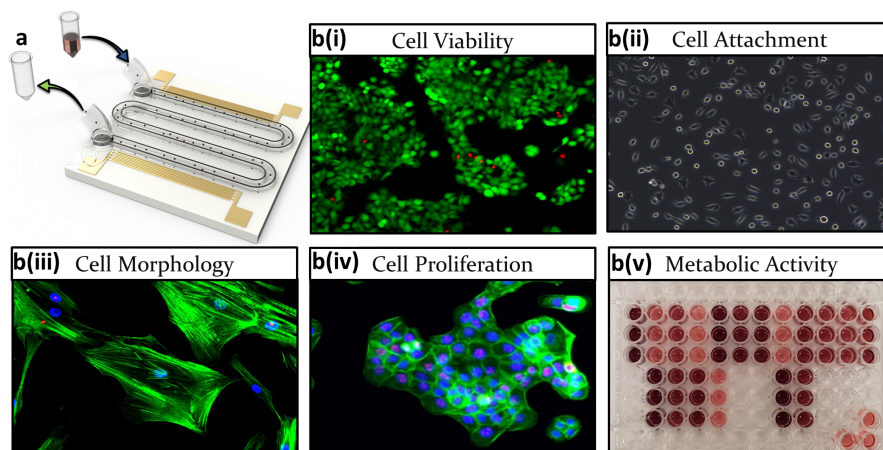


Figure 1: a) Design concept depicting the serpentine channel and IDT design. Distinct cell types are fed (indicated by the blue arrow) into the system at a regulated flow rate, exposed to ultrasound and retrieved (indicated by the green arrow) prior to seeding into tissue culture plastic (TCP) for b) a range of assessment and screening techniques.

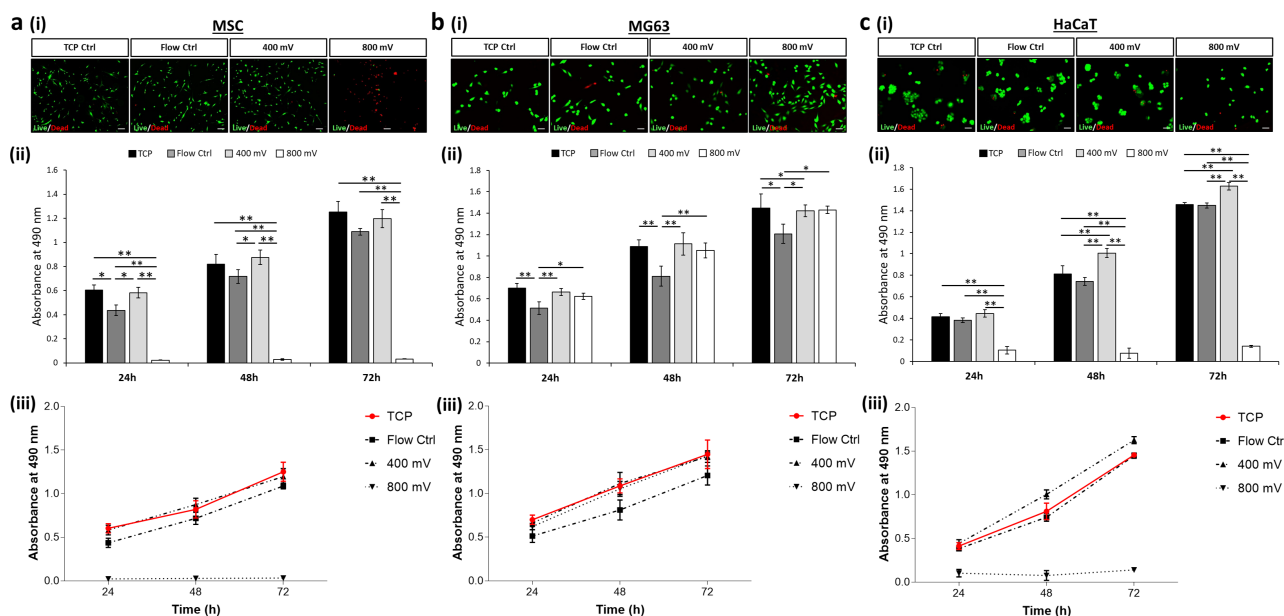


Figure 2: Increased channel height ($50 \mu\text{m}$ channel height; $10 \mu\text{L min}^{-1}$) presents enhanced acoustic effects while enabling larger a) Mesenchymal Stromal Cells (MSC) and b) MG63 cell extraction. Reduced flow rate ($5 \mu\text{L min}^{-1}$; $25 \mu\text{m}$ channel height) modulates metabolic activity of c) HaCaT while retaining a high degree of cell viability. (a-c)(i) Live/dead (green/red) fluorescence staining 24 h post-exposure and (ii) formazan absorbance (MTS assay; metabolic activity). MTS assay data analyzed using one-way ANOVA with Tukey post hoc testing. (iii) Growth rate extracted from MTS data. All data presented as mean \pm SD from triplicate samples ($n = 9$). Scale bar, $50 \mu\text{m}$. Statistically different samples are denoted by * $p < 0.05$, ** $p < 0.005$.

Results

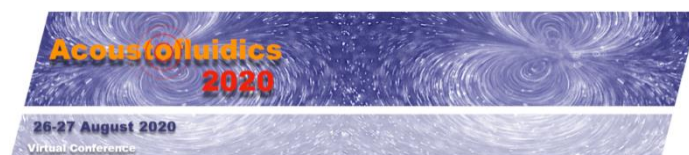
We note a range of behaviours, whereby exposed cell lines, experienced an inability to attach, sustain morphological alterations and measurable metabolic activity variations,[1] whilst returning a high level of live percentage (Fig. 2(i)) and an unaffected proliferation rate. We observe a consistent increase in metabolic activity (Fig. 2(ii-iii)) of acoustically exposed cells as compared to the flow control (i.e. direct comparison), post-exposure. Firstly, the reduced cell metabolic activity for the MSCs exposed to a 800 mV signal (Fig. 2a(ii); $50 \mu\text{m}$ high channel; $10 \mu\text{L min}^{-1}$) is observed due to the high percentage of dead cells encountered. MSCs are the most mechano-sensitive of the cells tested in this study and therefore is expected to be most susceptible to death when stressed. Secondly, the relative increase in metabolic activity observed for the 400 mV HaCaT cell line scenario (Fig. 2c(ii-iii)) as compared to the flow control and TCP control. This further suggests that the acoustic exposure contributes directly to an increase in metabolic activity. Thirdly, whilst a high proportion of living HaCaT cells were retrieved (Fig. 2c(i)), the significant drop in metabolic activity (Fig. 2c(ii-iii)) is due to an excessive stress inflicted by the prolonged exposure of higher acoustic intensities, rendering the cessation of normal biological function whilst preserving the cell membrane and structure. This ability to preserve its structural integrity can be attributed to the high levels of keratin in HaCaT cells that act to safeguard the cell under their normal function in the skin. This observation is an indication of the shortfall presented by simplistic live/dead assay as evidence for cell viability. Here, the reported live/dead percentage would serve as a “false positive” when used to substantiate cell viability in an acoustofluidic platform as it is contrasting in nature when compared to the cell metabolic activity.

Conclusion

Our data show differences in cell behaviour in response to acoustic stimulation, aspects that are not evident when using standard live/dead stains as a single readout of biocompatibility. This has critical implications for the methodologies used to evaluate the biocompatibility of acoustofluidic devices and platforms, making a case for the inclusion of a broad panel of cellular readouts. The variations and chronic thresholds are cell type-specific and thus, safe operation ranges should be considered whilst developing acoustic based microfluidic platforms with reference to the cell type used. Our findings also reveal a tantalising hint towards a correlation between acoustic exposure, cell stiffness and cellular metabolism,[1] which if understood, could be harnessed for therapeutic applications in the future.

References

- [1] C. Devendran, J. Carthew, J. E. Frith, A. Neild. *Adv. Sci.*, **6**, 1902326 (2019).
- [2] D. J. Collins, B. Morahan, J. Garcia-Bustos, C. Doerig, M. Plebanski, A. Neild. *Nat. Commun.*, **6**, 8686 (2015).



Two-dimensional patterning of swimming cells using hybrid acoustic wave devices

Mingyang Cui^{1*}, Philip V. Bayly¹, Susan K. Dutcher², and J. Mark Meacham^{1†}

¹Department of Mechanical Engineering and Material Science, Washington University in St. Louis, St. Louis, MO 63130, USA

*E-mail: cui mingyang@wustl.edu, †E-mail: meachamjm@wustl.edu, URL: <https://meachamlab.wustl.edu/>

²Department of Genetics, Washington University School of Medicine in St. Louis, St. Louis, MO 63110, USA

Introduction

Cell separation, manipulation, and isolation are essential to various chemical, biological, and biomedical applications. Among microfluidic approaches (e.g., technologies exploiting hydrodynamic, dielectrophoretic, magnetic, and optical steering), acoustofluidics permits size-selective, contact- and label-free particle manipulation. However, it is difficult to trap highly-motile microswimmers like the single cell algae *Chlamydomonas reinhardtii* (CR) without excessive device heating to achieve the high required trapping force. We have found that traditional polydimethylsiloxane (PDMS)-based surface acoustic wave (SAW) devices driven at ~10 and ~25 MHz are unable to trap (and subsequently release) CR cells without a loss of motility, as the operating temperature exceeds that which the cells can tolerate (see Fig. 1). A hybrid SAW device incorporating a glass microchannel that supports bulk acoustic waves (BAW) was able to align swimming CR cells to pressure nodal regions at both frequencies without affecting cell function or viability. Here, we extend this finding to develop an approach for two-dimensional (2D) patterning of CR cells. CR cells are positioned in a 2D grid using SAW to create a standing BAW field in a wet-etched square glass microchamber. Finally, the hybrid device enables single cell per well trapping and analysis of individual cell behavior using dilute cell suspensions.

Experimental

Soft lithography (PDMS) or wet etching (glass) was used to fabricate straight channels (width = 545 μm , depth = 50 μm) or square chambers (side length = 545 μm , depth = 22 μm), which were bonded to 128° Y-cut, X-propagating lithium niobate (LiNbO₃) substrates with pairs of interdigital transducers (IDTs) designed to operate at 10 and 25 MHz (spacing of 100 and 40 μm , respectively). The IDTs were created using standard photolithography, thermal evaporation (Cr/Au, 10 nm/80 nm), and a liftoff process. The PDMS microchannel was bonded to LiNbO₃ after plasma treatment, and the glass channel was adhered to LiNbO₃ using SU-8 2005 as an adhesive layer. IDTs were driven by an amplified sinusoidal signal at resonant frequencies identified by visual observation of particle focusing near design frequencies. For thermal analyses, channel temperature was measured using an IR camera under the same operating conditions used for CR cell trapping. Temperature measurements were compared to brightfield microscopy of the cell focusing progression to correlate excessive heating with cell viability. Biciliated wild-type (strain CC-125) cells were obtained from the Dutcher Lab at Washington University in St. Louis. Cells were prepared at $\sim 5 \times 10^6$ cells/mL for 2D patterning experiments and diluted 10X for single-cell trapping and analysis. For single-cell trapping studies, the dilute suspension was loaded into the actuated acoustofluidic device and imaged using a 100X objective at 2000 frames per second. Post processing and image analysis (e.g., ciliary waveform tracing) were performed using a custom MATLAB program.

Results and discussion

At low voltages, the relatively weak acoustic radiation force had a negligible effect on CR cells swimming in a PDMS microchannel driven at ~10 and ~25 MHz. Cells were focused using higher drive voltages (up to $V = 25 V_{pp}$ applied for 30 s); however, upon release (i.e., removal of acoustic excitation), it was discovered that cells were no longer moving because the temperature had rapidly increased above their thermotolerance threshold (Fig. 1; note $f = 9.62$ MHz for the cases shown in Fig. 1, but behavior is representative of both operating frequencies). In contrast, the glass-based SAW device successfully trapped cells in tight nodal lines at both frequencies at a lower applied voltage ($V = 15 V_{pp}$), and even at an equivalent drive voltage ($V = 25 V_{pp}$), the rate of temperature increase in the glass microchannel was significantly lower than in its PDMS counterpart.

We used the device with a square microchamber for 2D patterning of swimming CR at ~10 and ~25 MHz (Fig. 2). The CR cells were tightly confined to pressure nodes under acoustic actuation (Fig. 2C; again, note $f = 9.64$ MHz for the case shown in Fig. 2C, but behavior is representative of both operating frequencies). Nodal locations corresponded to a standing BAW field within the square chamber. Importantly, when devices were

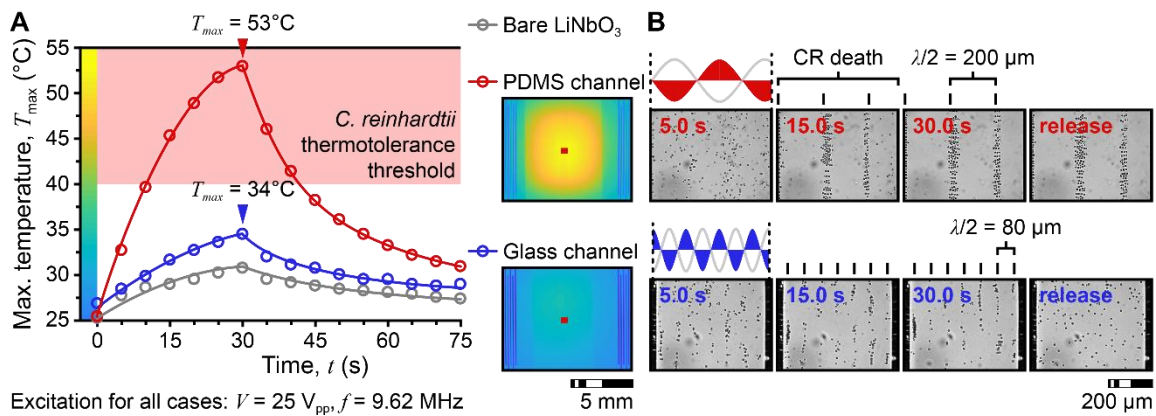


Figure 1: Response to temperature fluctuations of *C. reinhardtii* cells swimming in acoustofluidic microchannels. (A) Temperature increase/decrease during acoustic excitation and recovery for bare LiNbO₃, and LiNbO₃ with PDMS and glass microchannels. Thermographic images show the maximum attained temperature field for each case. (B) Cell focusing and viability following ultrasound exposure. Cells swim freely after release in the glass channel but remain at nodal positions in PDMS channels indicating a loss of viability.

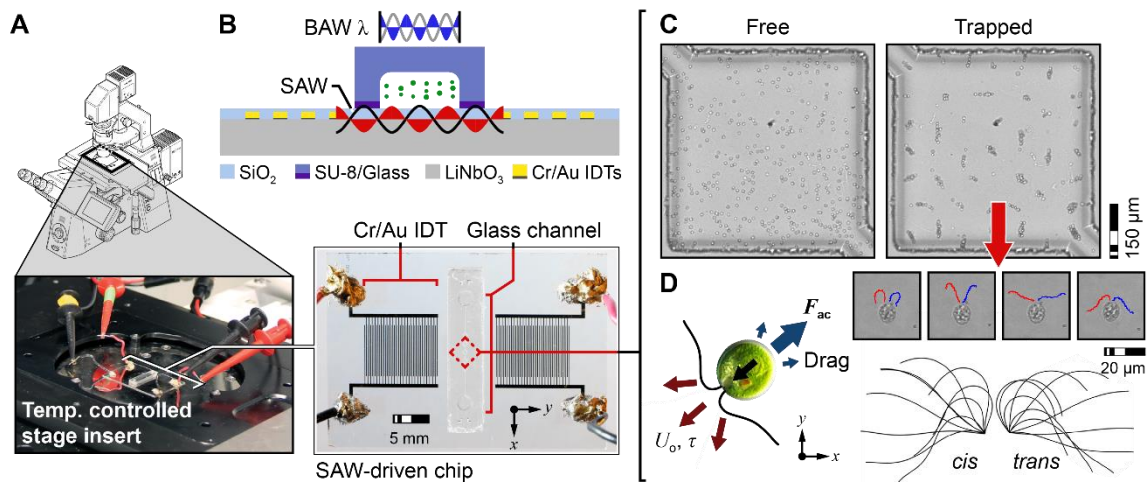


Figure 2: Two-dimensional (2D) patterning of swimming *C. reinhardtii* cells. (A) Device assembly and experimental setup. (B) Schematic illustration of the two-dimensional CR trapping device. (C) Patterning of swimming CR cells in a 2D grid. (D) Single-cell trapping and analysis of ciliary waveform for biciliate CC-125 cells.

loaded with dilute cell suspensions, we were able to trap, observe, and measure single cell behavior. Conventional analysis of ciliary waveform for biciliates like CC-125 is challenging due to the requirement for high magnification and the tendency of cells to rapidly leave the field of view. Waveform analyses of acoustically-confined CR cells were qualitatively similar to previous studies involving uniciliate mutants; however, trapping of biciliates enables observation of slight differences in the motion of the *cis* (closest to the eye spot) and *trans* cilia (Fig. 2D).¹ Further, quantitative measures (beat frequency, curvature, and amplitude) were also comparable to accepted values.

Conclusion

We demonstrated that a glass-based SAW device can pattern swimming cells while maintaining a safe operating temperature. Standing BAW yield primary radiation forces large enough to hold the cell body in place without affecting motion of the cilia. By extending our earlier hybrid device from 1D to 2D we not only pattern populations of cells but also achieve single cell per well trapping of biciliate CR cells. This result significantly improves the flexibility of our device for biomedical applications involving highly-motile microswimmers.²

Acknowledgements

This work was supported by the National Science Foundation, under Grant No. CMMI-1633971. Fabrication of glass SAW devices was conducted in the Institute of Materials Science and Engineering (IMSE) cleanroom at Washington University in St. Louis. The authors thank Dr. Mathieu Bottier for supporting cell preparation.

References

- [1] M. Bottier, K.A. Thomas, S.K. Dutcher, and P.V. Bayly, *Biophys J* **116**, 1292-1304 (2019).
- [2] M. Kim, E. Huff, M. Bottier, S.K. Dutcher, P.V. Bayly and J.M. Meacham, *Soft Matter* **15**, 4266-4275 (2019).

Acoustic separation of viable and dead cells using high-density medium

Karl Olofsson¹, Björn Hammarström¹ and Martin Wiklund¹

¹Department of Applied Physics, KTH Royal Institute of Technology, Stockholm, Sweden
 E-mail: karlolo@kth.se URL: <https://www.kth.se/profile/karlolo>

Introduction

Acoustic binary separation of mixed cell population suspensions takes advantage of sign differences in acoustic contrast factor to displace cell populations into either the pressure node or the anti-node. This cell size insensitive separation approach has the benefit of being less dependent on the balance between flowrate and acoustic energy density in the channel compared to regular size dependent time-of-flight separation [1]. Here we highlight some of the results from a recently published article where we used a high-density medium (Iodixanol) to spatially separate viable and dead cells in a binary fashion [2]. The binary separation was possible due to the novel finding that the mechanical properties of a dead cell, with a compromised cell membrane, are a function of the surrounding medium.

Separation efficacy depends on Iodixanol concentration

Using a straight, 375 μm wide channel with an attached piezo, actuated with a frequency modulation scheme (4.06 ± 0.05 MHz @ 1 kHz rate), we studied the necessary density modifying Iodixanol concentration for displacing viable K562 cells to the anti-node while retaining fixed K562 cells in the pressure node. Fixed K562 cells were used as a model for dead cells since they exhibit a permeabilized cell membrane. By characterizing the final trapping position of viable and fixed cells in micrographs divided into zones along the channel length (node, intermediate and anti-node) (Figure 1A) over an Iodixanol concentration range (0-30%), we found that 30% v/v Iodixanol was needed to change the acoustic contrast factor sign from positive to negative for all viable K562 cells (Figure 1B). At this Iodixanol concentration level, the fixed cells were retained in the pressure node (Figure 1C). Viable, fixed and dead cells were distinguished through fluorescent labeling.

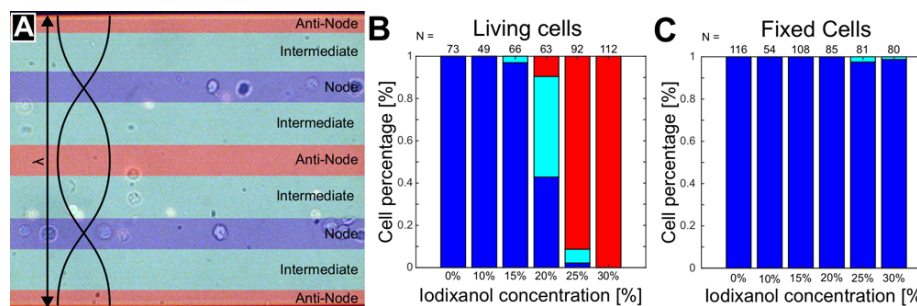


Figure 1: Separation efficacy was quantified from micrographs with zones along the channel length; pressure node (blue), intermediate (cyan) and pressure anti-node (red) (A). Cells were manually classified as living or dead depending on fluorescence and placed in either of the three zones. The graphs show the percentage of living (B) and fixed (C) K562 cells found in each zone. Figure adapted from ref [2].

Separation of viable and dead cells

While the change in acoustic contrast factor sign from positive to negative for viable cells in high-density medium is not surprising, the key finding herein is that fixed cells exhibits a positive contrast factor in high-density medium. To verify that this effect was not exclusive to the K562 cell line or dependent on the PFA fixation, we induced two natural death conditions (osmotic shock and starvation) on the K562, MCF7 and A498 cell lines. Spatial separation between a mixed population of viable and naturally dead cells were investigated in a 30% v/v Iodixanol concentration. It was found that osmotic shock and starvation treated cells also exhibited the same effect with a retained positive acoustic contrast factor in high-density medium. Cells from both death conditions were trapped in the pressure node in all cell lines while the viable counterpart was found in the pressure node (Figure 2).

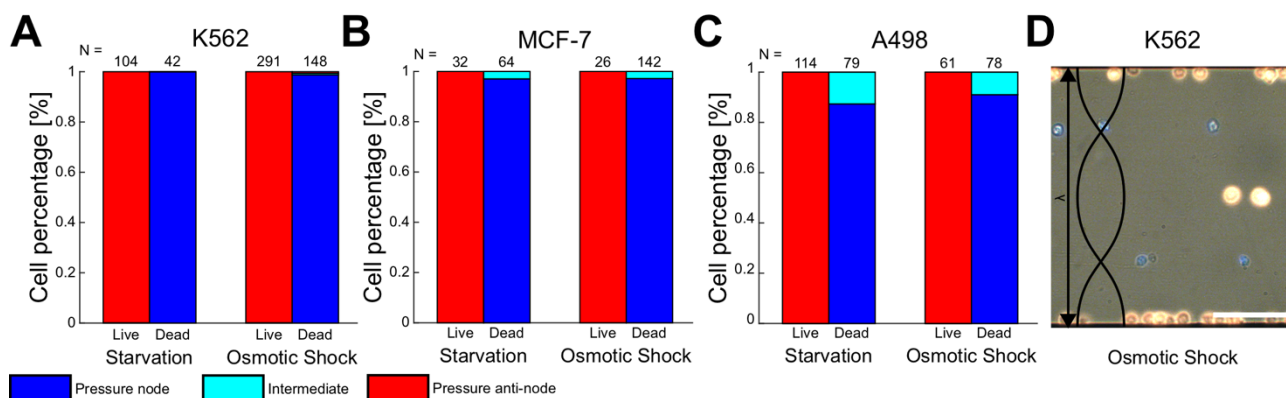


Figure 2: Mixed suspensions of viable and dead K562 (A), MCF-7 (B) and A498 (C) containing 30 v/v Iodixanol were studied under the influence of acoustic radiation force. The final trapping location of cells was counted in the node (blue), intermediate (cyan) and the anti-node (red) zone. Bar plots show the relative cell count for viable and dead cells in respective zone. A representative image of trapped viable (orange) and osmotic shock treated (blue) K562 cells during acoustic manipulation is shown in (D). Scale bar is 100 μm . Figure adapted from ref [2].

Dynamic mechanical properties of dead cells

The positive acoustic contrast factor of dead cells over the Iodixanol concentration range in covered in this study can be attributed to the compromised cell membrane. The compromised cell membrane allows the surrounding liquid to enter the cell and alter the mechanical properties. As an example, in the high-density medium case, the medium will enter the dead cell and lower the compressibility and increase the density and in combination with the remaining cell organelles provides enough contrast to scatter the ultrasonic wave (Figure 3). This explanation is in line with other studies where fixed and dead cells has been mechanically characterized or used in acoustophoresis [3,4].

The robust and simple binary sorting of viable and dead cells shown here is a promising technique in cell applications where high viability purity is needed in small cell populations such as single cell sequencing.

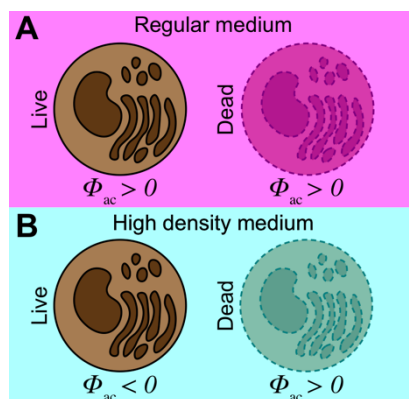


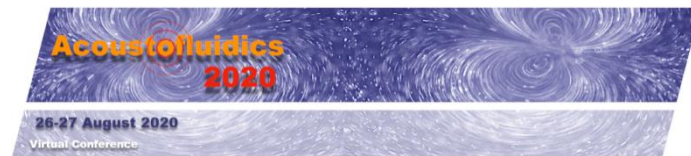
Figure 3: The acoustic contrast factor of a cell depends on the acousto-mechanical difference between surrounding fluid and the. In media regularly used in acoustofluidic applications, both viable and dead cells have a positive contrast factor (A). When the medium density is increased, the acoustic contrast factor of viable cells changes sign, while the surrounding fluid is internalized in the dead cell through the compromised cell membrane, altering the acousto-mechanical properties (B).

Conclusion

We have presented a binary sorting approach to viable and dead cells using a high-density medium where we take advantage of the compromised cell membrane of dead cells. A key finding herein is that the mechanical properties of dead cells is a function of the mechanical properties of the suspension liquid.

References

- [1] A. Lenshof, C. Magnusson and T. Laurell. *Lab Chip* **12**, 1210-1223 (2012).
- [2] K.Olofsson, B. Hammarström, and M. Wiklund. *Lab Chip* **20**, 1981-1990 (2020).
- [3] K.W. Cushing, F. Garafalo, C. Magnusson, L. Ekblad, H. Bruus and T. Laurell. *Anal Chem* **89**, 8917-8923 (2017).
- [4] M.C. Zalis, J.F. Reyes, P. Augustsson, S. Holmquist, L. Roybon, T. Laurell and T. Diederborg. *Integr Bio* **8**, 332-340 (2016).



Motility-based sperm selection using surface acoustic waves

Junyang Gai¹, Reza Nosrati¹, and Adrian Neild¹

¹ Department of Mechanical and Aerospace Engineering, Monash University, Clayton, Victoria 3800, Australia

E-mail: Adrian.Neild@monash.edu, URL: <https://www.labformicrosystems.com/>

E-mail: Reza.Nosrati@monash.edu, URL: <https://www.labformicrosystems.com/>

Introduction

Assisted reproductive technologies (ART), such as intrauterine insemination (IUI), in vitro fertilization (IVF) and intracytoplasmic sperm injection (ICSI), is an essential technology for dealing with infertility issues. However, the current success rate of ART only peaks at 33% per cycle due to multiple reasons (e.g. aneuploidy, egg ages)¹. Over the past decades, scientists and clinicians are motivated to improve several clinical techniques to improve this situation, one important procedure which is responsible for both the success rate of conception and pregnancy outcome is high quality sperm selection². However, current clinical sperm selection technique still suffers from complex, experience-based manual procedures³.

Here, working towards the goal of building a tunable and automated platform for high quality sperm selection, we presented an active sorting method for motility-based sperm selection with the potential to sort based on morphology with surface acoustic wave microfluidics. As a means of manipulating micro-sized object in microfluidic system, surface acoustic wave has shown great capabilities in sorting, patterning and alignment of immotile regular-shape cells and objects. However, scant attention has been paid for manipulating motile organism with complex morphological structures like sperms using surface acoustic wave.

In this study, with the virtual deterministic lateral displacement system (vDLD), motility-based sperm separation is achieved by creating a virtual pathway that motile sperm can swim along in the microfluidic channel while the immotile sperm and debris is remained in the mainstream without any influence.

System Description

Figure. 1(a)-(b) show a schematic of the system. Here, raw semen is introduced from one of the outlets with 0.1 $\mu\text{L}/\text{min}$ while the sheath flow is injected from another inlet with 1 $\mu\text{L}/\text{min}$. By adjusting the flow rate of the buffer 9 times more than the sample flow rate, the sample can be confined within 1/3 region of the channel which allows live motile sperm to swim into the sheath flow and recovered at a separate outlet. Since both acoustic radiation force and flow drag force is correlated with cell size, size-based separation can potentially be achieved when acoustic radiation force is balanced by flow drag force gradient. The magnitude of flow drag force is characterized so it's not large enough to compensate for acoustic radiation force, immotile sperm which follows the mainstream is collected at one outlet while motile sperm can be guided to the pressure nodes, swim across the laminar flow streamlines and exit the channel at a different outlet.

Results

Figure.1 (c)-(f) show a 60% increase from $31.57 \pm 7.01 \mu\text{m}/\text{s}$ to $51.04 \pm 10.78 \mu\text{m}/\text{s}$ of selected sperm in terms of curvilinear velocity (VCL) compared with raw sample ($p \leq 0.0001$ with t test with Welch's correction). In addition, an improvement from $21.7 \pm 10.5 \mu\text{m}/\text{s}$ to $33.78 \pm 4.85 \mu\text{m}/\text{s}$ in straight line velocity (VSL) ($p \leq 0.05$) was also achieved, which indicates the selected sperm have both higher velocity and more effective velocity, while less motile or immotile sperms were left in the discarded cell population. And this improvement in velocity can either be attributed to higher beating frequency of the flagellar wave (BCF) or larger value of wave amplitude (ALH).

Sperm morphology, especially head morphology, has clear relations with DNA integrity as morphological variations is the result of non-orthodox DNA configurations⁴. Although using a size-based selection system, we didn't manage to find significant size differences for the cell groups we collected from both outlets compared with raw semen sample (figure.2 (a)-(b)), which means (1) the size difference among the same type of cells is not obvious enough to be detected by this acoustofluidics separation system, (2) when it comes to motile cells, the motility plays an more important role during the separation process. To further prove the quality of the selected sperm, DNA Integrity is evaluated for the sperm collected from both outlets (figure.2 (c)). a 38% improvement is witnessed between raw sample and selected sample, meaning the vDLD system is capable of selecting sperm with better DNA Integrity.

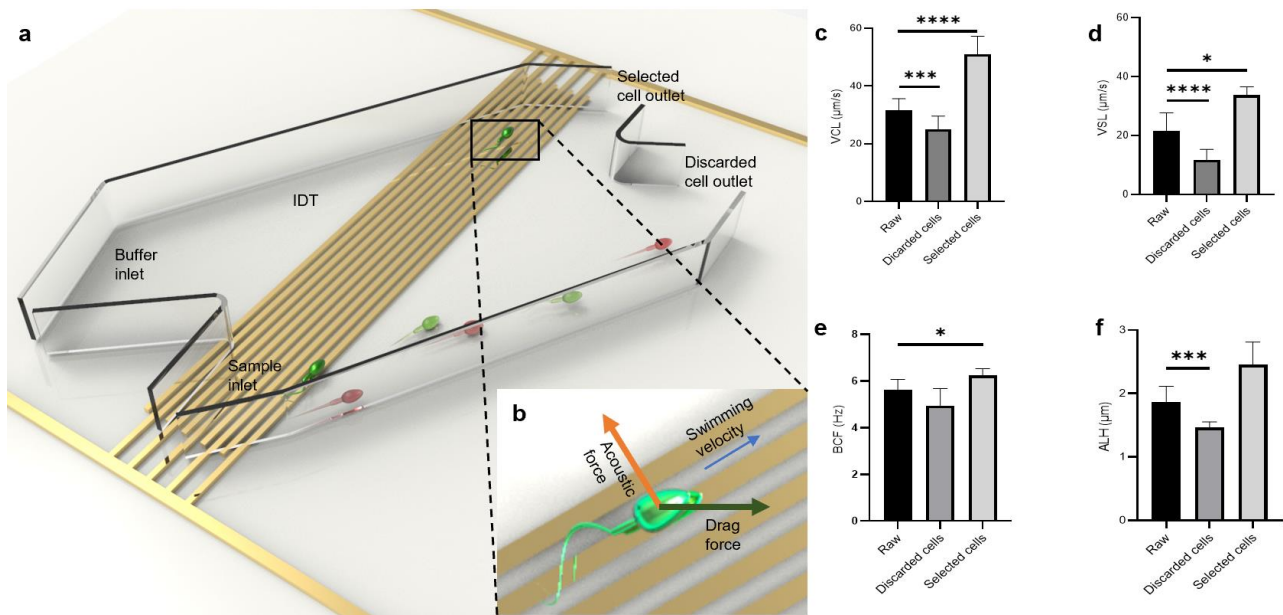


Figure 2: Device working principle and selection quality (a) Device schematic. (b) Sperm free body diagram. (c) Sperm curvilinear velocity. (d) Sperm straight line velocity. (e) Sperm beat cross frequency. (f) Sperm lateral head displacement.

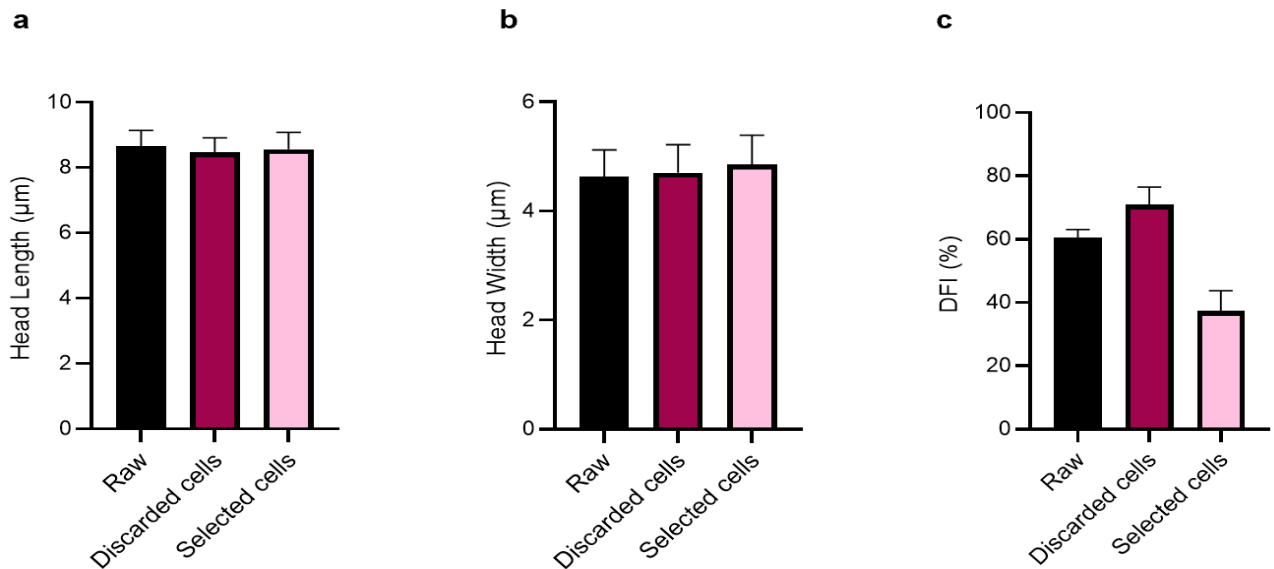


Figure 2: Sperm quality-morphology and DNA Integrity. (a) Head length, (b) Head width, (c) DNA Fragmentation Index

Conclusion

A system has been demonstrated that motility-based sperm selection can be achieved using surface acoustic waves utilizing the phenomenon that sperm motion can be guided by SSAW. In terms of size-based separation, although using a platform which is designed for size-based sorting, we find out motility plays a major role during the separation procedure when cell size difference is not significant ($<1\mu\text{m}$).

References

- [1] R. M. Schultz, *Science (80-.)*, 2002, **296**, 2188–2190.
- [2] G. Ricci, S. Perticarari, R. Boscolo, M. Montico, S. Guaschino and G. Presani, *Fertil. Steril.*, 2009, **91**, 632–638.
- [3] N. E. Skakkebaek, E. Rajpert-De Meyts, G. M. Buck Louis, J. Toppari, A.-M. Andersson, M. L. Eisenberg, T. K. Jensen, N. Jorgensen, S. H. Swan, K. J. Sapra, S. Ziebe, L. Priskorn and A. Juul, *Physiol. Rev.*, 2015, **96**, 55–97.
- [4] R. Nosrati, P. J. Graham, B. Zhang, J. Riordon, A. Lagunov, T. G. Hannam, C. Escobedo, K. Jarvi and D. Sinton, *Nat. Rev. Urol.*, 2017, **14**, 707–730.

Advanced cell manipulation with vortex-based acoustical tweezers

M. Baudoin^{1,2}, J-L Thomas³, R. Al Sahely¹, J.-C. Gerbedoen¹, Z. Gong¹, A. Sivery¹, O. Bou Matar¹, N. Smagin¹ and A. Vlandas¹

¹ Univ. Lille, CNRS, Centrale Lille, Yncréa ISEN, Univ. Polytechnique Hauts-de-France, UMR 8520 - IEMN, SATT Nord, F-59000 Lille, France

E-mail: michael.baudoin@univ-lille.fr, URL: <http://films-lab.univ-lille1.fr/michael/michael/Home.html>

² Institut Universitaire de France, 1 rue Descartes, 75005 Paris, France

³ Sorbonne Université, CNRS, Institut des NanoSciences de Paris, INSP, F-75005 Paris, France

Context

The ability to pick up and manipulate micro-objects selectively with single-beam optical tweezers [1] have led to tremendous developments in physics and microbiology, highlighted by the nobel prizes of S. Chu and A. Ashkin. Here selectivity refers to spatial selectivity, i.e. the ability to pick up individual objects and manipulate them among a collection. Nevertheless, optical tweezers have stringent limitations for life science owing to (i) reported phototoxicity inducing detrimental effects on biological tissues, (ii) their inability to operate in vivo in optically opaque media, and (iii) the limited range of forces, which can be applied on biosamples (typically < 20pN).

In acoustics, the ability to collect particles [2] and cells [3] at the nodes or antinodes of standing waves have been reported early on. More recently, the combination of high frequency transducers with microfluidic devices has enabled to refine this principle to capture [4], manipulate precisely [5-6] or sort micro-objects [7] depending on their acoustic properties. In standing wavefields however, the multiplicity of nodes and anti-nodes precludes any selectivity, since multiple objects will be trapped at the different nodes or antinodes with no possible differential movement between them. In addition it is necessary to position some transducer and/or reflectors on both sides of the manipulated sample and in each direction wherein manipulation is envisioned.

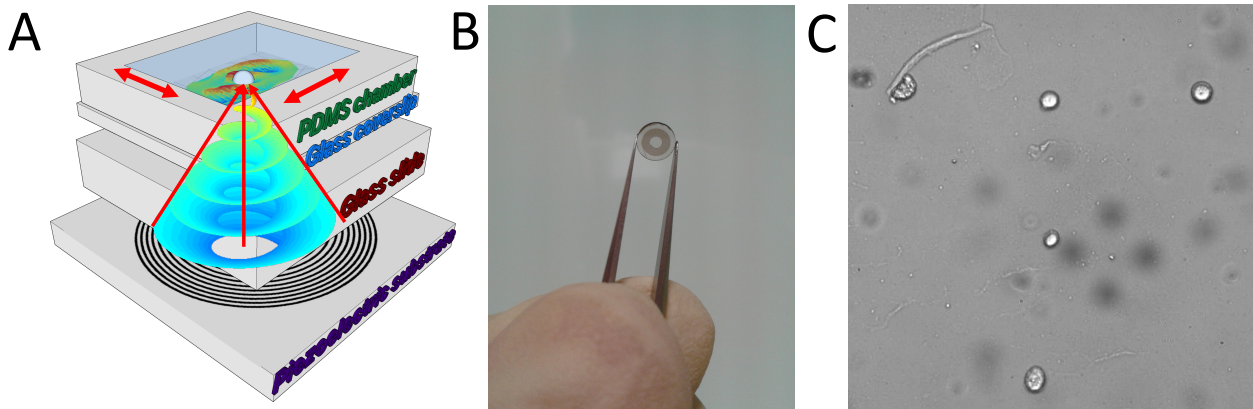


Figure 1: A. Schematic of the experimental setup: a focused acoustic vortex is synthesized with spiraling electrodes sputtered at the surface of a piezoelectric substrate and activated at 45 MHz with a function generator combined with an amplifier. The vortex focuses in a glass slide before reaching a microfluidic chamber wherein cells are manipulated. B. Picture of 45 MHz acoustic tweezers trapped by conventional tweezers (diameter of the tweezer: 3mm). C. Five free MDA-MB-231 cells positionned to form the letter T.

The design of 3D single-beam selective acoustical tweezers analogous to their optical counterpart nevertheless required to overcome many challenges: (i) Spatial selectivity requires to tightly localize the acoustic energy in a reduce portion of space where the target particle will be trapped, without perturbing other locations. In optics this goal is achieved with focused waves. But in acoustic many particles (solid particles, most cells,...) are expelled from (not attracted to) the focal point of a focused wave, which precludes their use for most applications. (ii) In the case of a single beam tweezers, the acoustic signal comes from only one side. Hence the wave has a progressive component along the axis of propagation which tends to push the particle in this direction. Hence, trapping particle in this

direction is particularly challenging.

These two paradoxes have been solved recently [8] by using specific wavefields called focused acoustical vortices. These focused helical waves [9] concentrate spatially the acoustic energy. But the existence of a phase singularity on the central axis leads to a pressure minimum at the focal point surrounded by a ring of high intensity, which enables 3D particles trapping of particles with a positive contrast factors. Nevertheless, the system used in early pioneering work on vortex-based acoustical tweezers [8] was cumbersome, opaque, and hardly scalable to higher frequencies to manipulate smaller particles such as cells.

Outline of the work

In this presentation we will show how the combination of vortex-based acoustical traps, acoustic holography and wave synthesis with interdigitated transducer can be combined [10] to achieve advanced cell selective manipulation [11]. First we will show free cells individual manipulation and positioning in a microfluidic chamber. Second, we will show how these selective tweezers enable to pick up a single cell out of cluster and bring it in contact to another cluster. Third, we will demonstrate high speed manipulation of cells with forces one order of magnitude larger (200 pN) than the highest forces reported for cells manipulation with optical tweezers (in the viability range), obtained without affecting the cells viability and with less than 2mW of acoustic power. Finally we will conclude this presentation by showing how the spatial selectivity could be further improved to reach resolutions at the cell level but also inherent 3D trapping capabilities of vortex-based tweezers.

Method

The results presented in this work have been obtained with some 45 MHz active holographic tweezers. Basically, the binarized hologram (two opposite phases) of a one-sided focused acoustical vortex is sputtered under the form of metallic electrodes at the surface of a piezoelectric medium. These electrodes are activated at ~ 45 MHz with a function generator coupled with an amplifier leading to the synthesis of an acoustical vortex (see Fig. 1.A for a representation of an isophase surface of a vortex). The vortex focuses inside a glued glass slide before reaching a mobile microfluidic chamber (made of a glass coverslip covered with a PDMS microchamber) wherein cells are manipulated. This microfluidic chamber is coupled with the glass slide with a drop of silicon oil. A suspension of cancer cells MDA-MB-231 is loaded on the glass coverslip, initially treated with Cytop to reduce cells adhesion, and manipulated by activating the tweezers and moving the glass coverslip compared to the glass slide with a X,Y motorized stage. The signal generated by the acoustical tweezers at the bottom of the microfluidic chamber is characterized with a Polytech UHF-120 laser Doppler vibrometer and compared to simulations performed with an angular spectrum code. The force of the produced acoustic trap (at a given acoustic power) is measured by moving a cell at increasing speed until the particle escapes from the trap and deducing the force from the balance with the Stokes drag. It is compared to numerical simulations of the force obtained with the angular-spectrum based expression of the force derived by Sapozhnikov and Bailey [12].

Conclusion

The unprecedented spatial selectivity and maximum forces (~ 200 pN) accessible with vortex based acoustical tweezers open some unique perspective to investigate cells adhesion or mechanotransduction, cells interaction in spatially organized co-cultures but also acoustic spectroscopy and tissue engineering. In addition both the selectivity and maximum forces could be further improved in the future by (i) improving thermal management of the device and (ii) further increasing the operating frequency.

References

- [1] Ashkin A, Dziedzic JM, Bjorkholm JE, Chu S. *Opt. Lett.* **11**:288-90 (1986)
- [2] R.W. Boyle, *Ultrasonics, Science Progress* **23**: 75-105 (1928).
- [3] Baker NV., *Nature* **239**:398-99 (1972)
- [4] Collins DJ, Morahan B, Garcia-Bustos J, Doerig C, Pleansku M, Neild A., *Nat. Commun.* **6**:8686 (2015)
- [5] Tran SBQ, Marmottant P, Thibault P., *Appl. Phys. Lett.* **101**:114103 (2012)
- [6] Ding X, Li P, Lin S-C, Kirali B, Yue H, et al. *PNAS*, **109**:11105-9 (2012)
- [7] Lenshof A, Laurell T., *Chem. Soc. Rev.* **39**:1203-17 (2010)
- [8] Baresch D, Thomas J-L, Marchiano R. *Phys. Rev. Lett.*, **116**:024301 (2016)
- [9] Baudoin, M., Thomas, J.-L., *Annu. Rev. Fluid Mech.*, **52**: 205-234 (2020)
- [10] Baudoin M, Gerbedoen J-C, Riaud A, Bou Matar O, Smagin N, Thomas J-L., *Sci. Adv.* **5**:eaav1967 (2019)
- [11] Baudoin M, Thomas J-L, Al Sahely R., Gerbedoen J.-C. , Gong Z., Sivery A. , Bou Matar O. , Smagin N. and Vlandas A. , under revision *Nat. Commun.* (2020)
- [12] Sapozhnikov OA, Bailey MR., *J. Acoust. Soc. Am.* **133**:661-76 (2013)

A Microfluidic Platform for Acoustic Particle Focusing in Hydrogel Droplets

Maria Tenje, Hannah Pohlit, and Anna Fornell

Department of Materials Science and Engineering, Science for Life Laboratory, Uppsala University, 75121 Uppsala, Sweden
 E-mail: maria.tenje@angstrom.uu.se, URL: <http://www.materialvetenskap.uu.se/embla>

Introduction

Droplet microfluidics has emerged as a useful technology for miniaturisation of biological experiments [1]. Recently, encapsulation of cells in hydrogel droplets has gained increased attention [2]. Hydrogels are a class of materials that consist of cross-linked polymer chains that do contain large amounts of water. Compared with water-in-oil droplets, hydrogel droplets provide a 3D scaffold for the encapsulated cells to grow in and thereby better mimic the natural environment of the cells (the extracellular matrix). We have previously shown acoustic focusing of beads and cells in water-in-oil droplets [3], and here we show for the first time acoustic focusing of beads and cells in hydrogel droplets. This opens up for the generation of more complex hydrogel structures where the position of the encapsulated particles needs to be controlled.

Experimental

In Figure 1 an illustration of the concept is shown. The microfluidic channels were etched in silicon by deep reactive ion etching, and the chip was sealed with a glass lid. The dimensions of the main channel were $380\ \mu\text{m} \times 100\ \mu\text{m}$ (width \times height). A half wavelength acoustic standing wave field was generated in the main channel by actuating a piezoelectric transducer (1 mm thickness, APC-840) that was glued on the silicon side of the chip. In the bead focusing experiments the dispersed phase consisted of 3% 4arm-PEG10K-Acrylate, 0.1% photoinitiator (lithium phenyl-2,4,6-trimethylbenzoylphosphinate), 10 μm diameter green fluorescent polystyrene beads and 0.5 μm diameter red fluorescent beads. The 0.5 μm beads were added for visualisation of the droplets. In the cell focusing experiments instead of beads, astrocyte cells were suspended at a concentration of 2×10^7 cells/mL and 1% GelMA (gelatin methacrylate) was added to provide cell adhesion sites for the cells. The continuous phase consisted of heavy mineral oil with 1% Span80 surfactant. The fluid flows were controlled by syringe pumps, and if not stated otherwise the flow rate of the dispersed phase was $1.0\ \mu\text{L}/\text{min}$ and the flow rate of the continuous phase was $1.5\ \mu\text{L}/\text{min}$. The hydrogel droplets were cross-linked on the chip with a handheld UV-lamp (365 nm wavelength). After cross-linking, the droplets were collected and washed to remove the oil, and then the droplets were studied in a microscope.

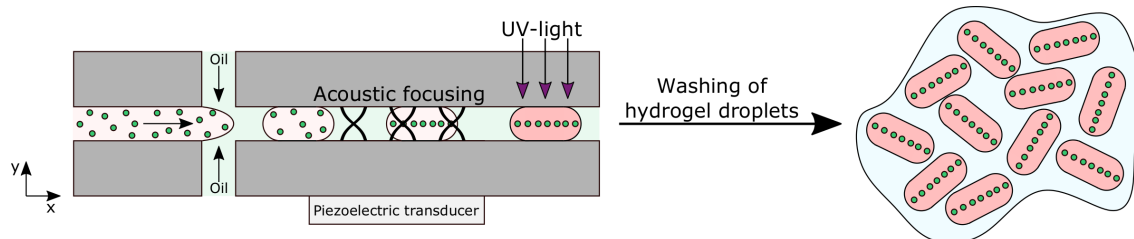


Figure 1: Droplets composed of hydrogel precursor solution (PEG (polyethylene glycol) or a combination of PEG and GelMA), photoinitiator and particles (beads or cells) are generated. The droplets pass along the acoustic focusing channel where the particles are focused along the centre-line of the droplets (i.e. the pressure nodal line). Next, the hydrogel precursor droplets are cross-linked using UV-light which freezes the encapsulated particles at their positions. The droplets are collected and washed to transfer them from the oil to an aqueous solution.

Results and discussion

In the first set of experiments droplets with beads were generated. Without the acoustics applied, the 10 μm beads were randomly positioned in the droplets, but with the acoustics applied the beads were focused along the centre-line of the droplets. Images of the droplets after cross-linking and washing are shown in Figure 2. Without the acoustics applied $24 \pm 12\%$ (s.d.) of the 10 μm beads were positioned in an area $\pm 10\%$ from the centre-line of the droplets compared with $89 \pm 19\%$ (s.d.) with the acoustics applied.

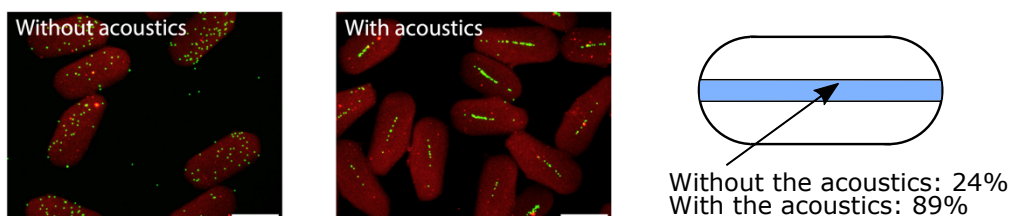


Figure 2: Left: Photos of cross-linked hydrogel droplets containing beads. Without the acoustic applied the 10 μm beads are randomly distributed in the droplets. With the acoustics applied (1.88 MHz, 30 $V_{\text{peak-peak}}$) the 10 μm beads are focused along the centre-line of the droplets. Right: The distribution of 10 μm beads without and with the acoustics applied.

The length of the droplets could be varied by changing the flow ratio between the dispersed and continuous phases, Figure 3. As seen in the figure it was possible to focus beads in both long and short droplets.

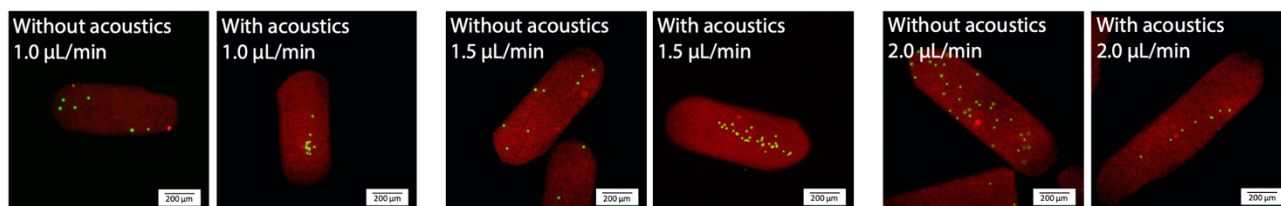


Figure 3: Photos of cross-linked hydrogel droplets of different lengths without and with the acoustics applied (1.89 MHz, 18 $V_{\text{peak-peak}}$). The flow rate of the continuous phase was kept constant at 1.5 $\mu\text{L}/\text{min}$ and the flow rate of the dispersed phase is indicated in the photos.

In the next experiment focusing of astrocyte cells was investigated. Droplets containing cells were generated and the acoustics was applied. Thereafter the droplets were cross-linked and washed. The droplets were incubated in cell media at 37 $^{\circ}\text{C}$ overnight and a live-dead staining was performed. As seen in Figure 4, the acoustics caused the cells to be focused, and it can also be seen that many of the cells were still alive after 24 hours.

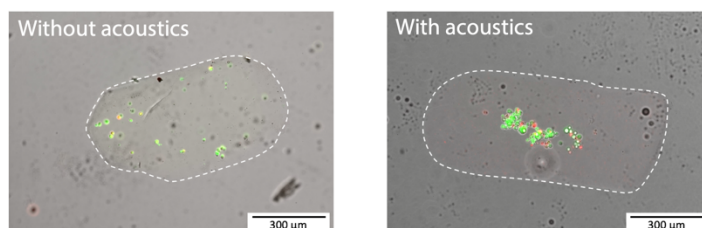


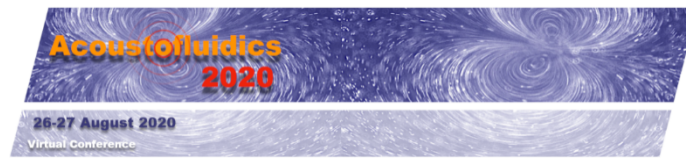
Figure 4: Photos of cross-linked hydrogel droplets containing astrocyte cells. Without the acoustics applied the cells are randomly distributed. With the acoustics applied (1.87 MHz, 30 $V_{\text{peak-peak}}$) the cells are focused along the centre-line of the droplet. The photos are taken after 24 hours of incubation. Living cells appear green (calcein stain) and dead cells appear red (propidium iodide stain). The dashed lines indicate the border of the droplets.

Conclusion

In this work we have fabricated a microfluidic platform to control the position of encapsulated particles in hydrogel droplets. With the acoustics applied 89 \pm 19% of 10 μm polystyrene beads were positioned in an area \pm 10% from the centre-line of the droplets compared with 24 \pm 12% without the acoustics applied. We also show that the method can be used for focusing astrocyte cells encapsulated in hydrogel droplets. We believe this technology will open up for new applications of hydrogel droplets where the position of particles needs to be precisely controlled.

References

- [1] M. Tenje, A. Fornell, M. Ohlin, J. Nilsson. *Analytical Chemistry* **90**, 1434-1443 (2018).
- [2] H. Huang, Y. Yu, Y. Hu, X. He, O. Berk Usta, M. Yarmush. *Lab on a Chip* **17**, 1913-1932 (2017).
- [3] A. Fornell, J. Nilsson, L. Jonsson, P.K. Periyannan Rajeswari, H. Joensson, M. Tenje. *Analytical Chemistry* **87**, 10521-10526 (2015).



Generating ordered cardiac tissue models using acoustic cell patterning

Ekaterina Pchelintseva¹, Ilona Sunyovzsky², James P. K. Armstrong¹, Alice Agliano¹, Bruce W. Drinkwater³, Cesare Terracciano², Molly M. Stevens^{1,4}.

¹Department of Materials, Faculty of Engineering, Imperial College London

E-mail: ekaterina.pchelintseva13@imperial.ac.uk

²National Heart and Lung Institute, Faculty of Medicine, Imperial College London

³Department of Mechanical Engineering, University of Bristol

⁴Department of Bioengineering, Faculty of Engineering, Imperial College London

Introduction

This experimental work aims to develop an acoustically-patterned cardiac cell culture model as a novel drug screening platform. Our platform will improve the gold standard monolayer cultures, currently used for assessment of cardiotoxicity in drug discovery industry. Herein, we demonstrate a solution-based approach to patterning cardiomyocytes on a multielectrode array (MEA). We describe the fabrication of the device and optimization of patterning parameters, as well as the proof-of-principle for acoustic patterning of live human induced pluripotent stem cell (hiPSCs) derived cardiomyocyte (iPSC-CMs).

Solution-based acoustic patterning

Microscopic cellular organisation is key to the successful engineering of functional bioinspired tissues. In cardiac muscle, alignment of cardiomyocytes plays a major role in the synchronization of conduction and contraction. However, the gold standard for drug screening, monolayers of hiPSC-CMs, are limited by a lack of native tissue organization. Therefore, it is paramount to preserve the naturally-occurring anisotropy of the cardiac muscle when developing functional cell and tissue models.

Acoustic cell manipulation therefore offers a non-invasive, label-free and cytocompatible solution to cell alignment, which can quickly and reproducibly generate uniformly patterned tissue constructs for cardiac drug screening [1,2,3,4]. Importantly, an electrical output must be observed in order to determine the effect of the candidate compounds on the cells. Multielectrode arrays (MEAs) therefore can be used as substrates for acoustic patterning, providing the information on conduction velocity and field potential duration of the platform.

We designed and fabricated a first generation of MEA-housing acoustic patterning devices, which were inspired by previously published work [1,3]. The central cavity in our devices was 50 x 50 mm to fit the MEA (Figure 1A). However, the large dimensions of the cavity compromised the quality of the patterning (Figure 1B, C). These findings were confirmed by computational modelling (Figure 1D, E). Therefore, the second-generation device included a 3D-printed base to separate the MEA from the acoustic components (Figure 1F). The 3D-printed base contains a groove for precise and consistent positioning of the MEA within the device. The MEA is then covered with a custom-cut silicone gasket, on top of which the acoustic patterning component is positioned. All the components are clamped together to ensure a tight seal. Such modular design allowed to minimise the dimensions of the central cavity, leading to an improvement of the patterning quality at the recording field of the MEA, consistent with the modelling predictions (Figure 1D, E, F, G).

When we patterned fixed MDA-MB-231 on an MEA, the cellular array was misaligned relative to the electrodes (Figure 1G). Therefore, we reduced the patterning frequency to yield 400 μm separation, resulting in alignment with every other electrode array (Figure 1H).

When patterning live cells, the cell-cell and cell-surface interactions can lower the quality of the patterning. However, during the patterning of live iPSCs on Matrigel-functionalised MEA, the pattern was visible after 1 minute, with the cells fully patterned at 5 minutes (Not shown). Furthermore, when hiPSC-CMs were patterned on the MEA, the pattern was maintained over 24 hours (Figure 1I).

Conclusion

In summary, we have developed a device for solution-based cell patterning for cardiac tissue engineering with functional output. Ongoing work involves analysis of the electrical activity of patterned and unpatterned hiPSC-CM cultures using MEAs. Drug screening assays, using common drugs such as isoproterenol and metoprolol, will be set up to test the performance of our platforms. Finally, upon completion of the proof-of-concept studies, we aim to implement disease-specific hiPSCs into our cardiac tissue constructs.

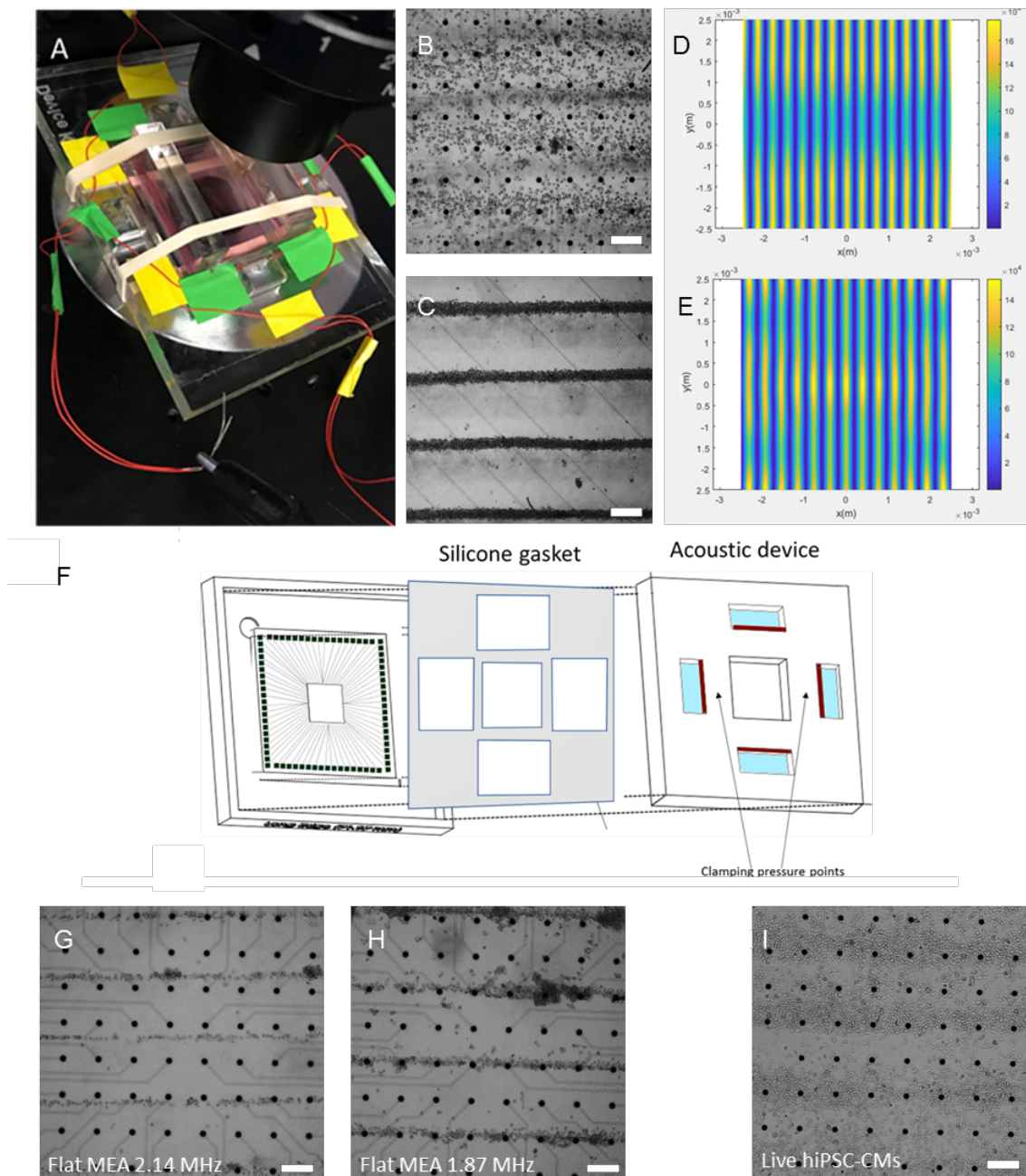


Figure 1: Design and characterization of solution-based acoustic patterning device. (A) Acrylic posts strapped to a first-generation patterning device immobilises MEA inside the central cavity. (B) Distorted linear cell pattern in the centre of the MEA. (C) Higher quality uniform linear cell pattern off-centre of the MEA. (D, E) Huygens models of the dependence of relative acoustic pressure field on the central cavity dimensions (yellow high pressure, blue low pressure). Dimensions of central cavity are 50 x 50 mm in panel D and 30 x 30 mm in panel E. (F) Second generation of modular acoustic patterning devices. (G) High quality uniform linear cell pattern in the center of the MEA in the modular device. (H) Acoustically patterned MDA-MB-231 on flat MEA at 2.14 MHz. (I) Acoustically patterned MDA-MB-231 on flat MEA at 1.87 MHz. 50% of the electrode arrays are aligned with the patterned cells. (J) Acoustically patterned live hiPSC-CMs after on flat MEA at 1.87 MHz after 24 h of culture. Scale bars = 200 μ m.

References

- [1] Armstrong, J.P.K., et al. (2018) *Advanced Materials*. 30(43):1802649
- [2] Armstrong, J. P. K., et al. (2019) *Lab Chip*. 19, 562:573
- [3] Tian, L., et al. (2016) *Nat. Comm.* 7:13068
- [4] Serpooshan, V., et al. (2017) *Biomaterials*.2017. 131:47-57.

A portable acoustofluidic based chemiluminescence biosensor

Xian Chen¹, Bohua Liu¹, Wei Pang¹ and Xuexin Duan¹

¹State Key Laboratory of Precision Measuring Technology & Instruments, College of Precision Instrument and Optoelectronics Engineering, Tianjin University, Tianjin 300072, China
E-mail: xduan@tju.edu.cn, chenxian@tju.edu.cn

Introduction

Quantitation of protein biomarker featured with portability, rapidity, and high sensitivity meets the requirement of point of care technology. There are various immunosensors for the detection of PSA, such as the electrochemical immunosensors [1], the fluorescence immunosensors [2], the photothermal immunosensors [3], and so on. The above sensors exhibit remarkable detection performance in the clinically relevant range for PSA (4-10 ng/mL). Nevertheless, the electrochemical immunosensors generally experience the time-consuming interface modification process, and rely on the extra electrochemical workstation to accomplish targets detection. The fluorescence immunosensors usually utilize the sophisticated optical system for the fluorescence excitation and optical signal amplification. The photothermal immunosensors may influence the bioactivity of PSA while the temperature is up to 70 °C. These factors are not allowed to be neglected in the practical POCT applications. Herein, we introduce a portable smartphone-enabled microfluidic platform for chemiluminescence (CL) biomarker detection based on acoustic tweezers approach, which can trap microparticles and enhance the biomolecular binding so that the dynamic biomarker quantification could be completed within 10 minutes. This work provides new insights into the design and application of integrated biosensors for point-of care testing in the complicated samples.

Method

Figure 1 shows the schematic of the acoustically enhanced smartphone detection system. The primary antibodies modified polystyrene microparticles (PS-Ab1), prostate specific antigen (PSA), and secondary antibodies (anti-PSA-HRP) are injected into the microfluidic channels simultaneously. Under the actuation of acoustic resonator, they were dynamically trapped, concentrated, and enhanced binding by the acoustic streaming. When further injected with the chemiluminescent substrate, the concentrated particles would induce the local concentration improvement of PSA, so that the intensity of emitted blue light (origin from the CL reaction) could be captured by the smartphone without extra accessories.

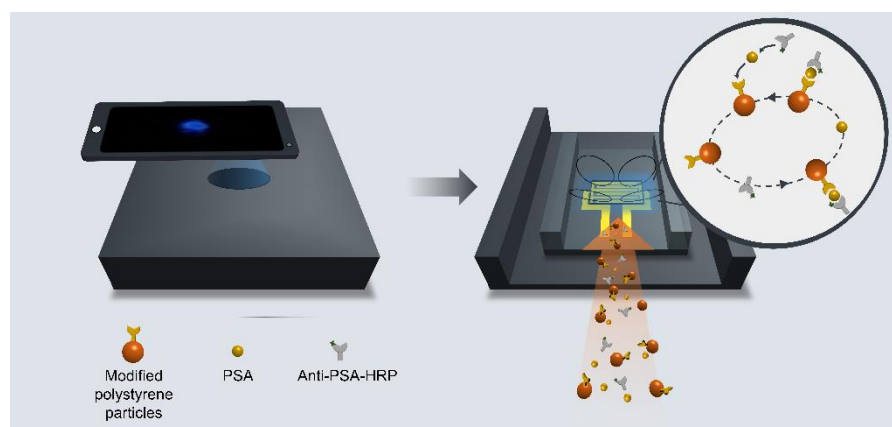


Figure 1: Schematic of smartphone-enabled detection system.

Results

Figure 2 shows the optimizations of the experimental conditions and the relationship between the concentration of PSA and the intensity of blue light. When applying the appropriate power, the acoustic streaming will trap and concentrate the particles and accelerate the antigen-antibody reaction. We compared different input power (Figure 2(a)) and the flow rate (Figure 2(b)). It turns out that the emitted intensity is optimized by applying 10 mW with the flow rate of 1 μ L/min. Figure 2(c) demonstrates the results of PSA detection with a detection limit of 0.1 ng/mL, revealing a linear relationship from 0.5 ng/mL to 10 ng/mL (Figure 2(d)).

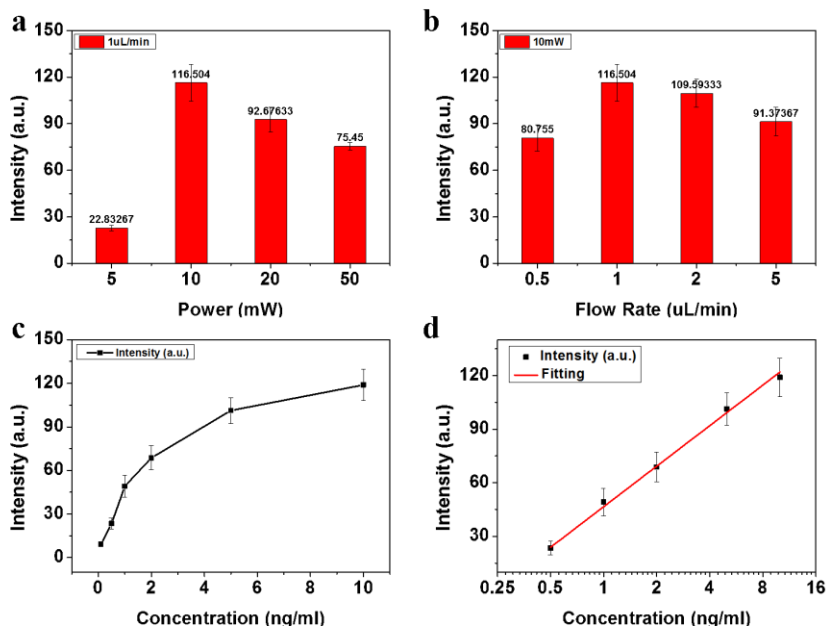


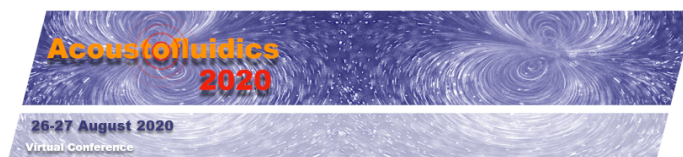
Figure 2: Chemiluminescence intensity with different input power (a) and flow rate (b). Response curve of PSA detection in buffer (c) and linear relationship (d).

Conclusion

This work demonstrates a portable smartphone-enabled immunosensor based on the acoustofluidic approach. Acoustic streaming achieved the particle trapping and enhances the antigen-antibody reaction, and further increase the local concentration of PSA. The detection limit of PSA is as low as 0.1 ng/mL, and it exhibits a linear response in the range from 0.5 ng/mL to 10 ng/mL, covering the diagnostic gray zone of PSA. The novel platform does not require bulky and expensive optical instruments, which is suitable for point-of-care applications.

References

- [1] "A novel electrochemical immunosensor for highly sensitive detection of prostate-specific antigen using 3D open-structured PtCu nanoframes for signal amplification," Chen, Y., Yuan, P. X., Wang, A. J., Luo, X., Xue, Y., Zhang, L., & Feng, J. J., *Biosensors and Bioelectronics*, 126, 187 (2019).
- [2] "Quantitative Lateral Flow Strip Sensor Using Highly Doped Upconversion Nanoparticles," He, H., Liu, B., Wen, S., Liao, J., Lin, G., Zhou, J., & Jin, D., *Analytical chemistry*, 90, 12356 (2018).
- [3] "Ti3C2 MXene quantum dot-encapsulated liposomes for photothermal immunoassays using a portable near-infrared imaging camera on a smartphone," Cai, G., Yu, Z., Tong, P., & Tang, D, *Nanoscale*, 11, 15659 (2019).



Highly efficient acoustophoretic single cell-supernatant separation inside nanoliter droplets

Michael Gerlt¹, Dominik Haidas², Alexandre Ratschat¹, Philipp Suter¹, Petra Dittrich² and Jürg Dual¹

¹ETH Zürich, Zürich, SWITZERLAND, ²ETH Zürich, Basel, SWITZERLAND

This contribution reports a novel method for cell-supernatant separation inside nanoliter droplets with separation efficiencies for single cells of 100% at flow speeds of 2 mm/s. Cells are focused in nanoliter droplets using bulk acoustic waves before the droplet is split at a bifurcation into a supernatant- and a cell-containing droplet. The method enables upconcentration of cells, cell washing, and the separation of supernatant in droplet microfluidic applications.

Droplet microfluidics offers great opportunities for high-throughput screening. However, it is still challenging to implement routine processes like cell and particle enrichment or separation into the format of droplet microfluidics, which are required in many widely-used assays in the field of single-cell analysis or ligand-acceptor binding studies. Currently only few methods are available to separate the cell in microscale droplets before analysis relying on magnetic [1], dielectric [2], hydrodynamic [3] and acoustic [4] forces. However, the methods are often not robust and lack in throughput or separation efficiency. In this work, we present an optimized separation procedure based on acoustophoresis, in a simple chip design that separates cells from the supernatant at a much higher separation efficiency than [3, 4], faster flow speeds than [2] and without particle labeling [1].

The microfluidic devices were produced using standard cleanroom processes. Microfluidic channels with a depth of 180 μm were dry etched into a silicon wafer. Subsequently, a glass plate was anodically bonded and the wafer was diced into single chips by means of a wafer saw. Fused silica capillaries were glued into the channels from the side of the chip. A piezo electric transducer was glued on the back of the devices. Particle or cell containing droplets are generated in a T-junction inside the chip. After acoustic focusing of the particles inside the droplets, they are split at a bifurcation. The particles are held in position by the acoustic forces counteracting the strong recirculation zones inside the droplet (Fig.1). Numerical investigations show that the continuous phase influences strength and distribution of the acoustic field inside the droplet. Conditions are beneficial for acoustic separation, if the continuous phase exhibits acoustic properties close to the dispersed phase (Fig.2). Therefore, we chose Olive oil for further experiments. Next, we conducted a thorough experimental characterization of the devices (Fig.3). At split ratios of 40% and below, separation efficiencies above 95 % can be obtained for flow speeds up to 5 mm/s and high particle concentrations of 93 particles per droplet. At higher split ratios, a strong decrease of the separation efficiency was observed. We used 5 μm polystyrene particles for the characterization, since they are monodisperse and exhibit acoustic properties close to yeast cells. To verify the applicability of the process for single cell-supernatant separation, we lowered the concentration such that there was a significant amount of droplets containing only one particle and exchanged the PS particles with yeast (Fig.4. & Table 1). Out of 162 droplets, not a single particle escaped into the side channel at a flow speed of 2 mm/s and a split ratio of 40%. Even for very high flow rates of 8.2 mm/s (532 ± 15 Droplets/min), a mean separation efficiency of above 77% can be achieved.

We developed an acoustofluidic microchip, which is capable of highly efficient cell-supernatant separation in microscale droplets. In the future, the process will also be characterized for other cell types and integrated into a versatile high-throughput screening platform.

REFERENCES

1. D. Lombardi and P. S. Dittrich, "Droplet microfluidics with magnetic beads: a new tool to investigate drug-protein interactions", *Anal. Bioanal. Chem.*, 2011, **399**, 347–352.
2. S. I. Han, H. Soo Kim and A. Han, "In-droplet cell concentration using dielectrophoresis", *Biosens. Bioelectron.*, 2017, **97**, 41–45.
3. M. Hein, M. Moskopp and R. Seemann, "Flow field induced particle accumulation inside droplets in rectangular channels", *Lab Chip*, 2015, **15**, 2879–2886.
4. A. Fornell, J. Nilsson, L. Jonsson, P. K. Periyannan Rajeswari, H. N. Joensson, and M. Tenje, "Controlled Lateral Positioning of Microparticles Inside Droplets Using Acoustophoresis," *Anal. Chem.*, vol. 87, no. 20, pp. 10521–10526, 2015.

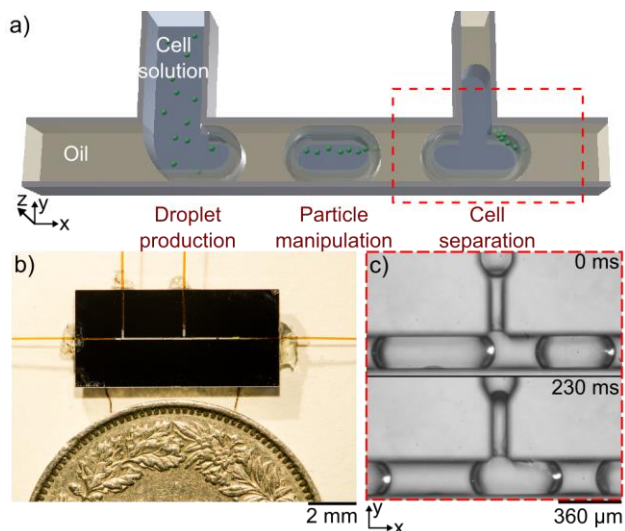


Figure 1: Working principle of the cell separation in microscale droplets. a) Sketch of the design. b) Photographs of the silicon chip. c) Micrograph series of a typical separation experiment (5 μm fluorescent Polystyrene (PS) Particles in white).

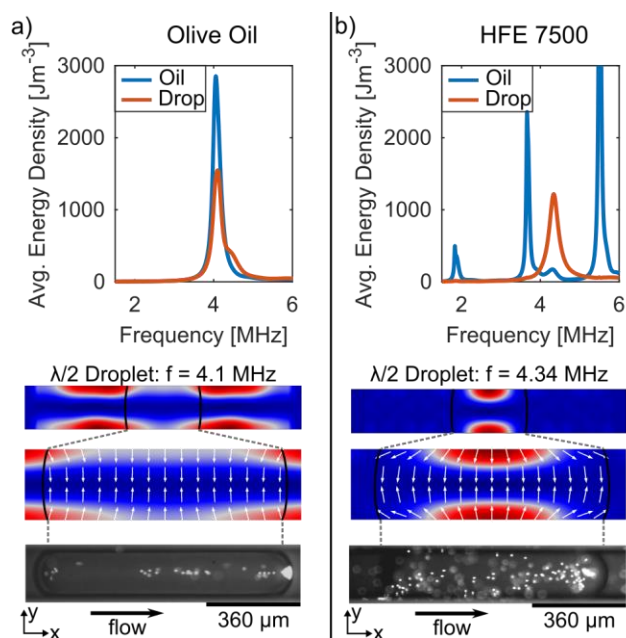


Figure 2: Influence of the continuous phase properties (olive oil left, HFE right column) on particle separation in droplets. The graphs on the top of the figure show the influence of the frequency on the average acoustic energy density in the channel and the droplet, respectively. The two pictures in the middle show the Gorkov potential at optimal frequencies for the droplet. Cells will migrate to the minimum of the potential (blue). The pictures on the bottom show an experiment with 5 μm fluorescent polystyrene particles. Olive oil produces a favorable acoustic field for focusing.

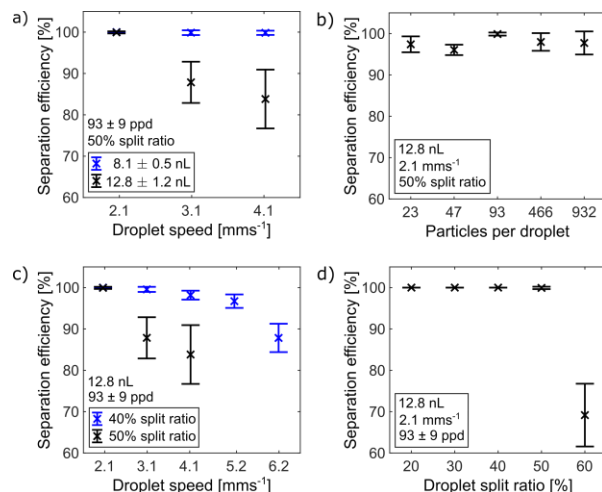


Figure 3. Influence of various experimental parameters on the separation efficiency (SE) for multiple PS particles. Increasing droplet speed and droplet volume, leads to a decrease in SE. A SE above 90% can be maintained even at high particle concentrations. A split ratio above 50% leads to a rapid decrease in SE.

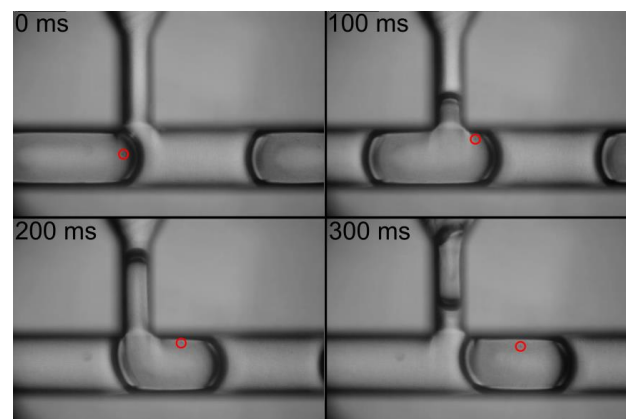


Figure 4. Micrograph series of single yeast cell separation. The yeast cell is marked with a red circle. Droplet volume 12 nL, droplet speed 2mm/s, split ratio 40%.

Speed [mm/s]	Volume [nL]	Particle	Particles [#]	P to side [#]
2.06	12.2 \pm 0.2	PS	162	0
		Yeast	36	0
4.12	12.12 \pm 0.04	PS	203	17
		Yeast	102	4
8.24	10.53 \pm 0.3	PS	171	67
		Yeast	126	29

Table1. Results of Single Particle separation in nanoliter droplets. A very low particle concentration was used leading to 0.8 ± 0.8 Particles per droplet. Only the droplets containing one particle were counted. At a speed of 2 mm/s, not a single particle escaped into the side outlet. The split ratio was at around 40%.

Charting cell properties through their acoustophoretic migration in a gradient of density and compressibility

Mahdi Rezayati Charan¹, and Per Augustsson¹

¹Department of Biomedical Engineering, Lund University, Lund, Sweden
 E-mail: per.augustsson@bme.lth.se, URL: <http://bme.lth.se/staff/augustsson-per/research/>

Introduction

Iso-acoustic focusing (IAF) can provide phenotypic information about cells that can be utilized for cell classification and acoustic separation based on their effective acoustic impedance (Z) [1], Fig. 1. This property was recently shown to be closely linked to cells' states and enabled determination of live vs dead cells [2]. We present 3D-measurements of acoustophoretic migration of neutrophils in both homogeneous and inhomogeneous media in stop-flow. We track the acoustophoretic migration of a set of neutrophils through a smooth gradient in acoustic impedance and monitor their iso-acoustic point (IAP) where the acoustic impedance of the medium equals the effective acoustic impedance of the cell. Our measurements reveal that the accuracy of the measurement depend on the radial location of the cell, the temporal development of the diffusing acoustic impedance gradient, and the amplitude of the sound field.

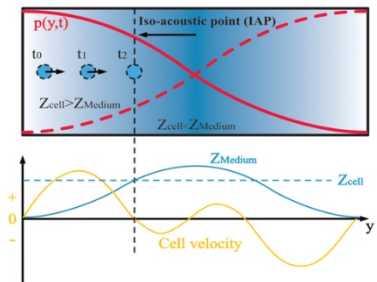


Figure 1: The principle of IAF, where cells are brought to their iso-acoustic point in an acoustic impedance (Z) gradient.

Experimental method

An acoustofluidic glass and silicon chip was glued to a piezoceramic transducer resonant at 2 MHz. The chip has a straight channel of width $W = 375 \mu\text{m}$ to support a single node standing wave. It has inlets for introducing a central stream of a high impedance medium containing iodixanol, flanked on both sides by low impedance media containing the cells. To map the development of the diffusing acoustic impedance gradient, we added fluorescent tracer molecules to the central fluid. After initially injecting cells and media at high flow velocity, we stop the flow and record images for both cells and fluids in two different fluorescence channels, Fig. 2. 3D-trajectories of neutrophils were computed by general defocusing particle tracking (GDPT) [3].

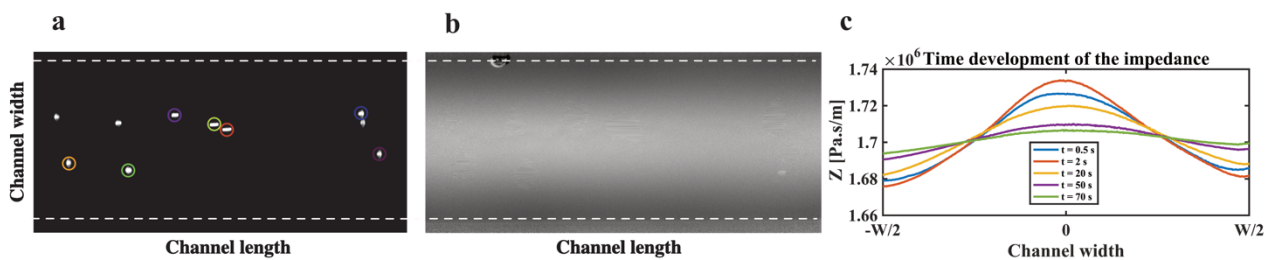


Figure 2: (a) A snapshot of 7 cells during their migration through an acoustic impedance gradient and (b) the corresponding fluorescent tracer intensity image that maps the acoustic impedance gradient. Colored circles denote the locations of the cells. (c) The temporal development of the acoustic impedance gradient.

Results and discussion

We first studied neutrophil migration in the radial cross section in homogenous media. Fig. 3 shows three different regimes of neutrophil trajectories and their corresponding velocity distributions. For low impedance medium (1.66 MPa·s/m), neutrophils have a positive contrast factor ($\Phi > 0$) meaning that they move toward pressure node while for higher impedance (1.76 MPa·s/m), neutrophils have a negative contrast ($\Phi < 0$) and they migrate towards the walls. For intermediate acoustic impedance (1.70 MPa·s/m), acoustically transparent neutrophils ($\Phi \sim 0$) do not experience radiation forces and therefore follow the acoustic streaming rolls.

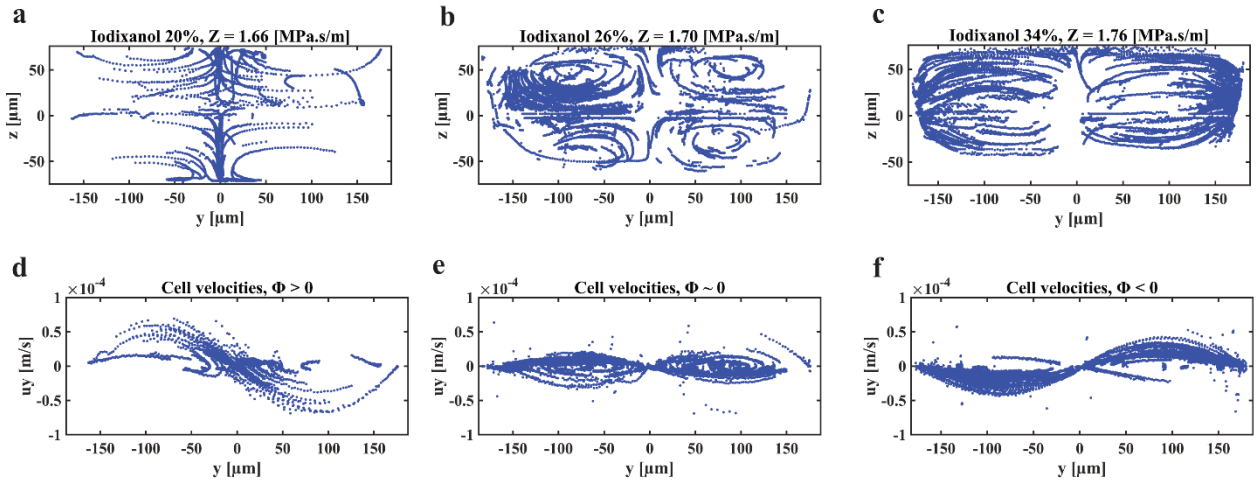


Figure 3: Neutrophil migration in homogenous media. Scatter plots of (a-c) the radial position of neutrophils over time for an acoustic impedance of (a) 1.66 MPa.s/m, (b) 1.70 MPa.s/m and (c) 1.76 MPa.s/m and (d-f) the corresponding y -component of the velocities.

We then studied acoustic migration for a set of neutrophils in an acoustic impedance gradient. Fig. 4 (a) illustrates how they first plummet due to fluid relocation after the onset of sound and they then slowly migrate toward the channel center, Fig. 4(b). Fig. 4(c) shows that the velocities of the cells are initially high as they migrate through the low impedance medium and they then slow down abruptly as they approach their IAP. Fig. 4(d) shows the measured IAP as a function of time indicating that cells reach their IAP after 15 seconds and thereafter a stable reading can be carried out during approximately 20 seconds. The measurement breaks down when the cells has reached the channel center and diffusion has then flattened the acoustic impedance gradient to a value that is below the effective acoustic impedance of the cell. The measurement will fail if the acoustic field cannot transport cells to their IAP before diffusion flattens the acoustic impedance gradient.

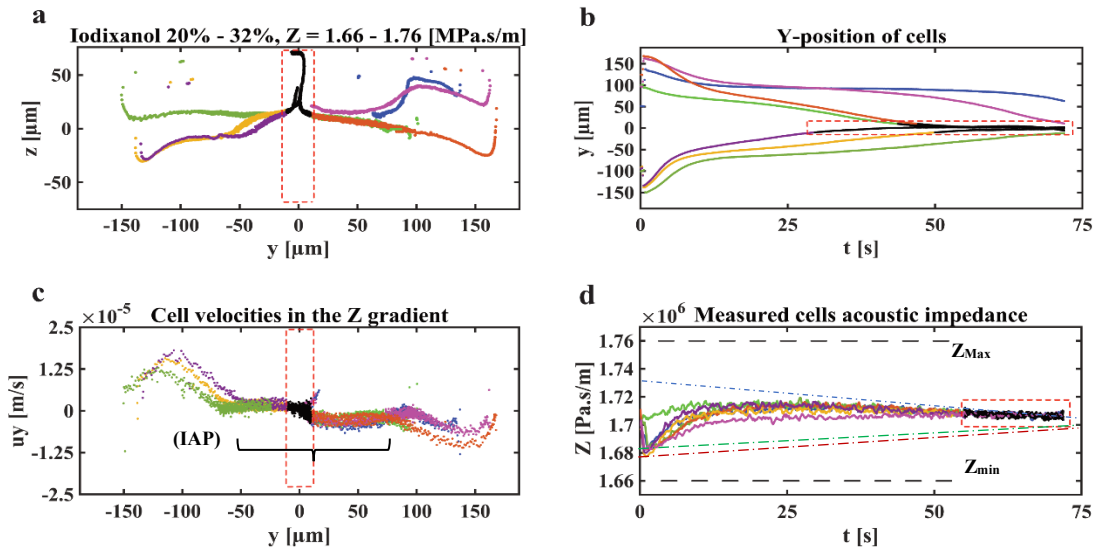


Figure 4: Migration in an acoustic impedance gradient for a set of neutrophils. Scatter plots of (a) their radial positions and (b) their lateral position (y) as a function of time. (c) The velocity along y for neutrophils over 60 seconds. (d) Time development of the measured neutrophil acoustic impedance. Dashed coloured lines represent the change in impedance of the medium at each wall (green and red) and at the centre (blue) due to diffusion. Red rectangles and black dots demark time and location for breakdown of the IAP measurement. Moving average filtering ($n=5$) was applied to (c and d).

Conclusion

By studying 3D acoustic migration of neutrophils, we can describe how they approach their IAP. At the conference we will show data for more cell types as well as data for the influence of cell buoyancy in IAF.

References:

- [1] Augustsson, P., Karlsen, J., Su, H. *et al. Nat Commun* **7**, 11556 (2016).
- [2] Olofsson, K., Hammarström, B., Wiklund, M., *Lab Chip*, **20**, 1981-1990 (2020).
- [3] Barnkob, R., Kähler, C.J., Rossi, M., *Lab Chip*, **15**, 3556-3560 (2015).

Refraction of Acoustic Vortex Beams in an Inhomogeneous Medium

Xudong Fan¹ and Likun Zhang¹

¹National Center for Physical Acoustics and Department of Physics and Astronomy, University of Mississippi, University, Mississippi 38677, USA
 E-mail: xfan1@go.olemiss.edu, zhang@olemiss.edu, URL: <https://physics.olemiss.edu/>

Introduction

Prior studies on acoustic vortex beams focus on the homogeneous media. However, in practical situations and applications, media can be inhomogeneous. Here, we study the propagation of acoustic vortex beams in an inhomogeneous medium, specifically in a linearly stratified medium. We observe a series of behaviors of the propagation relevant to the evolutions of intensity profile, phase distribution, and angular momentum transport. These evolutions of the vortex fields relate to interactions of the vortex with medium inhomogeneity.

Numerical observation

Figure 1(a) shows the simulated wave amplitude in a three dimensional computation domain where the vortex beam bends upwards towards the direction of sound speed descent (+z direction) due to the refraction. Figure 1(b) displays the phase distortions on y-z plane at two different propagating distance x. We find the vortices are stretched in the stratified z direction as the beam propagates.

Figure 2(a) shows the evolution of the wave amplitude during the propagation, where we observe the asymmetry of wave amplitude in the non-stratified y direction relative to central line (y=0). This asymmetry can be explained by the interaction between the acoustic vortices and the medium inhomogeneity [Figure 2(b)]. Figure 2(c) shows the trajectory of the vortex center identified from the singular point of the phase distribution. The singular trajectory is compared with a horizontally-emitted eigenray from a point source (black dashed line) and a beam from the same source but without the vortex phases (red line). Figure 2(d) shows a three-dimensional streamline starting from (0,0,0.25λ), revealing that the streamline twisting around the vortex center (singular trajectory) is untwisted from certain distance.

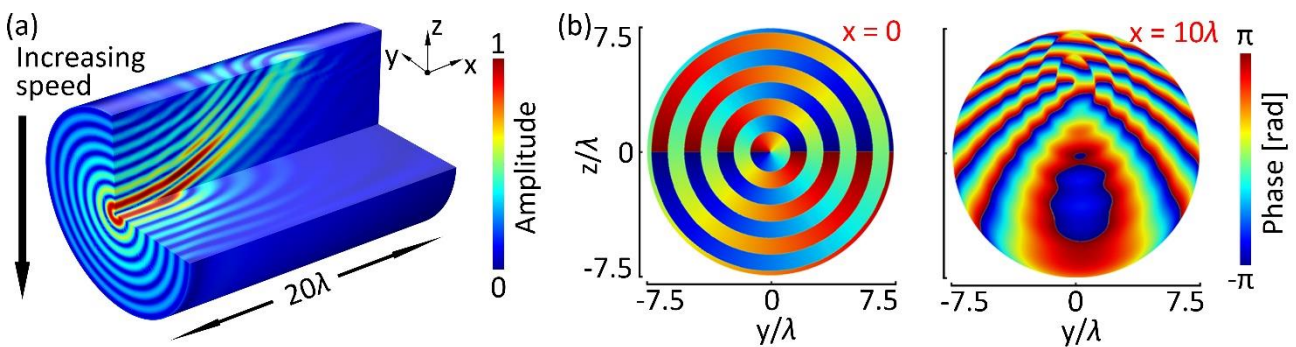


Figure 1: (a) Simulation of a vortex beam bending in a stratified medium. (b) Stretching and distorting of the phase on y-z cross sections at different propagating distances x. Figure from [1].

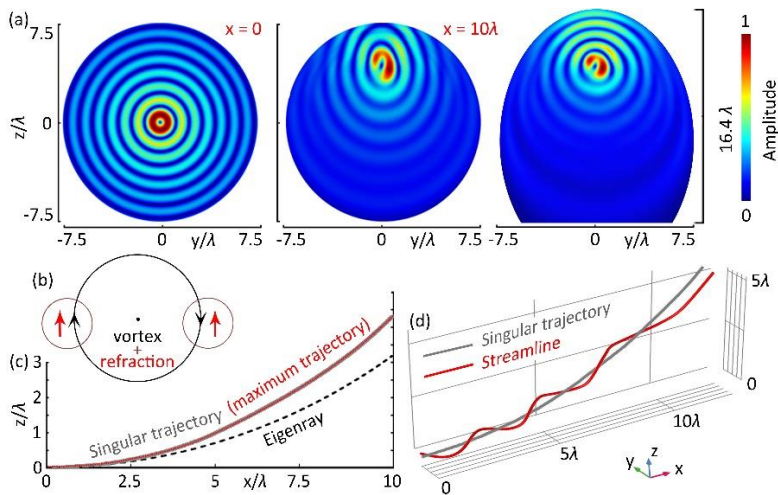


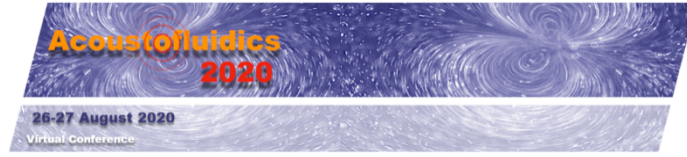
Figure 2: (a) Stretching and distorting of amplitude on y - z cross sections at different propagating distance $x=0$ (left) and $x=10\lambda$ (middle), and on the cross section normal to the singular trajectory through the singular point at $x=10\lambda$. (b) Mechanism of amplitude asymmetry. (c) Singular trajectory on z - x plane (gray solid line) versus a horizontally emitted eigenray (black dashed line) and a maximum amplitude trajectory from an ordinary Bessel beam (red dotted line). (d) A three-dimensional streamline twisting around the vortex center (singular trajectory) is untwisted from certain distance. Figure from [1].

Conclusion

We have found some interesting and unusual phenomena of the acoustic vortex beam propagating in an inhomogeneous medium that we recently published in [1]. Evolution of orbital angular momentum during the propagation will also be presented. Potential applications will be addressed. We are looking forward to presenting for the international acoustofluidics community at *Acoustofluidics 2020 Virtual Conference* on 26 - 27 August 2020.

References

- [1] Xudong Fan, Zhenguang Zou, and Likun Zhang, *Phys. Rev. Research* **1** (3), 032014R (2019).



Streaming in a Kundt's tube of an arbitrary diameter

Alen Pavlic¹, Jürg Dual¹

¹Institute for Mechanical Systems, ETH Zurich, 8092 Zurich, Switzerland
E-mail: apavlic@ethz.ch, URL: <http://www.expdyn.ethz.ch/>

Introduction

Kundt's tube is a well-known experiment for measuring the speed of sound in fluids [1]. In 1876, Dvorak [2] observed a steady fluid flow in a Kundt's tube, i.e. the acoustic streaming, and ever since, the challenge of analytically modelling such flows exists. In 1884, Rayleigh derived the first analytical solution [3], which assumes a 2D channel geometry, and a small viscous boundary layer thickness. Rayleigh's solution predicts that the fluid flows from a velocity antinode to the node along the middle of the channel, and in the opposite direction near the wall. The direction of the flow was later validated experimentally by Andrade [4].

Here, we present an analytical solution for the streaming in a Kundt's tube without restrictions on the tube diameter with regards to the viscous boundary layer thickness and acoustic wavelength. The solution is used to investigate the streaming patterns in some cases that are beyond the scope of Rayleigh's theory.

We show that when the viscous boundary layer thickness becomes comparable to the tube diameter, Rayleigh streaming disappears, and only the oppositely directed Schlichting streaming remains. When the acoustic wavelength is large compared to the tube radius, the transitions between different streaming regimes appear at constant critical ratios between viscous boundary layer thickness and tube radius.

Problem statement

The viscous fluid, initially at rest, is placed in an infinite circular cylindrical tube with an inner diameter of $2a$. Two counterpropagating harmonic weakly decaying travelling waves are assumed in the fluid (pseudo-standing wave), oriented along the axis of the tube. Thermal effects are neglected, and the fluid motion is therefore governed by the Navier-Stokes equations, the continuity equation, and the equation of state, namely,

$$\rho \frac{\partial \mathbf{v}}{\partial t} + \rho(\mathbf{v} \cdot \nabla)\mathbf{v} = -\nabla p + \eta \nabla^2 \mathbf{v} + \left(\eta_B + \frac{\eta}{3}\right) \nabla(\nabla \cdot \mathbf{v}), \quad (1)$$

$$\frac{\partial \rho}{\partial t} + \nabla \cdot (\rho \mathbf{v}) = 0, \quad (2)$$

$$p = p(\rho) \quad (p_1 = c_f^2 \rho_1 \rightarrow \text{at the first order}). \quad (3)$$

The three variables in the governing equations are the velocity \mathbf{v} , pressure p , and density ρ . Material constants defining the viscous fluid are the equilibrium density ρ_0 , the speed of sound c_f , and the dynamic and bulk viscosity, η and η_B , respectively. The problem is constrained by the no-slip boundary condition at the wall.

By applying a regular perturbation technique, the problem can be solved in successive steps of increasing order in terms of small Mach number. The perturbed variables can then be written in a series form, namely, $(\) = (\)_0 + (\)_1 + (\)_2 + \dots$, where the subscript denotes the order in the perturbation expansion, and where $(\)_1 \gg (\)_2$.

Results

The defined problem has been divided into the first- and second-order problems, and solved in two consecutive steps. The procedure of solving the problem analytically is described in detail by Pavlic and Dual [5]. The solution has no restriction on the thickness of the viscous boundary layer δ . Here, we use the derived expression for the streaming velocity $\langle \mathbf{v}_2 \rangle$ and use it for numerical analysis of the evolution of streaming patterns inside the tube.

The analysis revealed, as indicated in Figure 1, three distinct regimes of streaming possible within a Kundt's tube. When the ratio $\mathcal{E} = a/\delta$ is larger than a critical ratio \mathcal{E}_R , we observe only the Rayleigh streaming, which is directed from velocity node towards the antinode along the middle of the tube, and in the opposite direction near the wall. As the radius of the tube is decreased with respect to δ , and \mathcal{E} is between critical ratios \mathcal{E}_R and \mathcal{E}_S , the coexistence of the Rayleigh and the oppositely directed Schlichting streaming is observed. If the radius is decreased further, below \mathcal{E}_S , only the Schlichting streaming remains.

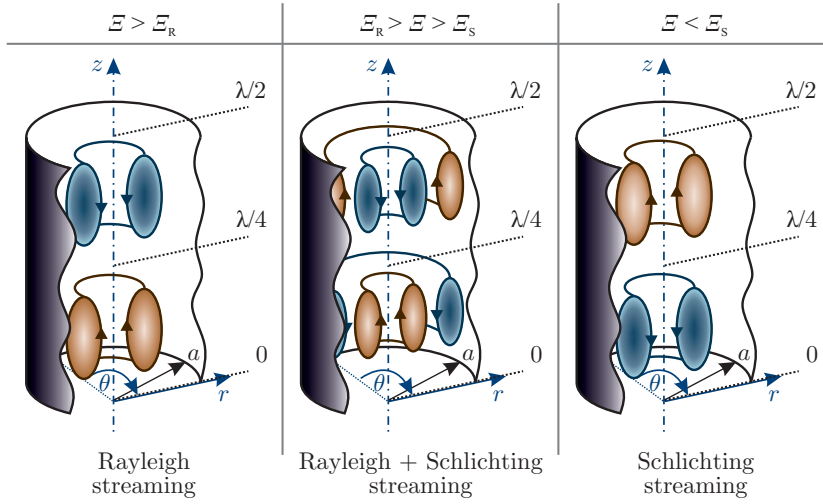


Figure 1: Different streaming regimes that depend on the ratio $\mathcal{E} = a/\delta$, and its value compared to critical ratios \mathcal{E}_R and \mathcal{E}_S . In the limit of large acoustic wavelength relative to the tube radius ($\lambda \gg a$), the critical ratios are $\mathcal{E}_R = 14.2$ and $\mathcal{E}_S = 5.4$, and appear to be invariant with respect to the material properties. The ratios are estimated based on the Eulerian streaming velocity fields.

Critical ratios \mathcal{E}_R and \mathcal{E}_S , at which the transitions between streaming regimes appear, were found to be invariant of material properties when the acoustic wavelength $\lambda = c_f/f$ is large compared to the tube radius. The distinct values appear to be $\mathcal{E}_R = 14.2$ and $\mathcal{E}_S = 5.4$. When the acoustic wavelength is smaller than $\sim 10a$, the critical ratio \mathcal{E}_R increases. Some exemplary streaming patterns for an oil are depicted in Figure 2. The frequency of the pseudo-standing wave with a pressure amplitude (at $z = 0$) of 100 kPa is 100 kHz. The oil used for the analysis has the dynamic viscosity of $\eta = 41.5$ mPa s, the bulk viscosity of $\eta_B = 89.3$ mPa s, the density of $\rho_0 = 922.6$ kg/m³, and the speed of sound of $c_f = 1445$ m/s.

The streaming patterns shown in Figure 2 indicate the reversal of the streaming direction as the relative radius is decreased from $\mathcal{E} = 22.5$ ($> \mathcal{E}_R$) to $\mathcal{E} = 3.33$ ($< \mathcal{E}_S$). Furthermore, the non-periodicity of the streaming pattern along the axis of the tube (z) is visible. This is due to the decoupling of the exponential amplitude dependency of the first-order solution to the sum of exponential and sinusoidal parts at the second order. Additionally, the magnitude of the streaming velocity at the center of the tube converges to the simplified solution by Schuster and Matz [7], provided that $\mathcal{E} \gtrsim 20$.

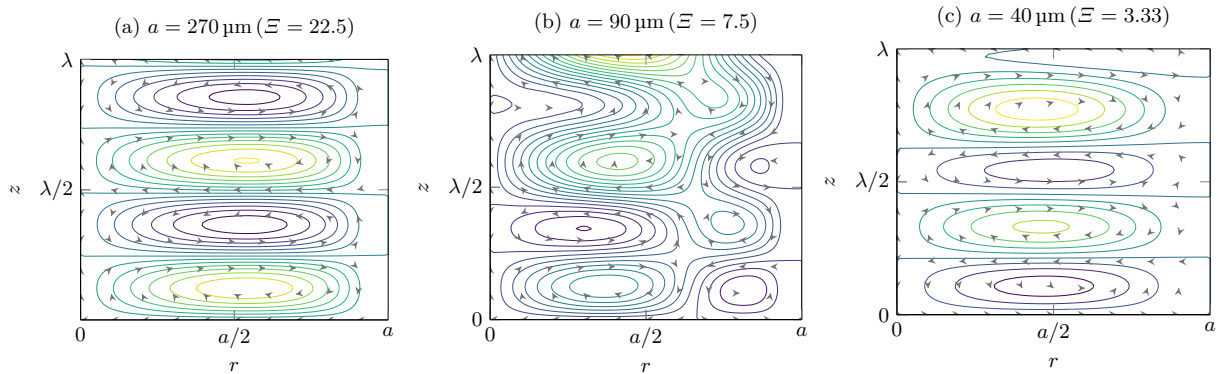


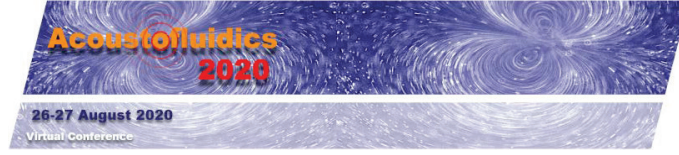
Figure 2: Eulerian streamlines inside oil, at 100 kHz and with a pressure amplitude of 100 kPa. The arrows indicate the direction of the flow, and reveal the reversal of the direction of the streaming as the relative radius is decreased from (a) $\mathcal{E} = 22.5$ to (c) $\mathcal{E} = 3.33$.

Conclusion

The patterns that result from the analytical solution for the streaming in a Kundt's tube reveal an interesting and complex steady behaviour in such systems. This could be used to improve the design of microfluidic devices for acoustic manipulation of microparticles and cells, since the viscous boundary layers can be comparable to the geometry. The solution presented herein is especially applicable in the scope of the surface acoustic wave (SAW) technology, where two opposing decaying travelling waves are often used for excitation [7].

References

- [1] A. Kundt. *Annalen der Physik* **203**, 497-523 (1866).
- [2] V. Dvorak. *Annalen der Physik* **157**, 42-73 (1876).
- [3] L. Rayleigh. *Philosophical Transactions of the Royal Society of London* **175**, 1-21 (1884).
- [4] E. N. D. C. Andrade. *Proceedings of the Royal Society of London A* **134**, 445-470 (1931).
- [5] A. Pavlic and J. Dual. Submitted (2020).
- [6] K. Schuster and W. Matz. *Akustische Zeitschrift* **5**, 349-352 (1940).
- [7] C. Devendran, T. Albrecht, J. Brenker, T. Alan, and A. Neild. *Lab on a Chip* **16**, 3756-3766 (2016).



Reversal of interparticle radiation forces acting on micro particles induced by bulk acoustic standing waves in a microchannel

Sazid Zamal Hoque¹, and Ashis Kumar Sen¹

¹Department of Mechanical Engineering, IIT Madras, Chennai, India
E-mail: ashis@iitm.ac.in, URL: <http://www.ashislab.in>

Introduction

The ability to use acoustics wave to manipulate micro objects (such as microparticles, droplets, cells etc.) solely based on their mechanical properties in microfluidics is known as acousto-microfluidics. This microfluidics technology has proven to be gentle, contact less and biocompatible thus revolutionized in biomedical applications [1]. Depending on the wave scattering, the acoustic forces can be divided broadly into two components, viz. primary and secondary radiation force. Primary radiation force mainly arises due to the scattering of the incident wave on a particle, whereas secondary force is experienced because of the interactions of scattered radiations of a particle from its neighbouring particles [2].

Despite the increasing use of acousto-microfluidics, the extent to which microparticle of various sizes and shapes can be manipulated using acoustic standing wave has not been thoroughly addressed. Specifically, the interparticle force acting on a pair of particles positioned out of the nodal plane is not well understood [3,4]. Here, we report the interparticle acoustic radiation forces acting between a pair of spherical particles suspended in a liquid medium exposed to a standing bulk acoustic wave. A three-dimensional (3D) numerical model based on the perturbation technique and the tensor integral method is employed to predict the interparticle force for a pair of particles placed arbitrarily to the standing wave.

Numerical modelling

We have carried out a 3D simulation to estimate the secondary radiation force between two particles which takes into account the re-scattering effects of the incident wave. Based on the perturbation theory, total acoustic radiation force acting on a particle can be obtained as[5],

$$\mathbf{F}_t = - \int_{\partial V} \left[\left\{ -\frac{\rho_0}{2} \langle |v_1|^2 \rangle + \frac{\rho_0}{2c_0^2} \langle (\partial_t \phi_1)^2 \rangle \right\} + \rho_0 \langle v_{1,i} v_{1,j} \rangle \right] \mathbf{n}_j dA \quad (1)$$

where, ρ_0 and c_0 is the unperturbed density and speed of sound and v_1 is the first order velocity field. The integration is carried out over a close interface ∂V surrounding the particle and \mathbf{n}_j is the unit normal vector pointing outward from the particle surface. The above equation can be used to find both primary and secondary radiation force acting on a particle. The primary radiation force arises due to the interaction of scattered waves from the particle and the suspended medium and secondary radiation force arises due to re-scattered waves from other particles.

Results and discussion

We study the effects of particle position away from the nodal plane on the interparticle force (see Figure 1a). The analytical expression for the interparticle force experienced by a pair of particles located at the nodal plane is given as follows[3],

$$\mathbf{F}_s = -\pi k^4 E_{ac} R_1^3 R_2^3 f_{11} f_{12} \left\{ 3/(k\delta_x)^4 + O([k\delta_x]^{-2}) \right\} \mathbf{n}_x \quad (2)$$

where k, E_{ac} and δ_x are wave number, radius, acoustic energy density and interparticle distance. R_1, R_2 and f_{11}, f_{12} denotes the radius and dipole coefficient of particle 1 and 2 respectively. The variation of dimensionless interparticle force (F_s^*) with the dimensionless vertical distance (in y-direction) between the particles ($k\delta_y$) for different values of the dimensionless horizontal distance (in x-direction) between the particles ($k\delta_x$) in case of a pair of equal and unequal sized particles is depicted in Figure 1b. The interparticle forces for a pair of particles placed symmetrically about the pressure node (i.e. $\delta_{y_1} = \delta_{y_2} = \delta_y/2$) is symmetric. The results show that, for $k\delta_x = 0.26$, the F_s^* is repulsive (i.e. particles in a pair repel each other) for $k\delta_y > 0.13$ and the force F_s^* becomes attractive (i.e. particles

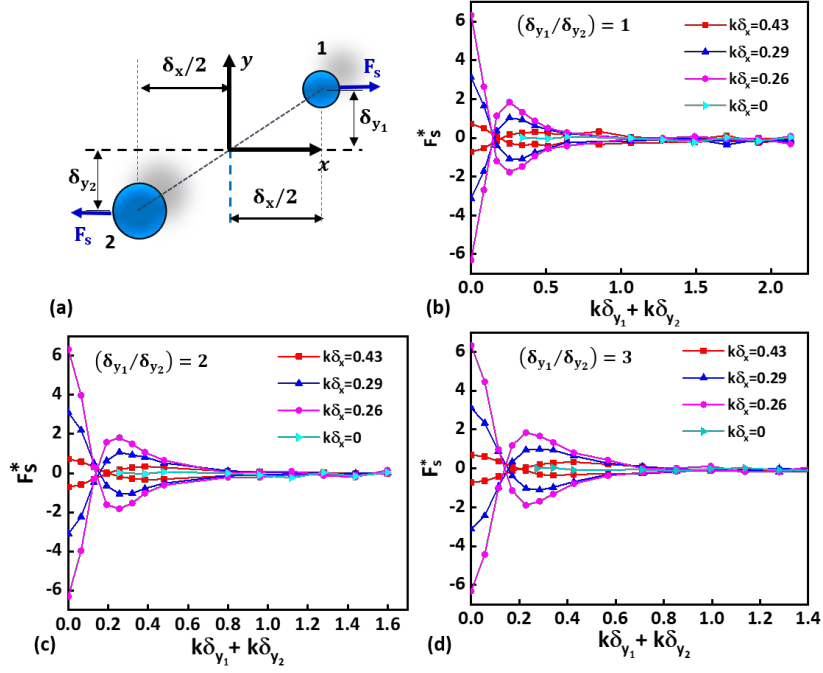


Figure 1: (a) Schematic of the positions of the particles about the nodal plane. The variation of dimensionless interparticle force (F_s^*) predicted using the numerical model with dimensionless vertical distance (in y-direction) between the particles, $k(\delta_{y1} + \delta_{y2})$ for different values of the dimensionless horizontal distance (in x-direction) between the particles ($k\delta_x$) in case of a pair of equal and unequal sized particles, for (b) $(\delta_{y1}/\delta_{y2}) = 1$ and (c) $(\delta_{y1}/\delta_{y2}) = 2$. (d) $(\delta_{y1}/\delta_{y2}) = 3$.

in a pair attract each other) for $k\delta_y < 0.13$. Similarly, for $k\delta_x = 0.29$ and 0.43 , the critical $k\delta_y$ is found to be 0.15 and 0.2 respectively. The interparticle force (F_s^*) is found to be negligible at a much larger distance of the particles from the nodal plane, $k\delta_y > 0.85$.

The interparticle force between a pair of particles located asymmetrically about the nodal plane, for $(\delta_{y1}/\delta_{y2}) = 2$ and 3 are presented in Figure 1c and 1d. The results show that the interparticle force is independent of the actual positions of the particles from the pressure nodal plane (since the interparticle forces are the same for $\delta_{y1}/\delta_{y2} = 2$ and 3) and only depend on the interdistance between the two (or sum of their positions from the nodal plane, $(\delta_{y1} + \delta_{y2})$ and the horizontal interdistance $k\delta_x$. For a fixed $k\delta_x$, the y-interdistance between the particles, $k(\delta_{y1} + \delta_{y2}) = 0.22$, at which the maximum repulsive force occurs is independent of $(\delta_{y1}/\delta_{y2})$. Similar to the $\delta_{y1} = \delta_{y2}$ case, the interparticle forces for a pair of particles placed asymmetrically to the pressure node is also found to be symmetric. The interdistance between the particles, $k(\delta_{y1} + \delta_{y2}) \approx 0.13$ for $k\delta_x = 0.26$, at which nature of the force changes from repulsive to attractive occurs is also independent of the ratio $(\delta_{y1}/\delta_{y2})$.

Conclusion

We elucidated the interparticle radiation force acting on a pair of particles placed away from the pressure nodal plane in a microchannel. We observed that, particles tend to attract each other along the pressure nodal plane which is attributed to the interparticle forces acting between them. Further, a transition in the nature of the interparticle force from attractive to repulsive at a critical interdistance between the particles and the nodal plane is observed. The fundamental understanding from our study will further help in explaining the dynamical behaviour of a pair of particles in a fluid exposed to bulk standing wave.

References

- [1] T. Laurell, F. Pettersson, and A. Nilsson, Chem. Soc. Rev. **36**, 492 (2007).
- [2] A. Lenshof, C. Magnusson, and T. Laurell, Lab Chip **12**, 1210 (2012).
- [3] G.T. Silva and H. Bruus, Phys. Rev. E - Stat. Nonlinear, Soft Matter Phys. **90**, 1 (2014).
- [4] D. Saeidi, M. Saghafian, S. Haghjooy Javanmard, B. Hammarstrom, and M. Wiklund, J. Acoust. Soc. Am. **145**, 3311 (2019).
- [5] J.H. Lopes, M. Azarpeyvand, and G.T. Silva, IEEE Trans. Ultrason. Ferroelectr. Freq. Control **63**, 186 (2016).

Session 3 - Physical Acoustics

Invited Speaker

ACOUSTIC RADIATION FORCE AND TORQUE ON NONSPHERICAL SMALL PARTICLES

[Glauber T. Silva](#)

Universidade Federal de Alagoas, BRAZIL

Contributed Talks

REPELLER AND ATTRACTOR VORTICES GENERATED IN SESSILE DROPLETS BY SWIRLING SURFACE ACOUSTIC WAVES

[Shuren Song](#), [Jia Zhou](#), and [Antoine Riaud](#)

Fudan University, CHINA

FLEXIBLE/BENDABLE ACOUSTOFLUIDICS BASED ON ZnO/AI SHEET SURFACE ACOUSTIC WAVES

[Yong Wang](#)^{1,2}, [Ran Tao](#)^{2,3}, [Qian Zhang](#)¹, [Jin Xie](#)¹, and [Yong Qing Fu](#)²

¹*Zhejiang University, CHINA*, ²*Northumbria University, UK*, and

³*Shenzhen University, CHINA*

THERMAL-GRADIENT-INDUCED FAST CONVECTION IN ACOUSTOFLUIDIC DEVICES

[Wei Qiu](#)¹, [Jonas H. Jørgensen](#)², [Enrico Corato](#)¹, [Henrik Bruus](#)², and [Per Augustsson](#)¹

¹*Lund University, SWEDEN* and ²*Technical University of Denmark, DENMARK*

THEORY OF TEMPERATURE-DEPENDENT EFFECTS IN ACOUSTOFLUIDICS INCLUDING THERMOVISCOUS BOUNDARY LAYERS

[Jonas Helboe Jørgensen](#) and [Henrik Bruus](#)

Technical University of Denmark, DENMARK

THEORY OF ACOUSTIC STREAMING AND ACOUSTIC RADIATION FORCE OF A SOLID PARTICLE IN A VISCOELASTIC FLUID

[Jonas Fankhauser](#), [Alexander A. Doinikov](#), and [Jürg Dual](#)

ETH Zürich, SWITZERLAND

MICROSTREAMING INDUCED BY AN ACOUSTICALLY EXCITED GAS BUBBLE - EXPERIMENTS AND COMPARISON TO THEORY

[Sarah Cleve](#), [Gabriel Regnault](#), [Alexander A. Doinikov](#), [Cyril Mauger](#), [Philippe Blanc-Benon](#), and [Claude Inserra](#)

University of Lyon, FRANCE

Flash Talks

POLY(N-ISOPROPYLACRYLAMIDE) MICROGELS AS SOLUBLE MARKERS FOR VISUALIZATION OF ACOUSTIC ENERGY ABSORPTION IN AQUEOUS SOLUTIONS

Amin Rahimzadeh and Regine von Klitzing
Technische Universität Darmstadt, GERMANY

ACOUSTIC CHARACTERIZATION OF POLYDIMETHYLSILOXANE (PDMS) FOR MICROSCALE ACOUSTOFLUIDICS

Guangyao Xu and Xiasheng Guo
Nanjing University, CHINA

A NUMERICAL STUDY OF THE COUPLING LAYER BETWEEN A PIEZOELECTRIC BULK TRANSDUCER AND A GLASS DEVICE

William N. Bodé and Henrik Bruus
Technical University of Denmark, DENMARK

ALGEBRAIC RADIATION FORCE EXPANSIONS BEYOND KING, YOSIOKA AND KAWASIMA, AND GOR'KOV, AND RELATED INVESTIGATIONS OF SHAPE DYNAMICS

Philip L. Marston
Washington State University, USA

ANALYTICAL PREDICTION OF ACOUSTIC RADIATION FORCES IN SOFT-WALLED MICROCHANNELS DRIVEN BY STANDING SURFACE ACOUSTIC WAVES

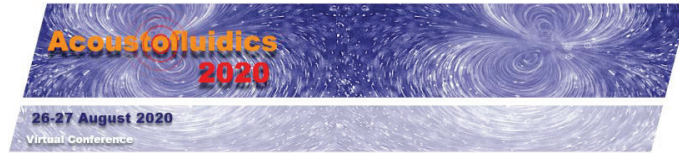
Nitesh Nama¹ and Rune Barnkob²
¹University of Michigan, USA and ²Technical University of Munich, GERMANY

AN ANGULAR SPECTRUM BASED FORMULA OF THE 3D ACOUSTIC RADIATION TORQUE APPLIED ON A PARTICLE OF ARBITRARY SIZE AND SHAPE BY AN ARBITRARY ACOUSTIC FIELD

Zhixiong Gong¹ and Michael Baudoin^{1,2}
¹University of Lille, FRANCE and ²Institut Universitaire de France, FRANCE

CLUSTER STRUCTURATION OF PARTICLE MIXTURE IN MULTI-NODE ACOUSTIC LEVITATION WITH OPTICAL EXCLUSION

Nathan Jeger-Madiot, Mauricio Hoyos, and Jean-Luc Aider
ESPCI, FRANCE



Acoustic radiation force and torque on nonspherical small particles

Glauber T. Silva

Instituto de Física, Universidade Federal de Alagoas, Maceió, Brazil
 E-mail: gtomaz@fis.ufal.br, URL: <http://www.if.ufal.br/~gaf>

Introduction

All of us in acoustofluidics community know, at least to a certain extent, how the radiation force of acoustic waves command particles inside control chambers and microchannels. At the fundamental level, the radiation force arises because the particle changes the linear-momentum flux of the incident wave. Perhaps the knowledge we have on this force is widespread thanks to the elegant and simple approach based on the Gorkov's potential theory [1], an amalgam of the acoustic potential and kinetic energies of a stationary field. From the modeling standpoint, this is very convenient because only an analytical or numerical representation of the incoming wave is required. Two assumptions are necessary to use Gorkov's method. The particle must be much smaller than the acoustic wavelength, which widely valid in acoustofluidic applications. And strictly speaking, the theory works only for spherical particles. The last restriction poses a question: up to which level can Gorkov's potential theory be used for nonspherical particles? This is not mere theoretical curiosity but has implications in acoustofluidic systems since nonspherical bio-particles (cells and microorganisms) are plentiful. Besides, the emergence of autonomous micro/nanorobots propelled by ultrasonic waves relies on the use of robots with nonspherical geometries [2].

With less popularity in acoustofluidics, the radiation torque can also appear on particle caused by an incident wave. The effect is tantamount to the momentum arm of the linear-momentum flux regarding a point inside the particle [3]. An additional ingredient is required for radiation torque take place, namely, particle anisotropy. Thus far, there is no simple description of the radiation torque on a nonspherical particle, except for ideal standing or traveling plane waves. Additionally, the connection between the acoustic spin and radiation torque only for spherical particles was recently established [5,6]. Again we may ask, can we use spherical theories for the radiation torque on nonspherical particles?

In this talk, I will present our latest results in order to answer these questions in the acoustofluidics context [7]. An extension of the Gorkov's theory and new expressions of the radiation torque will be presented considering a small spheroidal particle with an arbitrary aspect ratio. Case studies involving two crossed plane waves and a cylindrical acoustofluidic chamber will also be discussed.

Wave-particle interaction

To obtain the radiation force and torque exerted on a particle, we have to analyze how an incoming wave interacts with the particle. Here, the particle, considered as a prolate spheroid, interacts with an acoustic wave of angular frequency ω . The particle's major semiaxis a is much smaller than the acoustic wavelength. The surrounding fluid has density ρ_0 and compressibility β_0 . In Fig. 1, we sketch the particle and incoming wave. The acoustic fields representing the incident wave are pressure p and fluid velocity $\mathbf{v} = (v_x, v_y, v_z)$. The particle position is denoted by vector \mathbf{r}_0 . Since the spheroidal particle is invariant under rotations around its major axis, we use two Euler angles, α (azimuthal) and β (polar), to represent its orientation, $\mathbf{d} = d(\cos \alpha \sin \beta, \sin \alpha \sin \beta, \cos \beta)$.

Acoustic radiation force

Using the partial-wave expansion method, we demonstrate the radiation force on the spheroidal particle \mathbf{F}^{rad} is minus the gradient of the potential energy U ,

$$\mathbf{F}^{\text{rad}} = -\nabla U, \quad (1a)$$

$$U = \pi a^3 \left[\frac{\beta_0 f_{00}}{3} |p|^2 - \frac{\rho_0}{2} \left(f_{10} |(v_x \cos \alpha + v_y \sin \alpha) \sin \beta + v_z \cos \beta|^2 + \frac{1}{2} f_{11} [|v_x \sin \alpha - v_y \cos \alpha|^2 + |v_x \cos \alpha \cos \beta + v_y \sin \alpha \cos \beta - v_z \sin \beta|^2] \right) \right]_{\mathbf{r}=\mathbf{r}_0}. \quad (1b)$$

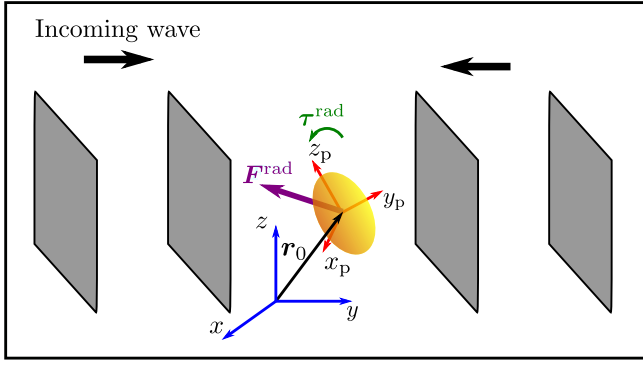


Figure 1: The prolate spheroidal particle in yellow interacts with an arbitrary incoming wave (gray rectangles). The particle frame $O_p(x_p, y_p, z_p)$ is fixed at the particle's geometric center. Regarding the laboratory frame $O(x, y, z)$, the spheroid is placed at \mathbf{r}_0 . The generated radiation force \mathbf{F}^{rad} and torque $\boldsymbol{\tau}^{\text{rad}}$ are also depicted.

The quantity f_{00} is the monopole scattering factor, while f_{10} and f_{11} are the axial and transverse dipole factors, respectively. These coefficients are obtained by solving the acoustic scattering problem for the spheroid with appropriate boundary conditions. The method to calculate the radiation force based on Eq. (1a) is valid for a stationary wave with arbitrary character.

Acoustic radiation torque

The acoustic radiation torque imparted by an arbitrary wave on the particle is given in terms of the linear momentum flux tensor \mathbf{P} and the acoustic spin density \mathbf{S} ,

$$\boldsymbol{\tau}^{\text{rad}} = -\pi a^3 \left[\chi (\mathbf{e}_{z_p} \times \mathbf{P} \cdot \mathbf{e}_{z_p}) - \frac{(ka)^3}{24} \chi^2 \omega (\mathbf{S} - S_{z_p} \mathbf{e}_{z_p}) \right]_{\mathbf{r}_p=0}, \quad (2a)$$

$$\mathbf{P} = \frac{\rho_0}{2} \text{Re}[\mathbf{v}_p \mathbf{v}_p^*], \quad \mathbf{S} = \frac{\rho_0}{2\omega} \text{Im}[\mathbf{v}_p^* \times \mathbf{v}_p], \quad (2b)$$

where ‘Re’ and ‘Im’ are the real and imaginary parts of a complex variable, respectively, $\chi = f_{11} - 2f_{10}$ is the gyroacoustic factor of the particle, and k is the wave number. Note the radiation torque is given in the particle frame, with Cartesian unit vectors being \mathbf{e}_{x_p} , \mathbf{e}_{y_p} , and \mathbf{e}_{z_p} . In this frame, the fluid velocity is denoted by \mathbf{v}_p .

Conclusion

The main results obtained here are the extension to Gorkov's potential theory and new expressions for the radiation torque on nonspherical particles. The effects of fluid viscosity and particle compressibility will be outlined in the presentation.

References

- [1] L. P. Gor'kov, Sov. Phys.-Dokl. **6**, 773 (1962).
- [2] K. J. Rao, F. Li, L. Meng, H. Zheng, F. Cai, and W. Wang, Small **11**, 2836-2846 (2015).
- [3] J. P. Leão-Neto, J. H. Lopes, and G. T. Silva, J. Acoust. Soc. Am. **147**, 2177-2183 (2020).
- [4] G. T. Silva, J. Acoust. Soc. Am. **136**, 2405-2413 (2014).
- [5] I. D. Toftul, K. Y. Bliokh, and M. I. Petrov, and F. Nori, Phys. Rev. Lett **123**, 183901 (2019).
- [6] J. H. Lopes, E. B. Lima, J. P. Leão-Neto, and G. T. Silva, Phys. Rev. E **101**, 043102 (2020).
- [6] E. B. Lima, J. P. Leão-Neto, A. S. Marques, G. C. Silva, J. H. Lopes, and G. T. Silva, Phys. Rev. Applied **13**, 064048 (2020).

Repeller and Attractor vortices generated in Sessile Droplets by Swirling Surface Acoustic Waves

Shuren Song¹, Jia Zhou¹, Antoine Riaud^{1*}

¹State Key Laboratory of ASIC and System, School of Microelectronics, Fudan University, Shanghai, China
 E-mail: antoine_riaud@fudan.edu.cn.

Introduction

Acoustic streaming in droplets is a promising approach for particle concentration in sessile droplets [1]. So far, all methods have used plane surface acoustic wave (SAW) [2]. Another option for particles or cells concentration in sessile droplets could be acoustic vortices. These waves, denoted W_l [3], are classified according to their topological order l . In particular, the waves carry an orbital angular momentum (OAM) proportional to l that can be transmitted to the fluid to induce a flow rotation (Fig 1.a, c). In addition to the azimuthal flow proportional to the topological order l of the vortex, a theoretical study for unbounded cylindrical tubes indicates the existence of axial flow that can be reversed depending on the size of the vortex eye [3]. While the azimuthal acoustic streaming flow has previously been observed experimentally[4], the transition between attractor vortices (negative axial velocity) and repeller vortices (positive axial velocity) remains unseen.

In this paper, we improve previous swirling SAW transducers [5, 6] (Fig 1.b) to generate acoustic vortices with no eye (W_0 , Fig 1.a) or with very large eyes (W_{15} , Fig. 1.c). We then apply the General Defocusing Particle Tracking (GDPT) [7] to follow the 3D trajectory of 10 μm diameter red fluorescent particles carried by the hydrodynamic vortices in sessile droplet. To minimize the influence of the acoustic radiation pressure on the beads, we use acoustic-impedance matched water-glycerin mixture. The droplets volume in each experiment is 2 μL . In the experiment, W_{15} and W_0 transducers are excited with 20 MHz and 30 MHz frequency, respectively.

Results and Discussion

We experimentally observe attractor and repeller hydrodynamic vortices.

W_0 acoustic vortices generate two azimuthal hydrodynamic vortices in the sessile droplet (shown in Fig. 2 (a)), with a strong downward axial streaming (84 $\mu\text{m/s}$) along the central axis of the droplet (Fig. 2 (c)). This axial flow qualifies the W_0 streaming as an attractor hydrodynamic vortex.

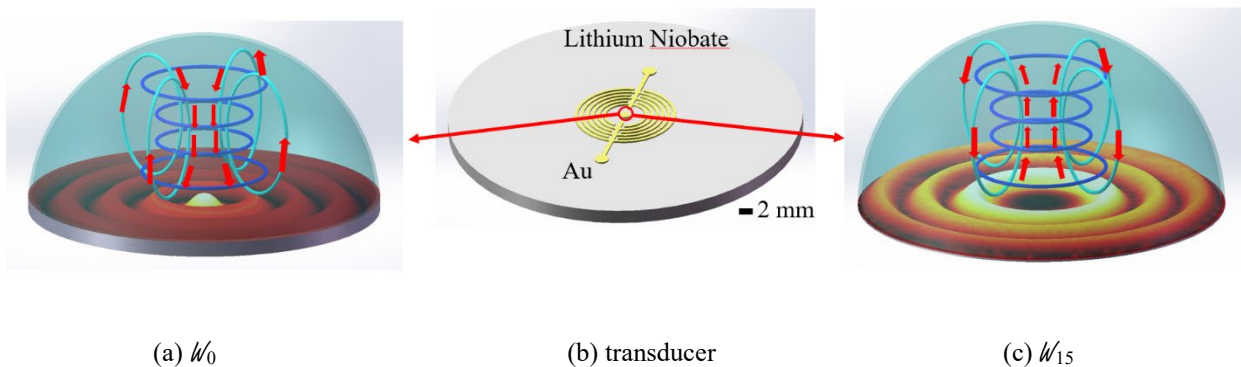


Figure 1: (a,c) Acoustic streaming generated by swirling SAW in sessile droplets. Blue and cyan lines represent azimuthal flow and axial flow, respectively. The swirling SAW is shown at the bottom of the vortex, with the eye in black (Fig. c). (b) W_0 Swirling SAW transducer.

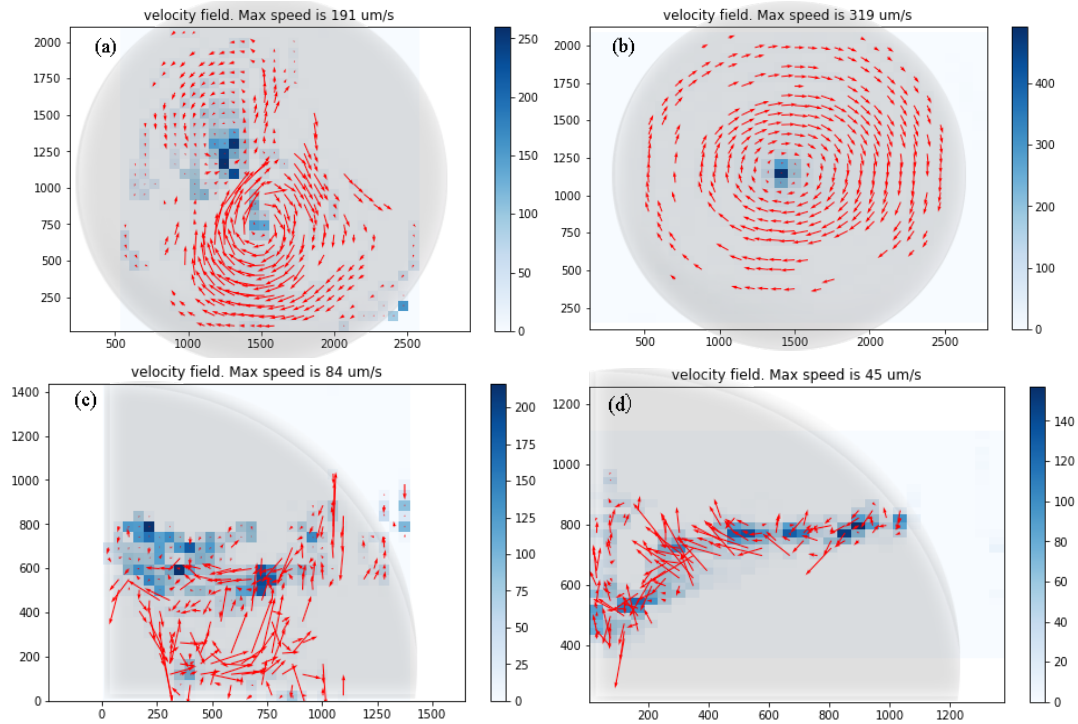


Figure 2: (a, b) Top view of the flow velocity fields deduced from the GDPT data for topological order (a) $l = 0$, (b) $l = 15$. (c,d) Side view of the flow velocity fields, (c) $l = 0$, (d) $l = 15$. The arrows indicate the flow velocity, and the shade of blue the number of particles observed in each region. The droplet outline is a guide for the eye.

W_{15} acoustic vortices (Fig. 2(b)) produce only one azimuthal hydrodynamic vortex. Unlike the W_0 , the axial streaming is pointing upward (Figure 2(d)), which qualifies it as a repeller hydrodynamic vortex. Even though the axial flow reversal was observed as predicted by the theoretical model, the W_0 vortex produced an attractor vortex and the W_{15} produced a repeller vortex, which is the opposite of the ideally long tube case. Our numerical simulations (data not shown) suggest that the acoustic vortex is focused and strengthened by the curved surface of the droplet, yielding a dominating streaming from the opposite direction.

Conclusion

We have experimentally observed repeller and attractor vortices depending on the swirling SAW topological order. In our next work, we will systematically study the condition of appearance of these vortices, including the top surface curvature, the effect of the topological order and viscosity. This study may guide future efforts to design of future swirling SAW transducers for the concentration of particles in sessile droplets.

References

1. Destgeer, G., et al., *Acoustofluidic particle manipulation inside a sessile droplet: four distinct regimes of particle concentration*. Lab on a Chip, 2016. **16**(4): p. 660-667.
2. Li, H., J.R. Friend, and L.Y. Yeo, *Surface acoustic wave concentration of particle and bioparticle suspensions*. Biomedical Microdevices, 2007. **9**(5): p. 647-656.
3. Riaud, A., et al., *Cyclones and attractive streaming generated by acoustical vortices*. Physical Review E, 2014. **90**(1): p. 013008.
4. Hong, Z.Y., J. Zhang, and B.W. Drinkwater, *Observation of Orbital Angular Momentum Transfer from Bessel-Shaped Acoustic Vortices to Diphasic Liquid-Microparticle Mixtures*. Physical Review Letters, 2015. **114**(21): p. 214301.1-214301.5.
5. Laude, V., et al., *Subwavelength focusing of surface acoustic waves generated by an annular interdigital transducer*. Applied Physics Letters, 2008. **92**: p. 094104.
6. Riaud, A., et al., *Selective Manipulation of Microscopic Particles with Precursor Swirling Rayleigh Waves*. Phys.rev.applied, 2017. **7**(2): p. 024007.
7. Barnkob, R., C.J. Kähler, and M. Rossi, *General defocusing particle tracking*. Lab on a Chip, 2015. **15**(17): p. 3556-3560.

Flexible/bendable acoustofluidics based on ZnO/Al sheet surface acoustic waves

Yong Wang^{1,2}, Ran Tao^{2,3}, Qian Zhang¹, Jin Xie¹, and Yong Qing Fu²

¹The State Key Laboratory of Fluid Power and Mechatronic Systems, Zhejiang University, Hangzhou 310027, China

E-mail: ywang_mems@zju.edu.cn

²Faculty of Engineering and Environment, Northumbria University, Newcastle upon Tyne, UK

³Shenzhen Key Laboratory of Advanced Thin Films and Applications, College of Physics and Optoelectronic Engineering, Shenzhen University 518060, China

Introduction

Acoustic wave technologies, especially thin film surface acoustic waves (SAWs) have been extensively investigated for microfluidics and lab-on-a-chip applications [1-3]. However, there are still challenges remaining in SAW based microfluidics, such as effective and long range wave propagation across the surface and liquid transportation along the curved surfaces. Recently, microfluidic streaming has been realized using flexible ZnO/polymer based SAW devices [4]. Nevertheless, there are significant challenges with realizing efficient microfluidic actuation due to significant dissipation of acoustic energy into polymer substrates. In this work, we fabricated ZnO thin film SAW devices on different thickness Al sheets (with thickness from 50 to 1500 μm) for microfluidics. We have achieved efficient transportation of the droplets across a wide range of substrate geometries, including inclined, vertical, inverted, lateral and bendable surfaces using thin Al sheet (200 μm thick) based SAW devices. Moreover, we have demonstrated that ZnO/Al sheet SAWs have better pumping performances than those of conventional ZnO/Si SAWs with the same electrode designs. Our work shows great potentials for flexible/bendable acoustofluidics using thin film SAWs.

Device design and characterization

ZnO thin films of $\sim 5 \mu\text{m}$ thick were deposited onto commercial Al sheets with thicknesses from 50 to 1500 μm using DC magnetron sputtering. SAW devices were then fabricated on ZnO/Al sheet substrates by patterning Cr (20 μm)/Au (100 μm) films to form the IDT electrodes using conventional lift-off processes. Figure 1 shows the effects of Al sheet thickness on generation of wave modes when the device wavelength is 200 μm , while the Al sheet thickness is decreased from 1500 μm to 50 μm . It can be seen that as the Al sheet thickness is decreased from 1500 μm to 50 μm , the wave modes are gradually changed from Rayleigh modes to hybrid modes and consequently to pure Lamb wave modes.

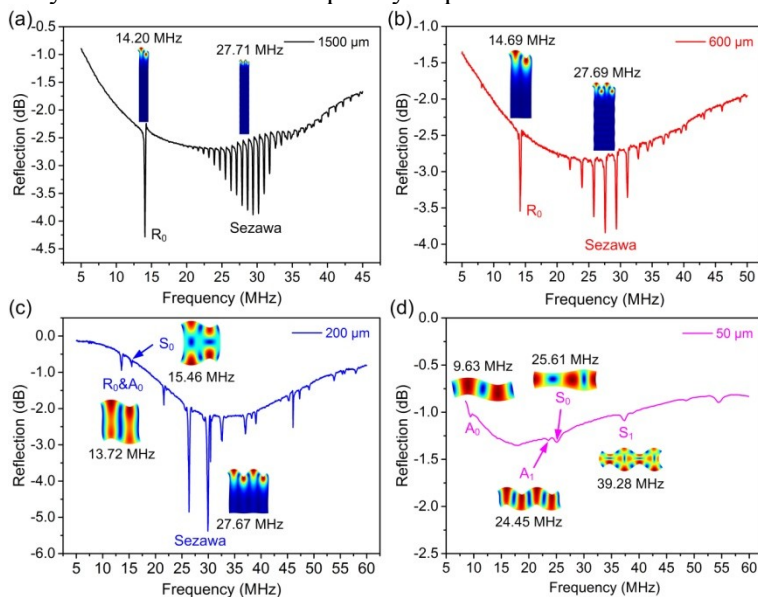


Figure 1: FEM simulations and experimental verifications of wave vibration modes and their corresponding frequencies for ZnO thin film SAW devices with 200 μm wavelength and varied Al sheet thicknesses of (a) 1500 μm , (b) 600 μm , (c) 200 μm and (d) 50 μm . When the Al sheet thickness is larger than the device wavelength, the SAW devices show fundamental Rayleigh mode and Sezawa mode. When the Al sheet thickness is equal to the device wavelength, A_0 mode and pseudo-Rayleigh mode are hybridized together and pseudo- S_0 mode and Sezawa mode are also obtained. With the further decrease of Al sheet thickness to 50 μm , the wave vibration modes are changed into pure Lamb wave modes.

Pumping performance comparisons between ZnO/Al and ZnO/Si SAWs

Figures 2(a) and 2(b) show droplet pumping images driven by ZnO/Al sheet SAWs and ZnO/Si SAWs, respectively. As the SAW propagating velocity in Al sheet is smaller than that in Si substrate, the Rayleigh angle of ZnO/Al sheet SAWs in water is larger than that of ZnO/Si SAWs. The SAW streaming force direction is following the Rayleigh angle. Therefore, in comparisons with ZnO/Si SAWs, the droplet's lateral deformation caused by ZnO/Al sheet SAWs is larger. Figures 2(c) and 2(d) show droplet pumping performance comparisons between ZnO/Al sheet SAWs and ZnO/Si SAWs. Clearly, ZnO/Al sheet SAWs have better pumping performances than those ZnO/Si SAWs, which can be attributed to their larger Rayleigh angles (32°), higher electromechanical coupling coefficients and reduced contact angle hysteresis [3].

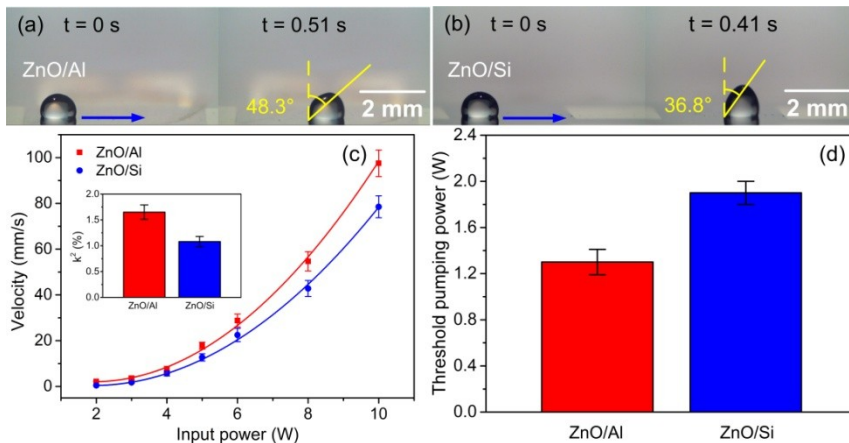


Figure 2: Droplet pumping images driven by (a) ZnO/Al sheet (1.5 mm thick) SAWs and (b) ZnO/Si SAWs with the same electrode designs (wavelength of $64 \mu\text{m}$). (c) Droplet average pumping velocities for ZnO/Al and ZnO/Si SAWs under different input powers, the insert shows electromechanical coupling coefficients k^2 of the SAW devices. (d) Droplet threshold pumping powers for ZnO/Al sheet SAWs and ZnO/Si SAWs.

Demonstration of flexible/bendable acoustofluidics

Figure 3(a) shows threshold pumping power comparisons for different thick Al sheet SAWs using different modes. Results show that Al foil ($50 \mu\text{m}$ thick) SAWs present worse pumping performances than those of thicker Al sheet SAWs due to the large deformation and damping of Al foil substrates at high RF powers. Besides, for Al foil based Lamb waves, the pumping performance of A_0 mode was better than that of S_0 mode. However, for thin Al sheet ($200 \mu\text{m}$ thick) SAWs, their pseudo-Rayleigh modes present comparable pumping performances with those of thicker Al sheet SAWs. Since thin Al sheets also have good deformability and re-deformability, finally we have demonstrated efficient transportation of droplets along inclined, curved, vertical, inverted and lateral surfaces using thin Al sheet SAWs, as shown in Figure 3(b).

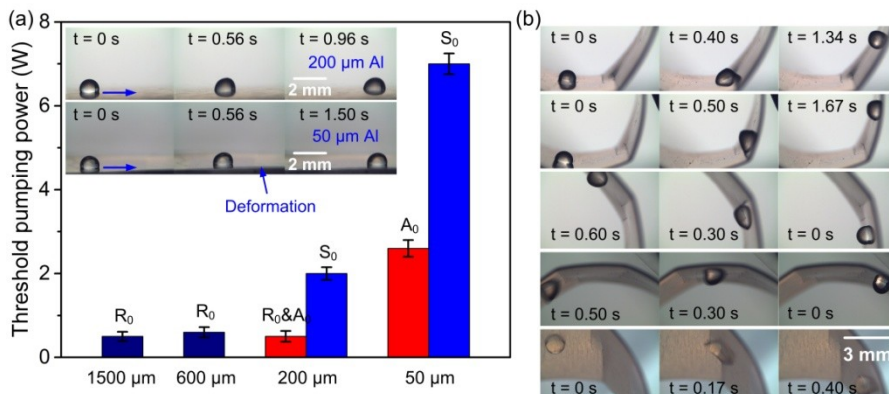


Figure 3: (a) Droplet threshold pumping power comparisons for different thick Al sheet SAWs (wavelength of $200 \mu\text{m}$) driven using different wave modes, the inserts show droplet pumping images driven using A_0 mode of thin Al sheet SAWs and Al foil ($50 \mu\text{m}$ thick) SAWs. (b) Droplet pumping images along curved and lateral surfaces using thin Al sheet SAWs.

Conclusion

We have demonstrated efficient transportation of droplets along horizontal, inclined, vertical, inverted, lateral and arbitrarily shaped surfaces using thin Al sheet SAWs. We have also shown that ZnO/Al sheet SAWs present better microfluidic pumping performances than those of conventional ZnO/Si SAWs with the same electrode configurations. Our work opens a new route for flexible SAW devices to perform complex smart microfluidic systems.

References

- [1] R. Tao, J. Reboud, H. Torun, et al., Lab on a Chip **20**, 1002-1011 (2020).
- [2] Y. Wang, X. Tao, R. Tao, et al., Sensors and Actuators A: Physical **306**, 111967 (2020).
- [3] R. Tao, G. McHale, J. Reboud, et al., Nano letters **20**, 3263-3270 (2020).
- [4] H. Jin, J. Zhou, X. He, et al., Scientific reports **3**, 2140 (2013).

Thermal-gradient-induced fast convection in acoustofluidic devices

Wei Qiu¹, Jonas H. Jørgensen², Enrico Corato¹, Henrik Bruus², and Per Augustsson¹

¹Department of Biomedical Engineering, Lund University, Lund, Sweden

E-mail: wei.qiu@bme.lth.se, <http://bme.lth.se/research-pages/nanobiotechnology-and-lab-on-a-chip/>

²Department of Physics, Technical University of Denmark, Kongens Lyngby, Denmark

Introduction

Inhomogeneities in density and compressibility between miscible aqueous solutions in microscale acoustofluidic devices induce an acoustic body force \mathbf{f}_{ac} acting on the fluids [1]. The induced fluid stabilization [2] and streaming suppression [3,4] trigger several new applications, e.g. iso-acoustic focusing [2] and submicrometer particle manipulation [5]. In previous studies, the inhomogeneities are generated by adding solute molecules to the solution. Considering that the water density and compressibility are temperature dependent, it can be foreseen that inhomogeneities can instead be induced in acoustofluidic devices by heating. In this study, we generate thermal gradients in a microchannel by heating the medium using light, and discover a convective flow that is two orders of magnitude faster than the gravity driven convection in the cavity and one order of magnitude faster than the boundary-driven acoustic streaming.

Materials and experimental methods

A standard glass-silicon-glass sandwiched chip with a 360- μm -high and 760- μm -wide long straight channel is used, under which a PZT transducer with a thickness of 2 mm is bonded, see Fig. 1. The transducer is actuated at the frequency of 0.953 MHz with an acoustic energy density $E_{ac} \approx 14.2$ Pa in the channel. Carotenoids with a mass concentration of 0.5 wt% are added to milli-Q, of which the absorption peak is in the wavelength of blue light. A focused light with a peak wavelength of 470 nm from an LED is shone below the chip, which is absorbed by the medium to induce the heat. The absorption fulfills the Beer-Lambert law, and therefore a temperature gradient in z direction is generated. The 3D flow fields are mapped by tracking the motion of 1.1- μm -diameter polystyrene particles using a general defocusing particle tracking technique [6].

Results and discussions

The experiments are conducted under three different conditions, i.e. with only sound on, with only light on, and with both sound and light on, and the measured flow fields are shown in Fig. 2. Here light means the blue light for generating thermal gradients. When only sound field is present, the typical

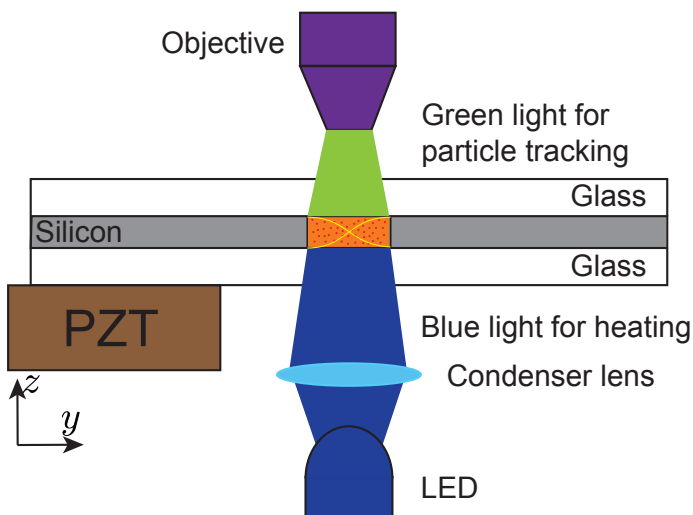


Figure 1: Sketch of the cross sectional view of the acoustofluidic silicon chip (gray) sandwiched by two glass layers. The microchannel is filled with milli-Q containing 0.5 wt% carotenoids (orange). The piezoelectric transducer (brown) excites half-wavelength standing-wave field (yellow) at 0.953 MHz. The blue light is shone to the microchannel from an LED below the chip, after being focused by a condenser lens (light blue), which is absorbed by the medium and hence generates thermal gradients. Red fluorescent particles, of which the excitation wavelength is in green, are used as the tracers, and their motion is recorded by the optical system (purple) above the chip.

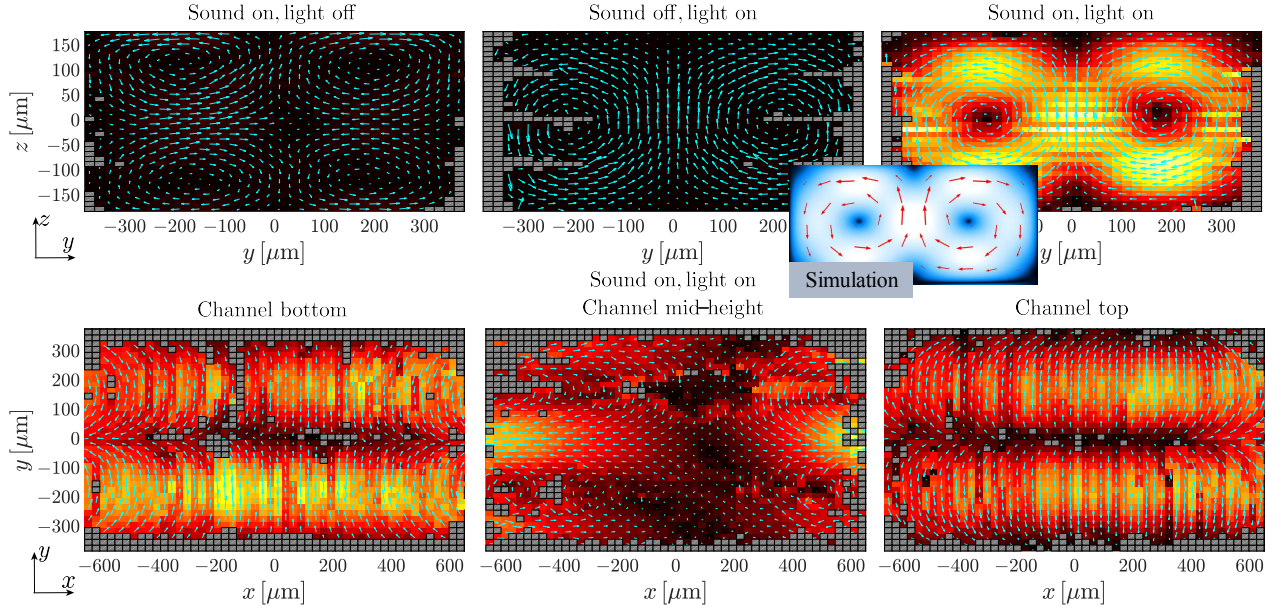


Figure 2: Measured 3D flows projected onto 2D planes. The upper row shows the flows observed in the vertical y - z cross section of width $W = 760 \mu\text{m}$ and height $H = 360 \mu\text{m}$ under three conditions, i.e. with only sound on, with only light on, and with both sound and light on. The lower row shows the flows observed in the horizontal x - y plane of length $L = 1300 \mu\text{m}$ and $W = 760 \mu\text{m}$ with both sound and light on at three different z positions, i.e. channel bottom, channel mid-height, and channel top. Color plot represents the flow velocity amplitude from $0 \mu\text{m s}^{-1}$ (black) to $165 \mu\text{m s}^{-1}$ (white). The arrows (cyan) indicate the flow direction and their length only indicates the relative velocity amplitude in each plot. Spatial bins with no data points are excluded (gray). The simulation shows the flow field in the y - z plane with sound and light on.

boundary-driven acoustic streaming with the characteristic quadrupolar flow roll structure is observed. When blue light is shone onto the microchannel, the medium absorbs the light fulfilling the Beer-Lambert law, leading to a temperature gradient in z direction. Therefore, the classic Rayleigh-Bénard convection with two big rolls in y - z cross section is observed. It should be noted that boundary-driven streaming (the velocity amplitude $|\mathbf{v}_{\text{str}}| \approx 15 \mu\text{m s}^{-1}$) is faster than the Rayleigh-Bénard convection ($|\mathbf{v}_{\text{con}}| \approx 4 \mu\text{m s}^{-1}$) in this case.

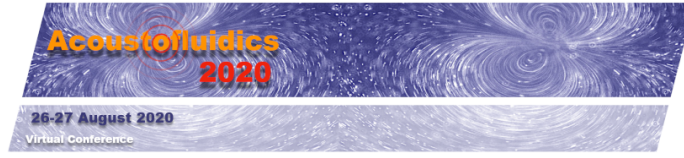
When both sound field and thermal gradients are present, the flow field changes drastically. Two big rolls are observed in y - z cross section with a velocity amplitude ($|\mathbf{v}_{\text{fas}}| \approx 165 \mu\text{m s}^{-1}$) one order of magnitude higher than that of the unperturbed acoustic streaming. In addition, the in-plane motion is also observed in the x - y plane, indicating that the flow rolls are mainly in the y - z plane, but are also oblique in the x - y plane. The generation of this fast convection can be explained using the theory of acoustic body force \mathbf{f}_{ac} . In this experiment, the light heats up the fluid from beneath while the silicon walls transport the heat away, thus cooling the sides of the channel. So a thermal gradient is induced in the y and z directions with the highest temperature at the center of channel bottom. The thermally induced gradients in the compressibility and density creates \mathbf{f}_{ac} that drives the flow. This process always keeps going because the cooler liquid is heated instantaneously once arrives the bottom. Therefore a fast convection is generated when thermal gradients are present, which is significantly different from the case where the inhomogeneities are created by different solutions. The high velocity of the convection here is mainly due to the large \mathbf{f}_{ac} compared to the hydrostatic pressure in this length scale. The in-plane motion in x - y plane is attributed from the thermal gradients in x direction, which is caused by the Gaussian profile of the light intensity.

Conclusion

In this study, we observed a thermal-gradient-induced fast convection in an acoustofluidic device, which can be explained by the theory of \mathbf{f}_{ac} . More detailed analysis will be provided in the conference, and we believe this new phenomenon will trigger some interesting applications in this field.

References

- [1] J. T. Karlsen, P. Augustsson, and H. Bruus. Phys. Rev. Lett. **117**, 114504 1-6 (2016).
- [2] P. Augustsson, J. T. Karlsen, H.-W. Su, H. Bruus, and J. Voldman. Nat. Commun. **7**, 11556 1-9 (2016).
- [3] J. T. Karlsen, W. Qiu, P. Augustsson, and H. Bruus. Phys. Rev. Lett. **120**, 054501 1-6 (2018).
- [4] W. Qiu, J. T. Karlsen, P. Augustsson, and H. Bruus. Phys. Rev. Appl. **11**, 024018 1-11 (2019).
- [5] D. Van Assche, E. Reithuber, W. Qiu, T. Laurell, B. Henriques-Normark, P. Mellroth, P. Ohlsson, and P. Augustsson. Sci. Rep. **10**, 3670 (2020).
- [6] B. Barnkob, C. J. Kähler, and M. Rossi. Lab Chip **15**, 3556-3560 (2015).



Theory of temperature-dependent effects in acoustofluidics including thermoviscous boundary layers

Jonas Helboe Jørgensen and Henrik Bruus

Department of Physics, Technical University of Denmark, Kongens Lyngby, Denmark
 E-mail: jonashj@fysik.dtu.dk, URL: <http://www.fysik.dtu.dk/microfluidics>

Introduction

We study theoretically temperature-dependent effects in acoustofluidics including thermoviscous boundary layers and the surrounding solids. By including thermodynamics, our work extends work by Bach and Bruus of perturbative viscous acoustofluidics with effective boundary conditions [1], which enables 3D simulations [2]. By including solids, we also extend the prior thermoviscous acoustic theory limited to fluids [3]. We go beyond the perturbative approach of Refs. [1-3] by including the thermal fields in an iterative procedure, which allows for simulations of systems with higher acoustic energy density.

The theoretical development includes: (1) separation of time and length scales, (2) analytically solving thermal and viscous boundary layers, (3) imposing effective boundary conditions on the acoustic pressure, on the elastic displacement, as well as on the time-averaged streaming and heating, and (4) deriving equations for both acoustic and time-averaged fields in the bulk of the system.

We apply our theory in two experimentally relevant examples that show how temperature can affect acoustic streaming: Either by the temperature field created by the acoustic wave, or by an externally controlled thermal field.

Theoretical framework

We leave the piezoelectric transducer out of the analysis and only represent it by an oscillating displacement condition on part of the surface of the elastic solid. The response of the fluid embedded in the elastic solid to this oscillating-displacement boundary condition is controlled by the hydro-, elasto-, and thermodynamic governing equations of the coupled thermoviscous fluid and linear elastic solid. The solid is described in the Lagrangian picture by the fields of the density ρ_{sl} , the displacement \mathbf{u} , and the temperature T . The governing equations are the transport equations for the momentum density $\rho_{fl}\partial_t\mathbf{u}$, and temperature T [5]. The fluid is described in the Eulerian picture by the fields of the density ρ_{fl} , the pressure p , the velocity \mathbf{v} , the temperature T , and the energy per mass unit ϵ . The boundary motion includes Stokes drift, and the governing equations are the transport equations for the densities of mass ρ_{fl} , momentum $\rho_{fl}\mathbf{v}$, and internal energy $\rho_{fl}\epsilon$ [3,5],

$$\mathbf{v} + \mathbf{u} \cdot \nabla \mathbf{v} = \frac{\omega}{i} \mathbf{u}, \quad \rho_{sl} \partial_t^2 \mathbf{u} = \nabla \cdot \boldsymbol{\sigma} \quad \partial_t T + \frac{\gamma - 1}{\alpha_p} \partial_t (\nabla \cdot \mathbf{u}) = \frac{\gamma}{\rho_{sl} c_p} \nabla \cdot (k_{th} \nabla T) \quad (1)$$

$$\partial_t \rho_{fl} = -\nabla \cdot (\rho \mathbf{v}), \quad \partial_t (\rho_{fl} \mathbf{v}) = \nabla \cdot (\boldsymbol{\sigma} - \rho_{fl} \mathbf{v} \mathbf{v}), \quad \partial_t (\rho_{fl} \epsilon + \frac{1}{2} \rho_{fl} v^2) = \nabla \cdot [k_{th} \nabla T + \mathbf{v} \cdot \boldsymbol{\sigma} - \rho_{fl} \mathbf{v} (\epsilon + \frac{1}{2} v^2)], \quad (2)$$

where $\boldsymbol{\sigma}$ is the stress tensor for fluids and solids, respectively. Acoustofluidic devices are typically driven in the frequency range $f = 1 - 20$ MHz with the corresponding fast acoustic time scale $t = \frac{1}{\omega} = \frac{1}{2\pi f} = 8 - 160$ ns. The time scale τ associated with the hydrodynamic and thermal flow is longer, $\tau \approx 10$ ms [5]. The slow thermo-hydrodynamic and fast acoustic time scales are thus separated by 4-5 orders of magnitude. Following Karslen and Bruus [4], we therefore solve the fast and slow dynamics separately. We describe any given physical field as $Q_{phys} = Q_0 + \text{Re} [Q_1 e^{-i\omega t}]$, where Q_0 is a stationary field, and Q_1 is the stationary amplitude of a rapidly oscillating acoustic field.

Acoustofluidic systems also exhibit a separation of length scales. The continuity of the velocity field, stress, heat flux, and thermal field across the fluid-solid boundary, results in the appearance of thermal and viscous boundary layers of thickness δ_t and δ_s , respectively. These boundary layers are localized near fluid-solid interfaces, and their dynamically-defined widths are small [5], typically $\delta_t \lesssim \delta_s \lesssim 500$ nm, which is more than two orders of magnitude smaller than a typical device size around 100 μm . Both the fast oscillating acoustic field and stationary field are split into a narrow boundary layer field, which is solved analytically, and a bulk field, which is solved numerically.

General effects of thermal corrections and two specific examples

The inclusion of the thermal fields gives a set of important corrections to the purely viscous theory. In the case of acoustic streaming, the following three effects are important: (1) the time averaged slip velocity is corrected by the thermal boundary layer (important for travelling or rotating acoustic fields), (2) the temperature dependency of the viscosity leads to an acoustic body force, and (3) inhomogeneities in the stationary compressibility and density fields create an acoustic force [4].

To highlight the importance of these thermal effects, we present two numerical simulations. In Fig. 1, we show the streaming field in a square capillary tube actuated by two perpendicular standing waves. When $\frac{\pi}{2}$ out of phase, these two waves create a rotating wave in the channel. For a rotating wave, the thermal correction for the slip velocity and the acoustic body force, created by the temperature dependency of the viscosity, is important. In Fig. 1 we show this thermal effect, and also how accurately the effective boundary conditions are matching a full simulation.

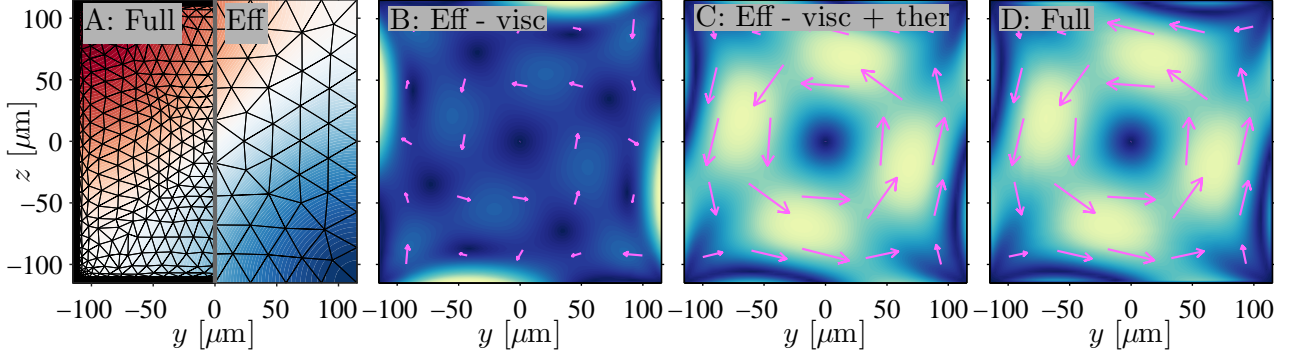


Figure 1: Simulation of a 230- μm -wide square channel with two perpendicular standing waves actuated $\frac{\pi}{2}$ out of phase and acoustic energy density 470 Pa [6]. (A) The rotating acoustic pressure field at $t = 0$. The mesh for the full and effective boundary simulations illustrate the computational gain of using the effective boundary theory. (B) Effective model including only viscous boundary layers. (C) Effective model with thermoviscous boundary layers. (D) Full model. The color scale and arrows show the streaming velocity 0 – 420 $\mu\text{m/s}$.

The second example reveals the importance of an externally controlled thermal field T_0 and of the acoustic body force appearing via the T_0 -dependent stationary compressibility and density fields [4]. In Fig. 2A is shown the temperature field T_0 around a heating wire placed just above a microfluidic channel, and in Fig. 2B-C how this T_0 , when big enough, leads to streaming dominated by the thermally-induced the acoustic body force.

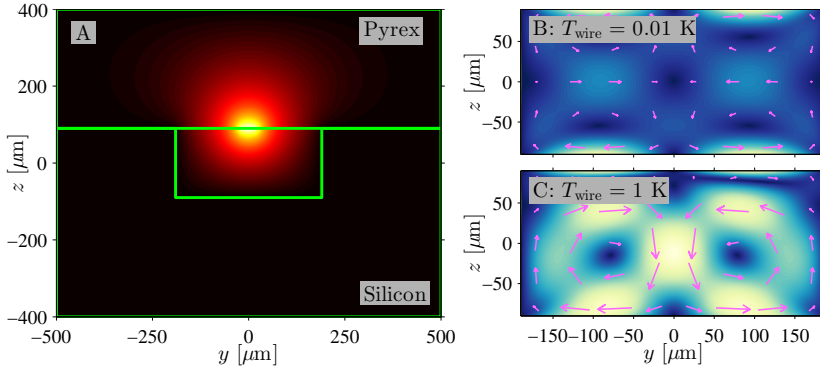


Figure 2: A silicon chip with a Pyrex lid enclosing a fluid channel with a traditional half-wave horizontal acoustic field. (A) The thermal field in the fluid and solid due to a heating wire at the bottom of the lid with set temperature T_{wire} . (B) Boundary-driven streaming from 0 (blue) to 82 $\mu\text{m/s}$ (yellow) for $T_{\text{wire}} = 0.01$ K and acoustic energy density $E_{\text{ac}} = 60$ Pa. (C) Same as (B) but for $T_{\text{wire}} = 1$ K. Here, the streaming is dominated by bulk-driven streaming.

Conclusion and outlook

The presented theory opens up for the possibility to include internal acoustic heating and externally-controlled thermal fields, such as a heating wire or a light beam. Furthermore, the effective boundary conditions allow us to perform 3D simulations including thermal fields and thus to take into account thermal effects hitherto neglected in numerical modeling of acoustofluidic devices.

Acknowledgements. This work was supported by Independent Research Fund Denmark, Natural Sciences grant no. 8021-00310B.

References

- [1] J. S. Bach and H. Bruus 2018 J. Acoust. Soc. Am. **144**, 766-984 (2018). [pdf]
- [2] N.R. Skov et al. AIMS Mathematics, **4**, 99-111 (2019). [pdf]
- [3] P.B. Muller and H. Bruus Phys. Rev. E, **90**, 043016 (2014). [pdf]
- [4] J.T. Karlsen, Per Augustsson, and H. Bruus Phys. Rev. Lett. **117**, 114504 (2016). [pdf]
- [5] J.T. Karlsen and H. Bruus Phys. Rev. E, **92**, 043010 (2015). [pdf]
- [6] M. Antfolk et al. Lab Chip **14**, 2791-2799 (2014) [pdf]

Theory of Acoustic Streaming and Acoustic Radiation Force of a Solid Particle in a Viscoelastic Fluid

Jonas Fankhauser¹, Alexander A. Doinikov¹, and Jürg Dual¹

¹Department of Mechanical and Process Engineering, Institute for Mechanical Systems, ETH Zürich, Zürich, Switzerland

E-mail: fankhauser@imes.mavt.ethz.ch, URL: <https://expdyn.ethz.ch>

Introduction

A classical problem in acoustophoresis involves the scattering of an acoustical wave by a spherical particle or droplet. Many solutions to this problem exist covering a wide range of the material models of the fluid and the particle, and are valid in different physical limits. To the best of our knowledge, all of these solutions assume either an inviscid fluid or a Newtonian fluid surrounding the particle. While these models are a good approximation for fluids commonly used in applications such as water or air, they fail to describe liquids with a component of long polymer chains that induce elasticity under shear strain, a noteworthy example being blood [1].

In this context, we have developed a theoretical model for a spherical solid particle suspended in a viscoelastic fluid and we obtained analytical solutions for the first-order acoustic scattering fields, the second-order acoustic streaming fields, and the time-averaged acoustic radiation force.

Problem Statement

We solve analytically the problem of a spherical linear elastic particle suspended in a viscoelastic fluid undergoing shape oscillations of all orders due to an incident axisymmetric wave. The behaviour of the fluid is described by the compressible Oldroyd-B model. The model's linear momentum equation is given by [2]

$$\rho \left(\frac{\partial \mathbf{v}}{\partial t} + \mathbf{v} \cdot \nabla \mathbf{v} \right) = -\nabla p + \eta_f \left[\nabla \mathbf{v} + (\nabla \mathbf{v})^T - \frac{2}{3}(\nabla \cdot \mathbf{v})\mathbf{I} \right] + \zeta_f(\nabla \cdot \mathbf{v}) + \boldsymbol{\tau}$$

where $\boldsymbol{\tau}$ is the stress tensor related to the viscoelastic part of the fluid, given implicitly as

$$\boldsymbol{\tau} + \lambda_M \left[\frac{\partial \boldsymbol{\tau}}{\partial t} + \mathbf{v} \cdot \nabla \boldsymbol{\tau} - \boldsymbol{\tau} \cdot \nabla \mathbf{v} - (\nabla \mathbf{v})^T \cdot \boldsymbol{\tau} \right] = \eta_p \left[\nabla \mathbf{v} + (\nabla \mathbf{v})^T - \frac{2}{3}(\nabla \cdot \mathbf{v})\mathbf{I} \right] + \zeta_p(\nabla \cdot \mathbf{v})\mathbf{I}$$

and η_f , ζ_f , η_p , and ζ_p are the shear and bulk viscosities of the fluid and the polymer component respectively, and λ_M is the Maxwell relaxation time.

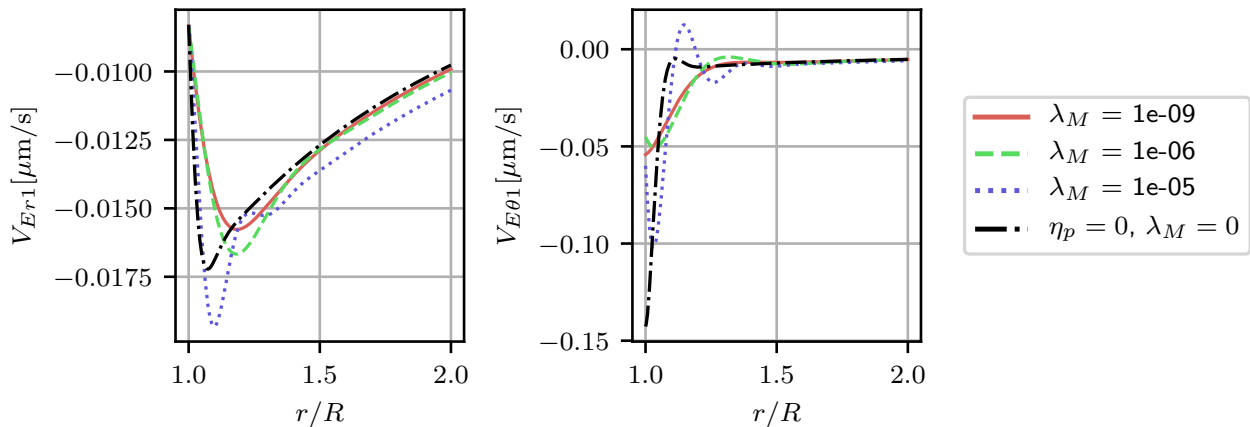


Figure 1: Parameter sweep of the relaxation time for the Eulerian streaming velocity coefficient of the first mode in radial and tangential direction. The parameters are $\rho_0 = 1000 \text{ kg/m}^3$, $c = 1500 \text{ m/s}$, $\eta_f = 0.001 \text{ Pas}$, $\eta_p = 0.009 \text{ Pas}$, $\zeta_f = 0$, $\zeta_p = 0$, $f = 100 \text{ kHz}$, $p = 1 \text{ bar}$, $R = 50 \text{ μm}$.

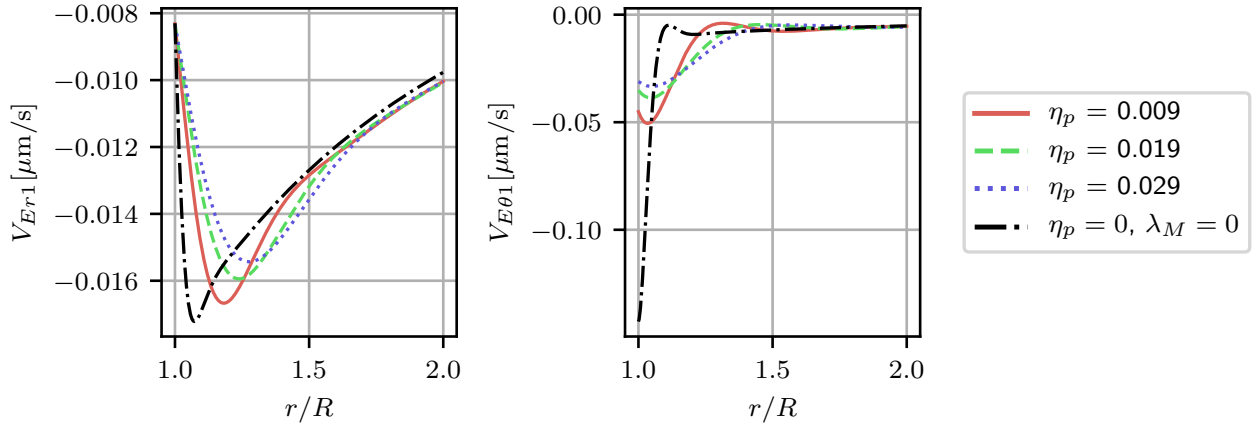


Figure 2: Parameter sweep of the shear viscosity of the polymer component for the Eulerian streaming velocity coefficient of the first mode in radial and tangential direction. The parameters are the same as above and the relaxation time is $\lambda_M = 1 \mu\text{s}$.

The problem is tackled by applying the methods of perturbation theory. Our resulting model imposes no restriction on the particle diameter, the wavelength, or the viscous boundary layer thickness, and is exact up to second order.

The Oldroyd-B model introduces additional fluid parameters and, therefore, new dimensionless ratios that define regimes of certain physical behaviour, most notably the ratio of the excitation period and the Maxwell relaxation time λ_M . Other effects related to the time period of the incident fields are frequency dependencies of both total shear and total bulk viscosity of the fluid

$$\eta_c = \eta_f + \frac{\eta_p}{1 - i\omega\lambda_M}, \quad \zeta_c = \zeta_f + \frac{\zeta_p}{1 - i\omega\lambda_M}$$

for the first-order acoustic problem.

Acoustic Streaming in a Viscoelastic Fluid

The effect of nonlinear, time-averaged flows, induced by a harmonic excitation is called acoustic streaming. We compute the acoustic streaming fields from the derived theory in two independently developed computer programs implemented in Wolfram Mathematica and Python. Figure 1 shows the effect of decreasing relaxation time of the fluid for a constant frequency of the incident plane travelling wave. As the relaxation time approaches the excitation period, we observe not only a significant change of the streaming velocity amplitudes but also a change of sign of the tangential coefficients in certain regions.

Displayed in Fig. 2 are the same coefficients, now swept across a range of shear viscosity of the polymer part of the fluid.

Acoustic Radiation Force in a Viscoelastic Fluid

We report a significant increase in acoustic radiation force due to viscoelastic effects. Our simulations suggest, for a $50 \mu\text{m}$ polystyrene particle, the addition of polyethylene glycol (PEG, $\eta_p = 0.009 \text{ Pas}$, $\lambda_M = 1 \mu\text{s}$) to water will increase the radiation force by over an order of magnitude. This has implications for experimental work, where PEG is commonly used.

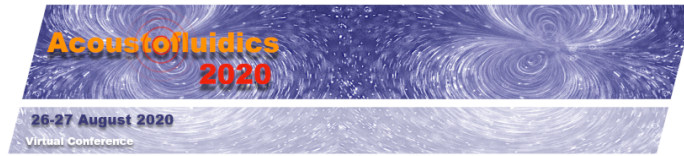
The effects for other fluids often encountered in biomedical applications are currently under investigation.

Conclusion

We have developed a theoretical model of the nonlinear dynamics of a solid particle in an acoustically excited viscoelastic fluid and showed the importance of viscoelastic effects. A Python framework shall be provided to conveniently compute the resulting streaming fields and the acoustic radiation force for any viscoelastic fluid.

References

- [1] Chmiel, H., I. Anadere, and E. Walitza. "The determination of blood viscoelasticity in clinical hemorheology." *Biorheology* 27.6 (1990): 883-894.
- [2] A. Morozov and S. E. Spagnolie, *Introduction to Complex Fluids, in Complex Fluids in Biological Systems*. (Springer, New York, 2015), pp. 3-52.



Microstreaming induced by an acoustically excited gas bubble – experiments and comparison to theory

Sarah Cleve^{1,*}, Gabriel Regnault¹, Alexander A. Doinikov¹, Cyril Mauger¹, Philippe Blanc-Benon¹, Claude Insera²

¹Univ Lyon, École Centrale de Lyon, INSA de Lyon, CNRS, LMFA UMR 5509, F-69134 Écully CEDEX, Lyon, FRANCE

²Univ Lyon, Université Lyon 1, INSERM, LabTAU, F-69003, LYON, France, Lyon, FRANCE

*now at: Physics of Fluids group, MESA+ Institute for Nanotechnology and Technical Medical (TechMed) Center, University of Twente, P.O. Box 217, 7500 AE, Enschede, THE NETHERLANDS
E-mail: s.cleve@utwente.nl

Introduction

Microbubbles are used in a large number of medical ultrasound applications. If these acoustically excited bubbles oscillate nonspherically or translationally, they are known to induce a relatively slow steady flow in the vicinity of the bubble. This flow, called microstreaming, goes along with shear stresses which can be exploited in medical treatment, e.g. by so-called sonoporation [1]. The detailed mechanisms of such treatments are however not yet fully understood. Our study therefore aims to provide a fundamental understanding on the exact nature of microstreaming induced by acoustically excited, nonspherically oscillating microbubbles. Experimentally, we show a large variety of streaming patterns which depend mainly on the dominant mode of oscillations, but also on more subtle details in the bubble dynamics [2]. Theoretically, a newly developed theory confirms the variety of patterns and succeeds in a so far qualitative comparison to the experiments.

Methods

For the experiments, gas bubbles are created by short, focused laser pulses (Nd:YAG pulsed laser, $\lambda = 532$ nm). The bubbles under consideration range between $40 \mu\text{m}$ and $80 \mu\text{m}$ in radius and are trapped in a cubic water tank (width 8 cm) in an acoustic standing field. The driving frequency of the transducer is fixed to 31.25 kHz and the acoustic pressure at the bubble position is varied between 5 kPa and 25 kPa. Through variation of the bubble size and of the acoustic pressure the nature of the bubble oscillations can be controlled: they will either show pure radial oscillations or exhibit surface oscillations [3], in our case the modes 2, 3 or 4. The bubble dynamics is captured with backlighting and a high speed camera (Phantom V12.1) at 180 kfps. In order to visualize the microstreaming flow around the bubble, fluorescent tracer particles (ThermoFisher, $0.71 \mu\text{m}$ diameter) are added to water and illuminated by a thin laser sheet. The acquisition rate for the microstreaming is 600 Hz.

The theoretical model [4] for the microstreaming induced by a nonspherically oscillating bubble assumes the bubble dynamics (bubble size, complex modal amplitudes, oscillating frequency) to be known and takes these as input parameters. No restrictions are imposed on the ratio of the bubble radius to the viscous penetration depth, that means no restrictions on the bubble size and on the fluid viscosity. According to the model, microstreaming is generated due to the interaction of two nonspherical modes, n and m , oscillating at the same frequency. The general set of equations has been derived and then applied to specific cases: the interaction of the radial mode 0 with an arbitrary surface mode (case $n - 0$), the interaction of the translational mode 1 with an arbitrary surface mode (case $n - 1$), the self-interacting mode n (case $n - n$) and the interaction of two arbitrary modes n and m (case $n - m$, with $n > m \geq 2$). All cases together cover the full range of possible interactions.

Results

The dynamics of the bubble surface is axisymmetric and can be expressed as a sum of different zonal modes. Mathematically, this means in spherical coordinates (r, θ, φ) that the bubble contour r_s can be decomposed over a sum of Legendre Polynomials P_n :

$$r_s = R_0 + \sum_{n=0}^{\infty} a_n e^{-i2\pi f_n t} P_n(\cos \theta),$$

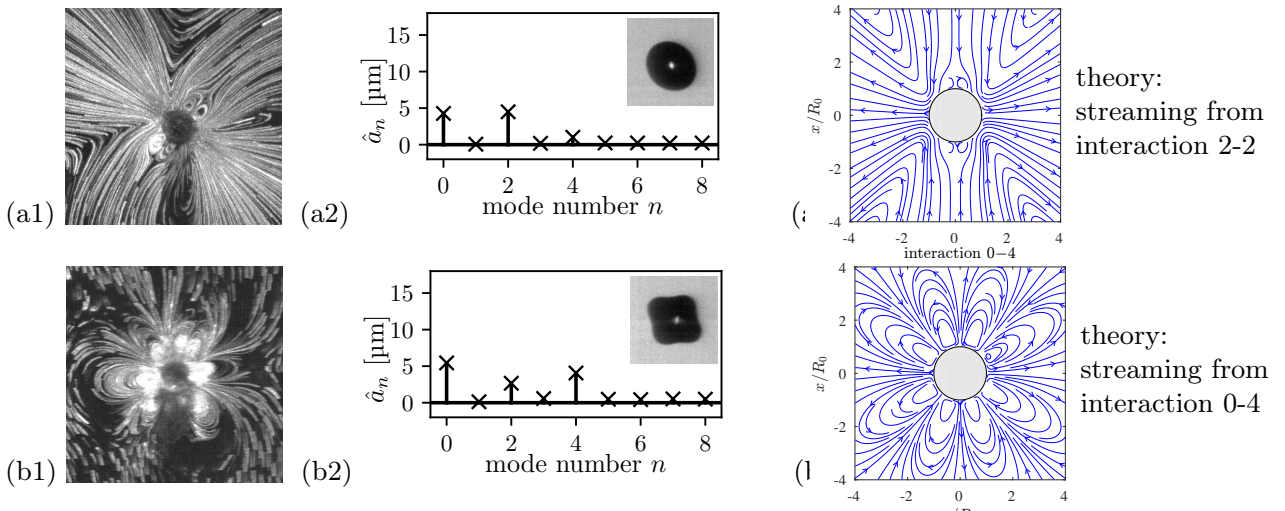


Figure 1: Two example streaming patterns (a1,b1) together with the corresponding bubble dynamics (absolute value of modal amplitudes \hat{a}_n) (a2,b2) and a theoretical result giving the same type of pattern (a3,b3). The respective experimental acoustic pressures and bubble radii at rest are (a) $p_a = 34.5$ kPa and $R_0 = 49.7$ μm , and (b) $p_a = 17.9$ kPa and $R_0 = 56.5$ μm .

where a_n are the complex modal amplitudes of the mode n oscillating at the frequency f_n and R_0 is the radius at rest of the bubble. Practically, we can reduce the infinite sum to a few relevant modes. In Fig. 1 (a2) for instance, only the radial mode 0 and the mode 2 appear in the bubble dynamics. The corresponding, experimentally observed streaming pattern is shown in Fig. 1 (a2). It shows a cross-like shape with two small pairs of recirculation zones close to the bubble. As the two modes 0 and 2 are oscillating at different frequencies (due to parametric excitation of the mode 2), we do not expect a streaming pattern due to the interaction of the two modes. Furthermore, the mode 0 alone does not lead to microstreaming. Consequently, the only interaction expected to lead to streaming is the self-interacting mode 2. Indeed, we obtain the same type of pattern when considering the self-interacting mode 2 in the theoretical model, see Fig. 1 (a3). A second example is shown in Fig. 1 (b). Here, the bubble dynamics reveals components of the modes 0, 2 and 4. Consequently, a several interactions will contribute to the total streaming pattern. A first qualitative comparison to theory suggests however that the dominant interaction is the interaction between the modes 0 and 4, which leads to the pattern of eight lobes around the bubble.

Conclusion

We have experimentally shown a large variety of streaming patterns linked to the bubble dynamics of nonspherically oscillating microbubbles. These patterns are due to nonlinear effects, which can be described by an analytical model. The qualitative comparison between experiments and theory reveal very satisfying results, a more quantitative evaluation including the effect of several simultaneous interactions is under way.

Acknowledgement

This work was supported by the LABEX CeLyA (ANR-10-LABX-0060) of Université de Lyon, within the program “Investissements d’Avenir” (ANR-16-IDEX-0005) operated by the French National Research Agency (ANR). A.A.D. gratefully acknowledges the financial support from Institut National des Sciences Appliquées de Lyon (INSA de Lyon).

References

- [1] I. Lentacker, I. De Cock, R. Deckers, S. De Smedt and C. Moonen. *Advanced drug delivery reviews* **72**, 49-64 (2014).
- [2] S. Cleve, M. Guédra, C. Mauger, C. Inserra, P. Blanc-Benon. *Journal of fluid mechanics*, **875**, 597-621 (2018).
- [3] M. P. Brenner, D. Lohse and T. F. Dupont. *Physical Review Letters*, **75.5**, 954 (1995).
- [4] A.A. Doinikov, S. Cleve, G. Regnault, C. Mauger, C. Inserra. *Physical Review E*, **100(3)**, 033105 (2019); and **100(3)**, 033104 (2019); and **101(1)**, 013111 (2020).

Poly(N-isopropylacrylamide) Microgels as Soluble Markers for Visualization of Acoustic Energy Absorption in Aqueous Solutions

Amin Rahimzadeh, and Regine von Klitzing

Department of Physics, Technische Universität Darmstadt, 64289 Darmstadt, Germany
 E-mail: Rahimzadeh@fkp.tu-darmstadt.de

Introduction

During propagation of an acoustic wave in a liquid, it attenuates mainly due to the viscous effects and creates an internal flow, which is called streaming. The experimental methods for measurements of the acoustic energy absorption are classified in mechanical, optical and electrical approaches. The most common technique is the measurement of wave attenuation using the pulse-echo method[1]. Optical measurements have been developed based on Debye-Sears effect[2]. In this work, a novel method is presented to visualize the acoustic energy absorption in aqueous solutions experimentally. Poly(N-isopropylacrylamide) (PNIPAM) microgels are soluble in many liquids such as water. They respond to the temperature—above their volume phase transition temperature (VPTT) of 32 °C—by shrinking in the solvent due to the breakage of their hydrogen bonds[3]. Then, they become insoluble in the water; their optical density increases and can be visualized in the medium. In the present study, acoustic waves energy is used as a new source to break the hydrogen bonds while the solution temperature maintains below (VPTT). Therefore, by calculating the required amount of energy for breaking the hydrogen bonds in the solution, the acoustic energy absorption in the solution is visualized and quantified experimentally.

Experimental

Poly(N-Isopropylacrylamide) (PNIPAM) ($M_n \approx 40,000$) was purchased from Sigma-Aldrich, Germany, and was dissolved in Milli-Q water in two different concentrations of 0.2 wt.% and 1 wt.% and stirred over one night. A piezoceramic transducer (SOAR Tech., China) with 2.28 MHz resonance frequency was used to generate acoustic waves. The sinusoidal RF signal was generated via a function generator (TOE 7404, TOELLNER, Germany) and amplified by an RF amplifier (ENI AP400B 21121). 1 ml of a microgel solution was poured inside a PMMA cuvette ($12.5 \times 12.5 \times 45 \text{ mm}^3$) and attached to the transducer surface by two-component latex glue. Three input voltages of 7.2, 8, 10 V_{pp} with 2.28 MHz frequency are applied using the function generator. Schematic representation of the experiments is shown in Fig. 1.

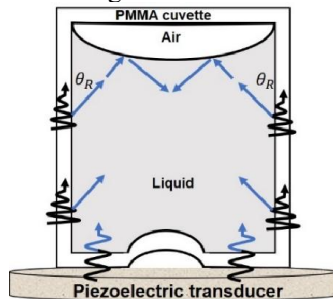


Figure 1: Schematic of the present experiment and acoustic wave propagation into the PNIPAM solution. The base of the PMMA cuvette has a bump that spaces the center of the cuvette out the piezoelectric surface. Acoustic waves propagate to liquid vertically from below and the walls similar to Rayleigh waves by θ_R . The wave beams partially reflect on the liquid-air interface and make a high-energy concentrated zone.

Results and discussion

The PNIPAM microgels were dissolved and distributed in the water homogeneously. The dissipation of wave energy provides the required energy for breaking the hydrogen bonds. In 1ml of each 1wt.% and 0.2 wt.% solutions, there is respectively 10 mg and 2 mg of PNIPAM microgels. According to the molecular mass of NIPAM monomer (113.16 g/mol), the approximate amount of NIPAM monomer in 1ml of 1wt.% and 0.2 wt.% solutions respectively is 10^{-4} and 0.2×10^{-4} mol inside the cuvette. In order to break the hydrogen bonds of NIPAM-water with thermal energy, one needs to provide about 5 kJ/mol of NIPAM in the water[4]. Hence, one should provide approximate energy of 0.5 and 0.1 J to break the whole hydrogen bonds inside 1 ml of 1wt.% and 0.2wt.% solutions, respectively. When the hydrogen bonds break, the microgels collapse and become insoluble in water. As a result, their optical density increases—the solution becomes turbid—and can be visualized by a regular camera. The more hydrogen bonds break, the higher turbidity arises until the whole medium becomes fully turbid. The acoustic energy absorption pattern (shown by turbidity) of 1 wt.% microgel solution is visualized sequentially for 2.28 MHz and 10 V_{pp} actuation in Figure 2. Continuous actuation of the solution accumulates the absorbed energy until the hydrogen bonds start to break, resulting in turbidity from the bottom corners (after around 15s). The turbidity further extends

to the medium due to more energy absorption and hydrogen bond breakage until the whole medium becomes turbid. In order to quantify the energy absorption by microgel solution, image processing by MATLAB is performed. The images were converted to grayscale, where a pixel can have a value between 0 and 255. The former belongs to the black color, and the latter corresponds to the complete white. Thus, in order to make a pixel completely white ($0.5/Total\ number\ of\ pixels$) J and ($0.1/Total\ number\ of\ pixels$) J energy is provided for 1wt.% and 0.2wt.%, respectively. By employing the equation (1), acoustic energy absorption during the actuation is quantified for both solution concentrations in different input voltages, shown in Fig. 3. Higher microgel concentration results in higher solution viscosity. Besides, absorption of acoustic wave energy depends on the liquid viscosity. That is why the 1wt.% solution becomes turbid much faster than 0.2wt.% solution despite its higher hydrogen bonds.

$$Power\ Absorption\ (W) = \frac{0.5\ or\ 0.1\ W}{Total\ number\ of\ pixels} \times \frac{sum\ of\ pixel\ values}{255} \quad (1)$$

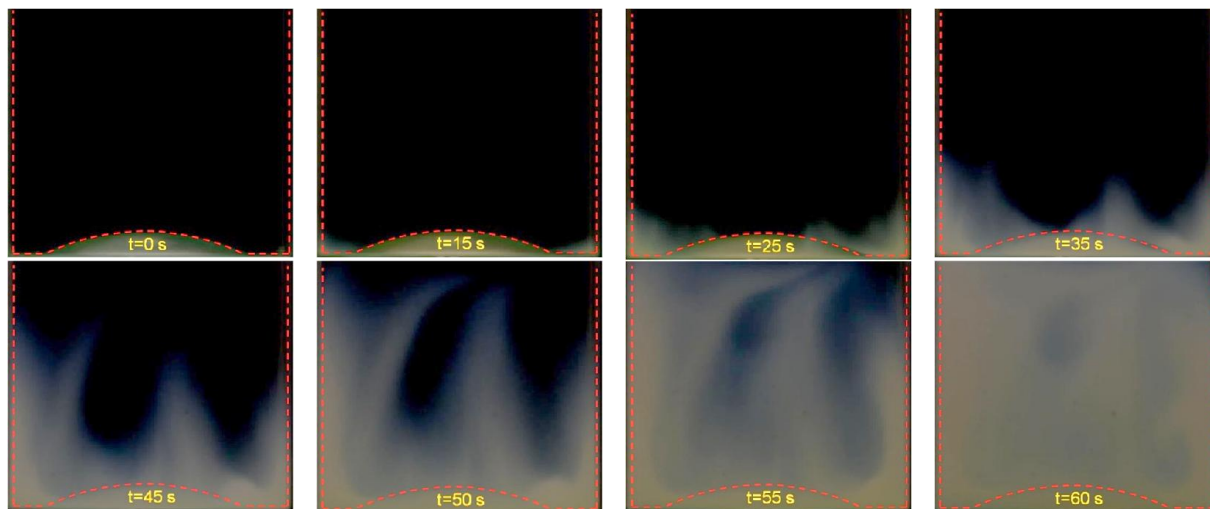


Figure 2: Acoustic wave energy absorption (turbidity) mechanism during ultrasonic (2.28 MHz, 10 V) actuation of 1 wt.% microgel solution.

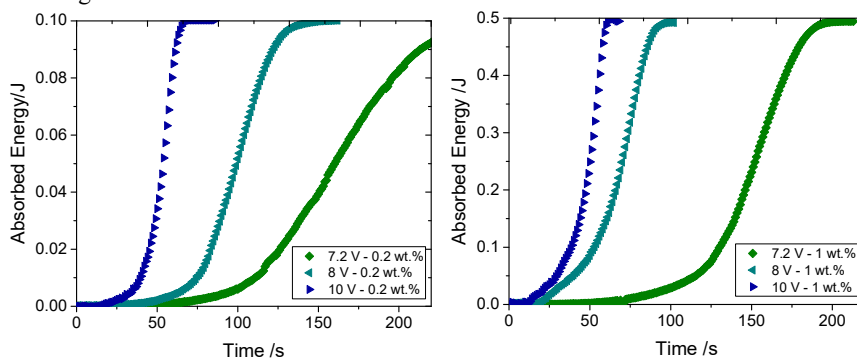


Figure 3: Acoustic energy absorption during ultrasonic actuation of (Left) 1 wt.% and (Right) 0.2 wt.% microgel aqueous solutions. Higher viscosity due to higher concentration results in faster energy absorption.

Conclusion

In this work, a novel method is introduced for measurement of ultrasonic energy absorption in aqueous solutions by using a water-soluble marker—that upon absorbing a certain amount of energy undergoes a volume phase transition. PNIPAM water-soluble microgels, as the markers, collapse and become insoluble in the medium when their hydrogen bonds break by the acoustic wave energy. As a result, their optical density increases, and can be distinguished and visually captured in the solvent. The absorption of the acoustic wave energy from the captured images is quantified by calculating the total energy required to break the hydrogen bonds. In addition, since the different microgel concentration results in solutions with different viscosity, effects of liquid viscosity on acoustic wave absorption is studied as well.

References

- [1] J.M.M. Pinkerton. Nature **160**(4056), 128-129 (1947).
- [2] P. Debye, F.W. Sears. National Academy of Sciences **18**(6), 409 (1932).
- [3] R. Pelton. Advances in Colloid and Interface Science **85**(1), 1-33 (2000).
- [4] L. Tavagnacco, E. Zaccarelli, E. Chiessi. Phys Chem Chem Phys **20**(15), 9997-10010 (2018).

Acoustic characterization of polydimethylsiloxane (PDMS) for microscale acoustofluidics

Guangyao Xu, Xiasheng Guo

Key Laboratory of Modern Acoustics (MOE), Department of Physics, Collaborative Innovation Center of Advanced Microstructure, Nanjing University, Nanjing 210093, China
 E-mail: guangyao931210@gmail.com

Introduction

Polydimethylsiloxane (PDMS) is a typical soft viscoelastic material widely used in acoustofluidics, with the advantages of being chemically inert, optically transparent, thermally stable, acoustically isotropic among other merits like low cost and easy to fabricate. However, due to its high attenuation, acoustic characterization of PDMS material is difficult, especially for its shear wave parameters. In this study, we proposed a systematic method to measure wave velocity and attenuation coefficient of both longitudinal (L) and shear (S) waves in PDMS. Measurements were carried out across the frequency band between 3.0-7.0 MHz in five sample groups, corresponding to different base-agent mixing ratios σ and curing temperatures T , $(\sigma, T) = (10:1, 85^\circ\text{C}), (7:1, 85^\circ\text{C}), (5:1, 85^\circ\text{C}), (10:1, 65^\circ\text{C}),$ and $(10:1, 100^\circ\text{C})$. The results are then compared to the existing data.[1-3]

Methods

The two different methods (method A and B) share the same experimental setup illustrated in Fig. 1(a). In Step I, the upper surface of fused silica (FS) is exposed to air, with each forth and back signal group assigned an index n , i.e., $P_0^{(n)}(t)$ and $P_{r1}^{(n)}(t)$ denoted the n th acoustic pulses going upward and downward, respectively, with $n = 1, 2, 3, \dots$. In Step II, a PDMS sample attached to S1 lowered the amplitude of $P_{r1}^{(n)}(t)$ pulses, which were renamed as $P_{r2}^{(n)}(t)$. For each $P_0^{(n)}(t)$ travelling upwards from the bottom S0, the pulse can also go a round-trip between S0 and S2 (across the FS and PDMS), and those were recorded as $P_{r3}^{(n)}(t)$ at the transducer. The detailed wave transmission paths are illustrated in Fig. 1(b), in which only the pulses drawn in solid lines can be detected by the transducers.

With Method A, the S wave parameters were obtained by comparing the complex wave reflection coefficient at a solid surface before and after PDMS samples were attached, which is denoted as R_I and R_{II} , respectively. Obviously, the reflection coefficients are functions of the frequency f because of

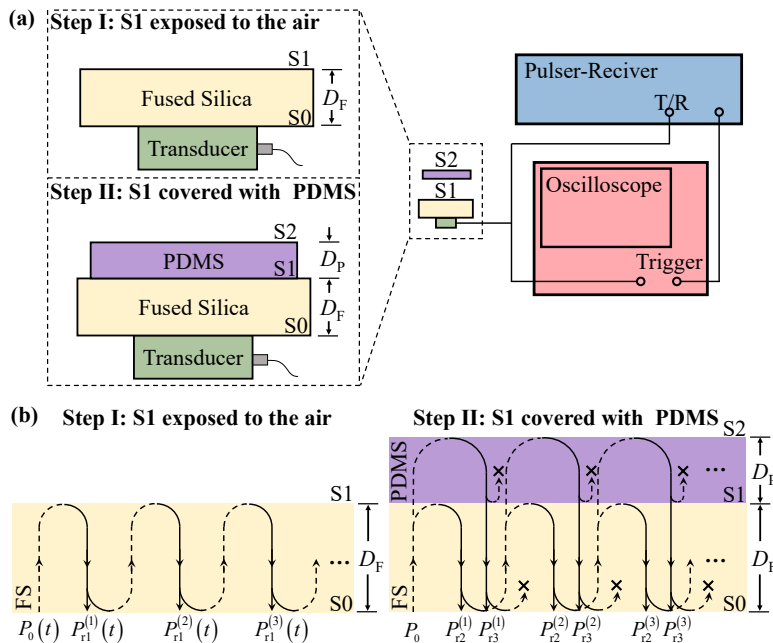


Figure 1: (a) The experimental setup shared by both measurement methods (A and B), The transducer was in contact with a FS disc, coupled through the couplant. Pulse signals generated by a pulser-receiver were used to excite a transducer (5.0 MHz central frequency) to excite L (or S) waves. Waves reflected back to the transducer were recorded before and after each sample was attached to S1 (the upper surface of FS). (b) Illustrations of the wave paths in the fused silica disk (FS, yellow) and the PDMS sample (PDMS, purple). All other pulses following more complicated paths are marked with crosses, and were discarded in signal processing.

the dispersion in PDMS. Considering the continuity conditions across S1, the wave velocity c_P (P=L or S for longitudinal or shear waves) and attenuation coefficient α_P are,[2]

$$c_P(f) = \frac{4\pi f A}{-B + \sqrt{B^2 - 4AC}}, \quad \alpha_P(f) = 2\pi f \sqrt{-\frac{1}{c_P^2} + \frac{2\rho_P}{\rho_F c_F c_P} \left(\frac{1 + R_{II}^* R_{II}}{1 - R_{II}^* R_{II}} \right) - \frac{\rho_P^2}{\rho_F^2 c_F^2}}, \quad (1)$$

where * denotes the complex conjugate, c_F and ρ_F are the wave velocity and density in FS, and

$$A = 1 + \left(\frac{1 + R_{II}^* R_{II}}{1 - R_{II}^* R_{II}} \right)^2 \tan^2 \phi_r, \quad B = -\frac{4\pi \rho_P f}{\rho_F c_F} \left(\frac{1 + R_{II}^* R_{II}}{1 - R_{II}^* R_{II}} \right) (1 + \tan^2 \phi_r), \quad C = \left(\frac{2\pi \rho_P f}{\rho_F c_F} \right)^2 (1 + \tan^2 \phi_r). \quad (2)$$

Hence, by calculating $R_{II}(f)$ through the measured pulse signals, $c_P(f)$ and $\alpha_P(f)$ can be determined. The L wave parameters were obtained using Method B, by interrogating wave transmissions in double-layered solid PDMS structures. The wave velocity and attenuation coefficient in PDMS, $c_P(f)$ and $\alpha_P(f)$ are then obtained from the phase difference between $P_{r2}(t)$ and $P_{r3}(t)$, written as

$$c_P(f) = \frac{-4\pi f D_P}{\phi_{r3}(f) - \phi_{r2}(f)}, \quad \alpha_P(f) = \frac{-1}{2D_P} \ln \left[\frac{-R_{FP} A_{r3}(f)}{T_{FP} T_{PF} A_{r2}(f)} \right]. \quad (3)$$

where R_{FP} and T_{FP} are the reflection and transmission coefficients from FS to PDMS, respectively, T_{PF} is the transmission coefficient from PDMS back to FS.

Results

The L and S wave results are shown in Fig. 2. The longitudinal wave velocity obtained here (1028.3-1030.6 m/s) is a bit lower than that reported by Tsou et al. (~ 1076.5 - 1119.1 m/s)[1] and Folds for RTV 615 (1083 m/s).[3] Meanwhile the shear wave velocity of SylgardTM 184 in the current measurements (109.0-124.3 m/s) is higher than that of RTV 615 reported by Madsen et al. (75-95 m/s).[2] The measured damping of longitudinal waves in SylgardTM 184 agree well with that reported by Tsou et al.,[1] but the shear wave attenuation coefficient show lower than that in RTV 615.[2]

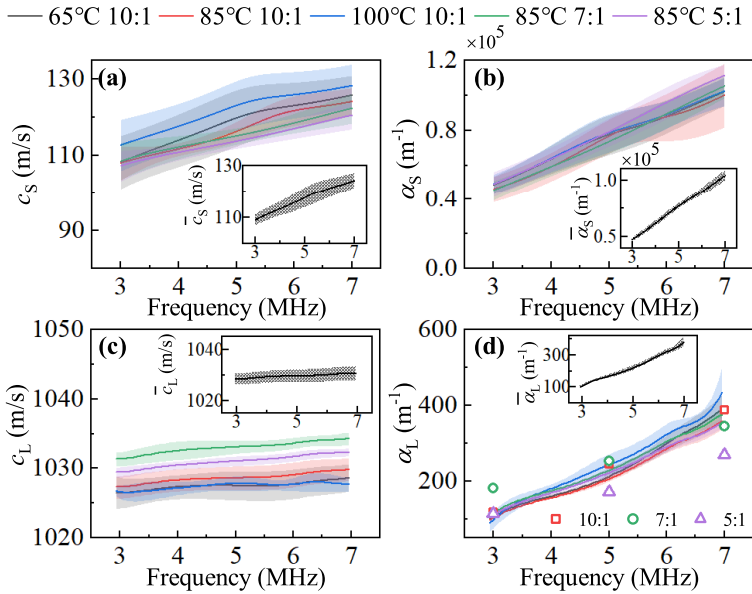


Figure 2: Measured wave velocities and attenuation coefficients in the five sample groups. (a)-(b) c_S and α_S measured through Method A. (c)-(d) c_L and α_L measured through Method B. The scattered markers in (d) are the results reported by Tsou *et al.*,[1] and the insets in each figure represent corresponding averaged data over all five groups.

Conclusion

This work reports a systematic study of the acoustic parameters of SylgardTM 184 PDMS, where the phase velocities and the attenuation coefficients of the longitudinal and shear waves are obtained from the same groups of samples. For the five sample groups studied here, corresponding to five different sample preparation protocols, intergroup deviations are found to be insignificant, especially regarding the damping of both longitudinal and shear waves. *Acoustofluidics 2020 Virtual Conference on 26 - 27 August 2020.*

References

- [1] J. K. Tsou, J. Liu, A. I. Barakat, and M. F. Insana. *Ultrasound Med. Biol.* **34**, 963 (2008).
- [2] E. L. Madsen, H. J. Sathoff, and J. A. Zagzebski. *J. Acoust. Soc. Am.* **74**, 1346 (1983).
- [3] D. Folds. *J. Acoust. Soc. Am.* **56**, 1295 (1974).

A numerical study of the coupling layer between a piezoelectric bulk transducer and a glass device

William N. Bodé and Henrik Bruus

Department of Physics, Technical University of Denmark, Kongens Lyngby, Denmark
 E-mail: winabo@dtu.dk , URL: <http://www.fysik.dtu.dk/microfluidics>

Introduction

In acoustofluidic devices driven by bulk piezoelectric transducers, the coupling layer between the transducer and the microfluidic chip is important, but remains poorly understood beyond 1D planar resonator models [1]. Here, we present numerical simulations of a PZT transducer coupled to a glass chip through a thin coupling layer consisting of either a solid glue or a viscous fluid.

Microfluidic system and numerical model

As our model system, we consider the capillary trapping device sketched in Fig. 1(a). The system was studied experimentally in Ref. [2] and theoretically in Ref. [3]. In the latter, the transducer and coupling layer was merely represented by an effective boundary condition, and to gain an insight in the physics of the coupling layer, we here extend the model of Ref. [3] by including the transducer and the coupling layer explicitly. For simplicity, we assume translation invariance along the channel axis x , and restrict our model to the vertical y - z cross-section at $x = 0$ as sketched in Fig. 1(b).

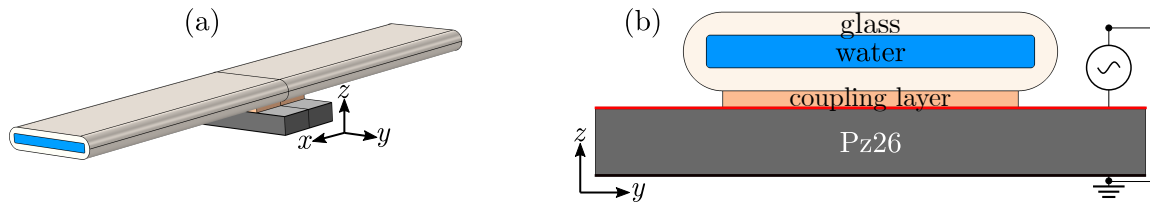


Figure 1: (a) 3D sketch of the acoustic trapping device with a long MEMpax glass capillary tube (beige) mounted on a PZT transducer (gray). (b) The modeled vertical 2D cross-section. The materials of each part are shown together with the grounded (black) and charged (red) electrode of the Pz26 transducer.

The model is implemented in the FEM-software COMSOL Multiphysics 5.4, using the weak-form-PDE method described in Refs. [4, 5]. In the model we include the following continuum fields: The electric potential scalar field $\varphi(\mathbf{r}, t)$ confined to the piezoelectric domain (Pz26), the displacement vector field $\mathbf{u}(\mathbf{r}, t)$ in the elastic-solid and piezoelectric domains, and the acoustic pressure scalar field $p_1(\mathbf{r}, t)$ in the fluid domains. Note that the coupling layer is either a solid or a fluid.

Coupling layer material and thickness

Traditionally, the coupling layer is either a viscous fluid (in Ref. [2] glycerol) to be able to separate and reuse the transducer and the chip, or a solid glue (in Ref. [5] superglue) for permanent and stable contact. We therefore investigate various types of coupling layers. We compute the resonance frequencies of the coupled system in the frequency interval from 3.37 to 4.49 MHz as a function of the coupling layer thickness Δ increasing from 1 to 100 μm for three different materials: MEMpax glass, ED-20 epoxy resin, and 99 vol.% glycerol and 1 vol.% water.

To illustrate the effect of introducing a coupling layer, we study the specific resonance $f_{\text{res}}^{(0)} = 3.756$ MHz that exists without a coupling layer. In Fig. 2 we track the development of $f_{\text{res}}^{(0)}$ into the resonance $f_{\text{res}}^{(\Delta)}$ as a coupling layer of thickness Δ is introduced, and Δ is increased from 0.5 to 100 μm (blue rims). In Fig. 2(a) the coupling layer material is the same glass as the capillary tube, implying zero acoustic contrast between the two. In this case, $f_{\text{res}}^{(\Delta)}$ persists even when Δ is increased to 100 μm . A similar plot is shown in Fig. 2(b), but now using solid epoxy as the coupling layer. Here, the acoustic contrast between the capillary, the coupling layer, and the Pz26 is large, and $f_{\text{res}}^{(\Delta)}$ dies out already at a epoxy-layer thickness of 12 μm , whereas new resonances f_{res} appear. Similarly, in Fig. 2(c), with fluid glycerol as the coupling layer. Now, $f_{\text{res}}^{(\Delta)}$ dies out already for $\Delta \approx 2$ μm .

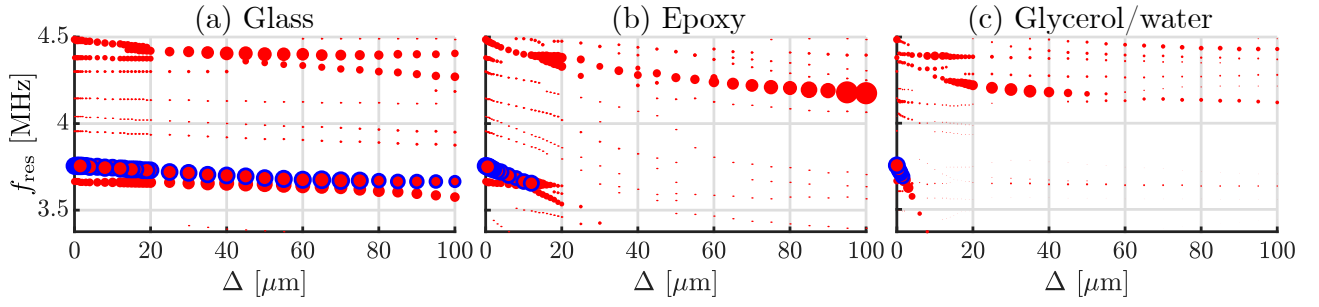


Figure 2: Resonance frequencies f_{res} (red dots) as a function of increasing coupling layer thickness Δ for three different coupling materials: (a) MEMpax glass, (b) ED-20 epoxy resin, (c) 99%-1% glycerol-water mixture. The development of the particular resonance $f_{\text{res}}^{(0)}$ into $f_{\text{res}}^{(\Delta)}$ is tracked as Δ increases (blue rims). The area of each point is proportional to the acoustic energy density E_{ac} .

The explanation of this striking effect may be sought in the speed c_{tr} of transverse sound waves in the materials, as this parameter constitutes the distinct material difference between them: MEMpax glass has $c_{\text{tr}}^{\text{glass}} = 3468$ m/s, ED-20 epoxy resin has $c_{\text{tr}}^{\text{epoxy}} = 1340$ m/s, while liquid glycerol cannot sustain a transverse wave and has $c_{\text{tr}}^{\text{glyc}} = 0$ m/s. To illustrate how the resonances depend on both the thickness Δ of the coupling layer and its transverse speed of sound c_{tr} , we define an artificial material "alpha-glass" with material parameters equal to glass apart from its transverse speed of sound being a factor α times that of the glass, $c_{\text{tr}}^{(\alpha)} = \alpha c_{\text{tr}}^{\text{glass}}$. For alpha-glass, the dependence of the resonance $f_{\text{res}}^{(\Delta)}$ on the coupling layer thickness Δ and the transverse sound speed $c_{\text{tr}}^{(\alpha)}$ is shown in Fig. 3.

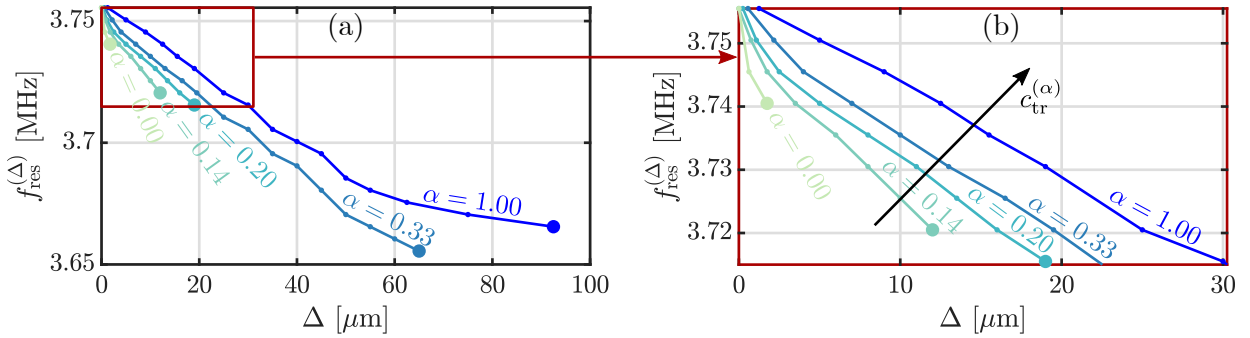


Figure 3: (a) $f_{\text{res}}^{(\Delta)}$ in α -glass as a function of coupling layer thickness Δ for $\alpha = 0.00, 0.14, 0.20, 0.33,$ and 1.00 , while keeping the other material parameters fixed. (b). A zoom-in on the thinnest layers.

Conclusion and outlook

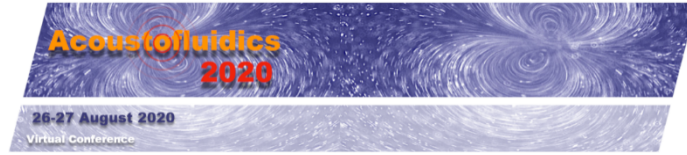
As a first step toward better understanding of the coupling layer, we have investigated three different coupling layer materials. We computed the development of the specific resonance frequency $f_{\text{res}}^{(0)}$ into $f_{\text{res}}^{(\Delta)}$ as a function of coupling layer thickness Δ . $f_{\text{res}}^{(\Delta)}$ is strongly dependent on Δ and the acoustic contrast of the coupling material. For the specific resonance, this effect can be attributed to the difference in transverse sound speed and not only the acoustic impedance. Other resonances having a more longitudinal-like character will be less sensitive, and probably more robust and thus useful in acoustofluidic applications. Despite its small volume fraction of the entire acoustofluidic device, the coupling layer plays a crucial role in the transmission of ultrasound waves from the PZT transducer to the microfluidic channel. A better understanding of this coupling layer is our next step in the development of more complete numerical models of acoustofluidic devices.

Acknowledgement

This work was supported by Independent Research Fund Denmark, Technology and Production Sciences, grant no. 8022-00285B.

References

- [1] P. Glynn-Jones, R.J. Boltryk and M. Hill. Lab on a Chip, **12**, 1417 (2012). [doi]
- [2] B. Hammarström, T. Laurell, and J. Nilsson. Lab on a Chip, **12**, 4296 (2012). [doi]
- [3] M. W. H. Ley and Bruus. Physical Review Applied, **8**, 024020 (2017). [pdf]
- [4] N. R. Skov, J. S. Bach, B. G. Winckelmann, and H Bruus. AIMS Mathematics, **4**, 99 (2019). [pdf]
- [5] W. N. Bodé, L. Jiang, T. Laurell, and H. Bruus. Micromachines, **11**, 292 (2020). [pdf]



Algebraic radiation force expansions beyond King, Yosioka and Kawasima, and Gor'kov, and related investigations of shape dynamics

Philip L. Marston¹

¹Physics and Astronomy Dept., Washington State University, Pullman, Washington, 99164-2814, USA
E-mail: marston@wsu.edu, URL: <https://physics.wsu.edu>

Introduction

King's leading-order expansion of acoustic radiation forces on rigid spheres in dissipation-free situations in 1934 was extended by others to compressible spheres for other situations of interest by 1962. In some more complicated situations, other algebraic results using wave-field properties are also helpful [1,2]. The present discussion emphasizes standing-wave situations where algebraic next-order terms going beyond Rayleigh scattering have been derived for spheres of interest [3-5]. Related early investigations of the shape of trapped drops and bubbles and temporally modulated radiation pressure are also placed in a recent context [6].

Dimensionless plane-standing-wave radiation force function Y_S

It has long been realized that for spheres in an ideal acoustic standing wave the radiation force depends on the wavelength $2\pi/k$, the sphere's radius a , the properties of the sphere and fluid, the peak-standing-wave magnitude P_S , and the position of sphere relative to the pressure nodes and antinodes. The position dependence of the force can be factored simply with a $|P_S|^2$ proportionality. For decades it has been useful to introduce a dimensionless radiation-force function factor Y_S that depends on the dimensionless frequency ka and the sphere and fluid properties [7,8]. Most early force discussions applied only when $ka \ll 1$ and predicted that in such situations Y_S is proportional to ka . Those expressions involved only Rayleigh scattering. To go beyond that approximation usually requires expressions involving spherical Bessel functions which complicates the construction of simple algebraic expressions for terms that are higher order in ka . This paper discusses a practical approach to such expansions for spheres of increasing size.

Next order term: Improved low-frequency plane-standing-wave radiation force function Y_{SLFC}

The starting point was find expressions for traveling and standing wave radiation forces using known scattering phase shifts δ_n for the n th order partial-wave associated with scattering of plane-waves by the sphere in the fluid of interest [8,9]. Expanding the δ_n in powers of ka [8] gives the factorization [3-5]:

$$Y_{SLFC}(ka) = Y_{SLF}(ka)[1 - (ka/x_0)^2], \quad (1)$$

where Y_{SLF} is the usual low-frequency expansion proportional to ka and x_0 is a constant that depends on the properties of the sphere and of the surrounding fluid. (By assuming that $Y_S = Y_{SLF}$, Y_S becomes linear in ka , and equilibrium locations in a vertical standing wave in gravity become independent of size for small spheres.) Notice that to the indicated order of expansion in (1), when $ka = x_0$, Y_{SLFC} vanishes and if ka increases through x_0 , there is a corresponding reversal of sign. Expressions for Y_{SLF} and x_0 are now known for several cases of interest including: fluid spheres, solid elastic spheres, and empty elastic shells [3-5]; x_0 depends on the monopole, dipole, and quadrupole scattering by the sphere. These results are confirmed by comparison of Y_{SLFC} with exact series expansions for Y_S in the ideal dissipation-free case [3-5]. In related work expansions for δ_n were also used to derive low-frequency expansions of the progressive wave dimensionless radiation force function Y_P and certain properties of backscattering [5,10].

Expansion of Bessel-standing-wave radiation force function Y_S

Consider now a Bessel standing wave where in cylindrical coordinates the standing-wave acoustic pressure p also depends on the radial coordinate R as well as on the axial coordinate z [8]:

$$p(z,R,t) = P_S \cos(\alpha kz) J_0(\mu R) \cos\omega t, \quad (2)$$

where J_0 is a Bessel function and $\mu = \sin\beta$ and $\alpha = \cos\beta$, where β is sometimes known as the conic angle wave-field parameter. The author has repeated the derivation of Eq. (1) for this case with the result that again Y_{SLF} is proportional to ka but now (along with material parameters and shell thickness) Y_{SLF} and x_0 also depend on β . Figure 1 shows an example for a solid shell and a comparison with the full spherical-Bessel-function-based series. Axisymmetric Bessel travelling waves are also of interest. They give a basis for expressing wave-fields of converging beams [11] and have special radiation force properties [1,2,5,8-10].

Equilibrium and dynamic shape of drops and bubbles in steady and modulated acoustic wave-fields

Low-frequency expansions of the interaction of sound with spheres are also useful in evaluating quadrupole (and higher-order) projections of radiation stresses on spheres [6,12,13]. Such projections are useful for approximating the equilibrium shape of acoustically trapped liquid drops and bubbles. The equilibrium shape is the result of a balancing between radiation stresses and surface stresses associated with surface tension [12-14]. The expansion in [14] (based also on [12] and [15]) applies to both drops and bubbles for many situations of interest and has good experimental support for nearly spherical objects with small ka . The shape of levitated drops is important in light scattering measurements [16,17]. Closely related is the analysis of the response of drops, bubbles, and liquid bridges to modulated acoustic radiation pressure [12,18-24].

Conclusions

Algebraic low-frequency radiation-force expansions beyond the ordinary ones, those based primarily on Rayleigh scattering [25-27], have been derived for various types of spheres in ideal fluids; see Eq. (1). These approximations are confirmed by comparison with the full spherical Bessel-function-based series expansions [3-5,10]. In a gravitational field the trapping position becomes size dependent. Related aspects of radiation stress projections affecting the shape and dynamics of drops and bubbles in acoustic wave-fields are noted.

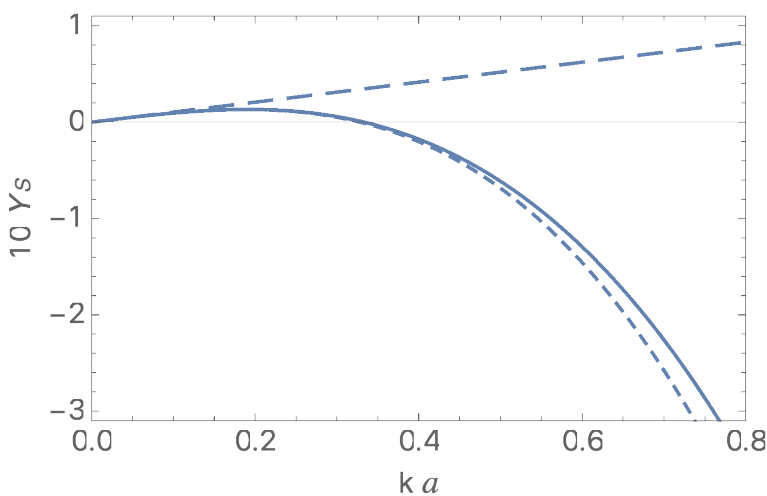
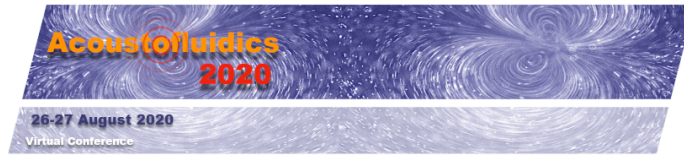


Figure 1: Computations of $10 Y_S$ are compared for an empty fused silica shell in water (where Y_S is the dimensionless standing-wave axial radiation force function) for an Eq. (2) wave-field with $\beta = 15^\circ$. Rayleigh scattering gives the line with long dashes, Y_{SLF} . The solid curve is the full series expansion using spherical Bessel functions, Eq. (17) of [8], while the curve with short dashes is Y_{SLFC} from Eq. (1) and algebraic expressions (depending material properties and on β) giving x_0 and Y_{SLF} . This comparison shows the utility of Y_{SLFC} in Eq. (1), the algebraic result.

References

- [1] P. L. Marston. *J. Acoust. Soc. Am.* **120**, 3518–3524 (2006).
- [2] M. A. Abdelaziz and D. G. Grier. *Phys. Rev. Research* **2**, 013172 (2020).
- [3] P. L. Marston. *J. Acoust. Soc. Am.* **142**, 1167–1170 (2017).
- [4] P. L. Marston. *J. Acoust. Soc. Am.* **142**, 3358–3361 (2017).
- [5] P. L. Marston. *J. Acoust. Soc. Am.* **146**, EL145–EL150 (2019).
- [6] P. L. Marston. *Phys. Rev. E* **100**, 057001 (2019).
- [7] T. Hasegawa, Y. Hino, A. Annou, H. Noda, M. Kato, and N. Inoue. *J. Acoust. Soc. Am.* **93**, 154–161 (1993).
- [8] P. L. Marston and L. Zhang. *J. Acoust. Soc. Am.* **141**, 3042–3049 (2017).
- [9] L. Zhang and P. L. Marston. *J. Acoust. Soc. Am.* **140**, EL178–EL183 (2016).
- [10] P. L. Marston. *J. Acoust. Soc. Am.* **145**, EL39–EL44 (2019).
- [11] T. D. Daniel, F. Gittes, I. P. Kirsteins, and P. L. Marston. *J. Acoust. Soc. Am.* **144**, 3076–3083 (2018).
- [12] P. L. Marston. *J. Acoust. Soc. Am.* **67**, 15–26 (1980).
- [13] P. L. Marston and D. B. Thiessen. *Annals of the New York Academy of Sciences* **1027**, 414–434 (2004).
- [14] T. J. Asaki and P. L. Marston. *J. Acoust. Soc. Am.* **97**, 2138–2143 (1995).
- [15] P. L. Marston, S. E. LoPorto-Arione, and G. L. Pullen. *J. Acoust. Soc. Am.* **69**, 1499–1501 (1981).
- [16] P. L. Marston and E. H. Trinh. *Nature* **312**, 529–531 (1984).
- [17] O. Jobe, D. B. Thiessen, and P. L. Marston. *J. Quant. Spectroscopy & Radiative Transfer* **202**, 147–153 (2017).
- [18] P. L. Marston and R. E. Apfel. *Journal of Colloid and Interface Science* **68**, 280–286 (1979).
- [19] P. L. Marston and R. E. Apfel. *J. Acoust. Soc. Am.* **67**, 27–37 (1980).
- [20] P. L. Marston and S. G. Goosby. *Physics of Fluids* **28**, 1233–1242 (1985).
- [21] T. J. Asaki, P. L. Marston, and E. H. Trinh. *J. Acoust. Soc. Am.* **93**, 706–713 (1993).
- [22] T. J. Asaki and P. L. Marston. *Journal of Fluid Mechanics* **300**, 149–167 (1995); omit 2π in Eq. (3).
- [23] G. Holt, P. Marston, and C. Everbach. *Nature Materials* **1**, 155 (2002).
- [24] S. F. Morse, D. B. Thiessen, and P. L. Marston. *Physics of Fluids* **8**, 3–5 (1996).
- [25] L. V. King. *Proc. R. Soc. London, Ser. A* **147**, 212–240 (1934).
- [26] K. Yosioka and Y. Kawasima. *Acustica* **5**, 167–173 (1955).
- [27] L. P. Gor'kov. *Sov. Phys. Dokl.* **6**, 773–775 (1962).



Analytical prediction of acoustic radiation forces in soft-walled microchannels driven by standing surface acoustic waves

Nitesh Nama¹ and Rune Barnkob²

¹Department of Surgery, University of Michigan, Ann Arbor, MI, USA

²Heinz-Nixdorf-Chair of Biomedical Electronics, Technical University of Munich, Munich, Germany
E-mail: rune.barnkob@tum.de

Introduction

Microsystems driven by surface acoustic waves (SAWs) and utilizing soft-walled microchannels have received large attention in recent years. Despite the significant advancements over the past few decades, their fundamental analysis have lagged behind those of hard-walled microsystems driven by bulk acoustic waves. Specifically, the availability of analytical closed-form expressions has been pivotal in improving the physical understanding and aiding the development of bulk-acoustic-wave-driven systems (such as in the assessment and analysis of separation efficiencies and device parameters [1] or for the determination of the *in situ* acoustic pressure amplitude via experimental acoustophoretic particle trajectories [2]). The lack of such analytical models for SAW-based microsystems has limited their development and the understanding of the involved basic physical phenomena. In this work, we present a simple, yet accurate, analytical description of the first-order acoustic pressure field, and the resulting acoustic radiation force on suspended microparticles, in a soft-walled microchannel driven by a standing surface acoustic wave. The analytical model reveals the precise nature of the acoustic fields and their dependence on system design parameters, resulting in not only an improved physical understanding but also providing the ability to tune the performance of such microsystems.

Analytical model

We consider a rectangular fluid domain of width w in the y -direction and height h in the z -direction. We begin by considering a superposition of two traveling surface acoustic waves to obtain a standing surface wave on the bottom boundary (substrate). The surface wave leaks into the fluid domain, resulting in an upwards-propagating pressure wave. Upon encountering the top wall, a fraction of the wave is reflected. The reflected wave is propagating downwards and similarly, a fraction of it is reflected as it encounters the bottom boundary (substrate). By considering superposition of these reflected waves (with progressively decreasing amplitudes), we obtain a series solution of the pressure field in the microchannel (we show for brevity here the case with only one top-wall reflection)

$$p_1^{1x} = -2ip_a \sin(k_y y) \left[e^{ik_z z} + R e^{ik_z(2h-z)} \right] e^{-i\omega t}, \quad (1)$$

where p_a is the acoustic pressure amplitude, R is the top wall reflection coefficient, ω is the angular frequency, and k_y and k_z are the wave numbers in the horizontal and vertical directions, respectively. This expression, coupled with the Helmholtz wave equation, allows us to calculate analytically the acoustic radiation forces on suspended microparticles via the work of Karlsen and Bruus [3].

Results

Figure 1(a,b) shows the analytically-obtained acoustic pressure field at three different times for three different values of the top-wall reflection coefficient R . Referring to Eq. 1, it can be deduced that for $R = 0$ (left column), there are no reflections from the top wall and the pressure solution reduces to a traveling wave in the vertical direction. For $R = R_0$ (center column), a fraction of the incoming wave is reflected from the top wall and the pressure solution is characterized by a vertical pseudo-standing wave. Lastly, for $R = 1$, the incoming wave is reflected completely at the top wall resulting in a vertical standing wave. These pressure solutions result in widely-differing radiation forces and particle trajectories as shown in Fig. 1(c,d). Figure 2 shows the comparison of the analytical model with $R = R_0$ (PDMS/water) to that of experimentally-validated numerical simulations taking into account not only the top-wall reflections, but also the reflections are the microchannel sidewalls [4].

Conclusion

We present a simple analytical model describing the first-order acoustic fields, and the resulting

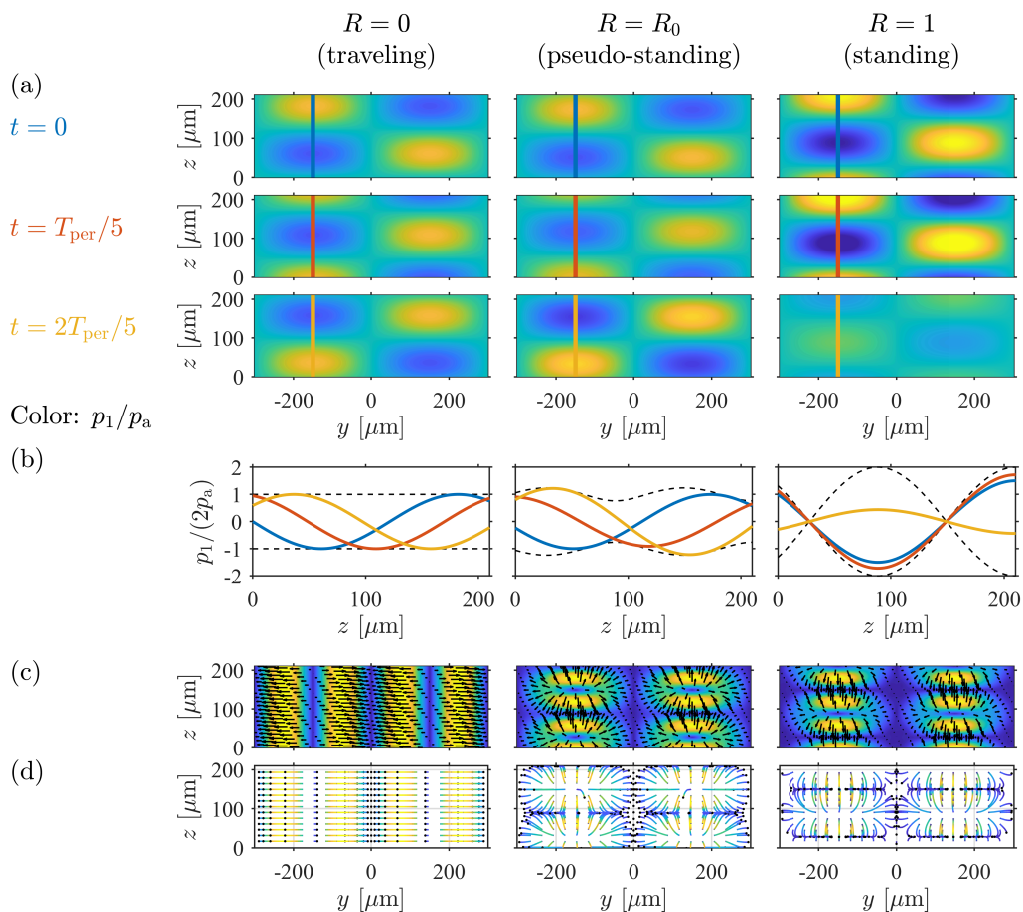


Figure 1: Analytical solutions for (a,b) the first-order acoustic pressure, (c) the second-order acoustic radiation forces on suspended particles, and (d) the resulting particle trajectories. Regardless of the reflection coefficient, R , the pressure field is characterized by a standing wave in horizontal direction. In contrast, the behavior in vertical direction shows a strong dependence on R resulting in a traveling wave, pseudo-standing wave, and a standing wave for $R = 0$ (left column), $R = R_0$ (center column), and $R = 1$ (right column), respectively.

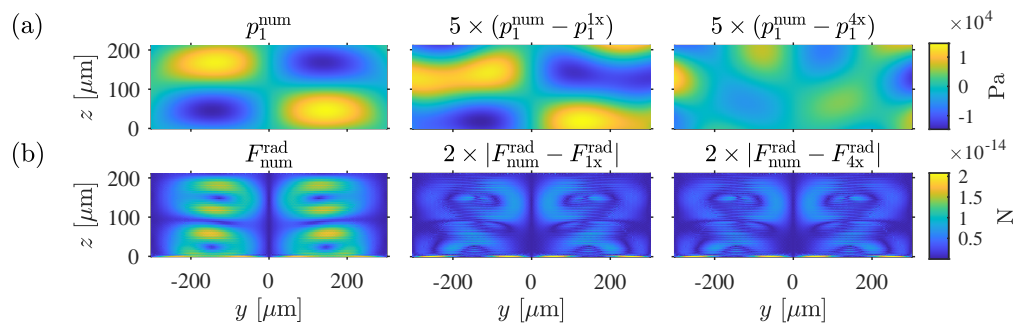
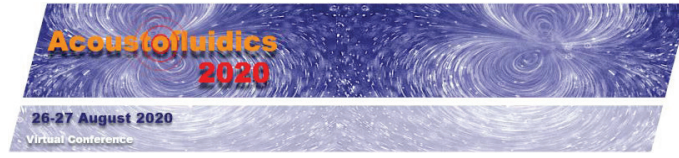


Figure 2: Comparison of the analytical predictions with experimentally-validated numerical simulations [4]. (a) First-order acoustic pressure p_1 . (b) Acoustic radiation force magnitude F^{rad} . The indices ‘1x’ and ‘4x’ refer to analytical solutions obtained by considering one and four terms of the series solution, respectively.

radiation force fields, in standing-SAW-driven soft-walled microchannels. We show the results for varying reflection coefficients and microchannel size (not shown in abstract) as well as their comparison and validation with experimentally-validated numerical simulations. The presented analytical model demonstrate good agreement with numerical simulations and paves the way for further development of SAW-driven soft-walled microsystems.

References

- [1] F. Garofalo, *Microfluidics and Nanofluidics* **23**, 90 (2019).
- [2] R. Barnkob, P. Augustsson, T. Laurell, and H. Bruus. *Lab Chip* **10**, 563-570 (2010).
- [3] J. T. Karlsen and H. Bruus, *Phys Rev E* **92**, 043010 (2015).
- [4] R. Barnkob, N. Nama, T. J. Huang, F. Costanzo, and C. J. Kähler. *Phys Rev Appl* **9**, 014027 (2018).



An angular spectrum based formula of the 3D acoustic radiation torque applied on a particle of arbitrary size and shape by an arbitrary acoustic field

Zhixiong Gong¹, and Michael Baudoin^{1,2}

¹Univ. Lille, CNRS, Centrale Lille, Yncra ISEN, Univ. Polytechnique Hauts-de-France, UMR 8520 - IEMN, F- 59000 Lille, France

E-mails: zhixiong.gong@iemn.fr, michael.baudoin@univ-lille.fr,
URL: <http://films-lab.univ-lille1.fr/michael>

²Institut Universitaire de France, 1 rue Descartes, 75005 Paris

Introduction

Sapozhnikov & Bailey [1] derived an elegant set of formulas to compute the three-dimensional (3D) acoustic radiation force (ARF) applied on a spherical particle of arbitrary size by an arbitrary acoustic field, based on the angular spectrum method (ASM) [1]. But acoustic field carrying angular momentum [2] can also transfer part of it to insonified particles through scattering and/or absorption of the incident beam, leading to rotation and/or translocation of the particles [3-4]. In the present work, we propose a set of ASM-based compact formulas, which enable to compute the acoustic radiation torque (ART) applied on a particle of arbitrary size and shape by an arbitrary field, from the prior knowledge of the incident field in one plane. This powerful tool is used (i) to derive quasi-analytical formula of the 3D torque applied on PE particles insonified by an "ideal" cylindrical Bessel beam and (ii) to compute the torque applied on a PS particle trapped at the center of a realistic one-sided focused vortex synthesized by single-beam active holographic tweezers, whose potential for selective manipulation of microparticles and cells has been previously demonstrated [5-6].

Methods

The detailed derivation of the 3D ART is given in Ref. [7]. Here, we briefly summarize the key formulas. Following the notation used in [8], the ART can be expressed in terms of incident (Φ_i) and scattered (Φ_s) acoustic potentials as

$$\mathbf{T} = \frac{\rho_0}{2} \text{Im} \left\{ \iint_{S_0} \left(\frac{\partial \Phi_i^*}{\partial r} \mathbf{L} \Phi_s + \frac{\partial \Phi_s^*}{\partial r} \mathbf{L} \Phi_i + \frac{\partial \Phi_s^*}{\partial r} \mathbf{L} \Phi_s \right) dS \right\}. \quad (1)$$

where "Im" takes the imaginary part of the indicated argument, * describes the complex conjugate and $\mathbf{L} = -i(\mathbf{r} \times \nabla)$ is the angular momentum operator. S_0 is the standard spherical shape in far-field enclosing the particle. To expand the incident beam in elementary spherical waves, we introduce the ASM-based beam-shape coefficients H_{nm} , such that

$$p_i = \frac{1}{\pi} \sum_{n=0}^{\infty} \sum_{m=-n}^n i^n H_{nm} j_n(kr) Y_n^m(\theta, \varphi), \quad (2)$$

with

$$H_{nm} = \iint_{k_x^2 + k_y^2 \leq k^2} S(k_x, k_y) Y_n^{m*}(\theta_k, \varphi_k) dk_x dk_y, \quad (3)$$

where j_n is the spherical Bessel function of the first kind, Y_n^m is the normalized spherical harmonics, $S(k_x, k_y)$ is the angular spectrum (the 2D spatial Fourier transform of the complex temporal harmonic amplitude of the field in a lateral plane), $k_{x,y}$ are the lateral components of wave number k , $\cos \theta_k = [1 - (k_x^2 + k_y^2)/k^2]^{1/2}$ and $\varphi_k = \arctan(k_y/k_x)$. Based on the scattering theory for a particle with known partial wave (scattering) coefficients A_n^m , the scattered pressure:

$$p_s = \frac{1}{\pi} \sum_{n=0}^{\infty} \sum_{m=-n}^n i^n H_{nm} A_n^m h_n^{(1)}(kr) Y_n^m(\theta, \varphi), \quad (4)$$

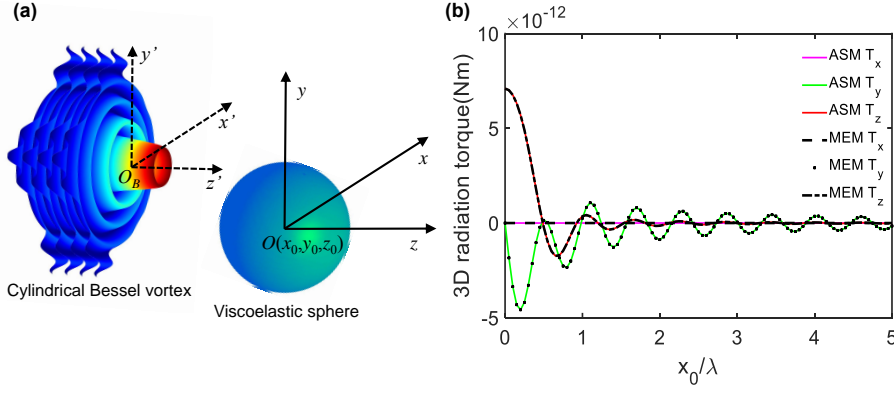


Figure 1: (A) Schematic of a cylindrical Bessel beam illuminating on a viscoelastic polyethylene (PE) sphere. (b) Three projections of ART versus the lateral offset along the x direction (no offset along y and z directions) calculated by the multipole expansion method (MEM) [8] and angular spectrum method (ASM) [7], respectively.

Note that $p_{i,s} = i\omega\rho_0\Phi_{i,s}$ with ω the angular frequency and ρ_0 the density of surrounding fluid. By substituting Eqs. (2) and (4) into (1) with some algebraic derivation, the three component of ART can be written as

$$T_x = -\frac{1}{4\pi^2\rho_0k^3c_0^2} \operatorname{Re} \left\{ \sum_{n=0}^{\infty} \sum_{m=-n+1}^n b_n^m C_n^m H_{nm}^* H_{n,m-1} \right\}, \quad (5)$$

$$T_y = -\frac{1}{4\pi^2\rho_0k^3c_0^2} \operatorname{Im} \left\{ \sum_{n=0}^{\infty} \sum_{m=-n+1}^n b_n^m C_n^m H_{nm}^* H_{n,m-1} \right\}, \quad (6)$$

$$T_z = -\frac{1}{2\pi^2\rho_0k^3c_0^2} \operatorname{Re} \left\{ \sum_{n=0}^{\infty} \sum_{m=-n}^n m D_n^m H_{nm}^* H_{nm} \right\}, \quad (7)$$

with $b_n^m = \sqrt{(n-m+1)(n+m)}$, $C_n^m = A_n^{m-1} + 2A_n^{m-1}A_n^{m*} + A_n^{m*}$, $D_n^m = A_n^m + A_n^m A_n^{m*}$.

Validation

To validate our formula, we first computed the acoustic radiation torque applied on a viscoelastic PE particle insonified by a cylindrical Bessel beam (see Fig. 1a) and compared to previous calculation obtained with the multipole expansion method [8]. For this purpose we first derived analytical expression of the ASM-based beam shape coefficients H_{nm} and then combined these formula with equations (5) to (7). Finally we compared the results with previous results [8] obtained with the angular spectrum method (see Fig. 1). In fact, it can be shown theoretically that the two sets of formula are strictly equivalent [9]. We also applied equations (5) to (7) to compute the acoustic radiation torque applied on PS spheres trapped at the center of a realistic one-sided focused vortex generated by some active holographic tweezers [5-6].

Conclusion

In this work, we present a set of compact formulas which enable straightforward computation of the 3D acoustic radiation torque applied by an arbitrary field on an arbitrarily-shaped particle, when the incident field is known in one plane. These formulas could help rationalize particles rotation and translocation observed when micro-particles and cells are selectively manipulated by flat holographic tweezers based on focused acoustical vortices [5-6] or collectively manipulated by static holograms [10].

References

- [1] O.A. Sapozhnikov, and M.R. Bailey. J. Acoust. Soc. Am. **133**, 661-676 (2013).
- [2] M. Baudoin and J.-L. Thomas. Annu. Rev. Fluid Mech. **52**, 205-234 (2020).
- [3] D. Baresch, J.-L. Thomas, and R. Marchiano. Phys. Rev. Lett. **121**, 074301 (2018).
- [4] A. Marzo, M. Caleap, B.W. Drinkwater Phys. Rev. Lett. **120**, 044301 (2018).
- [5] M. Baudoin, et al. Science Adv., **5**, eaav1967 (2019).
- [6] M. Baudoin, et al. Nature Commun, Under review, ArXiv2001.04162 (2020).
- [7] Z. Gong and M. Baudoin. J. Acoust. Soc. Am., Under review, arXiv:2004.11767 (2020).
- [8] Z. Gong, P.L. Marston and W. Li. Phys. Rev. Appl., **11**, 064022 (2019).
- [9] Z. Gong and M. Baudoin. J. Acoust. Soc. Am., In preparation (2020).
- [10] K. Melde, A.G. Mark, T. Qiu, Nature, **537**, 518-522 (2016).

Cluster structuration of particle mixture in multi-node acoustic levitation with optical exclusion

Nathan Jeger-Madiot, Mauricio Hoyos and Jean-Luc Aider¹

¹Laboratoire Physique et Mécanique des Milieux Hétérogènes (PMMH)

E-mail: nathan.jeger-madiot@espci.fr / mauricio.hoyos@espci.fr / jean-luc.aider@espci.fr

Introduction

Acoustofluidic field is used for many applications as for the focusing[1], the separation [2] or the trapping[3] of particles or cells. These approaches are based on the control of the acoustic radiation forces (ARF)[4]. For a classical standing wave resonator, the acoustic force is generated by matching the height of the cavity h with the acoustic frequency f_{ac} . If we want n acoustic node trapping, we have to make a cavity with a height equal to $n \lambda / 2$. Recently, Dumy and al. [5] has observed a new phenomenon resulting from an acoustic and optical coupling. They show that after the particles are trapped and aggregated at the center of the acoustic node, the particles can be ejected by applying to them a specific optical wavelength. Hereby we propose a new approach to structure multi-clusters in multi-nodes acoustic levitation combining microfluidic channels, the acoustic radiation forces (ARF) and the specific optical illumination.

2D ejection with the optoacoustic phenomenon

In a multi-nodes standing wave cavity, the particles can be trapped in a central cluster. After a short transient period and using the proper parameters, the clusters become circular monolayers levitating in the surrounding fluid. The control of the flow, the ARF and the optical illumination allows various manipulations. For example, on the figure 1, it is possible to eject the particles from the monolayer successively from the first to the last aggregate of the acoustic levitation column.



1: Examples of the optical ejection of particles coupled with multi-node acoustic levitation. After acoustic levitation, then the optical illumination ejects the particles f

Multi-particle aggregation : toward 3D construction

This approach can be extended to shape clusters simultaneously with several particles. Indeed, the optical ejection only appears if the optical wavelength corresponds to the absorbance of the particle. To proof this concept we have used a binary mixture of two type of particles. The first one is red and have absorption at a wavelength equal to $\lambda = 465nm$ and the second one with white color, which is not sensitive to the previous wavelength. By injecting a suspension of the mixture with an active opto-acoustic effect, we can trap simultaneously on all the aggregates, the white particles at the center with all around the red particles. See Figure 2.

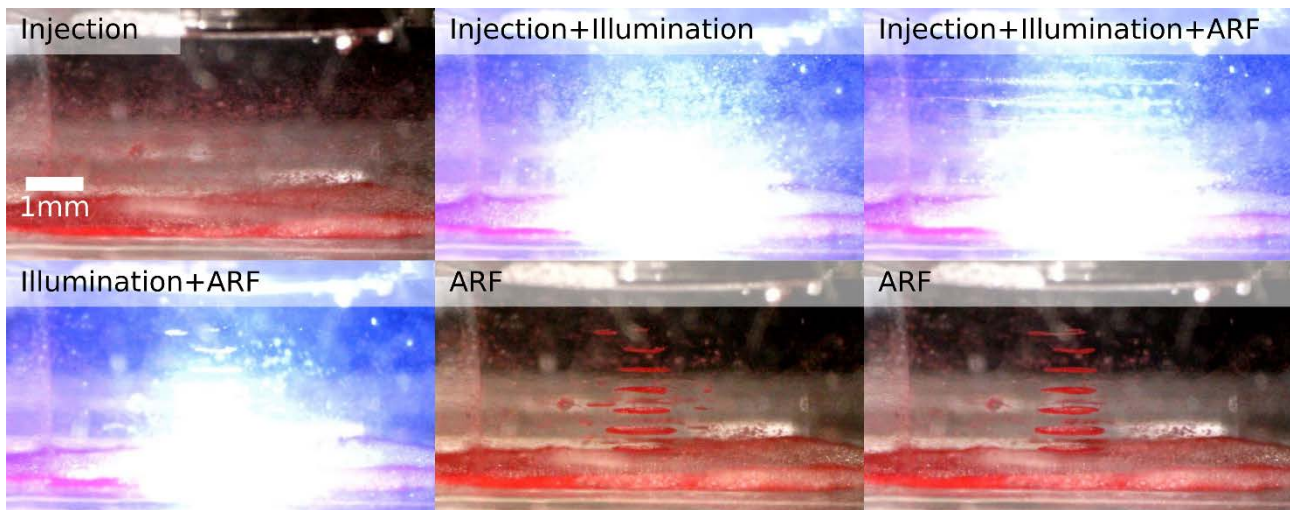


Figure 2: Example of multi-nodes structuration with a binary mixture. The mixture of particles is injected with a flowrate, then the optical illumination and the acoustic forces are triggered. Afterwards, the flowrate is stopped. After ten seconds, the illumination is turned off. These results show a large cluster of white particles enclosed by a circular ring of red particles.

Conclusion

With our set of experiments, we show different ways to manipulate and structure mixture of particles. One of the advantages of such approaches are the use of both optical absorption and acoustic properties. It offers a large panel of setting for the manipulation of particles.

References

- [1] G. Goddard, J. C. Martin, S. W. Graves, et G. Kaduchak, « Ultrasonic particle-concentration for sheathless focusing of particles for analysis in a flow cytometer », *Cytometry A*, vol. 69A, n° 2, p. 66-74, févr. 2006, doi: 10.1002/cyto.a.20205.
- [2] M. Wu, A. Ozcelik, J. Rufo, Z. Wang, R. Fang, et T. Jun Huang, « Acoustofluidic separation of cells and particles », *Microsyst. Nanoeng.*, vol. 5, n° 1, p. 32, déc. 2019, doi: 10.1038/s41378-019-0064-3.
- [3] M. Evander et J. Nilsson, « Acoustofluidics 20: Applications in acoustic trapping », *Lab. Chip*, vol. 12, n° 22, p. 4667, 2012, doi: 10.1039/c2lc40999b.
- [4] J. Friend et L. Y. Yeo, « Microscale acoustofluidics: Microfluidics driven via acoustics and ultrasonics », *Rev. Mod. Phys.*, vol. 83, n° 2, p. 647-704, juin 2011, doi: 10.1103/RevModPhys.83.647.
- [5] G. Dumy, M. Hoyos, et J.-L. Aider, « Observation of selective optical manipulation of particles in acoustic levitation », *J. Acoust. Soc. Am.*, vol. 146, n° 6, p. 4557-4568, déc. 2019, doi: 10.1121/1.5139640.

Session 4 - Acoustic Manipulation

Invited Speaker

THE ACOUSTIC HOLOGRAM AND ITS APPLICATION FACILITATED BY THE SPATIAL MODULATION OF ULTRASOUND

Peer Fischer^{1,2}, Zhichao Ma¹, Kai Melde¹, Athanasios G. Athanassiadis¹, and Tian Qiu^{1,2}
¹Max Planck Institute for Intelligent Systems, GERMANY and
²University of Stuttgart, GERMANY

Contributed Talks

LONG-DISTANCE MICROPARTICLE STEERING USING GIGAHERTZ ACOUSTIC STREAMING

Xinyi Guo^{1,2,3}, Zhichao Ma³, Rahul Goyal³, Moonkwang Jeong¹, Wei Pang², Peer Fischer³, Xuexin Duan², and Tian Qiu¹
¹University of Stuttgart, GERMANY, ²Tianjin University, CHINA, and
³Max Planck Institute for Intelligent Systems, GERMANY

NUMERICAL SIMULATION OF ACOUSTIC STREAMING GENERATED BY GHz AIN-THIN-FILM TRANSDUCERS ON AIN-SiO₂-BRAGG-REFLECTOR SUBSTRATES

André G. Steckel and Henrik Bruus
Technical University of Denmark, DENMARK

EFFECTS OF PARTICLE SHAPE ON ACOUSTOPHORETIC MANIPULATION OF NON-SPHERICAL MICROPARTICLES IN ULTRASONIC STANDING WAVES

Amir Tahmasebipour, Matthew R. Begley, and Carl D. Meinhart
University of California, Santa Barbara, USA

ACOUSTIC CELL PATTERNING FOR MUSCULOSKELETAL TISSUE ENGINEERING

James P.K. Armstrong¹, Sirli Treumuth¹, Bruce W. Drinkwater², and Molly M. Stevens¹
¹Imperial College London, UK and ²University of Bristol, UK

THREE-DIMENSIONAL MANIPULATION OF PARTICLE BY ACOUSTIC TWISTED FOCUSING BEAM

Xiangxiang Xia, Feiyan Cai, and Hairong Zheng
Chinese Academy of Sciences, CHINA

SIMULATED AND EXPERIMENTAL DEMONSTRATIONS OF ACOUSTIC HOLOGRAM ENHANCED PHASED ARRAYS FOR MANIPULATION

Luke Cox¹, Kai Melde², Anthony Croxford¹, Peer Fischer^{2,3}, and Bruce Drinkwater¹
¹University of Bristol, UK, ²Max Plank Institute for Intelligent Systems, GERMANY, and
³University of Stuttgart, GERMANY

Flash Talks

ACOUSTOFLUIDIC BIDIRECTIONAL MICROPUMP

Yuan Gao, Mengren Wu, Yang Lin, Weiqi Zhao, and Jie Xu
University of Illinois, Chicago, USA

CONTROLLED MANIPULATION AND ACTIVE SORTING OF PARTICLES INSIDE MICROFLUIDIC CHIPS USING BULK ACOUSTIC WAVES

Kyriacos Yiannacou and Veikko Sariola
Tampere University, FINLAND

ACOUSTIC TRAPPING AROUND OBSTACLES AND CORNERS

Asier Marzo¹, Marco A.B. Andrade², María A. Cuellar¹, Jaime Goñi¹,
Ryuji Hirayama³, and Diego Martínez³
¹*Universidad Pública de Navarra, SPAIN*, ²*Universidade de São Paulo, BRAZIL*, and
³*University College London, UK*

ACOUSTIC PARTICLE TRAPPING IN A SPHERICAL MICROCHAMBER

Bettina Sailer, Rune Barnkob, and Oliver Hayden
Technical University of Munich, GERMANY

ACOUSTIC EXTRACTION AND TRAPPING OF A DROPLET FROM A LIQUID-LIQUID INTERFACE

Robert Lirette, Joel Mobley, and Likun Zhang
University of Mississippi, USA

MICROPARTICLE PATTERNING ON BENDABLE AND FLEXIBLE SAW DEVICES

Sadaf MaramiZonouz, Mohammad Rahmati, and Richard Yongqing Fu
Northumbria University, UK

SONOLITHOGRAPHY AS A TOOL FOR IN-AIR PARTICLE MANIPULATION AND SURFACE PATTERNING USING BULK ULTRASONIC STANDING WAVES

Jenna M. Shapiro¹, Bruce W. Drinkwater¹, Adam W. Perriman¹, and Mike Fraser²
¹*University of Bristol, UK* and ²*University of Bath, UK*

The acoustic hologram and its application facilitated by the spatial modulation of ultrasound

Peer Fischer^{1,2,*}, Zhichao Ma^{1,*}, Kai Melde¹, Athanasios G. Athanassiadis¹, and Tian Qiu^{1,2}

¹Max Planck Institute for Intelligent Systems, Heisenbergstr. 3, 70569 Stuttgart, Germany

²Institute of Physical Chemistry, University of Stuttgart, Pfaffenwaldring 55, 70569 Stuttgart, Germany

E-mail: fischer@is.mpg.de, E-mail: zma@is.mpg.de, URL: <https://pf.is.mpg.de/>

Introduction

High-fidelity wave-front shaping is essential for a number of acoustofluidic applications, including the manipulation and assembly of particles and cells in a fluid. The acoustic hologram has recently emerged as a promising method to obtain complex acoustic fields with tailored pressure distributions [1]. We showed that by encoding the phase information in the topography of a 3D-printed plate, it is possible to generate sophisticated acoustic fields using only a single transducer. The resulting fields can be used for the manipulation of micro-particles and their assembly (see Figure 1).

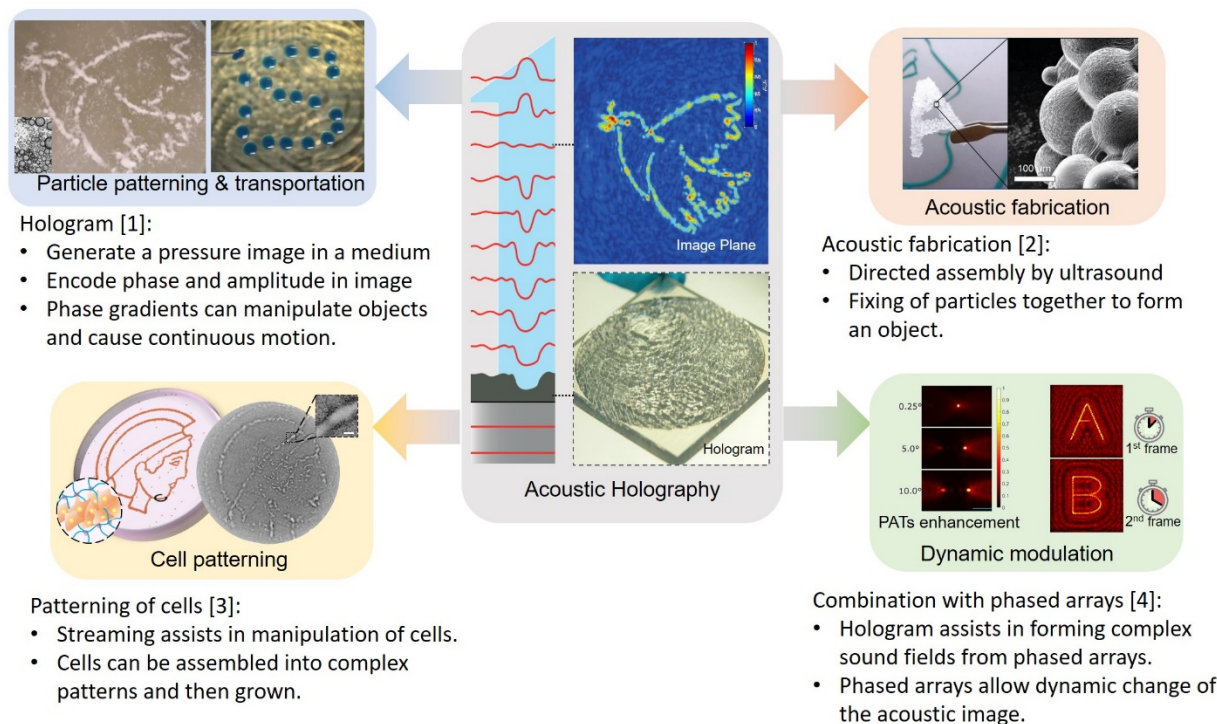


Figure 1: The acoustic hologram and its application in particle and cell manipulation, and its extension towards dynamic applications. Images in part adapted from [1,2,3,4].

A commercial 3D printer can be used to fabricate the holograms (phase-plates). For instance, a commercial printing material (Veroclear by Stratasys) has a typical sound speed for a hard plastic of ~ 2400 m/s. As an example, to encode a phase difference of 2π for ultrasound at 2 MHz regime relative to a wave travelling through water (sound speed ~ 1500 m/s), the hologram must show a thickness of 3.5 mm. This is readily achieved with commercial 3D printers. The lateral resolution of such printers is also below the wavelength of ultrasound ($750 \mu\text{m}$ in water). It now becomes possible to design and impart sophisticated phase and amplitude information onto the wavefront of an ultrasound field. This opens up many possibilities for acoustofluidics.

We showed that microparticles could be directly assembled along pressure maxima, which we have shown for PDMS particles that were coated with a suitable photopolymeric system to fix the structures after assembly – an approach we termed acoustic fabrication [2].

The acoustic radiation force together with the acoustic streaming flows also makes it possible to effectively transport cells in a fluid medium – here a biocompatible hydrogel – and to arrange these cells [3]. The acoustic streaming flows lead to recirculating convection fields inside the fluid medium (~ 10 's of $\mu\text{m/s}$) that transport the cells to regions of high acoustic amplitude (~ 10 - 100 kPa), where the cells are trapped in the pressure nodes and aggregate along the pattern generated by the hologram [3]. The cell aggregation completes within 1-2 minutes, after which the hydrogel medium undergoes gelation to immobilize the cell pattern. The patterned cells are transferrable for long-term cultivation or further analysis.

In all of these applications, the advantage of the hologram over a phased array is that it can much more finely shape the acoustic wave-front. However, its disadvantage is that the field is static. It would therefore be ideal if one could render the hologram fields dynamic. One promising direction is to combine a hologram with a phased array [4].

Another approach, which we will discuss here, is to try and directly manipulate the elements that shape the wave-front, thereby enabling the spatial modulation of ultrasound [5]. The challenge is that most induced changes in a material have little effect on the sound speed. Phase changes in materials can cause considerable changes in sound speed, but the energy requirement means that it becomes impractical to realize an entire 2D surface that can manipulate the sound wave. Alternatives must therefore be found – especially those that enable control and that are programmable, so that the amplitude and/or phase of an ultrasound field can be changed across its wave-front. We discuss our latest results.

References

- [1] K. Melde, A. G. Mark, T. Qiu, P. Fischer. *Nature* **537**, 518-522 (2016).
- [2] K. Melde, E. Choi, Z. Wu, S. Palagi, T. Qiu, P. Fischer. *Advanced Materials* **30**, 1704507 (2018).
- [3] Z. Ma, A. W. Holle, K. Melde, T. Qiu K. Poeppel, V. M. Kadiri, P. Fischer. *Advanced Materials* **32**, 1904181 (2020).
- [4] L. Cox, K. Melde, A. Croxford, P. Fischer, B. W. Drinkwater, *Phys. Rev. Applied* **12**, 064055 (2019).
- [5] Z. Ma, K. Melde, A.G. Athanassiadis, M. Schau, H. Richter, T. Qiu and P. Fischer, *under review*.

Long-distance microparticle steering using gigahertz acoustic streaming

Xinyi Guo^{1,2,3,4}, Zhichao Ma⁴, Rahul Goyal⁴, Moonkwang Jeong¹, Wei Pang^{2,3}, Peer Fischer⁴, Xuexin Duan^{2,3} and Tian Qiu^{1*}

¹ Cyber Valley Group, Institute of Physical Chemistry, University of Stuttgart, Pfaffenwaldring 55, 70569 Stuttgart, Germany.

E-mail: tian.qiu@ipc.uni-stuttgart.de

² State Key Laboratory of Precision Measuring Technology & Instruments, Tianjin University, Tianjin 300072, China.

³ College of Precision Instrument and Opto-electronics Engineering, Tianjin University, Tianjin 300072, China.

⁴ Max Planck Institute for Intelligent Systems, 70569 Stuttgart, Germany.

Introduction

Three-dimensional directional control of micro-objects in fluidic environments is important for a number of applications. Current approaches include optical [1] and acoustic tweezers [2], which require the trapped object to possess special material properties so that it can be manipulated. In contrast, hydrodynamic tweezers permit non-contact manipulation with no restrictions on the material properties [3]. However, they generally only work at close distance and in the proximity of solid boundaries, such as obstructions or cavities. This complicates the use of hydrodynamic tweezers for contactless manipulation of microparticles over large spatial distances. Recently, we reported an acoustofluidic tweezer using the acoustic streaming [4] at gigahertz frequencies for the three-dimensional (3D) position control of suspended microparticles [5]. Here, we demonstrate experimentally that a 500 μm glass bead can be stably trapped at a distance that is centimeters away from the acoustic resonator and that the trap can also steer the micro-object along a complex 3D trajectory. The reported method utilizes only the hydrodynamic force and shows relatively high accuracy in the achieved positioning. It has the potential to be developed as a versatile tool for the 3D manipulation of micro-objects and biological particles in fluids.

Generation of the gigahertz acoustic streaming

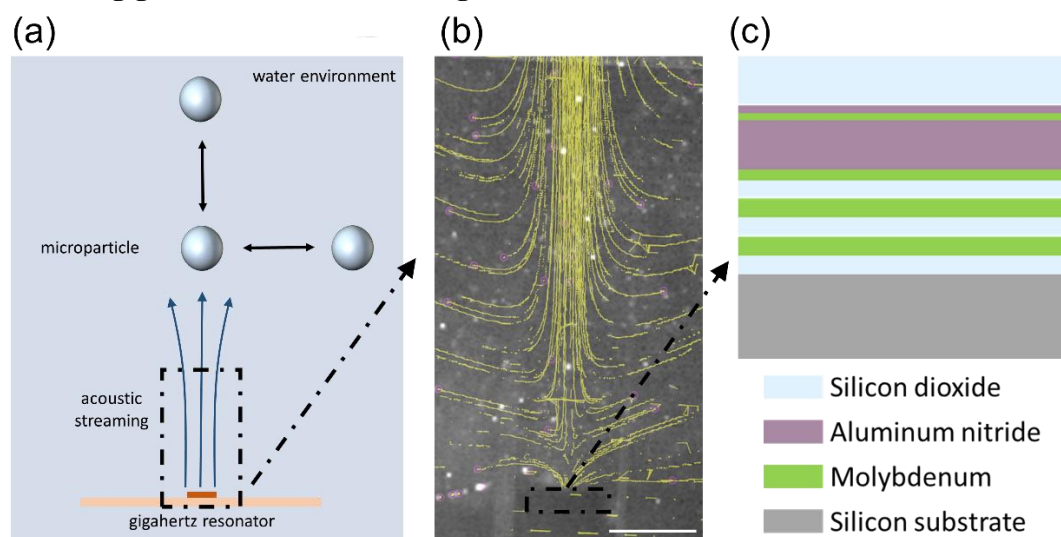


Figure 1: (a) Schematic of the microparticle steering based on the gigahertz acoustic streaming. (b) Streamlines (yellow lines) of the acoustic streaming generated by the gigahertz acoustic resonator. Area marked with the black rectangle corresponds to the resonator. The scale bar is 1 mm. (c) Resonator structure shown in a vertical cross-section.

Figure 1(a) shows the schematic of the microparticle manipulation system. The system is based on the acoustic streaming (Figure 1(b)) generated from a micro-fabricated gigahertz resonator (Figure 1(c)). Driven by a sinusoidal electric signal, the piezoelectric effect of the aluminum nitride layer converts the electric energy into the device vibration, and the gigahertz acoustic wave propagates into the liquid. As the acoustic attenuation

depends on the square of the frequency [6], the strong attenuation of this gigahertz sound wave leads to a high-speed jet flow that is perpendicular to the interface of the resonant surface. The streaming velocity increases nonlinearly as a function of the input electric power, and the velocity can be regulated over a wide range.

We observed that the fluidic jet can levitate the microparticle in the vertical direction, while it can also stably trap the particle by streaming in the horizontal direction. In the vertical direction, the acoustic streaming provides a force pointing upwards, which can levitate the particle and a stable trap position can be achieved. In the horizontal direction, the force balance results from the fluid pressure difference. As shown in Figure 1(b), the high-speed fluid motion at the center generates a low-pressure zone which forces the liquid at the outer regions to move inwards. The oblique flow provides opposing forces on the two sides of the particle, thus trapping it at the center of the fluid field.

Steering of a micro-object in a 3D trajectory

The experimental results of the dynamic positioning of a microparticle is realized in 3D space underwater. When increasing the power, the force of the streaming flow increases, thus the particle exhibits a net upward force for vertical position regulation (Figure 2(a)). The maximum distance between the particle and the resonator can exceed 25mm. Horizontal position control of the particle is realized by translating the acoustic resonator. When the position of the jet flow moves, the fluid provides a horizontal force pushing it back to the balanced position, which pushes the particle to trace the motion of the resonator.

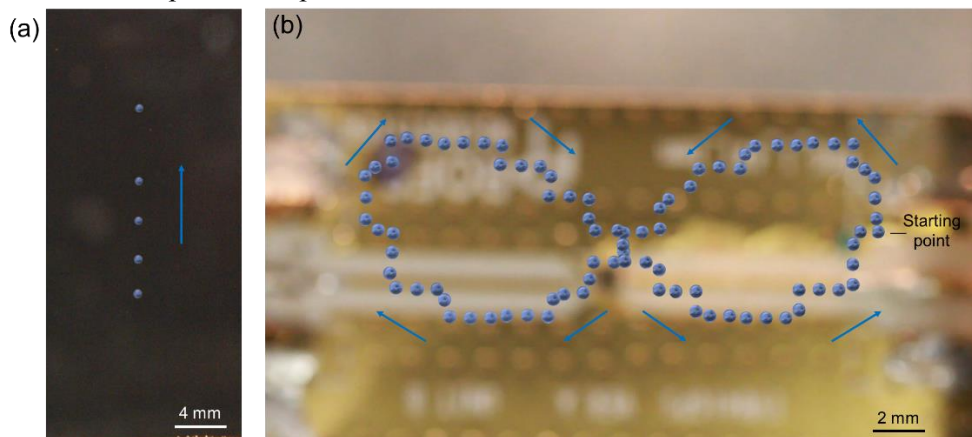


Figure 2: (a) The particle's vertical position is controlled by tuning the applied electric power to the transducer. From bottom to top: input power increases from 26 dBm to 28 dBm with a step of 0.5 dB. (b) Position control of a microparticle following a designed “butterfly” trajectory. The overlapped images show the particle positions from the top view, and the arrows indicate the moving direction.

We also realized the manipulation of the microparticle following a designed trajectory with the acoustofluidic tweezer system (Figure 2(b)). The trajectory is chosen and a motorized stage is manipulated to translate the resonator. Good position tracking of the microparticle is achieved as can be seen in Figure 2.

Conclusion

In summary, we develop a wireless manipulation method based on the acoustic streaming for the steering of microparticles over centimeter distances in liquid environments. The results show stable particle trapping and rapid particle transportation following complex trajectories in 3D. The approach is based on high-frequency electronics which opens the possibility that a miniaturized microsystem for untethered micro-object manipulation can be developed and implemented in end-effectors.

Acknowledgement

This work was partially supported by the Max Planck Society, the European Research Council under the ERC Grant agreement HOLOMAN (788296) and the Vector Foundation (P2020-0111).

References

- [1] D. G. Grier. *Nature* 424, 810-816 (2003).
- [2] K. Melde, A. G. Mark, T. Qiu, and P. Fischer. *Nature* 537, 518-522 (2016).
- [3] W. Cui, X. Duan, et al.. *Particle & Particle Systems Characterization* 35, 1800068 (2018).
- [4] H. Bruus, et al.. *Lab on a Chip* 11, 3579-3580(2011).
- [5] X. Guo, et al.. 2020 IEEE International Conference on Robotics and Automation (ICRA), June 2020.
- [6] D. J. Collins, Z. Ma, and Y. Ai. *Analytical chemistry* 88, 5513-5522 (2016).

Numerical simulation of acoustic streaming generated by GHz AlN-thin-film transducers on AlN-SiO₂-Bragg-reflector substrates

André G. Steckel and Henrik Bruus

Department of Physics, Technical University of Denmark, Kongens Lyngby, Denmark
 E-mail: angust@fysik.dtu.dk , URL: <http://www.fysik.dtu.dk/microfluidics>

Introduction

Gigahertz (GHz) acoustofluidics is an active and exciting field of research with many new challenges and applications, including chemical and biological detection [1], microfluidic mixing [2], on-demand droplet dispensing [3], and nanoparticle trapping [4]. To develop further the initial numerical modeling in the field [5], we apply here our recent 3D fully-coupled acoustofluidic model [6] to a generic GHz AlN-thin-film-transducer device presented in Ref. [2]. The model of the system takes into account the electro-, elasto-, and hydrodynamics as well as the strongly damped acoustics in the transducer, in the substrate below, and in the fluid and glass lid above. Typical acoustic wavelengths at 1.5 GHz are 1 μm (water) and 3 μm (SiO₂), so a GHz-acoustofluidic system of size 10 to 100 μm typically contains 10 - 100 acoustic wavelengths. The model reveals the complexity that arises from these many wavelengths, and we compute the acoustic streaming that is induced by the acoustic wave, as it is strongly attenuated within a distance of 50 μm from the surface of the AlN-thin-film transducer.

3D acoustic simulations of a piezoelectric GHz AlN-thin-film transducer in vacuum

Acoustofluidics for the GHz regime requires specially designed transducers, systems that resonate at those frequencies, and direct contact or close proximity between the transducer and the liquid. This is necessary because of the strong acoustic attenuation at GHz frequencies. At 1.5 GHz the characteristic attenuation length in water is about 12 μm , only 12 times the acoustic wavelength. By having the resonator embedded in the liquid, the energy transfer from the piezoelectric transducer is maximized. In Ref. [2], a pentagon-shaped GHz-AlN-thin-film transducer was placed on top of an AlN-SiO₂ Bragg reflector, resting on a silicon substrate, and used to generate strong acoustic streaming. Here, using our recent 3D acoustofluidic model implemented in COMSOL Multiphysics 5.4 [6] with material parameters for the AlN thin-film from Ref. [7], we model the acoustic modes in this system at first placed in vacuum. We show in Fig. 1 the resulting displacement field in the transducer and substrate when making three different assumptions for the absorption by the substrate.

We note in Fig. 1 the increased complexity of oscillation pattern of the displacement field that arises, when the 50- μm -side-length pentagon in the 100- μm -side-length square system is allowed to oscillate more freely at the high GHz frequencies by changing the absorption assumptions. Whereas some rare modes are found to have a displacement predominately in the vertical z -direction, the typical mode is a complex pattern exhibiting many small-wavelength structures across the surface.

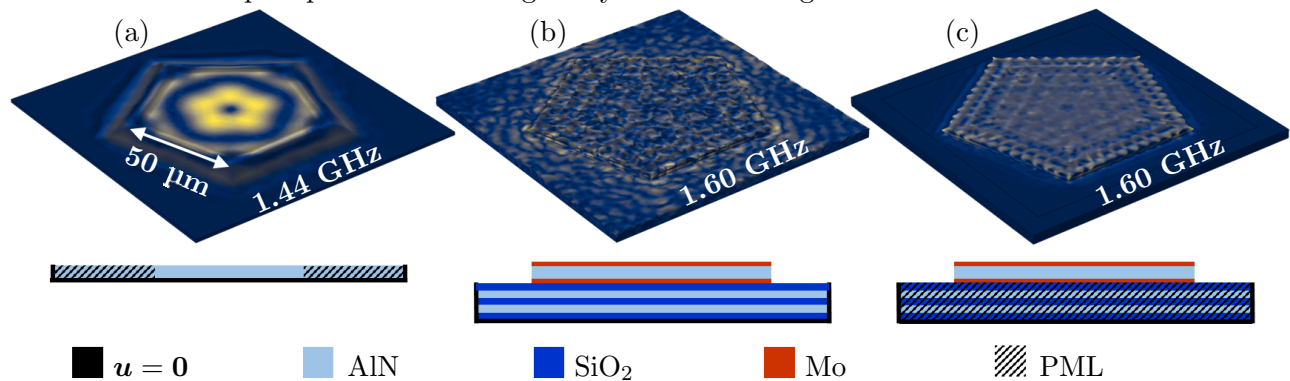


Figure 1: 3D simulations of the displacement field from 0 (blue) to 15 μm (yellow) in the GHz AlN-thin-film transducer from Ref. [2] using the different model assumptions that are illustrated by the respective sketches below each result. (a) A 100- μm square, 1.1- μm -thick AlN-thin-film in vacuum with zero displacement on the bottom and sides. The pentagon (50 μm side length) represents the top and bottom electrodes actuated by a $1\text{-}V_{\text{pp}}$ GHz-ac voltage. The area outside the pentagon is modeled as a perfectly absorbing medium (PML). (b) The same pentagon-shaped transducer protruding from the surface and with the 0.16- μm -thick metal electrodes included. It is placed on a AlN-SiO₂-Bragg reflector with five 0.64- μm -thick layers and with its bottom and side surfaces clamped. (c) The same as panel (b), but modeling the Bragg reflector as a perfect absorber (PML).

2D GHz acoustofluidic simulations of solids, piezoelectrics, and liquids with streaming

As shown in Fig. 2(a), we now insert the transducer of Fig. 1(b) in a larger system: the AlN-SiO₂ Bragg reflector is embedded in a 25- μ m-thick Si base, and a 40- μ m-high and 80- μ m-wide water domain is added above and enclosed in a 10- μ m-thick Pyrex casing. We simplify the simulation by restricting it to a vertical 2D cross section through the center of the device. Selected results using the method of Ref. [6] for simulating of the coupled Si-base-AlN-transducer-water-Pyrex system are shown in Fig. 2. In Fig. 2(a)-(c) is shown the displacement u_1 (up to 110 pm) of the elastic solids and the highly attenuated acoustic pressure p_1 (up to 890 kPa) in the water emanating from the transducer. The acoustic attenuation acts as a source for acoustic streaming, which we compute numerically using effective boundary layer theory [6]. The resulting streaming is shown in Fig. 2(d)-(f).

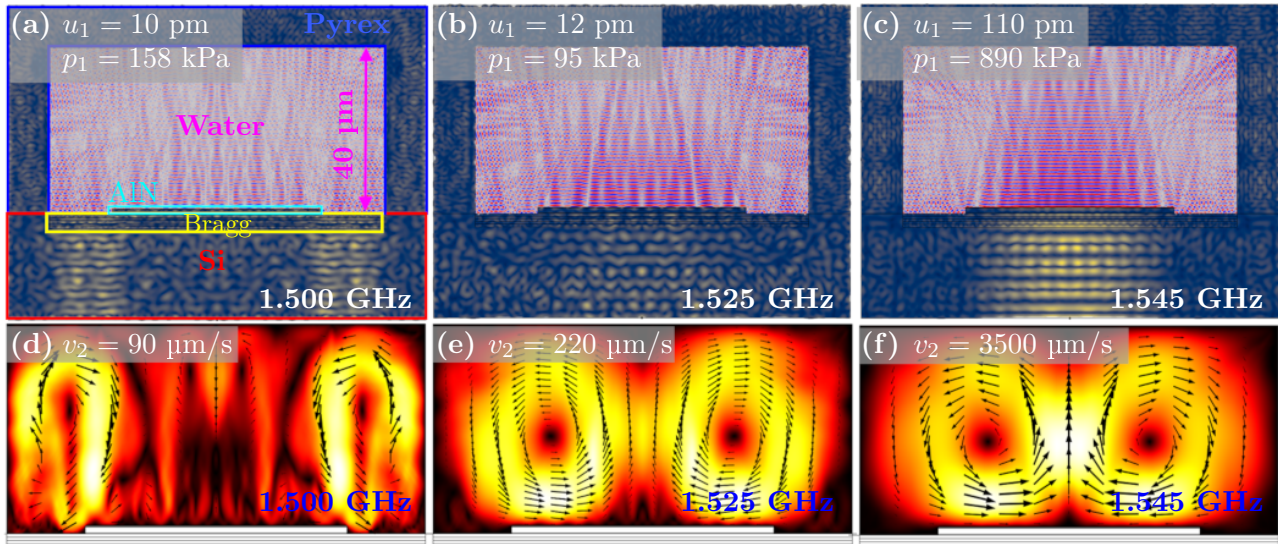


Figure 2: (a) Simulation at 1.500 GHz of the acoustic pressure p_1 in the water (magenta) above the AlN-thin-film transducer (cyan), and the displacement u_1 in the Pyrex (blue), the Bragg reflector (yellow), and the Si base (red). (b) The same, but for 1.525 GHz. (c) The same, but for 1.545 GHz. (d) Simulation of the acoustic streaming velocity v_2 corresponding to panel (a). (e) v_2 corresponding to (b). (f) v_2 corresponding to (c).

The three nearly identical actuation frequencies result in qualitatively different acoustic fields, but similar streaming patterns. At 1.500 GHz, a vertical standing wave is set up in the Si-substrate to the sides away from the transducer region. This results in two streaming rolls above the edges of the transducer. At 1.525 GHz, a weak increase in acoustic intensity is seen below the transducer. The result is two weakly overlapping streaming rolls above the transducer and closer to the center. At 1.545 GHz, a strong standing wave is established directly under the transducer. Given the moderate actuation of only 1 V_{pp}, the resulting streaming flow is fast (3.5 mm/s), and the two flow rolls are strongly overlapping with a maximum over the center of the transducer. The two-flow-roll pattern is a fairly robust feature, but the position and magnitude the flow rolls depends on the frequency.

Conclusion

We have shown that our recent 3D fully coupled acoustofluidic model [6] can be applied to GHz acoustofluidics, in particular to AlN-thin-film-transducer devices. The simulations shown here reveal how complex the acoustic fields are in detail, but they also indicate the overall stability of the streaming rolls, which is ensured by the strong attenuation of the acoustic waves within a 40- μ m-range from the transducer. Our model is a promising tool for future design studies of GHz acoustofluidic devices.

Acknowledgments

This work was supported by the BioWings project funded by the European Union's Horizon 2020 Future and Emerging Technologies (FET) programme, grant no. 801267.

References

- [1] W. Pang, H. Zhao, E.S. Kim, H. Zhang, H. Yuc, and X. Hu. *Lab Chip* **12**, 29 (2012). [doi]
- [2] W. Cui, H. Zhang, Y. Yang, M. He, H. Qu, W. Pang, D. Zhang, and X. Duan. *Appl. Phys. Lett.* **109**, 253503 (2016). [doi]
- [3] M. He, Y. Zhou, W. Cui, Y. Yang, H. Zhang, X. Chen, W. Pang, D. Zhang, and X. Duan. *Lab Chip* **18**, 2540 (2018). [doi]
- [4] W. Cui, L. Mu, X. Duan, W. Pang, and M.A. Reed. *Nanoscale* **11**, 14625 (2019). [doi]
- [5] W. Cui, W. Pang, Y. Yang, T.Li., and X. Duan. *Nanotechnol. Precision Eng.* **2**, 15 (2019). [doi]
- [6] N. R. Skov, J. S. Bach, B. G. Winkelmann, and H Bruus. *AIMS Mathematics*, **4**, 99 (2019). [pdf]
- [7] M.A. Caro, S. Zhang, T. Riekkinen, M. Ylilammi, M.A. Moram, O. Lopez-Acevedo, J. Molarius, and T. Laurila. *J. Phys.-Condens. Mat.* **27**, 245901 (2015). [doi]

Effects of particle shape on acoustophoretic manipulation of non-spherical microparticles in ultrasonic standing waves

Amir Tahmasebipour¹, Matthew R. Begley^{1,2}, and Carl D. Meinhart¹

¹ Department of Mechanical Engineering, University of California Santa Barbara, Santa Barbara, CA, USA
E-mail: atahmasebipour@uocsb.edu, URL: <https://sites.engineering.ucsb.edu/~microflu/>

² Materials Department, University of California Santa Barbara, Santa Barbara, CA, USA

Introduction

Use of acoustophoresis in microfluidic devices has been established as a robust yet gentle and label-free method to manipulate and assemble microparticles and cells, regardless of the fluid flow, in a fluid filled microcavity[1]. In order to create effective acoustophoretic fields, especially for particle-medium duos with low acoustic contrast, it is essential to excite strong resonant ultrasonic waves within the microchannels[2]. Micro-acousto-fluidic devices mainly use the so-called primary acoustic radiation force to move particles around. Given the time harmonic pressure fields in the fluid, these force fields can be calculated for the case of a compressible and spherical particle that is much smaller than the acoustic wavelength[3]. In this work, first we use a damped [4], 3D numerical simulations of a Bulk Acoustic Wave device to show three resonant ultrasonic standing wave modes used for patterning silica microbeads in water. Numerical characterization results of the PZT-actuated silicon-glass chip show a reliable agreement with the experimental data collected from the actual device. Next, in another 3D model we simulate a finite sized microparticle exposed to the previously calculated background pressure fields. Calculating the acoustic radiation force numerically, we show how this field on a single sphere changes when the size of the particle becomes comparable to the wavelength. We also show how relatively small non-spherical particles orient themselves in a standing half wave pressure field. We note that, compared to spherical particles of similar volume and acoustic contrast factor, comparatively small micro disks and micro rods experience higher acoustic radiation forces when in their preferred orientation.

Theory

The time harmonic pressure fields in a micro-acousto-fluidic chip form as a result of the fluid-structure interaction at the walls of the microchannel. The physics of the fluid, solid and piezoelectric domains of the device are governed by a perturbation theory analysis of the Navier-Stokes, linear solid mechanics and coupled piezoelectricity equations, respectively [4-5]. Naturally, non-linearities in the fluid domain give rise to the non-zero acoustic radiation force fields described based on the time-averaged pressure ($\langle p^2 \rangle$) and velocity ($\langle v_i v_i \rangle$) fields as $\mathbf{F}^{\text{rad}} = -\nabla U^{\text{rad}}$, attracting the particles to the minima of the potential field,

$$U^{\text{rad}} = \frac{4}{3} \pi a^3 \left[f_1 \frac{\kappa_{\text{fl}}}{2} \langle p^2 \rangle - f_2 \frac{3\rho_{\text{fl}}}{4} \langle v_i v_i \rangle \right], \quad (1)$$

where f_1 is the monopole and f_2 is the dipole acoustic scattering coefficient for particles with radius a , suspended in a fluid of density ρ_{fl} and compressibility κ_{fl} . From a numerical simulation of a finite sized particle in a background pressure field, the radiation force is calculated by integrating the kinetic, hydrostatic and convective momentum fluxes on S , the unperturbed surface of the particle [6],

$$\mathbf{F}^{\text{rad}} = \int_S \left(\frac{\rho_{\text{fl}}}{2} \langle v_i v_i \rangle \mathbf{n} - \frac{\kappa_{\text{fl}}}{2} \langle p^2 \rangle \mathbf{n} - \rho_{\text{fl}} (\mathbf{n} \cdot \mathbf{v}_i) v_i \right) dS, \quad (2)$$

where \mathbf{n} is the normal vector out of the particle. The second equation is appropriate for small and large particles.

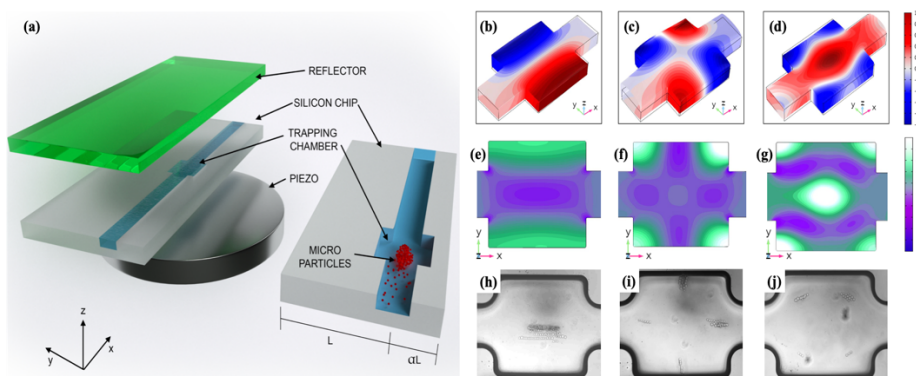


Figure 1: (a) Descriptive sketch of an asymmetric BAW device. (b)-(d) Normalized pressure field ($P_{\text{norm}} = 10 \text{ MPa}$) in the cavity with deformed (factor of 2500) solid walls for $\bar{f} = 1, \sqrt{2}, 2$, respectively. (e)-(g) Normalized force potential $U_{\text{norm}} = 60 \text{ pJ}$ for $\bar{f} = 1, \sqrt{2}, 2$, respectively. (h)-(j) Silica ($10 \mu\text{m}$) particle patterns in a square $800 \mu\text{m}$ chamber excited with peak to peak potential of 40 V at frequencies $\bar{f} = 1, \sqrt{2}, 2$, respectively.

Results and discussion

In Fig. 1(a), the asymmetric BAW device [7] with a square micro-chamber of size w is shown and sections (b)-(d) show three resonant pressure modes confined to the cavity. The normalized resonant frequencies $\bar{f} = f/f_0^{-1}$ are defined with respect to $f_0 = c_{fl}(2w)^{-1}$, which signifies the first resonant mode where a standing half wave forms along the principal walls of the chamber. By comparing the force potential fields of Fig. 1 (e)-(g), from 3D numerical simulations and experimental results shown in sections (h)-(j) in Figure 1, we can observe the relevance of the simulations in predicting silica microbead patterns and assembly schemes. However, These force fields are accurately calculated only for spherical particles with sizes much smaller than the wavelength. The effect of particle size on the accuracy of the solution presented in eq. 1 is investigated by taking a cubic domain of side w (as shown in Fig. 2(a)) and monitoring the changes to the integrated force (eq. 2) on a single finite sized particle placed at $\lambda/8$ from the pressure node. Figure 2(c) reveals that the accuracy of eq. 1 is limited by the size of the particle. Furthermore, not only doesn't the radiation force grow proportionally with the volume of the particle but for larger silica particles, it also shows a behavior opposite to the expected attraction towards the pressure node which can be attributed to the natural frequencies of an elastic sphere. Given the geometrical constraints and limitations of microfluidic devices when dealing with large particles, applying this dual quality of acoustophoresis proves to be challenging.

Focusing on particles much smaller than the wavelength, Fig. 2(c) shows that the volume is the main determinant of acoustic radiation force on particle-medium duos of constant contrast factor. Figures 2 (b) and (d) show how non-spherical particles with equivalent volume to a 10 micron microbead are defined with various aspect ratios and orientations. These particles are placed in various locations sweeping the entire domain to show the effects of particle shape and orientation on the applied acoustophoretic force field. Figure 2(e) shows that the radiation force field on cylindrical microparticles with aspect ratio close to unity is virtually identical to that of a micro-sphere. However, micro-disks and micro-fibers, having very low and very high aspect ratios, experience a deviated force field from that of a sphere where there may be an increase of up to 35 percent in the case of a thin disk. Additionally, non-spherical microparticles show the tendency to have a preferred orientation where the radiation force is maximized and the torques on the particle are minimized [8]. This quality can be used to create more complex patterns and provide more degrees of freedom to microparticle assemblies.

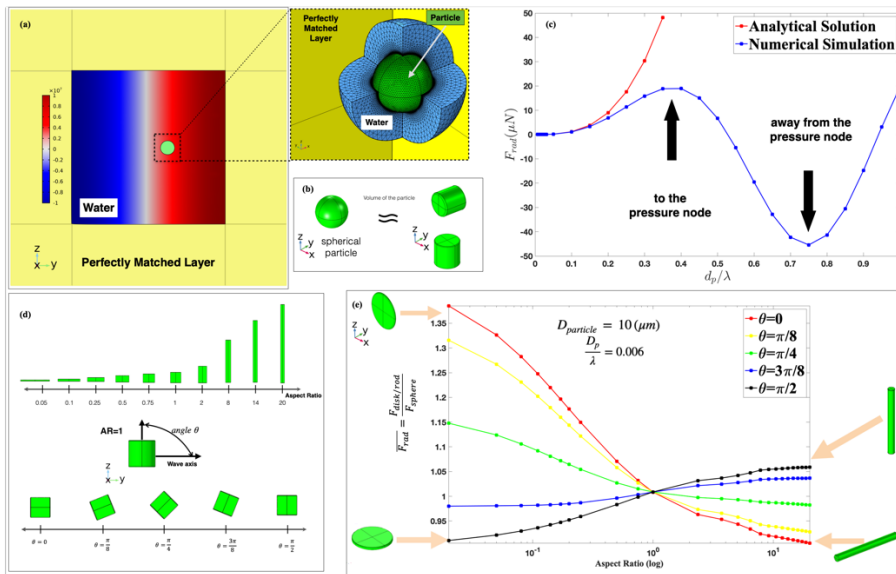


Figure 2: (a) Slice of the 3D numerical model of a single particle in standing half wave pressure field of magnitude $P_{norm} = 10$ MPa. (b) Schematic of non-spherical particles with equivalent volume to the spherical particle. (c) Acoustic radiation force on silica spherical particles in the background field for sizes up to λ . Maximum positive and negative radiation force to the pressure nodes are indicated. (d) Visual description of particle aspect ratio (AR) and rotation angle (θ) for micro-disks and micro-fibers. (e) Force field deviation from the generalized solution for a sphere, as affected by particle shape and orientation. The force fields are normalized over the entire domain.

Conclusion

We have used 3D numerical simulations to characterize pressure fields in a BAW device. Comparison with experimental particle assembly patterns show three different strong resonant modes in one chip. We apply this pressure field to a 3D model of finite sized particles and find that the analytically calculated radiation force does not predict the reversal of the behavior of particles with relatively large sizes. We also found that relatively small particles with high aspect ratios experience higher acoustic force fields compared to microbeads of equivalent volume and tend to have a preferred orientation.

References

- [1] P. Augustsson, C. Magnusson...and T. Laurell. *Anal. Chem.*, **84**, 7954-7962 (2012)
- [2] R. Moiseyenko, H. Bruus. *Phys. Rev. Appl.*, **11**, 014014 (2019)
- [3] M. Settnes, H. Bruus. *Phys. Rev. E*, **85**, 016327 (2012)
- [4] P. Hahn, J. Dual. *Phys. Fluids*, **27**, 062005 (2015)
- [5] J. S. Bach, H. Bruus. *J. Acoust. Soc. Am.*, **144**, 766-784 (2018)
- [6] R. Habibi, C. Devendran and A. Neild. *Lab Chip*, **17**, 3279-3290 (2017)
- [7] A. Tahmasebipour, L. Friedrich, M. Begley, H. Bruus, C. Meinhart. *J. Acoust. Soc. Am.*, **148**, 359-373 (2020)
- [8] F. Wijjiya, K. Lim. *Acta Acustica united with Acustica*, **101**, 531-542 (2015)

Acoustic cell patterning for musculoskeletal tissue engineering

James P. K. Armstrong,¹ Sirli Treumuth,^{1,2,3} Bruce Drinkwater,⁴ and Molly M. Stevens^{1,2,3}

¹Department of Materials, Imperial College London, London, UK

²Department of Bioengineering, Imperial College London, London, UK

³Institute of Biomedical Engineering, Imperial College London, London, UK

⁴Department of Mechanical Engineering, University of Bristol, Bristol, UK

E-mail: james.armstrong@imperial.ac.uk, m.stevens@imperial.ac.uk,

URL: www.jamespaularmstrong.co.uk, www.stevensgroup.org

Introduction

Many natural tissues exhibit cellular organization that is critical for their physiological function. In particular, musculoskeletal tissues often exhibit cellular alignment that either directly or indirectly contributes to their load-bearing capability. It is important to replicate these structural aspects when seeking to engineer functional tissue grafts or cell models. A number of methods have been explored for recreating the native organization in engineered tissues,[1] with ultrasound emerging as a prominent tool for cell manipulation.[2,3] Here, we have designed acoustic patterning devices that use ultrasound standing waves to form tunable arrays of viable cells. By immobilizing the patterned cells in different hydrogels, we have been able to use this platform technology to engineer musculoskeletal tissues with programmed cell architecture.

Acoustic Cell Patterning

Here, we report that acoustic radiation forces generated from ultrasound standing waves can be used to remotely direct the organization of cells for musculoskeletal tissue engineering. We have designed and fabricated acoustic patterning devices with orthogonal pairs of piezotransducers that can generate 1D or 2D ultrasound standing waves across a central cavity housing a cell culture dish. This set-up enabled sterile suspensions of cells to be remotely patterned *en masse* into geometric arrays using ultrasound frequencies in the range of 1-10 MHz (Fig. 1a). The cells accumulated at the acoustic pressure nodes, with the observed cell assemblies matching pressure field modeling and empirical measurements from 2D hydrophone scans.[4,5] The acoustic patterning process was shown to be rapid (<1 min for cells suspended in culture media) and responsive to dynamic changes in the applied ultrasound field (Fig. 1b).[4] In order to apply this acoustic cell patterning protocol for musculoskeletal tissue engineering, we next sought to immobilize the cellular arrays within different cell-compatible biomaterials, including hydrogels based on agarose, fibrin, Matrigel, norbornene-functionalized poly(ethylene glycol), collagen and gelatin methacryloyl (GelMA). While we observed consistent acoustic cell patterning across these different biomaterial systems, we noted that the higher viscosity precursor solutions negatively affected the quality of the formed arrays.[3] We developed a Voronoi tessellation algorithm to quantitatively determine these viscosity limits, and also the impact of different ultrasound frequencies, amplitudes, and exposure times.[5] This enabled thorough optimization of key parameters, which was used to generate biomaterials with highly uniform, densely-packed cell arrays.

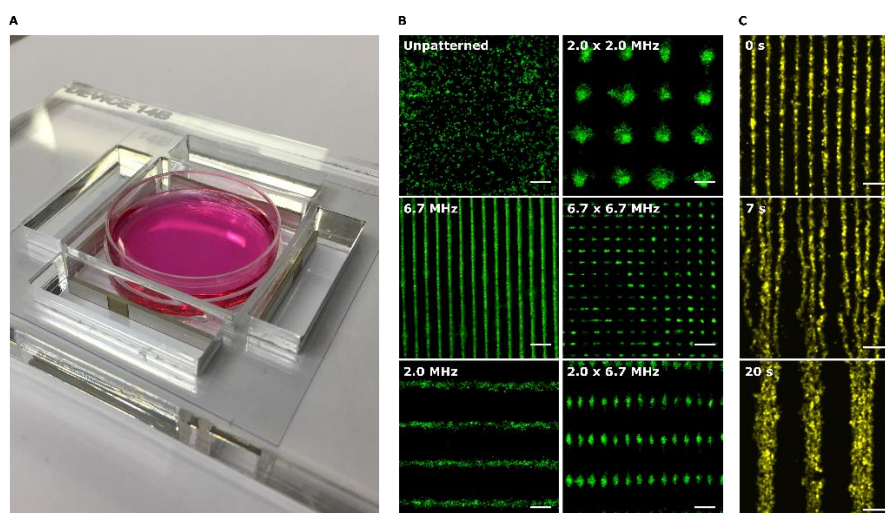


Figure 1: (a) Image of a typical acoustic cell patterning device. A cell culture dish is placed at the center of an orthogonal pair of piezotransducers, which were used to generate ultrasound standing waves and create static pressure fields for cell patterning. (b) These devices were used to form geometric arrays of cells that could be readily tuned by adjusting the pressure field parameters. (c) Dynamic acoustic cell patterning was demonstrated by starting with a high-frequency ultrasound field (6.7 MHz, 0 s) and then transitioning to a lower frequency field (2.0 MHz, 20 s). Scale bars: 200 μ m.

Musculoskeletal Tissue Engineering

We used acoustic patterning in combination with different cell-biomaterials systems for a range of musculoskeletal tissue engineering protocols. For example, 2.0-2.1 MHz ultrasound standing waves were used to pattern skeletal myoblasts into collagen-based hydrogels for skeletal muscle tissue engineering. Parallel cell fibers were chosen to mimic the anisotropic structure of the native tissue. Myoblasts patterned in type I collagen hydrogels contracted the surrounding biomaterial to produce high-density muscle fibers, anisotropic tensile mechanics, and a remodeled extracellular matrix. Indeed, the cell-mediated contraction was used in combination with static mechanical loads to generate, to the best of knowledge, the first instance of an engineered tissue construct exhibiting both cell-level orientation and widespread tissue alignment.[4] We used a similar acoustic field to pattern skeletal myoblasts in hydrogels of GelMA, a photo-crosslinkable form of denatured collagen. The covalently formed crosslinks, high weight fraction, and amorphous structure of the hydrogel enabled a maintained tissue size for long-term culture and unhindered observation of the later stages of tissue development. This model was used to demonstrate that acoustic cell patterning can significantly enhance myofibrillogenesis during skeletal muscle tissue engineering. Negligible myoblast fusion was observed in the unpatterned tissue controls after 7 d of myogenic differentiation, however, the acoustically-patterned muscle tissue exhibited upregulated MRF4, a key marker of myotube maturation, as well as the formation of large, multinucleated myotubes expressing key contractile proteins (α -myosin skeletal fast and tropomyosin, Fig. 2). These myotubes were aligned within the acoustically-patterned muscle fibers, with the patterning extending across entire tissue constructs (7 mm, \sim 350 cell widths).[4]

Finally, we sought to explore whether non-adherent hydrogels could be used for long-term retention of cellular arrays, with applicability in musculoskeletal tissue engineering protocols requiring extended culture periods. To this end, we acoustically-patterned primary cell cultures throughout the full volume of agarose hydrogels and performed a 6-week tissue engineering protocol. The resulting tissue constructs were then embedded, sectioned, and stained to reveal not only widespread extracellular matrix deposition but also the cultured cells located within their acoustically-patterned geometry.[6] It should be noted that for these acoustic cell patterning devices, we observed minimal heating in the central cavity ($<2.5^{\circ}\text{C}$ in 30 min), moreover, the field parameters used for tissue engineering had no significant effect upon the viability, proliferation, or differentiation of the ultrasound-exposed cells.[6]

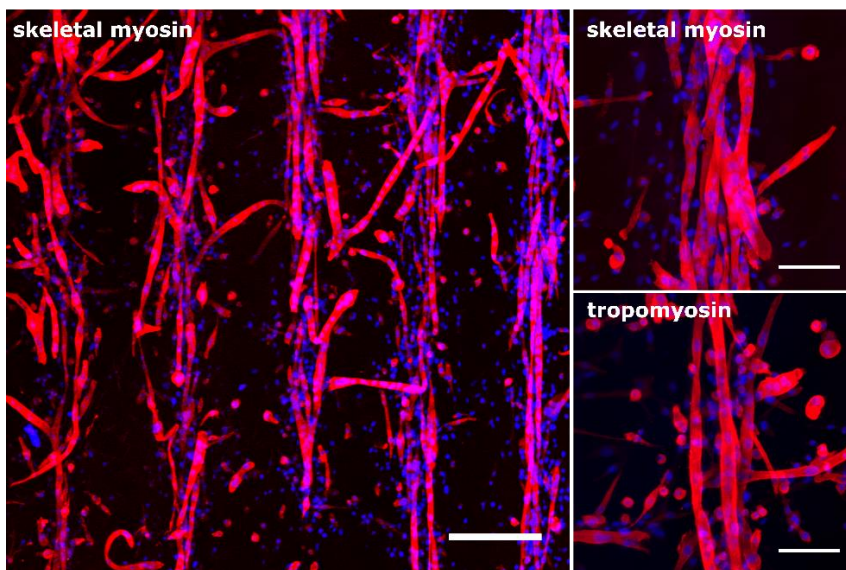


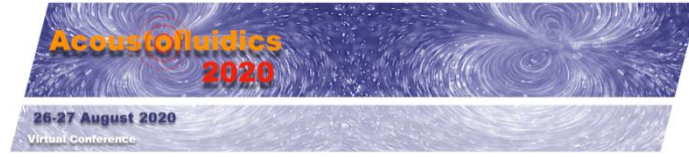
Figure 2: 2.0-2.1 MHz ultrasound standing waves were used to pattern skeletal myoblasts suspended in a 40 mg mL^{-1} GelMA precursor solution. After formation of the cell arrays, the GelMA was covalently crosslinked using a brief exposure to ultraviolet light. This allowed the cell array to be maintained in the absence of the ultrasound field. The cellularized biomaterial was then cultured for 8 d in myogenic medium. The resulting tissues were immunostained for the contractile proteins skeletal myosin and tropomyosin (red). This revealed aligned bundles of multinucleated myotubes, with the acoustic cell patterning enabling unidirectional myoblast fusion and cell-level orientation. Scale bars: $300\ \mu\text{m}$ (for low magnification images), $100\ \mu\text{m}$ (for high magnification images).

Conclusion

Here, we have demonstrated that acoustic devices supplying ultrasound standing waves can be used to remotely pattern cell arrays to generate cellular alignment across different musculoskeletal tissue engineering protocols. The ability to present organized cell structures over large length scales and extended time periods will be a critical factor in the engineering of functional tissue grafts and physiologically-relevant disease models. Indeed, the ability to rapidly and dynamically align label-free cells *en masse* using generic hydrogels and common cell culture apparatus makes this platform technology highly applicable to a host of next-generation tissue engineering strategies.

References

- [1] L. Ouyang *et al.* *Advanced Functional Materials* **30**, 1909009 (2020).
- [2] J. P. K. Armstrong and M. M. Stevens. *Trends in Biotechnology* **38**, 254-263 (2020).
- [3] A. Ozcelik *et al.* *Nature Methods* **15**, 1021-1028 (2018).
- [4] J. P. K. Armstrong *et al.* *Advanced Materials* **30**, 1802649 (2018).
- [5] J. P. K. Armstrong *et al.* *Lab on a Chip* **19**, 562-573 (2019).
- [6] Unpublished data.



Three-dimensional manipulation of particle by acoustic twisted focusing beam

Xiangxiang Xia¹, Feiyan Cai¹, and Hairong Zheng¹

¹Paul C. Lauterbur Research Center for Biomedical Imaging, Institute of Biomedical and Health Engineering, Shenzhen Institutes of Advanced Technology, Chinese Academy of Sciences, Shenzhen, China

E-mail: fy.cai@siat.ac.cn

E-mail: hr.zheng@siat.ac.cn

Introduction

Particle manipulation is very important for applications in fields such as physics, biology, and biomedical and medical sciences. Since Ashkin and Wu realized particle manipulation by light [1] and sound [2], respectively, particle manipulation by optical forces and acoustic forces has attracted a great deal of research attention. Sound manipulation has received more and more attention due to the advantages of deep penetration depth in light opaque media and weak biological damage. Recently, an acoustic wave with angular momentum is used to trap and rotate objects [3, 4], and the typical acoustic field is identified as acoustic vortex beam. However, most of the previous works of particle manipulation by acoustic vortex are in a two-dimensional plane or a small three-dimensional (3D) range. We investigate 3D spiral manipulation of particle for a large range with an acoustic twisted focusing beam, which induced by an acoustic metasurface structured logarithmic-spiral groove. Benefiting from the in-plane symmetry topologically breaking, the metasurface continuously modulates both amplitude and phase in the diffraction field to shape twisted focusing of the acoustic vortex beam, which is subwavelength confined and spatially spiraling with variant crescent-shaped transverse intensity profiles. Due to its rich structural degree of freedom upon aperiodic and continuously variant features, the metasurface provides a compact solution to generate and control sound vortices carrying scalable orbital angular momentum (OAM) [5]. Further, we exhibit acoustic angular momentum transfer to an acoustic absorptive matter, which is verified by a PDMS particle spiraling up in water in the acoustic field of the generated acoustic twisted focusing beam.

Design of acoustic metasurface

Consider the metasurface structured with one-armed coiling groove (blue region in Fig. 1a) for generating acoustic twisted focusing beam with the topological charge $m=1$. The coiling groove can be mathematically interpreted in polar (r, φ) coordinates: $r = ae^{b\varphi}$, where the radial coordinate is denoted by r and the angular coordinate by φ . The factor a and the azimuthal factor b determines the initial radius of spiral curve and the growth rate of rotation, respectively.

For the silicone acoustic metasurface, the groove is enclosed with two logarithmic-spiral curves, and the overall structural parameters of the two curves in the polar coordinates are expressed as: $r_1 = a_0 e^{b\varphi}$ and $r_2 = (a_0 + w)e^{b\varphi}$, respectively. The initial radii of the two curves are $a_0 = 4\text{mm}$ and $a_0 + w = 4.5\text{mm}$, where $w = 0.5\text{mm}$ is the width of the spiral groove, the azimuthal factor $b = 0.2$, and the logarithmic-spiral groove grows from $\varphi_1 = 0$ to $\varphi_2 = 10\pi$. The schematic view of the metasurface as shown in Fig. 1a.

Intensity distribution of acoustic twisted focusing beam

The numerically simulated intensity distributions of the twisted focusing beam on the x - z and y - z plane are shown in Figs. 1b where a twisted focusing beam forms in front of the metasurface. To further demonstrate the spatial intensity distribution, a summary of the simulated and measured intensity and phase distributions of the twisted focusing beam in x - y planes at different heights along the propagation direction ($z = 11\text{mm}$, 13mm , 15mm) are illustrated in Fig. 1c. As diffracted sound propagates, focuses of crescent transverse profiles are anisotropically formed as well as confined in a circular area of a diameter less than $\approx 1.3\text{mm}$ from the initialization at $z = 3.5\text{mm}$ till a distance of about $z = 25\text{mm}$, beyond which the sound density decaying and the confinement of transverse intensity profile gradually decreasing. The phase distributions explicitly show screw phase dislocation with a singularity at the center, which is the feature of acoustic vortex beam with continuous phase variation from $-\pi$ to π around its propagation axis.

Particle manipulation with the twisted focusing beam.

By using the acoustic twisted focusing beam, we can clearly observe the real-time PDMS particle 3D spiral manipulation on the side and top. Figure 2a shows the side view snapshots of the PDMS particle at the time of $t = 1.5\text{s}$, $t = 2.0\text{s}$, $t = 2.5\text{s}$, $t = 3.0\text{s}$. These snapshots demonstrate the PDMS particle can be translated along a 3D curved path, as the positions of the particle at different times shown in Fig. 2b. From the top view, as Fig.

2c shows, the PDMS particle manipulated in the twisted focusing field at the time of $t=1.5s$, $t=2.0s$, $t=2.5s$, $t=3.0s$. The positions of the particle at different times shown in Fig. 2d demonstrate the particle rotating along a circle path at the top view. Supplementary movie gives more details about the process. The experimental results perfectly confirm acoustic soft material can be 3D spiral manipulation with twisted focusing beam induced by an acoustic metasurface with logarithmic-spiral structure.

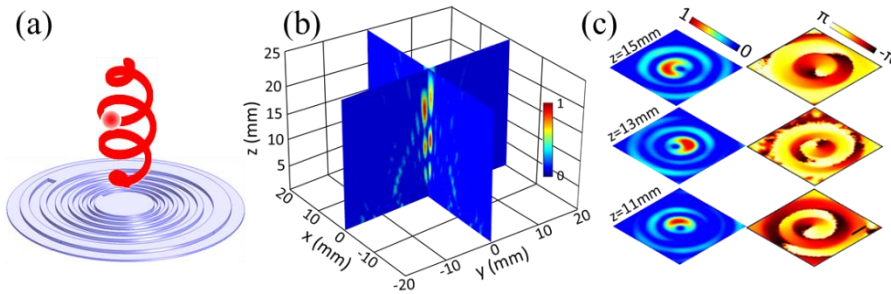


Figure 1: Pressure intensity distributions of acoustic twisted focusing beam. (a) Conceptual schematic of 3D spiral manipulation of a PDMS particle by using a twisted focusing beam generated by an acoustic metasurface. (b) The numerically simulated intensity distributions of the twisted focusing beam on the x-z and y-z plane. (c) The numerically simulated distributions of sound and phase fields on the x-y planes at different heights.

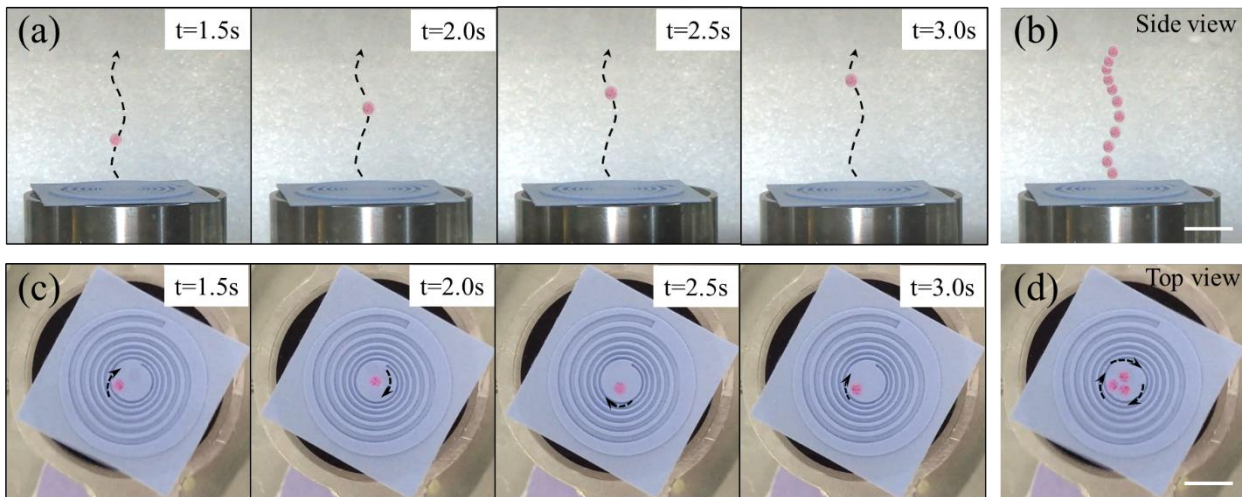


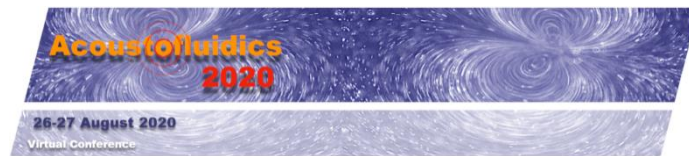
Figure 2: 3D spiral manipulation of a PDMS particle in water. (a) Side view snapshots of the PDMS particle at the time of $t=1.5s$, $t=2.0s$, $t=2.5s$, $t=3.0s$. (b) A set of images stacked together from side view showing the trajectory of the PDMS along a curved path. (c) Same as (a) but for top view. (d) Same as (b) but for top view, showing the trajectory of the PDMS particle along a curve path.

Conclusion

We demonstrate a 3D spiral manipulation of PDMS particle with an acoustic metasurface structured with logarithmic-spiral groove. In combination with the numerical simulation and experimental verifications, the metasurface is able to shape twisted focusing of acoustic vortex beam to be subwavelength confined during propagation with a long depth of focus. The diffracted beam spatially propagates with variant transverse intensity profiles in contrast to traditional spirally waves of invariant profiles. Due to the intrinsically rich degree of freedom to govern the interaction with sound, the acoustic metasurface is able to produce controllable and scalable OAM. The metasurface can potentially act as an inexhaustible-OAM turbine and opens a new opportunities for 3D dynamic manipulation of particles.

References

- [1] A. Ashkin. Phys. Rev. Lett. **24**, 156-159 (1970).
- [2] J. W. J. Acoust. Soc. Am. **85**, 2140-2143 (1991).
- [3] A. Marzo, S. A. Seah, B. W. Drinkwater. Nat. Comm. **6**, 9661 (2015).
- [4] T. Wang, M. Ke, P. Li. Appl. Phys. Lett. **109**, 123506 (2016).
- [5] H. Liu, et al., Adv. Opt. Mat. **2**, 1193-1198 (2014).



Simulated and Experimental Demonstrations of Acoustic Hologram Enhanced Phased Arrays for Manipulation

Luke Cox¹, Kai Melde², Anthony Croxford¹, Peer Fischer^{2,3} and Bruce Drinkwater¹

¹Department of Mechanical Engineering, University of Bristol, Bristol, United Kingdom

E-mail: luke.cox@bristol.ac.uk, URL: <http://www.bristol.ac.uk/engineering/people/luke-e-cox/index.html>

²Micro, Nano and Molecular Systems Group, Max Plank Institute for Intelligent Systems, Stuttgart, Germany

³Institute of Physical Chemistry, University of Stuttgart, Stuttgart, Germany

Introduction

The ability to shape ultrasound fields is important for particle manipulation, medical therapeutics, and imaging applications. If the amplitude and/or phase is spatially varied across the wave front, then it is possible to project “acoustic images.” This projection effect is most well known in optics but has previously been demonstrated successfully in underwater ultrasound using 3D printed holograms [1].

When attempting to form an arbitrary desired static sound field, acoustic holograms are superior to phased arrays due to their significantly higher phase fidelity – i.e. it is possible to use millions of pixels in the hologram, but phased arrays are limited by cost to 100-1000 emitters. However, holograms lack the dynamic flexibility of phased arrays. We demonstrate how to combine the high-fidelity advantages of acoustic holograms with the dynamic control of phased arrays with application to particle manipulation.

Holograms are used in conjunction with a 64-element phased array, driven with continuous excitation. Movement of the position of the projected hologram via phase delays that steer the output beam is demonstrated experimentally. This combination allows the creation of a much more tightly focused point than with the phased array alone, while still being reconfigurable. It also allows the complex movement at a water-air interface of a “phase surfer” along a phase track or the manipulation of a more arbitrarily shaped particle via amplitude traps. This approach opens the door for new applications with complex manipulation of ultrasound while minimizing the complexity and cost of the apparatus [2].

Information Density

The primary advantage of an acoustic hologram over a phased array is the increase in the information density, which scales with the number of independent phase channels (or pixels) of the system. For a phased array, this is equivalent to the number of individual transducer elements. For a printed acoustic hologram, this translates to the surfaces that can be resolved by the reconstructing wave (i.e., pixels of diffraction-limited size).

We use acoustic field simulations employing an iterative angular spectrum approach [1] to compare the performance in terms of the quality of a projected ‘R’-shaped field of an 11x11 element phased array with a 134x134 pixel acoustic hologram with the same surface area. The correlation coefficient between the generated field and the target for the phased array was 0.158, whereas for the hologram it was 0.683. This demonstrates that the much higher information density possible with a hologram leads to higher quality projected fields, however the hologram lacks any dynamic capabilities.

Steering the Holographic Sound Field

When all the elements of the phased array are fired in phase the output is a close approximation of a plane wave [3]. By applying phase delays this plane wave can be steered to propagate at a different angle. By placing a hologram on the phased array surface, we can steer the output field of the hologram by the steering angle of the plane wave. As the steering is controlled from the phased array this can be controlled dynamically. By steering this output field manipulation can be achieved. The experimental set up is illustrated in Figure 1.

Focused Point Movement

The movement of a focused point generated by a hologram was initially used as a validation that the system worked as expected. Using thermochromic film, which changes color in response to the acoustic pressure induced pressure changes, the fields could be visualized. This showed that the observed movement of the focused point agreed with acoustic field simulations. A small disk was then placed at the peak generated on the water surface by the high acoustic pressure field. The disk could be easily tracked with a camera and, by observing its location and movement, good agreement with prediction could be seen. These two measures provide confidence in the accuracy of the acoustic simulations.

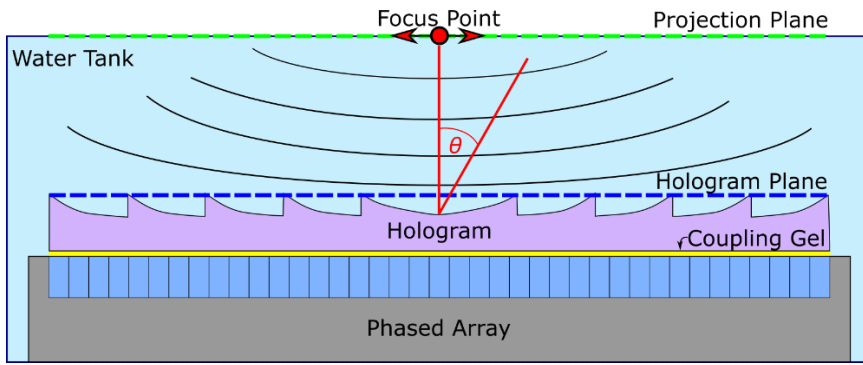


Figure 1: A diagram of the phased array and hologram system used in the experiments. A 64-element array at the bottom is able to steer the plane-wave output. This array is coupled to the 3D-printed hologram with a coupling gel. The red dot represents a particle trapped in the projection plane and moved in the directions indicated.

Phase Circle Manipulation

Having demonstrated that the combination of holograms and phased arrays worked as expected we turned our attention to more complex behaviour to demonstrate the full potential of this technique. Phase surfers have previously been demonstrated as a technique for creating dynamic motion with a static hologram [1]. In the original technique, a hologram was used to create a shaped pressure ridge on the water surface with a phase gradient. A small disk is held in place on the ridge via surface tension and travels down the phase gradient. We created a simple phase gradient around a circle. Using a static hologram this would carry the disk around the circumference of this circle indefinitely. In our system we steered the circle and tracked the location of the disk as it followed these varying paths. We found that the range of steering for this more complex system was more limited than for the focused point however the circular motion was still observed. The paths are shown in Figure 2 along with the average centre location, which also has reasonable agreement with acoustic field simulations. We found that this high-pressure circular ridge could also be used to manipulate a relatively large polystyrene sphere, suggesting more complex high-pressure traps generated by holograms may be viable for applications with a wider range of particles.

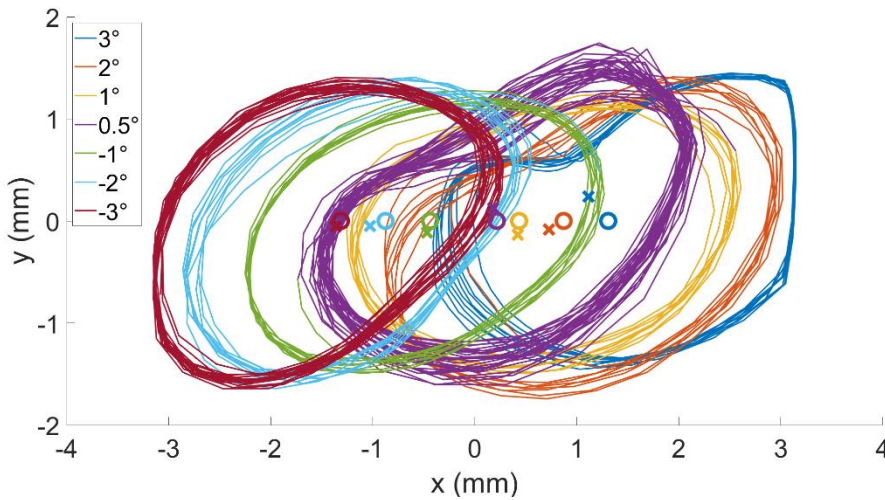


Figure 2: The behavior of the phase surfer on the circular phase gradient path. The tracked paths of the phase surfer as the beam is steered from an angle of 3° to -3° . The paths of different colors represent different steering angles. The correspondingly colored crosses are the experimental path centers and the circles the theoretical path centers.

Conclusion

We have shown that combining a multi-element phased array with a static hologram enables the generation of complex and dynamic ultrasound fields, which is promising for applications including particle manipulation. The approach was explored in both simulations and experiments and good agreement was observed. The approach offers a new route to spatial control of particles with no moving parts, which has potential to benefit a number of contactless processing applications.

References

- [1] Melde, K., et al. "Holograms for acoustics." *Nature* 537.7621 (2016): 518-522.
- [2] Cox, L., et al. "Acoustic Hologram Enhanced Phased Arrays for Ultrasonic Particle Manipulation." *Physical Review Applied* 12.6 (2019): 064055.
- [3] Drinkwater, B. W., and P. D. Wilcox. "Ultrasonic arrays for non-destructive evaluation: A review." *NDT & E International* 39.7 (2006): 525-541.

Acoustofluidic bidirectional micropump

Yuan Gao¹, Mengren Wu¹, Yang Lin¹, Weiqi Zhao¹, and Jie Xu¹

¹Department of Mechanical and Industrial Engineering, University of Illinois at Chicago, Chicago, IL
 E-mail: ygao51@uic.edu, URL: <https://xu.uic.edu/>

Introduction

Efficient transportation of fluids and microparticles is an important function in many biomedical applications. Comparing with conventional syringe pumps, microfluidic pumps have the advantage of easy integration with other on-chip functional units to realize portable micro total analysis systems (μ TAS) [1]. However, there still exist challenges in most microfluidic pumps, including complex fabrication processes, expensive materials and setup, and limited flow control. To address these issues, acoustic bubble has been employed as a promising tool in fluids and particle transportation [2]. For instance, the acoustic bubbles have been successfully applied in pumping and mixing fluids in microchannel with high efficiency [3, 4]. In this work, we develop a method via creating cavity structures inside a recirculated microchannel to trap air bubbles for generating bi-directional acoustic microstreaming flow for pumping fluids and biological samples (Fig. 1a). Based on theoretical calculation and experimental results, the flow direction and flow rates are accurately controlled in the microchannel by controlling the applied frequency and voltage applied to the piezoelectric actuator. Furthermore, the acoustic bubble-based pumping device is implemented in driving blood-mimicking fluid (BMF) and *Escherichia coli*, demonstrating potential real applications of bidirectional fluid flow control.

Experimental method

To avoid randomly trapped bubbles at the corner, we designed a ring-shaped recirculated channel to demonstrate the pumping flow. Two small ($120\ \mu\text{m} \times 175\ \mu\text{m}$) and two large ($320\ \mu\text{m} \times 275\ \mu\text{m}$) cavity structures were oppositely placed in the center of microchannel as shown in Fig. 1a. The Polydimethylsiloxane (PDMS) microchannel with pre-designed cavity structures was fabricated using standard soft lithography and mold replica technique. The PDMS microchannel was then bonded on glass microscope slide using plasma treatment. To activate the device, a piezoelectric transducer adhered to the glass slide, which was driven by a function generator and amplified by a voltage amplifier. Microparticle image velocimetry (μ PIV) was applied to quantitatively characterize the velocity field around the microbubbles (Fig. 1d and 1e).

Results and discussion

The working mechanism of this acoustofluidic bi-directional micropump is shown in Fig. 1a. Due to surface tension, air was passively trapped inside cavity structures and liquid-air interfaces were generated when liquid flow through the microchannel. When exposed to the acoustic field activated by an external piezoelectric transducer, the air-liquid interfaces started oscillate, and the microstreaming flow was generated as the driving frequency was close to the resonant frequency of the bubbles. The different sized cavity structures oppositely

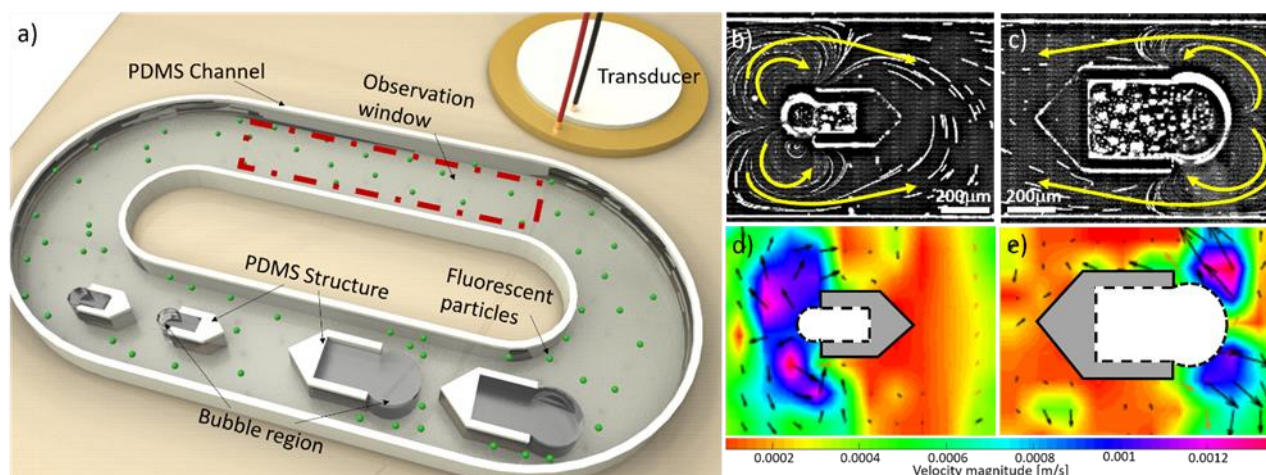


Figure 1: a) Configuration of the acoustofluidic bidirectional micropump device and piezoelectric transducer; b, c) acoustic microstreaming flow induced by different sized bubbles; d, e) the velocity profile inside the microchannel of the acoustofluidic bidirectional micropump device given by particle image velocimetry (PIV) measuring technique.

faced each other in the center of the lower channel. Thereby the opposite directional microstreaming flow was achieved by adjusting the applied frequency, as shown in Fig. 1b and 1c.

To further demonstrate the pumping behavior, we analyze images from a defined observation window, located at the center of the upper channel (Fig. 1a), and studied the movement of microparticles. Specifically, with the frequency of 24 kHz, the small bubbles were actuated and the microparticles were moving from right to left in the flow. Conversely, the oscillating large bubbles pump particles in the opposite direction by tuning the frequency to 19 kHz. To obtain the optimum pumping performance for the two directions at the constant voltage, the frequency was swept around theoretical resonant frequencies. From the results, the peak flow rate occurs when the driving frequencies are 19 kHz and 24 kHz, respectively (Error! Reference source not found. 2a). To further characterize the pumping behavior, we explored the influence of the applied voltage on the pumping performance. As shown in Fig. 2b and 2c, with increasing voltage, the pumping flow rate increased significantly. For the small bubbles induced counterclockwise flow, the flow rate rises from 50 nl/min to 1200 nl/min. For the large bubbles induced clockwise flow, the flow rate can achieve from 20 nl/min to 1600 nl/min.

According to a recent study on human blood viscosity [5], we added glycerol into DI water to adjust the viscosity and made the blood-mimicking fluid (BMF). As shown in Fig. 2d, the micropump is capable of driving up to 50% glycerol/water mixture, which is 8 times more viscous than water. In addition, we proved its performance for pumping *E. Coli*. It is important to test the viability of *E. coli* cells, since the cells could be damaged under strong forces. Fig. 3 shows the cell viability before and after 10 min actuation of the micropump. The cells highlighted by a yellow circle demonstrates a living cell, and the cell marked by a red circle indicates a dead one. From these results, we can conclude that the micropump does not cause perceptible damage to the cells after acoustic excitation, which makes it suitable for handling biological samples.

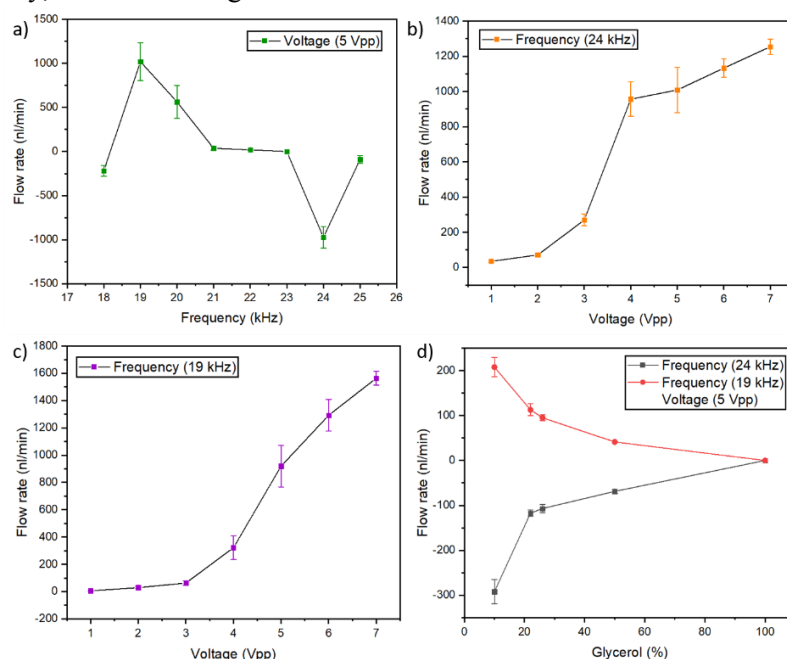


Figure 2: a) Plot of pumping flow rate versus driving frequency; b, c) pumping flow rate versus the voltage at frequency of 24 kHz and 19 kHz, respectively; d) plot of the pumping flow rate versus glycerol concentration at 5 Vpp demonstrating high viscosity fluid pumping.

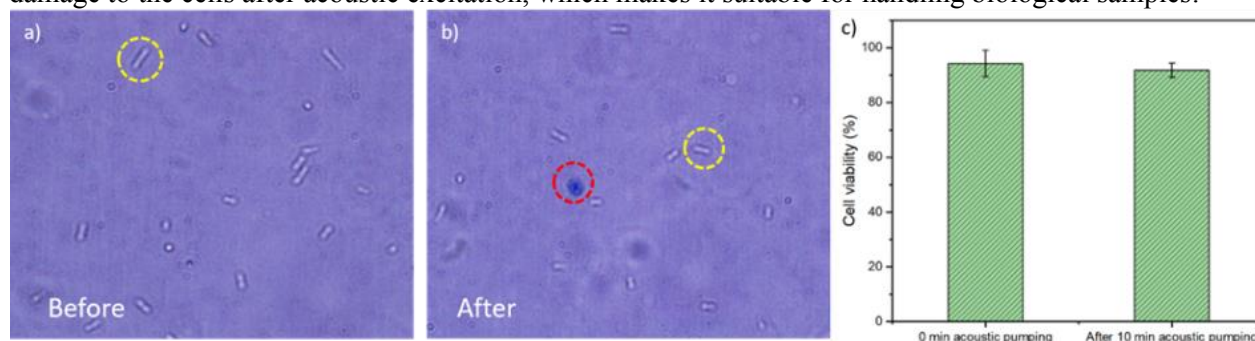


Figure 3: After acoustic excitation, most *E. coli* cells were still alive. The *E. coli* cell viability was evaluated at (a) 0 min; (b) 10 min; (c) cell viability test results before and after 10 min acoustic pumping.

Conclusion

In this study, a novel acoustofluidic bidirectional micropump was demonstrated for lab-on-a-chip applications. This inexpensive, portable and acoustofluidic bidirectional pump for transporting fluids and particles has great potential to integrate with other on-chip platforms for multiple biological and chemical applications, such as drug delivery, cell separation, and chemical analysis.

References

- [1] P. S. Dittich, K. Tachikawa and A. Manz. *Analytical Chemistry* **78**, 3887-3908 (2006).
- [2] A. Hashmi, G. Yu, M. Reilly-Collette, G. Heiman and J. Xu. *Lab on a Chip* **12**, 4216-4227 (2012).
- [3] A. R. Tovar, M. V. Patel and A. P. Lee. *Microfluidics and Nanofluidics* **10**, 1269-1278 (2011).
- [4] D. Ahmed, X. Mao, J. Shi, B. K. Juluri and T. J. Huang. *Lab on a Chip* **9**, 2738-2741 (2009).
- [5] M. Y. Yousif, D. W. Holdsworth and T. L. Poepping. *Experiments in Fluids* **50**, 769-774 (2011).

Controlled Manipulation and Active Sorting of Particles inside Microfluidic Chips using Bulk Acoustic Waves

Kyriacos Yiannacou¹ and Veikko Sariola¹

¹Faculty of Medicine and Health Technology, Tampere University, Tampere, Finland
 E-mails: kyriacos.yiannacou@tuni.fi, veikko.sariola@tuni.fi, URL: <http://research.tuni.fi/bmr-group>

Introduction

In this work, we present controlled manipulation of particles (~70 – 100µm) using bulk acoustic waves inside closed-channel microfluidic chips, by dynamically changing the frequency of a single ultrasound transducer in a closed loop manner. The position of the particles is tracked using machine vision and this information is used by the controller to decide which frequency to apply. Previously, similar manipulation methods have been successfully used to manipulate particles on a vibrating open plate.¹⁻⁴ In this paper, we show that such manipulation principles can work well also in closed-channel microfluidic devices. Closed-channel microfluidics poses a new problem for the method: one cannot manually place the particles at any given location inside the manipulation chamber, so performing calibration or learning experiments^{1,3} is difficult. We solved this problem by using a family of well-known machine learning algorithms called multiarmed bandits. Multiarmed bandit methods can achieve controlled manipulation with minimal learning: the device can successfully position a particle anywhere inside the chamber on its first try, by “learning as it goes”. We demonstrate that the method can be used to sort particles coming through one inlet into one of three different outlets, chosen at will. This method is robust to changes in chip/sample and object properties, such as changes in particle size, with the potential trade-off of longer manipulation times.

Methods

The schematic of our experimental setup is shown in Fig. 1a. The apparatus consists of a glass microfluidic chip, a piezoelectric transducer (CTS-Noliac, NCE 46, 15mm × 15mm × 2mm) mounted on the backside of the chip, a camera to image the particles inside the chip, a computer running the machine vision and control algorithms, a signal generator and an amplifier. Inside the chip, there is a rectangular chamber with dimensions of 7 mm × 6 mm × 0.15 mm.

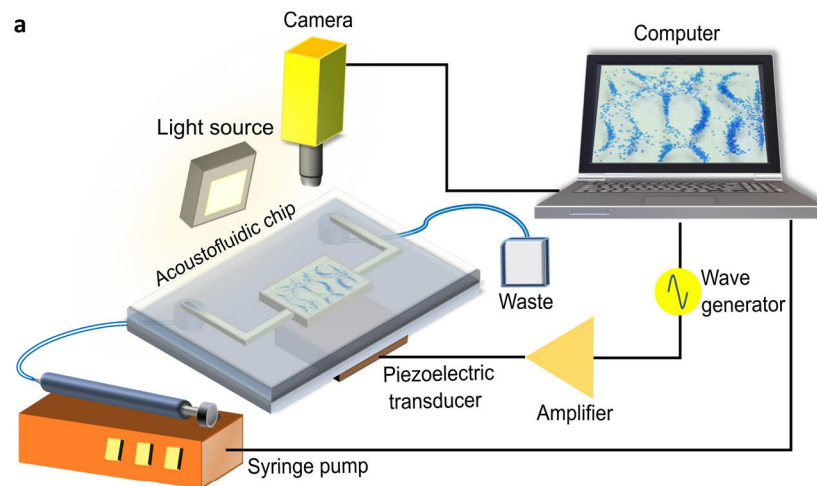
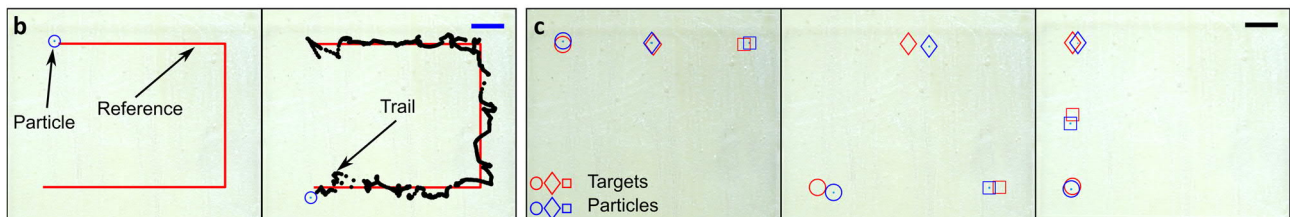


Figure 1: Schematic of the experimental setup and manipulation results. **a)** The experimental setup includes a glass microfluidic chip, actuated by a piezoelectric actuator. The particle motions and locations are captured by a camera and processed by a computer. A syringe pump is used to pump new particles to the chamber. **b)** Single particle manipulation: one particle is guided along a reference path. **c)** Multi-particle manipulation: three particles are driven to different target points within the chamber. All scale bars: 1 mm.



The control algorithms used to perform particle manipulation are UCB-1 and ϵ -greedy.⁵ Briefly, at each time step, with the probability ϵ , the ϵ -greedy algorithm applies any random frequency (*exploration*). Otherwise (with the probability $1 - \epsilon$), the algorithm chooses the frequency that has the best average reward in past (*exploitation*). The reward is simply how many pixels the particle has moved towards its target. The number of frequencies that the algorithm chooses from was 100, linearly spaced in the range 70 – 700 kHz. The second algorithm tested is UCB-1, which constructs a confidence interval for the rewards of each frequency, and optimistically assumes that each frequency will result movement equal to its upper confidence bound (UCB). The frequency with the highest UCB is chosen.

The rewards are expected to depend on the location of the particle inside the chamber: the rewards change as the particles moves about inside the chamber. Therefore, we incorporated an exponentially decaying memory to the controller: when taking the average rewards, the rewards are weighted proportional to λ^{-t} , where λ is the weight factor and t is the number of control steps since that reward.⁶ This exponentially decaying memory ensures as the particle moves inside the chamber, the rewards for playing different frequencies vary, and thus older rewards are discounted.

Results

To test how our method performs when manipulating a single particle, we generated a square-shaped path of waypoints around the chamber. When the particle was within 300 μm of a waypoint, a new waypoint along the path was chosen. The results are shown in Fig. 1b. The duration for completing the manipulation tasks varies for each run, from 20 minutes up to 2 hours.

Our method trivially extends to multiparticle manipulation: the reward is simply how much all particles move towards their targets on average. We tested such manipulation with three particles. In these experiments, we only used a few, coarsely spaced waypoints, as the manipulation is considerably slower (~ 1.43 hours) due to the coupled motion of the particles. The controller manages to uncouple the particle motion and move all the particles to their target points.

Finally, we demonstrated a practical application of our method in active particle sorting. For these experiments, a different chip with a single inlet and three different outlets was used (Fig. 2a). In our first experiments, we gave the controller a single way point, right at one of the outlets. The results for 30 particles sorting experiments (10 particles per outlet) are shown in Fig 2b. Out of 30 particles, 5 were missorted, with average sorting time of 13 min. The missortings were caused by a slight negative pressure at the middle outlet (Outlet 2, Fig. 2a): with a single way point, the controller may accidentally push the particle close to a wrong outlet and the particles were drawn into the wrong outlet due to the presence of this slight negative pressure. To avoid such missortings, we designed a second experiment where we added several of ‘guiding’ waypoints for the particles to follow, to avoid going too close to the wrong outlets (Fig. 2d, right). Fig. 2c shows the results. All 30 particles were correctly sorted, with the trade-off of slightly longer sorting times (average 20 min per particle)

Conclusions

In this work, we have demonstrated controlled 2D manipulation of single and multiple particles inside closed-channel microfluidic chips using a bulk acoustic waves from a single piezoelectric transducer. The method uses closed-loop control-based machine vision tracking of the particles and machine learning. We demonstrate active particle sorting using the method.

Our method can successfully position the particles with minimal learning and without any calibration experiments. Our method is not limited to predefined channel/chamber shapes but adapts to any environment, as long as the ultrasound power is sufficient to move the particles and different frequencies move the particles in a different way. Thus, our method paves the way towards acoustic manipulation in unstructured environments, perhaps even *in vivo*.

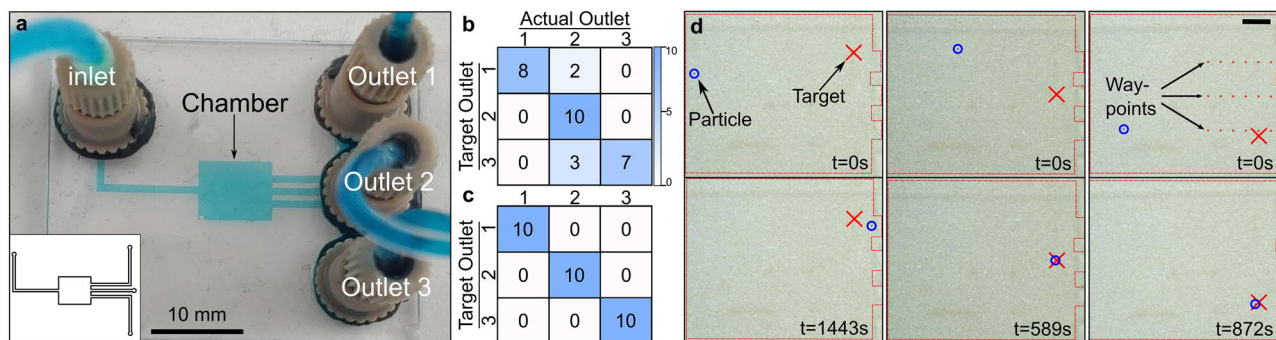


Figure 2: Particle sorting experiments. a) Photograph of the particle sorting chip. The chip consists of a single inlet and three outlets. b) Confusion matrix of particle sorting experiments with a single way point, placed right at each outlet. c) Confusion matrix of particle sorting experiments with multiple waypoints leading to each outlet. d) Snapshots of actual particle sorting experiments. Scale bar: 1 mm.

References

- 1 Q. Zhou, V. Sariola, K. Latifi and V. Liimatainen, *Nat. Commun.*, 2016, **7**, 12764.
- 2 K. Latifi, H. Wijaya and Q. Zhou, *Phys. Rev. Lett.*, 2019, **122**, 184301.
- 3 K. Latifi, A. Kopitca and Q. Zhou, *IEEE Access*, 2020, **8**, 20597–20606.
- 4 K. Latifi, H. Wijaya and Q. Zhou, in *2017 International Conference on Manipulation, Automation and Robotics at Small Scales (MARSS)*, IEEE, 2017, pp. 1–7.
- 5 V. Kuleshov and D. Precup, *J. Mach. Learn. Res.*, 2000, **1**, 1–48.
- 6 A. Garivier and E. Moulines, in *Lecture Notes in Computer Science (including subseries Lecture Notes in Artificial Intelligence and Lecture Notes in Bioinformatics)*, 2011, vol. 6925 LNAI, pp. 174–188.

Acoustic Trapping around Obstacles and Corners.

Asier Marzo¹, Marco A.B. Andrade², María A. Cuellar¹, Jaime Goñi¹, Ryuji Hirayama³, and Diego Martínez³

¹UpnaLab, Universidad Pública de Navarra, Pamplona, Spain
 E-mail: asier.marzo@unavarra.es, URL: <http://www.upnalab.com>
²Instituto de Física, Universidad de São Paulo, São Paulo, Brazil.
³Computer Science, University College London, United Kingdom.

Introduction

Acoustic Levitation can hold objects without physical contact due to the radiation forces exerted by certain sound fields. This technique can operate on different propagation media such as air or water-based solutions, and at scales ranging from micrometres to centimetres. Additionally, the materials that can be trapped include heavy gasses, liquids, solids, plastics, living matter or in general, any material that has enough acoustic contrast with the propagation medium. Consequently, acoustic levitation can become a fundamental tool for biosciences, chemistry or industrial micro-assembly. However, almost all the experimental and theoretical work has been centered on trapping in homogenous media and open space [1], yet most application scenarios involve obstacles in the domain. Being able to trap around obstacles or around corners would enable applications for in-vivo manipulation of particles inside the human body, contactless additive manufacturing on top of existing pieces, or retrieving samples from corners and inaccessible places.

Here, we theoretically explore using 2D models to what degree it is possible to trap around obstacles and corners. We start with a Finite Difference Time Domain (FDTD) simulation to calculate the total field (emitted + scattered) generated by each of the emitters. Then, by making linear combinations of these fields we can calculate the total field generated by all the emitters for a given emission amplitudes and phases. The Gor'kov potential at a certain point can be expressed as a function of the emission phases and minimized using an optimizer, thus creating a trap there. The negative gradient of the Gor'kov potential models the forces that a particle would experience inside the field [2]. We explore the possibility of trapping particles at different positions of a simulation with obstacles by analysing the maximum amplitude and minimum Gor'kov potential achievable at each point. As an initial exploration, the examples are $18 \times 18 \lambda$ (λ =wavelength) and contain 16 emitters at each side, e.g., for 40 kHz that would suppose a domain of 16×16 cm in air.

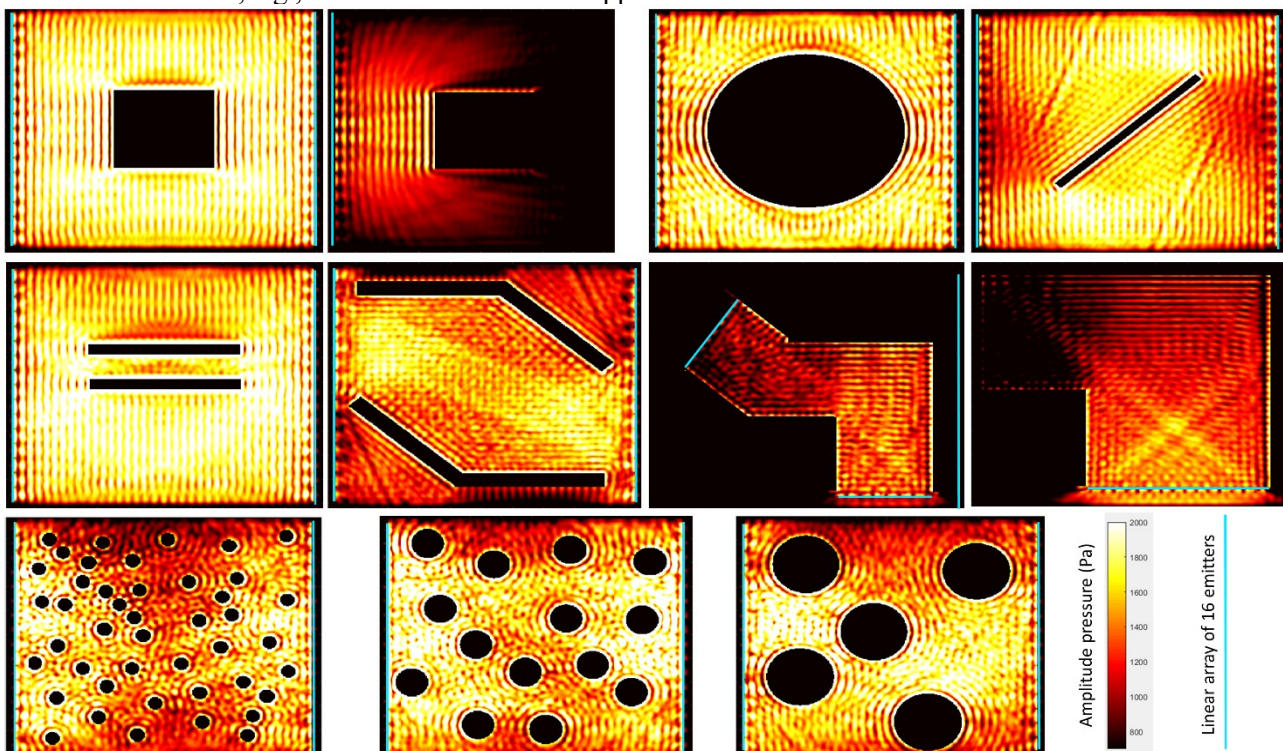


Figure 1: Amplitude pressure that can be obtained at each point when the array of emitters is focused at that point. The dimension of each simulation is 18×18 wavelengths (λ) and on each linear array there are 16 emitters.

Total acoustic field

The complex field generated by each emitter in a 2D domain is calculated using FDTDs with the linear wave equation, dividing the domain in 1024×1024 cells which makes each cell smaller than 0.02λ . The waves travel enough time to propagate 4 times along the domain, and then they are measured during 2 periods to transform the time simulation into the frequency domain. With the complex field generated by each emitter, any combination of their emission amplitudes and phases can be obtained by a linear combination of their emitted fields.

Focusing

To focus the array at a point, the phase of each emitter is set to the negative phase that it generates at that point. The arrays are focused at each point of the simulation and the amplitude there is measured. We show the maximum amplitude that can be focused at each position for different configurations in Figure 1. In general, it is not possible to focus at the other side of a large obstacle; around corners, the arrays can focus a certain depth around the corner.

Trapping

Traps at each point of the simulation can be created by minimizing the Gor'kov potential at that point, using the emission phases as parameters. We used the simplex method with 2000 iterations as implemented in the function *fminsearch* of Matlab 2017. Approximately, similar results to the focusing capabilities are obtained for trapping. As can be seen in Figure 2, the points where high amplitude pressure can be obtained are also points with minimum potential (i.e. yellow and light blue parts).

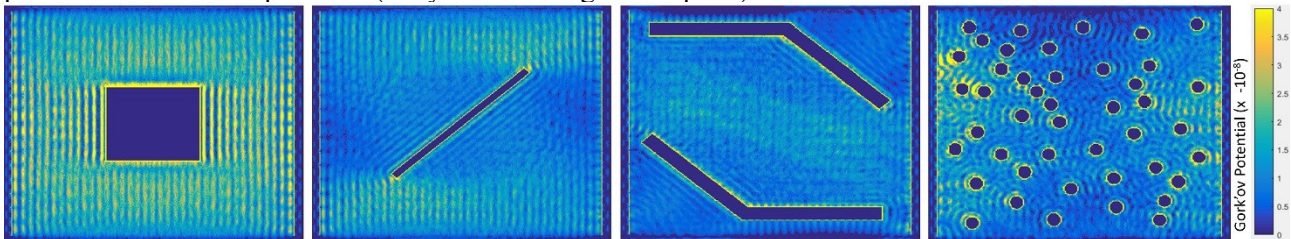


Figure 2: Gor'kov potential that can be obtained when it is minimized at each point as a function of the emission phases. The lower the potential, the stronger the trapping there; note that the scale bar is inverted. Simulations are $18 \times 18\lambda$ in size and have 16 emitters at both the left and right border. The potential is calculated for a 0.3λ diameter solid particle.

Towards the experiments

The experimental realization of the presented simulations is not trivial. Since the simulations are in 2D, we could use extruded experimental versions. Another possibility is to make the experimental obstacles flat on top of a surface and cover the top with a reflector lid. The major difficulty is how to obtain the total field of each emitter at each point of the experimental setup. We are exploring the following options:

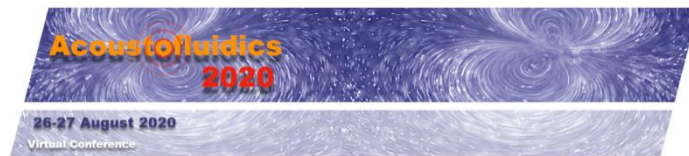
- Values from the simulations can be used for the experiment. However, any misalignment and variability in the emitters may render the simulation results no applicable to the experiments, especially for points where the trapping forces are very small.
- Measurements with a microphone. A needle microphone or a fragment of piezo can be used. If the experiments are done in air at 40 kHz, a microphone point smaller than 0.25 mm would be desired. To trap the particle and move it along a path, only 4 measurements around each path position need to be taken. Note the minimization of the Gor'kov at a point needs the spatial derivatives of the pressure.
- Schlieren photography or laser vibrometry may not have enough sensitivity to detect the emission of an individual emitter; also, Schlieren cannot get the phase with common methods. To solve the sensitivity problem or the lack of phase information, we propose the following method. The total amplitude field for different combinations of known emitting phases and amplitudes with all the emitters emitting at the same time will be captured several times. With enough “captures”, there are more known variables than unknowns and the total field for each emitter can be solved for.

Conclusion

We have shown 2D simulations for the focusing and trapping capabilities of ultrasonic arrays in domains which contain obstacles and corners. In general, we predict the possibility of trapping around small obstacles and around corners, with a limited reach. We have also discussed possible experimental realizations. A deeper exploration is needed to characterize better the capability of acoustic trapping to work around obstacles and corners. This capability can lead to contactless additive manufacturing and the development of in-vivo manipulation of drug capsules or surgical microbots.

References

- [1] A. Marzo, S. A. Seah, B. W. Drinkwater, D. R. Sahoo, B. Long, and S. Subramanian. Nature communications **6**, 8661 (2015).
- [2] H. Bruus. Lab on a Chip **12**(6), 1014-1021 (2012).



Acoustic particle trapping in a spherical microchamber

Bettina Sailer, Rune Barnkob, and Oliver Hayden

Heinz-Nixdorf-Chair of Biomedical Electronics, Department of Electrical and Computer Engineering, TranslaTUM, Technical University of Munich, Munich, Germany
E-mail: Bettina.Sailer@tum.de, URL: <https://www.ei.tum.de/lbe/home/>

Introduction

In this study we investigate the acoustic particle trapping in a spherical microchamber as a potential method for clinical research. The in vitro investigation of cell-cell-interaction of few 100 cells close to in vivo conditions is of particular interest as it potentially allows label-free optical inspection with subcellular resolution and only moderate limitations due to scattering. To identify disease mechanism or immunological interactions 2D or quasi 3D in vitro models, such as in droplets, on petri dish or various microfluidic drug assays are applied in laboratories but despite of decades of research no method is today established for preclinical research. For pre-/clinical research applications, we therefore investigate acoustic particle trapping in a spherical microchamber as a generic cell manipulation tool to explore novel in vitro cell experiments in 3D to cover any time constant of cell-cell interaction but do not depend on stochastic aggregates. Here, we report simulation work and the first verification steps with an experimental spherical cavity (SC) and polymeric beads.

Background theory

Considering a perfect spherical microchamber and following the work of Russell [1], the first-order pressure is given by solving the three-dimensional Helmholtz wave equation in spherical coordinates. The solution is given by $p_{nlm}(r, \theta, \varphi)$, where the mode shapes are identified using the (n, l, m) notation according to the number of nodal surfaces in the radial, polar, and azimuthal directions, respectively. For a water-filled spherical microchamber of 250 μm radius, the lowest eigenfrequency of 1.963 MHz corresponds to the degenerate pair of $(1, 1, m)$ modes, where a pressure nodal surface cuts through the spherical chamber. As a result, in the case of large-particle acoustophoresis with negligible influence from the acoustic streaming, the suspended microparticles are focused in the microchamber center by the acoustic radiation force. Several modes exist, but we highlight here the axisymmetric $(2, 0, 0)$ -mode at 4.238 MHz, which is characterized by a spherical nodal pressure surface to which particles can be focused via the acoustic radiation force. To verify the existence of such modes in a non-perfectly-spherical chamber with channel connections, we perform numerical simulations in COMSOL. The results are shown in Fig. 2A and 2D for the $(1, 1, 0)$ and $(2, 0, 0)$ modes, respectively.

Device design

The experimental acoustofluidic platform (see Fig. 1A) consists of a wet-etched microfluidic glass chip with an approximately 450- μm -diameter spherical microchamber (70 mm x 10 mm x 1 mm, IMT Masken und Teilungen GmbH, Switzerland). The chip is glued on a 2-MHz piezo transducer, which is temperature controlled via a Pt100 and a Peltier element. The flow chamber inlet and outlet are positioned at the respective ends of a straight microfluidic channel and the chip is connected with a pump and valve system for automated fluidic control. For testing of the traps we used 5- μm polystyrene beads. The dimensions of the etched SC are characterized via a 3D optical scans via confocal microscopy. Figure 1B and 1C show an almost perfect sphere for the SC with a 15-20 % deviation.

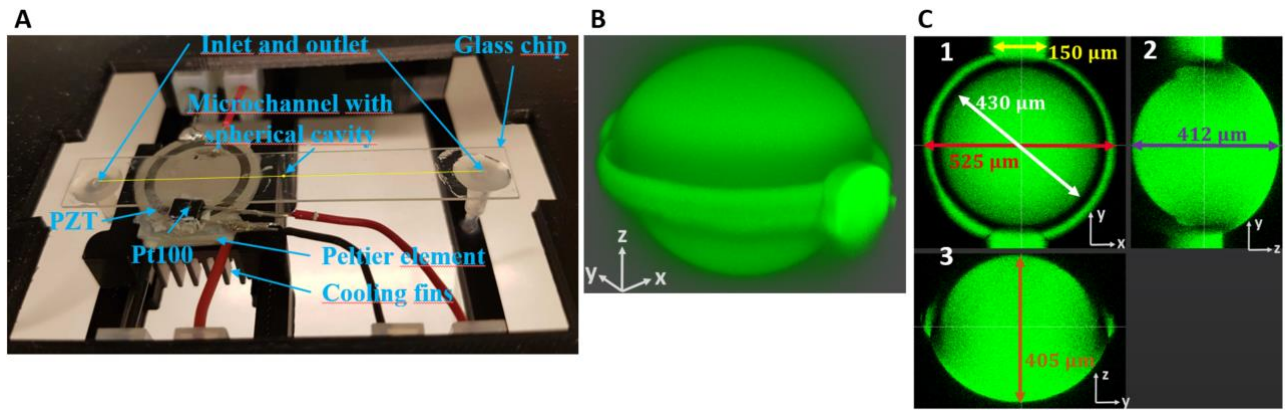


Figure 1: A) Photograph of temperature controlled acoustofluidic setup the glass chip mounted on a 3D-printed holder. B) 3D scan of the SC. C) Cross-sectional views of the SC at the maximum circumference. C1) top view C2) side view left and C3) side view right.

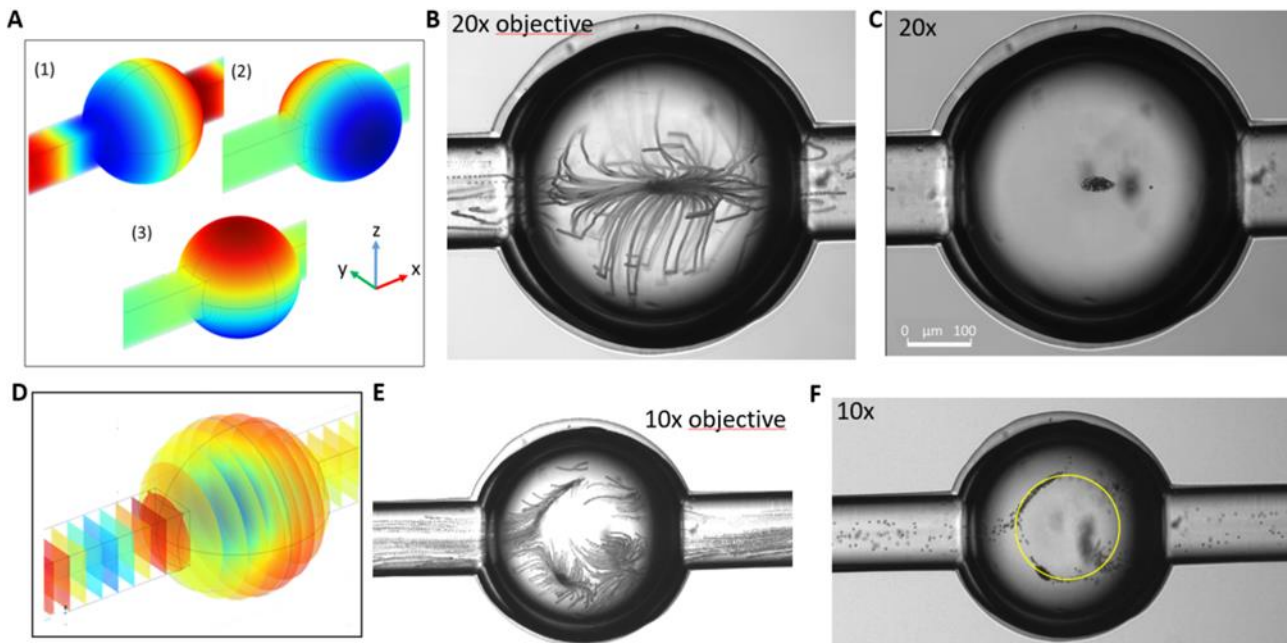


Figure 2: A) Numerical simulations of the natural frequencies for the (1,1,0)-modes in the spherical microchamber: $f_{110,1} = 2.011$ MHz, $f_{110,2} = 2.030$ MHz, and $f_{110,3} = 2.031$ MHz. B) Experimental particle trajectory in (1,1,0)-mode in stop-flow with 5- μ m PS beads. The beads are trapped into the center of spherical cavity due to the acoustic actuation, which is also shown in C). D) Simulation of the natural frequency for the (2,0,0)-mode ($f_{200} = 4.238$ MHz) with identical conditions to A). E) Experimental particle trajectories in (2,0,0)-mode with identical conditions to B).

Results

The acoustic manipulation functionalities were tested experimental and as shown in Fig. 2, the actuation of the predicted (1,1,0) and (2,0,0) modes has been achieved. For a modulated frequency of 1.875-1.950 MHz, the suspended PS microbeads (positive acoustic contrast) were focused to the pressure nodal point at the chamber center (Fig. 2B and 2C). For a modulated frequency of 3.90-4.10 MHz, the microbeads were focused to an approximate spherical nodal surface inside the chamber.

Conclusion

We have tested and verified the acoustic manipulation functionalities with theoretical and experimental model regarding to focusing, trapping, accumulating, and rotating of particles in a spherical microchamber. We could also proof their reproducibility. We will continue our research in qualitative trajectory experiments and specific validation with clinical samples. Further we will investigate in cheaper alternatives to etched glass chips. We hope to implement this acoustofluidic platform in a future biomedical application.

References

- [1] D. A. Russell. American Journal of Physics, **78**, 549-554 (2010).

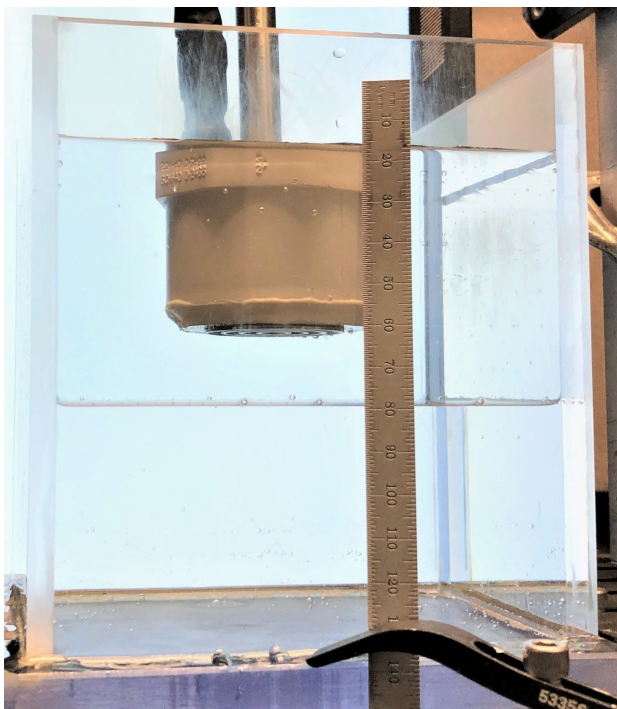
Acoustic extraction and trapping of a droplet from a liquid–liquid interface

Robert Lirette¹, Joel Mobley¹, and Likun Zhang¹

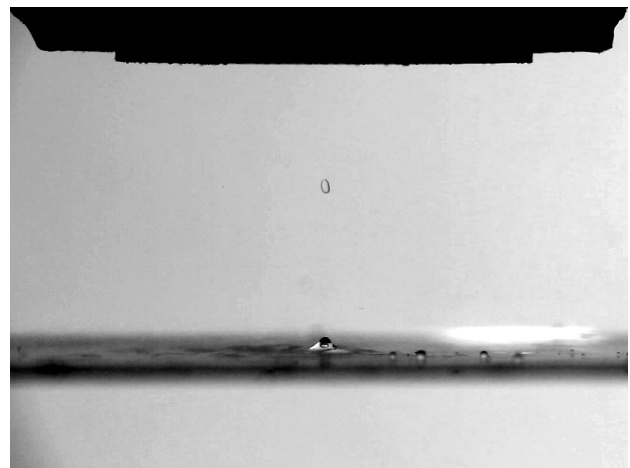
¹National Center for Physical Acoustics and the Department of Physics and Astronomy, University of Mississippi, University, Mississippi, USA
E-mail: rlirette@olemiss.edu, URL: <https://ncpa.olemiss.edu/>

Introduction

Trapping of objects by acoustic tweezers has been demonstrated for a variety of acoustic fields (for example as in [1, 2, 3, 4, 5]), where pulling was suggested by using non-diffracting beams [6, 7, 8, 9]. Single beam trapping has been demonstrated in 2 and 3 dimensions. Typically a standing wave field or a multi-elements array of transducers is required for stable trapping and pulling in 3 dimensions. Here we report on the extraction and stable 3D trapping of a fluid droplet from a liquid–liquid interface using a single ultrasonic transducer. A fluid to fluid boundary experiences a radiation force when ultrasound is incident on it [10, 11]. This radiation force can be either positive, away from the source, or negative, towards the source, depending on the material properties of the two fluids. In this work the negative radiation force exerted at a water to carbon tetrachloride (CCl_4) interface was used to better facilitate the extraction of a single droplet of the CCl_4 reservoir into the water.



(a)



(b)

Figure 1: (a) The tank and setup used for the experiment. The top fluid in the tank is water and the bottom fluid is CCl_4 . (b) A droplet of CCl_4 is trapped 12.8 mm below the transducer and has been transported upwards 12 mm by moving the source transducer. (Images originally published in [12].)

Acoustic fraxicon lens

The acoustic field used in this study for the extraction and trapping of droplets was generated by a single transducer which utilized an acoustic fraxicon lens [13]. The fraxicon is a flat phase-plate lens designed to mimic the properties of an axicon (which typically has a cone shape) by focusing incident acoustic radiation into a finite Bessel beam. It does this using partial-wavelength phasing steps positioned so that constructive interference occurs along a central line of focus. The fraxicon used for

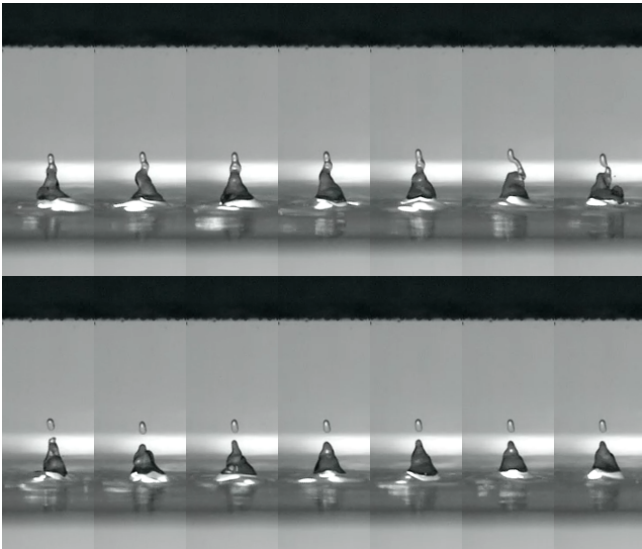


Figure 2: Still images taken from the high speed video of the extraction process. Each frame is taken 20 ms apart in order from top left to bottom right (Image originally published in [12]).

this work was machined out of aluminum and epoxied directly to a cylindrical piezoelectric crystal with a resonant frequency of 1.2 MHz. The unique near-field features provide a stable trapping region while the far-field focused Bessel beam facilitates the negative radiation force pull required to extract droplets as discussed in the following section.

Experiment

The experimental setup as shown in Fig. 1(a) consisted of a rectangular tank filled with 1 L of water on top of a 1 L reservoir of CCl_4 . The fraxicon transducer was operated within the water portion of the tank insonicating the fluid boundary pointing downwards from above. The fraxicon transducer was driven with a radio frequency amplifier at its resonant frequency which was monitored with a power meter. When the incident power was high enough to overcome the weight of the fluid and surface tension, a single droplet 1.5 mm tall and 0.8 mm wide was extracted from the fluid boundary and trapped by the acoustic field 11.8 mm from the front of the lens. The droplet size, shape, and distance from the lens remained consistent for various source powers ranging from 17 to 40 W. Video of the process was captured using an Edgetronic high speed video camera at 1000 frames per second. As can be seen in Fig. 2, the interface was deformed upwards into the water by the focused ultrasound beam. From this deformation a droplet of the CCl_4 was trapped in the near field region of the transducer. After trapping the droplet, it is able to be manipulated by moving the transducer as depicted in Fig. 1(b).

Conclusion

In this work we demonstrate experimentally the controlled extraction and trapping of a fluid droplet using a single beam ultrasonic source. The extraction is helped by the negative radiation force that can exist on the boundary between two carefully chosen fluids. Trapping is achieved by the unique features of the near-field radiation from a fraxicon lens based transducer. We look forward to presenting this work at the *Acoustofluidics 2020 Virtual Conference* on 26 - 27 August 2020.

References

- [1] J. Wu, The Journal of the Acoustical Society of America **89**, 2140 (1991).
- [2] Y. Choe, J. W. Kim, K. K. Shung, E. S. Kim, Applied Physics Letters **99**, 233704 (2011).
- [3] A. Marzo, et al., Nature Communications **6**, 8661 (2015).
- [4] D. Baresch, J.-L. Thomas, R. Marchiano, Phys. Rev. Lett. **116**, 024301 (2016).
- [5] M. Baudoin, et al., Science Advances **5**, eaav1967 (2019).
- [6] P. L. Marston, The Journal of the Acoustical Society of America **120**, 3518 (2006).
- [7] L. Zhang, P. L. Marston, Phys. Rev. E **84**, 035601 (2011).
- [8] X.-D. Fan, L. Zhang, Phys. Rev. Applied **11**, 014055 (2019).
- [9] C. E. M. Démoré, et al., Phys. Rev. Lett. **112**, 174302 (2014).
- [10] G. Hertz, H. Mende, Zeitschrift für Physik (now owned by Springer) **114**, 354 (1939).
- [11] R. T. Beyer, The Journal of the Acoustical Society of America **63**, 1025 (1978).
- [12] R. L. Lirette, J. M. Mobley, L. Zhang, Phys. Rev. Applied **12**, 061001 (2019).
- [13] R. L. Lirette, J. M. Mobley, The Journal of the Acoustical Society of America **146** (2019).

Microparticle Patterning on Bendable and Flexible SAW Devices

Sadaf MaramiZonouz¹, Mohammad Rahmati¹, and Richard Yongqing Fu¹

¹ Faculty of Engineering and Environment, Northumbria University, Newcastle upon Tyne, NE1 8ST, UK
E-mail: sadaf.maramizonouz@northumbria.ac.uk

Introduction

Flexible acoustofluidic platform can be a potential component in designing and manufacturing wearable devices, soft robotics and body conforming technologies and have shown promise in constructing bio-inspired and wearable point-of-care (POC) devices, clinical and biomedical technologies for collecting, manipulating and investigating bodily fluids [1]. For these types of applications, microfluidic devices are often required to be flexible to conform to arbitrary surfaces. Therefore, it would be crucial to understand new phenomenon which are linked with 3D distribution patterns of the particles and biological cells under acoustic waves in a flexible acoustofluidic device. Recently, new ideas in designing flexible, deformable and even stretchable ultrasonic and SAW devices have been explored [2-6] However, to the best of authors' knowledge, there are few studies on flexible thin film SAW devices used for patterning of microparticles and biological cells inside a microchamber or a microchannel.

This study aims to investigate acoustofluidics performance of flexible SAW devices bent in different curvatures and explore effects of bending curvatures on microparticle and cell patterning in a microchamber, through both experimental studies and numerical simulations. The flexible thin film SAW device on aluminium foil/sheet substrates used in this study, can be bent into both concave and convex geometries and the particles or cells can still be aligned in parallel by the SSAWs along the IDT direction. However, from the cross-sectional views along the vertical direction, the patterned lines of particle will not have a constant distance from the bottom of chamber to the top. From the top views, the distances between each two adjacent parallel lines ("line distance" in short) of the particles or cells can be varied. It was found that bending the flexible SAW devices in either concave or convex geometries results in the line distribution of particle patterns, to converge towards or diverge away from center of the curvature of the geometry, respectively.

Lamb Wave based SSAW on Al foil with 160 μm Wavelength

The effects of different bending curvatures of flexural ZnO Lamb wave device (Al foil substrate thickness of $\sim 50 \mu\text{m}$, wavelength of $160 \mu\text{m}$ and frequency of $f_{A0} = 13.00 \text{ MHz}$) on silica microparticle patterning were studied. The microparticle patterning results from the top and cross-sectional views are presented in Figure 1.

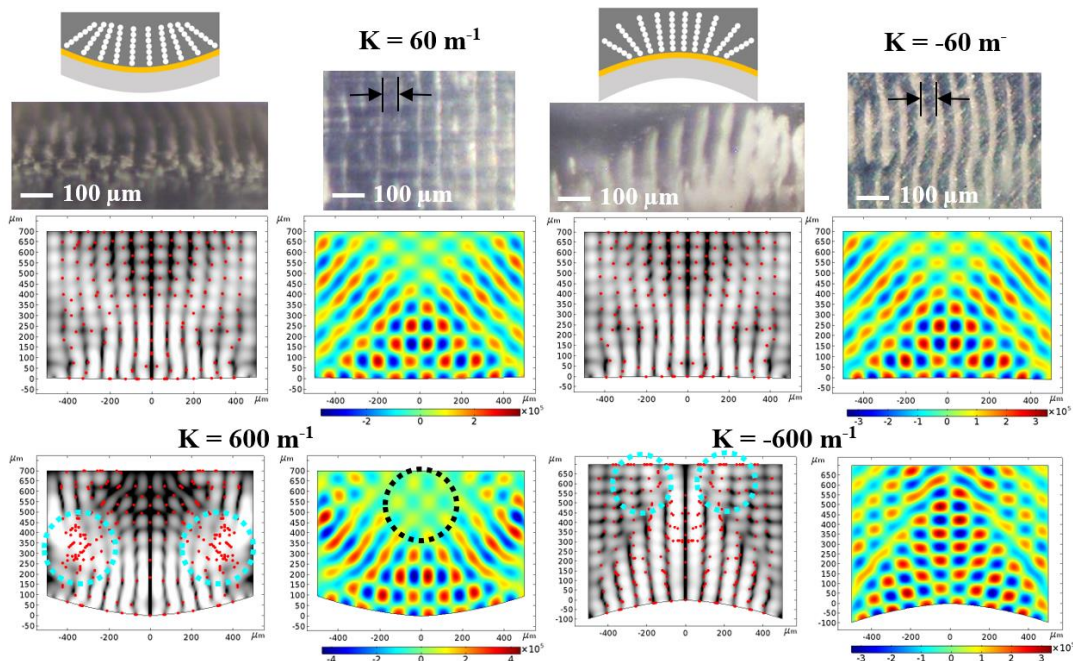


Figure 1: Schematic, experimental and simulation results for silica microparticle patterning on flexural Lamb wave device.

Rayleigh Wave based SSAW on Al plate with 160 μm Wavelength

The effects of different bending curvatures of ZnO Rayleigh wave device (Al plate substrate thickness of 200 μm , wavelength of 160 μm and frequency of $f_{R0} = 17.00$ MHz) on silica microparticle patterning were studied. The microparticle patterning results from the top and cross-sectional views are presented in Figure 2.

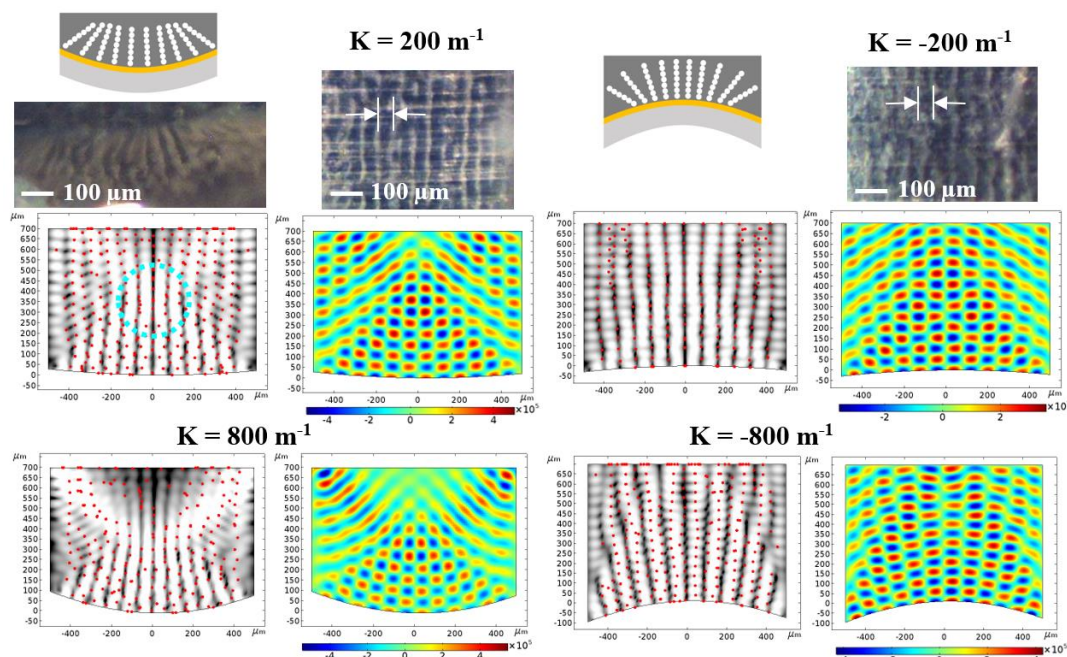


Figure 2: Schematic, experimental and simulation results for silica microparticle patterning on Rayleigh wave device.

Discussions and Conclusions

This research investigated the acoustofluidic behaviour of flexible SAW devices with various vibration modes and studied the effects of different bending curvatures of these flexible SAW devices on patterning of microparticles in a microchamber. Bending the flexible SAW devices in both concave and convex geometries affects the distribution of particle patterns and distribution of lines. The patterned lines become converged with a slope towards the centre of the curvature of the geometry or diverged with a slope away from centre of the curvature of the geometry, respectively, as it can be seen from the cross-sectional view.

For the concave geometries of the flexible SAW device, the particle pattern lines are diverged after converging and passing through the centre of curvature of the geometry. Increasing the curvature of the concave and convex devices will have different effects based on the curvature and the geometry. For the concave geometries, a stronger acoustic pressure node area is formed in the middle of the chamber which will draw the microparticles to this area. Also, the particle patterning is not regular at the two sides of the microchamber which is caused by the weak SSAW field on the side of the microchamber. Further increasing the curvature of the concave geometries results in the alignment of particles approximately parallel in the middle of the chamber. However, there is weak particle patterning in the two sides of the microchamber due to the weaker SSAW field in these areas. For the convex geometries, increasing the curvature of the devices will cause a stronger pressure anti-node area near the middle of the microchamber which will drive the particles away from these areas. With further increase in the curvature of the convex geometries, a weaker SSAW field acoustic pressure node area forms in the middle of the chamber near the top, and the particles accumulate there with low patterning efficiency.

We also compared particle patterning for both Lamb and Rayleigh wave devices. With the same concave geometry, particle alignment is more efficient near the surface of the Lamb wave device, but the patterning quality is nearly the same at higher parts of the chamber. Whereas, for the same convex geometry, the quality of the particle patterning is nearly the same on the surface of the device up until the middle of the chamber but for the Rayleigh wave device the patterning is more efficient at the top of the chamber, mainly because of the efficiency of wave energy dissipation into the liquid to form SSAWs.

Acknowledgement: UK EPSRC grant EP/P018998/1, Changfeng Jia from Xian Jiaotong University, China, Xiang Tao from Zhejiang University, China.

References

- [1] R. Tao, W. Wang, J. Luo, S. A. Hasan, et al., *Surface and Coatings Technology*, **357**, 587-594, 2019.
- [2] Y. Q. Fu, J. K. Luo, N. T. Nguyen, A. J. Walton, et al., *Progress in Materials Science*, **89**, 31-91, 2017.
- [3] R. Tao, G. McHale, J. Reboud, J. M. Cooper, et al., *Nano Letters*, 2020.
- [4] X. Tao, H. Jin, M. Mintken, N. Wolff, et al., *ACS Applied Nano Materials*, **3**, 1468-1478, 2020.
- [5] R. Tao, S. Hasan, H. Z. Wang, J. Zhou, et al., *Scientific reports*, **8**, 1-9, 2018.
- [6] Y. Liu, Y. Li, A. M. el-Hady, C. Zhao, et al., *Sensors and Actuators B: Chemical*, **221**, 230-235, 2015.

Sonolithography as a tool for in-air particle manipulation and surface patterning using bulk ultrasonic standing waves

Jenna M. Shapiro¹, Bruce W. Drinkwater¹, Adam W. Perriman², and Mike Fraser³

¹Faculty of Engineering, University of Bristol, Bristol, UK

E-mail: jenna.shapiro@bristol.ac.uk

²School of Cellular and Molecular Medicine, University of Bristol, Bristol, UK

³Department of Computer Science, University of Bath, Bath, UK

Introduction

Acoustophoretic techniques offer gentle, non-contact manipulation of individual and populations of particles within a fluid medium. Bulk ultrasonic standing waves generate acoustic radiation forces which guide particles typically to nodes of zero acoustic pressure, where those particles are in the Rayleigh regime (i.e. much smaller than the wavelength) [1]. Significant recent progress has enabled multiple millimetre-sized particles to be independently manipulated in air using phased arrays that utilise low cost 40 kHz transducers [2, 3]. Here we describe sonolithography, a technique which uses airborne bulk ultrasonic standing waves to manipulate much smaller particles and aerosols, in the μm -to- mm range, in air and pattern them onto substrates.

Working Principles of Sonolithography

In the sonolithography surface patterning system described here, an acoustic field is generated by the interference of ultrasonic standing waves generated by one or more pairs of 40 kHz piezoelectric transducers. A 3D printed support is used to house the transducers in fixed positions, with the centres of the transducers approximately 6 mm above a substrate. As solid particulates or nebulized droplets pass through the field from above, they are focused toward defined regions, and subsequently patterned as they land on a substrate. Fig. 1 schematically illustrates this process and provides examples of patterned 1-80 μm -scale water droplets and sand particles of hundreds of micrometres.

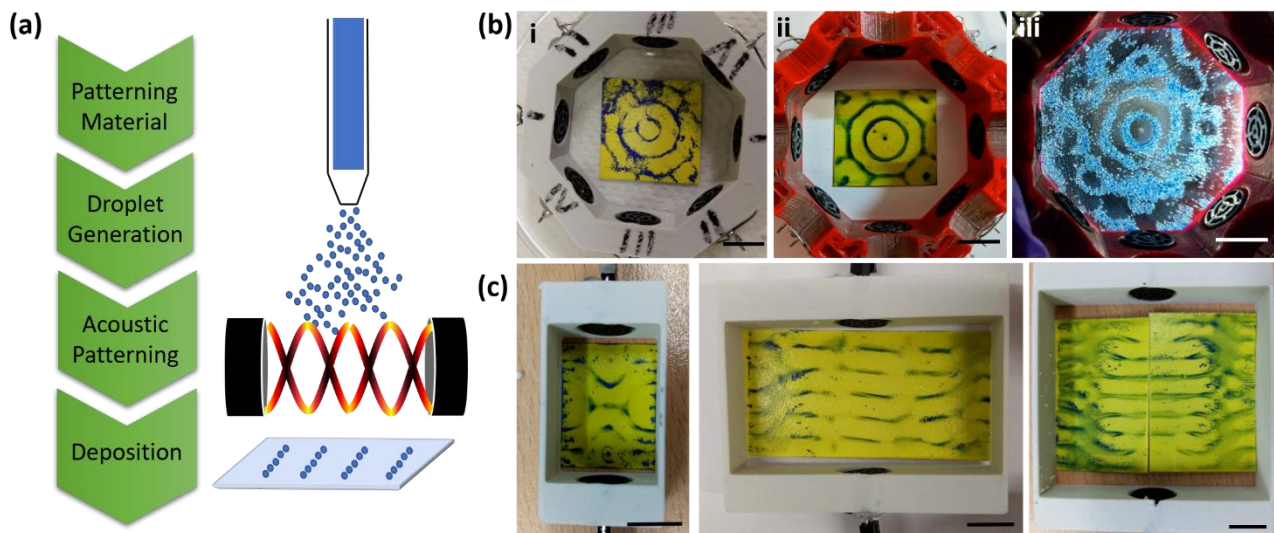


Figure 1: Sonolithography as a surface patterning technique. (a) Schematic drawing of the sonolithography process for a liquid material to be patterned. (b) Water (i, ii) and sand (iii) are used to visualise the patterning. Water sensitive paper is used as a substrate; a colour change from yellow to blue occurs where the surface comes into contact with aqueous solutions. In (i), 80 μm water droplets are patterned to nodes, whereas in (ii), 1-5 μm water droplets are patterned to anti-nodes. In (iii), larger sand granules pattern to nodes, while a finer powder can be observed in the central anti-node. (c) The resultant pattern can be affected by distance between transducers, as well as chamber width of the support array. Left: transducers are spaced $7/2 \lambda$ apart with a chamber width of 2 cm. Centre: transducers are spaced $7/2 \lambda$ apart with a chamber width of 5 cm. Right: transducers are spaced $11/2 \lambda$ apart with a chamber width of 5 cm. Scale bars in all photographs are 1 cm.

Patterning produced by sonolithography is dictated primarily by the acoustic field, rather than properties of the patterned or substrate materials. The acoustic field can be shaped by the number and positioning of transducer pairs, as well as by the properties of the wave (e.g. frequency, phase). Furthermore, manipulating the support array can also affect subsequent patterning, due to potential boundary effects or reflections, as shown in Fig. 1C.

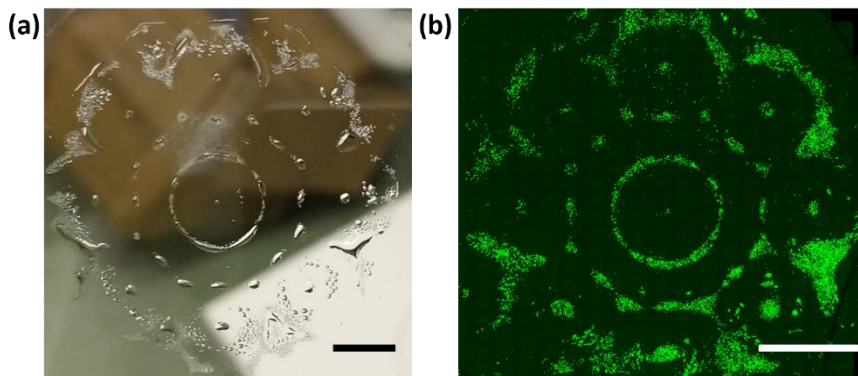


Figure 2: Patterning of cell adhesive regions with sonolithography. (a) Type I collagen was nebulized and acoustically patterned onto a tissue culture dish. The patterned dish was treated with bovine serum albumin to prevent non-specific cell binding. (b) GFP-HUVECs were seeded onto the patterned dish, and retained their patterning after one week in culture, as visualised with the tile-scan function of a widefield microscope. Scale bars are 1 cm.

Size Segregation of Droplets and Solid Particles

A size segregation effect was observed for both liquid and solid particles in the field (Fig. 1B), in accordance with various theoretical predictions [4,5]. In [4], this is due to the inclusion of thermal and viscous effects in the scattering theory whereas in [5] this is due to asymmetric drift forces. Both approaches suggest that for sufficiently small particles in air the sign of the acoustophoretic forces changes and such particles can experience large forces towards anti-nodal regions. In experiments performed with our 40 kHz airborne system, water droplets with diameters of 80 μm , produced by a piezoelectric droplet on demand generator were shown to migrate toward acoustic pressure nodes, which is expected from the widely used Gor'kov theory for small particles relative to the wavelength (8.6 mm at 40 kHz in air). However, water droplets between 1-5 μm produced by a medical nebuliser were patterned to the anti-node regions. We note that [5] predicts the sign change to occur at around 10 μm which is consistent with our observations. Similarly, for solid media, larger sand granules (~0.5 – 1 mm diameter) also localised to nodes, whereas finer powder deposits in the anti-nodes. Not only does the size segregation enable further control over regional deposition, but also can provide a tool to study particle size effects in airborne acoustophoresis.

Applications in Biofabrication

Biofabrication was explored as an initial application area for sonolithography. Fig. 2 shows patterned type I collagen on a tissue culture dish and subsequent cellular attachment to these regions. The collagen droplets were produced with a medical nebuliser, and as such were deposited in anti-node regions of an octagonal array, featuring four transducer pairs operating simultaneously. Patterning was achieved after thirty seconds of nebulization. Individual droplets were between 1 and 5 μm in diameter; patterning was achieved on a surface area of nearly 20 cm^2 . In order to prevent non-specific adhesion, non-patterned regions were blocked with bovine serum albumin. A human endothelial cell line, modified to express green fluorescent protein (GFP-HUVECs), was used to evaluate the patterning as HUVECs preferentially adhere to the collagen. In our protocol, cells were introduced and left to adhere for approximately ten minutes, prior to washing the dish and adding culture medium. The cells remained viable and confined to their initial patterned regions after one week in culture. Further work is in progress to examine the direct patterning of mammalian cells onto a surface using sonolithography.

Conclusion

Sonolithography is a straightforward technique which uses airborne bulk ultrasonic waves to pattern microscale particles and droplets over large surface areas (on the order of 10 cm^2). The size segregation observed indicates sonolithography's utility in exploring physical acoustic phenomena, as well as provides further control over patterning of materials. An initial case study in biofabrication illustrates sonolithography's utility. Furthermore, the limited constraints on patterned and substrate material, and wide variety of patterns which can be formed suggest many more potential applications.

References

- [1] H. Bruus. *Lab on a Chip* **12**, 1014-1021 (2012).
- [2] M. Prsbrey and B. Raeymaekers. *Physical Review Applied* **10**, 034066 (2018).
- [3] A. Marzo, A. Barnes and B. W. Drinkwater. *Review of Scientific Instruments* **88**, 085105 (2017).
- [4] J. T. Karlsen, H. Bruus. *Physical Review E* **92**, 043010 (2015).
- [5] H. Cxyz. *Acoustica* **70**, 23-28 (1990).

Abstract-Only Presentations

Acoustic Devices

ACOUSTO-MECHANICALLY ENHANCED OSTEMER-GLASS POLYMER HYBRID: TOWARDS CHEAPER ACOUSTOFLUIDIC DEVICES

Karl Olofsson, Elin Forss, Björn Hammarström, and Martin Wiklund
KTH Royal Institute of Technology, SWEDEN

MICROFLUIDIC FUNCTIONALITIES AND WIRELESS SENSING USING SURFACE ACOUSTIC WAVE ACTUATOR AND METAMATERIAL-BASED RESONATOR ON A SINGLE PLATFORM

Shahzad Zahertar¹, Ran Tao^{1,2}, Hamdi Torun¹, Pep Canyelles-Pericas³, and Richard Y.Q. Fu¹
¹Northumbria University, UK, ²Shenzhen University, CHINA, and ³University of Twente, NETHERLANDS

REDUCTION OF TAYLOR-ARIS DISPERSION BY LATERAL ACOUSTIC STREAMING

Pierre Gelin, Dominique Maes, and Wim De Malsche
Vrije Universiteit Brussel, BELGIUM

TWO-DIMENSIONAL MXENES EXFOLIATED AND SPIN-COATED USING SURFACE ACOUSTIC WAVE FOR GAS SENSING

Zerong Chen, Ran Tao, and JingTing Luo
Shenzhen University, CHINA

Bio-Acoustic Systems

A BEAD-BASED ACOUSTOFLUIDIC PLATFORM FOR TIME-CONTROLLED ENZYME REACTIONS IN DROPLETS

Zhenhua Liu, Anna Fornell, and Maria Tenje
Uppsala University, SWEDEN

ACOUSTIC LEVITATION OF *LEISHMANIA* PARASITES

Abelino Vargas^{1,2}, Diana C. Ochoa¹, Marcela Camacho^{1,2}, and Itziar González³
¹National University of Colombia, Bogotá, COLOMBIA, ²International Physics Center (CIC), COLOMBIA, and ³CSIC Spanish National Research Council, SPAIN

ANALYSIS OF A MICROPILLAR BASED QUARTZ CRYSTAL MICROBALANCE SENSOR

Siqi Ji and Hongwei Sun
University of Massachusetts, Lowell, USA

SORTING OF SAME-SIZED CELLS IN TWO-STAGE MICROCHANNEL VIA ACOUSTOFLUIDICS: A NUMERICAL ANALYSIS

Arash Mahboubidoust, Abas Ramiar, Kurosh Sedighi, and Donya Shahani
Babol Noshirvani University of Technology, IRAN

Physical Acoustics

ANALYZING PHYSICAL FIELDS AND PARTICLE MOTIONS INFLUENCED BY DIFFERENT DESCRIPTIONS OF PDMS IN THE MODEL OF SAW-PDMS ACOUSTOFLUIDICS

Zhengyang Ni and Xiasheng Guo
Nanjing University, CHINA

DEFECTS IN A NEW PERIODIC STRUCTURE FORMED BY TWO DIFFERENT SIDE BRANCHES

Mohamed El Malki
Mohammed First University, MOROCCO

DYNAMIC COATING OF ONE LIQUID BY ANOTHER BY EMPLOYING THE ACOUSTOWETTING PHENOMENON

Avital Reizman and Ofer Manor
Technion - Israel Institute of Technology, ISRAEL

MODELING OF ACOUSTIC ENHANCED ELECTROCHEMICAL POLISHING PROCESSES

Johannes Landskron, Sabrina Tietze, Conrad Wolf, and Klaus Stefan Drese
Coburg University of Applied Sciences and Arts, GERMANY

Acoustic Manipulation

A MULTI-CHANNEL PROGRAMMABLE AMPLIFIER FOR HIGH VOLTAGE HIGH FREQUENCY TRANSDUCER EXCITATION

Hiep X. Cao^{1,2}, Han-sol Lee^{1,2}, Dae W. Jung², Byungjeon Kang², Jong-Oh Park^{1,2}, and Chang-Sei Kim^{1,2}
¹Chonnam National University, KOREA and ²Korea Institute of Medical Microrobotics, KOREA

ACOUSTOPHORETIC MANIPULATION OF PARTICLES IN IMPEDANCE MISMATCHED SYSTEMS

Amal Nath and Ashis K. Sen
Indian Institute of Technology, Madras, INDIA

CONTROL OF A BULK ACOUSTIC WAVE MICRO-CHANNEL THROUGH FREQUENCY SHIFTING AND ITS APPLICATION TO CELL RECONCENTRATION

Ludovic Bellebon^{1,2}, Déborah François², Mauricio Hoyos¹, and Jean-Luc Aider¹
¹ESPCI Paris, FRANCE and ²Aenitis Technologies, FRANCE

DISPENSING AND MANIPULATION OF FEMTOLITRE DROPLETS BY INKJET NOZZLE

Dege Li¹, Bingfang Huang¹, Yi Cao¹, Chao Zheng¹, Yonghong Liu¹, and Yanzhen Zhang^{1,2}
¹China University of Petroleum, CHINA and ²Swinburne University of Technology, AUSTRALIA

ROBOTIC MICROFINGERS: ACOUSTIC ASSEMBLY AND MAGNETIC MANIPULATION

Xiaolong Lu^{1,2}, Hui Shen¹, and Ying Wei¹

¹*Nanjing University of Aeronautics and Astronautics, CHINA and*

²*Max-Planck Institute for Intelligent Systems, GERMANY*

WASHING ELECTROPORATED CELLS USING SURFACE ACOUSTIC WAVE (SAW)

Fangda Wu¹, Mao Mao², Fan Yuan², Ming Hong Shen¹, and Xin Yang¹

¹*Cardiff University, UK and* ²*Duke University, USA*

Acousto-mechanically enhanced OSTEMER-glass polymer hybrid: Towards cheaper acoustofluidic devices

Karl Olofsson¹, Elin Forss¹, Zakiya Yassin¹, Björn Hammarström¹ and Martin Wiklund¹

¹Department of Applied Physics, KTH Royal Institute of Technology, Stockholm, Sweden
 E-mail: karlolo@kth.se URL: <https://www.kth.se/profile/karlolo>

Introduction

Classic materials used in transversal bulk acoustic waves (BAW) devices, such as silicon and glass, are appreciated for their mechanical properties which enables efficient resonant actuation of ultrasonic waves within a microfluidic cavity. The high acoustic impedance of the classical materials compared to the liquid within embedded microcavities is vital. But with the high material and fabrication cost associated with silicon and glass, all-polymer acoustofluidic devices has been proposed as a cheaper option to enable mass produced disposable BAW acoustofluidic devices [1,2]. Here, we propose a trade-off between the classic materials and polymers; mechanically enhanced polymer hybrids. By using a mixture of off-stoichiometry thiol-enes (OSTE) and glass beads, we show the possibility of combining the easy and cheap fabrication using polymers while augmenting the acousto-mechanical properties.

OSTE-glass acousto-mechanical characterization

The polymer base in this work is the commercial OSTE formulation OSTEMER 322 (Mercene Labs, Sweden) which is developed for microfluidic devices. The two curing steps (UV and thermal at 110 °C) allows molding and subsequent bonding to most materials. The first UV curing step crosslinks parts of the monomers and renders the OSTEMER flexible (comparable to PDMS). Free epoxy groups in the partly crosslinked OSTEMER 322 can then be used for bonding to a surface material of choice during the second thermal cure.

In this work, we used a PDMS injection mold to fabricate 34x34x3.76 mm³ OSTEMER 322 samples with different volume ratios of polydisperse glass bead (40-70 μm SiLibeads Type S, SILI) mixed into the monomer solution. OSTEMER-glass hybrid samples were mechanically characterized in a pulse-echo measurement setup using a 2.25 MHz transducer, aluminum buffer rod and a custom-made holder (Figure 1A). The speed of sound was measured by time-of-flight between the first and second echo, where the second echo traveled through the known thickness of the sample. The speed of sound increased from 2483 ± 8 m s⁻¹ in pure OSTE to 2983 ± 32 m s⁻¹ (mean ± std, N=5) in OSTEMER/glass 40% v/v (Figure 1B). Together with density measurements using Archimedes' principle, the acoustic impedance was increased from 3.30 ± 0.01 MPa s m⁻¹ to 5.30 ± 0.06 MPa s m⁻¹ in OSTE/glass 40% v/v (Figure 1C). The pressure reflection coefficient at an interface against water ($Z = 1.48 \text{ MPa s m}^{-1}$) was enhanced from 0.38 in pure OSTEMER to 0.56 in OSTE/glass 40% v/v (Figure 1D). The acoustic attenuation increased with glass bead volume fraction which we believe is due to the increased scattering in the glass-OSTEMER interfaces (data not shown).

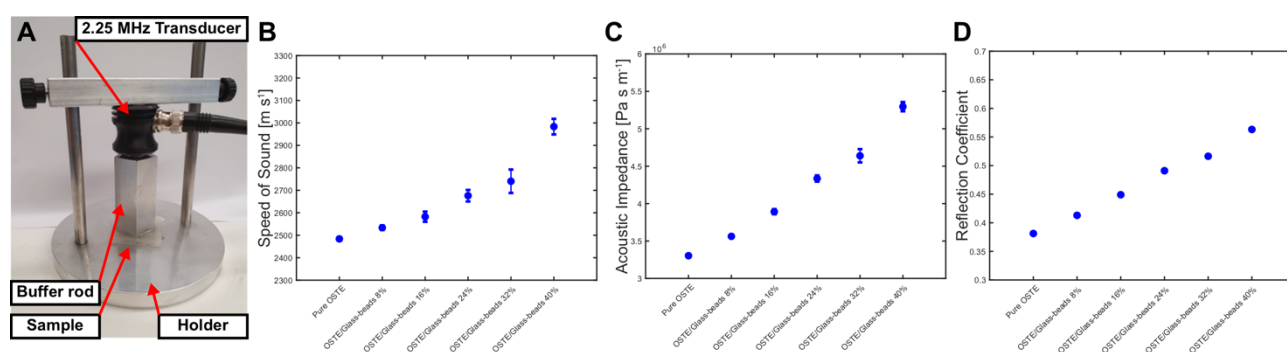


Figure 1: Utilizing a pulse-echo measurement setup (A) and a time-of-flight methodology, the speed of sound (B) in OSTE samples containing a volume ratio of glass beads ranging from 0-40 % was measured. Using density measurements of these samples, the acoustic impedance (C) and the pressure reflection coefficient at an interface against water ($Z=1.48 \text{ MPa s m}^{-1}$) was calculated (D).

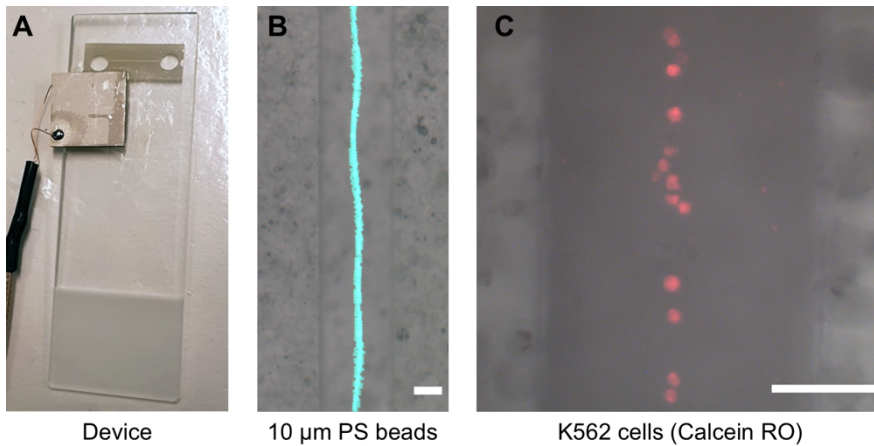


Figure 2: Overview of the acoustofluidic device consisting of an OSTEMER/glass 40% v/v block with an embedded 265 μm wide channel bonded to a glass slide with an attached piezo (A). At 14 V_{pp} actuation voltage and 2.5 MHz actuation frequency, 10 μm fluorescent polystyrene beads (B) and Calcein Red-Orange stained K562 cells were forced into the channel center.

OSTE-glass acoustofluidics device

Since the OSTE/glass 40% v/v polymer hybrid exhibited the most enhanced acousto-mechanical properties, compared to pure OSTE, we used this formulation to manufacture a microfluidic channel. A PDMS negative mold, produced from a micro-milled PMMA positive master, was used to cast the rectangular microchannel geometry (265 μm wide channel) embedded in an OSTEMER/glass block. After the UV cure, the OSTE/glass was bonded against a regular microscopy slide during the thermal curing step to close the microchannel. A piezo with resonance frequency 2.5 MHz was connected to wires and glued to the bottom of the glass slide (Figure 2A). At the driving frequency of 2.5 MHz we observed the actuation of the $\lambda/2$ resonant mode inside the channel and could manipulate the position of 10 μm polystyrene (PS) beads (B) and Calcein Red-Orange stained K562 leukemia cells (C).

To quantify the acoustic energy density and pressure amplitude, trapping velocities for 5 μm polyamide beads along the channel width, acquired from PIV measurements, was fitted against acoustic energy density. At 14 V_{pp} actuation voltage over the piezo, an approximate pressure amplitude of 1 kPa and an energy density of 1 J/m³ was measured. It should be noted that the device geometry shown here is not optimized for the material properties of OSTE/glass 40% v/v and further improvements to the energy density and pressure amplitude should be expected in an optimally designed device.

Possibilities for new polymer hybrids

Since OSTEMER 322 requires a first UV curing step to crosslink the monomers, a translucent mechanically augmenting material, in our case glass beads, had to be used. With already existing or future polymers, there are possibilities to further expand on the mechanically enhanced polymer hybrid concept with other augmenting materials. A prime opaque candidate would be metals such as wolfram or steel powder/nanoparticles which has high density and low compressibility. Using powder or nanoparticles should also address the increased attenuation coefficient since the particle size will be much smaller than the wavelength.

Conclusion

The concept of combining the cheap and easy fabrication of polymers with the good mechanical properties of classic acoustofluidic device materials in polymer hybrids has good potential. We hope that the promising OSTE/glass results inspires the community to further explore this subject to allow future commercialization of mass-produced transversal BAW acoustofluidic devices.

References

- [1] R.P. Moiseyenko and H. Bruus. *Physical Review Applied* **11**, 014104 (2019).
- [2] A. Mueller, A. Lever, T.V. Nguyen J. Comolli and J. Fiering. *J. Micromech. Microeng* **23**, 125006 (2013).

Microfluidic Functionalities and Wireless Sensing using Surface Acoustic Wave Actuator and Metamaterial-based Resonator on a Single Platform

Shahrzad Zahertar¹, Ran Tao^{1,2}, Hamdi Torun¹, Pep Canyelles-Pericas,³ Richard Y.Q. Fu¹

¹Faculty of Engineering and Environment, Northumbria University, Newcastle upon Tyne NE1 8ST, UK
E-mail: shahrzad.zahertar@northumbria.ac.uk

²Shenzhen Key Laboratory of Advanced Thin Films and Applications, College of Physics and Optoelectronic Engineering, Shenzhen University, Shenzhen, 518060, P. R. China

³Department of Integrated Devices and Systems, Faculty of Electrical Engineering, Mathematics and Computer Science, University of Twente, Enschede 7522NH, The Netherlands

Introduction

There have been advances in micro and nanotechnologies allowing development of lab-on-chip (LOC) devices that can be used for continuous health monitoring and disease diagnostics. These LOC devices usually consist of different units for handling liquid samples and sensing, which require separate development effort and impose integration challenges. Surface acoustic wave (SAW) devices have been widely used for liquid manipulation functions and metamaterials have been demonstrated for high-sensitivity sensing applications. Electromagnetic metamaterials offer wireless sensing capabilities with high quality factors [1], however, performing microfluidic functions is not possible. On the other hand, SAW actuators are excellent for microfluidics [2] but achieving high sensitivity sensors using SAW is challenging due to attenuation [3]. A concept of combining electromagnetic metamaterial-based sensors and surface acoustic wave (SAW) actuators on a single platform has been developed as an integrated LOC device with sensing and liquid manipulation capabilities [4]. In this work, we propose a circular interdigitated transducer (IDT) design for both sensing and actuation purposes. The device works as a SAW actuator for microfluidic functions in radio frequencies, whereas the same device is used as metamaterial-based resonator in microwave frequencies for sensing.

Wave Characterisation

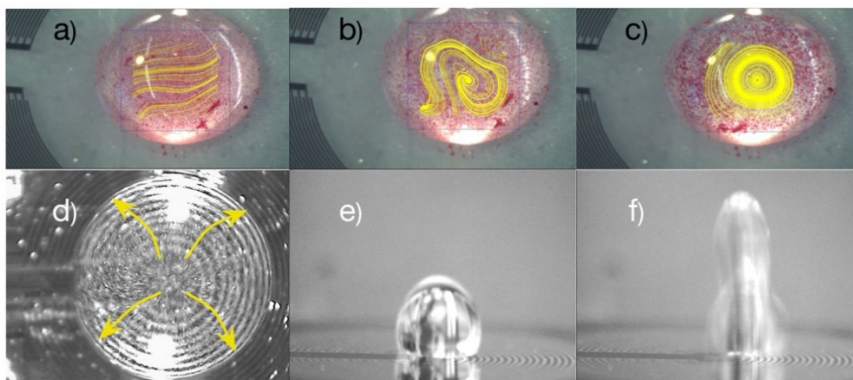


Figure 1: a-c) Streaming of polystyrene particles in a DI droplet. d) Streaming pattern observed in the droplet when the surface of the device is treated by CYTOP e-f) jumping and jetting of droplet observed on a hydrophobically treated surface by CYTOP and by increasing the power.

A circular IDT pattern was designed and fabricated using standard lithography and lift-off processes. The metal used in fabrication is gold with a thickness of 120 nm, and the substrate is 500 μm -thick lithium niobate. The wavelength of the IDTs is 200 μm . Due to crystal structure of the lithium niobate substrate, the sound velocity would be different depending on the direction of the wave on the surface. The functional frequency of the SAW actuator to achieve microfluidic applications is determined based on the wavelength of the IDTs and the sound velocity in the substrate. The speed of acoustic wave on lithium niobate is 3980 m/s. When power is applied to electrode pads of SAW actuators in their operating frequency and by increasing power, different microfluidic functions such as streaming, jetting and nebulisation can be realised respectively. Figure 1(a-c) show a fabricated circular IDT design, where a droplet consisting of polystyrene particles was placed on the device and streamlines are shown from beginning towards the end of the experiment. In the next step, in Figures 1(d-f), the surface was hydrophobically treated with CYTOP and a droplet was placed in the inner circles of IDTs. At the beginning in Figure 1(d), the power was 500 mW and streaming was observed, however by

increasing power to ~ 5 W, jetting was achieved as shown in Figure 1(e-f). Streaming and jetting were observed in these experiments as the Rayleigh waves were transferred from substrate into the droplet. For the next set of experiments, a glass slide of $50\ \mu\text{m}$ thick was put on top of the fabricated device (with a thin layer of water in between) and a droplet was placed on the glass in centre of IDTs as shown in Figure 2(a-c). Then, power was applied to electric pads of the device. Figure 2(a-c) show streaming of the polystyrene particles inside DI droplet when the glass was hydrophobically treated, and power was increased from 1.1 W to 8.4 W, respectively. The streaming was more pronounced when power was higher as can be inferred by comparing the speed of particles in Figure 2(a-c). When the surface was hydrophilic and the power was increased to ~ 15 W, nebulisation was realised as depicted in Figure 2(d-f). Since a glass was placed between the surface and the droplet, Lamb wave was translated into the droplet through a superstrate inducing streaming and nebulisation.

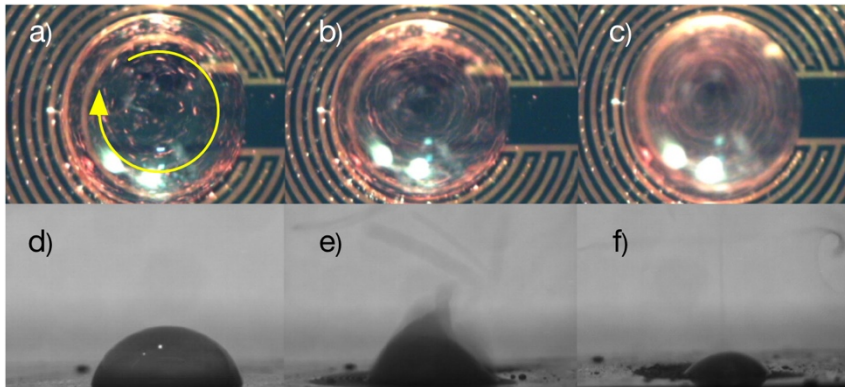


Figure 2: a-c) Streaming of polystyrene particles in a DI droplet when a glass is put between the substrate and the droplet, the power applied is 1.1 to 8.4 from (a) to (c) leading to a more dominant streaming. d-f) Nebulisation of the droplet was observed when the power was increased to 15 W. A glass slide of $50\ \mu\text{m}$ thick is put on top of the fabricated device with a thin layer of water in between.

Electromagnetic Characterisation and Simulation

For the electromagnetic characterisation, a loop antenna connected to one of the ports of a Vector Network Analyser (VNA) was utilised to excite the device and s_{11} characterisation of the device was obtained. When a device is exposed to electromagnetic waves through the antenna, circulating currents can be generated within the device based on the direction of electric and magnetic field, resulting in a magnetic frequency that can be utilised for sensing. For this purpose, in our experiments, scattering parameters were obtained when the device was electrically loaded by a droplet of deionised (DI) water as shown in Figure 3(a). A shift in the resonant frequency towards higher frequencies was observed when a droplet was placed on the device due to a decrease in effective conductive path of the resonator; indicating sensing capability of the device. Also, the electromagnetic response was simulated using CST Studio. The magnetic excitation settings and the simulated device are shown in inset of Figure 3(b).

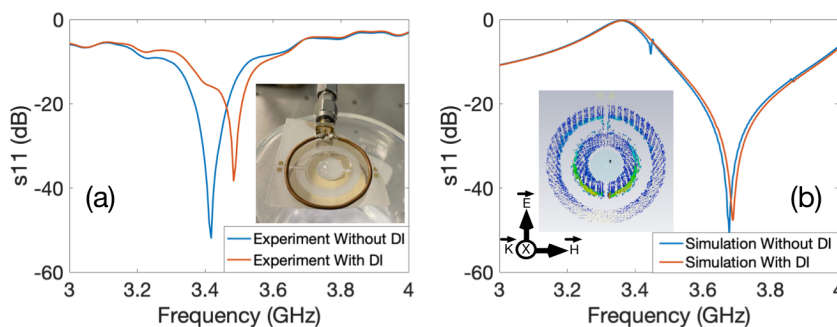


Figure 3: a) The experimental results in the presence and absence of DI droplet. The experiment setup is shown as inset of the figure. b) Corresponding simulation results for the excitation setting shown in the inset of the figure.

Conclusion

Sensing and actuation capabilities of a circular IDT design are investigated in this paper. This particular design is beneficial for streaming, jetting, nebulisation as well as sensing liquid on device. Sensing is performed in microwave frequencies and microfluidic functions are performed in radio frequencies. Results indicate that this device can be successfully used as an integrated platform using a single design for different microfluidic functionalities and also sensing applications.

References

- [1] H. Torun, F. Cagri Top, G. Dundar, and A. D. Yalcinkaya, "An antenna-coupled split-ring resonator for biosensing," *J. Appl. Phys.*, vol. 116, no. 12, 2014.
- [2] J. Friend and L. Y. Yeo, *Rev. Mod. Phys.*, 2011, 83, 647–704.
- [3] X. Ding, P. Li, S.-C. S. Lin, Z. S. Stratton, N. Nama, F. Guo, D. Slotcavage, X. Mao, J. Shi, F. Costanzo and T. J. Huang, *Lab Chip*, 2013, 13, 3626.
- [4] S. Zahertar, Y. Wang, R. Tao, J. Xie, Y. Q. Fu, and H. Torun, "A fully integrated biosensing platform combining acoustofluidics and electromagnetic metamaterials," *J. Phys. D: Appl. Phys.*, 2019.

Reduction of Taylor-Aris dispersion by lateral acoustic streaming

Pierre Gelin¹, Dominique Maes², and Wim de Malsche¹

¹ μ Flow group, Department of Chemical Engineering, Vrije Universiteit Brussel, Brussels, Belgium
E-mail: Pierre.Gelin@vub.be

²Structural Biology Brussels, Vrije Universiteit Brussel, Brussels, Belgium

Introduction

Variations in the axial velocity of a pressure drive flow unavoidably leads to the spreading of a narrow injected band and thus to a wider residence time. This phenomenon is often referred to as Taylor-Aris dispersion¹, and is unavoidable in flow systems where lateral mass-transport is limited compared to transport in the axial direction. This limits the performance of flow reactors and separation devices (e.g. chromatographic separations). Several attempts have been made to reduce Taylor-Aris dispersion in flow devices. Passive techniques include the introduction of flow disrupting structures to create lateral mass transport² and the generation of Dean vortices³. These techniques, however, depend on the primary axial flow. Ideally, lateral convection and the axial flow are independent. Active techniques include the actuation of magnetic particles, thereby disrupting the Poiseuille flow⁴, and the generation of vortices with electro-osmotic flows⁵. Both techniques require the addition of either particles or a salt which might be detrimental for the performance of the reactor.

In the present work, acoustic streaming is proposed and evaluated to enhance lateral convection in open rectangular channels intended for chromatographic separations. Fast mixing in microfluidic channels with acoustic streaming has been demonstrated previously in the context of microreactors⁶. However, this is the first time that acoustic streaming is applied to reduce Taylor-Aris dispersion in a chromatographic context.

Chip design and experimental procedure

The microfluidic chip consists of rectangular injection channels ($120\ \mu\text{m} \times 33\ \mu\text{m}$) and a detection channel ($375\ \mu\text{m} \times 33\ \mu\text{m}$) perpendicular to each other. To induce acoustic streaming, a standing pressure wave was generated inside the microfluidic cavity. The chip was connected to a piezoceramic element which was driven at a frequency of 1.875 MHz. The presence of acoustic streaming was confirmed by visualization the trajectories of $1\ \mu\text{m}$ diameter fluorescent polystyrene particles. To evaluate Taylor-Aris dispersion in the rectangular channel, narrow fluorescent sample plugs were injected. The plugs were visualized with an inverted fluorescence microscope equipped with a CCD camera. The plugs were further analyzed in MATLAB and dispersion was determined by the method of moments.

Acoustic streaming

The streaming velocities measured from the top of the detection channel ($375\ \mu\text{m} \times 33\ \mu\text{m}$) are represented in Figure 1. Streaming was induced at a voltage of $62\ V_{p-p}$ where a maximal velocity of $979\ \mu\text{m/s}$ is observed. The average streaming velocity over to total cross section of the channel was calculated to be $163\ \mu\text{m/s}$.

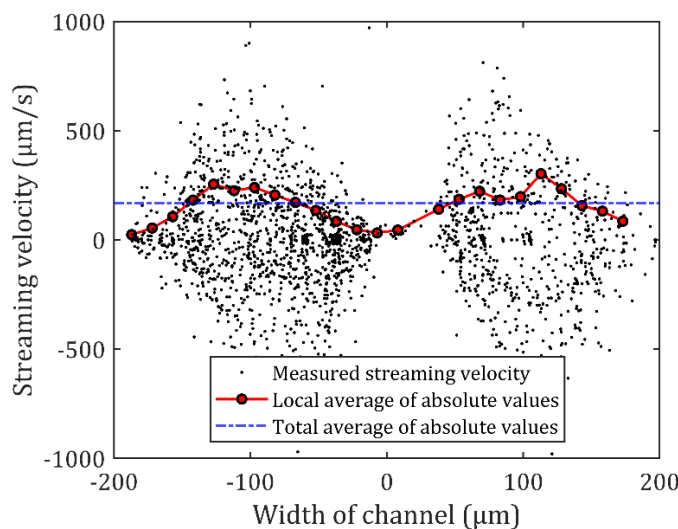


Figure 1: Streaming velocities of $1\ \mu\text{m}$ particles in a $375\ \mu\text{m} \times 33\ \mu\text{m}$ microfluidic channel. The average magnitude of the acoustic streaming was calculated to be $163\ \mu\text{m/s}$ at an actuation voltage of $62\ V_{p-p}$.

Reducing Taylor-Aris dispersion

The effect of acoustic streaming on Taylor-Aris dispersion is visualized in Figure 2. Acoustic streaming has a clear effect on the width of the injected bands. Moreover, the higher the applied voltage and thus the velocity of the acoustic streaming, the more pronounced this effect. Note that the asymmetry of the plug without actuation is eliminated by the introduction of acoustic streaming. For chromatographic separations, a more quantitative representation of dispersion is given in terms of plate heights (Figure 3). At high enough velocities, dispersion rises linearly with a slope which is referred to as the f_0 -value. A linear fit of the obtained plate heights without the presence of acoustic streaming revealed a f_0 -value of 7.84 which is close to the theoretically expected value of 7.029⁷. Acoustic streaming reduced dispersion significantly, f_0 -value of 5.22 and 3.56 were obtained for an actuation voltage of 56 V_{p-p} and 70 V_{p-p}, respectively.

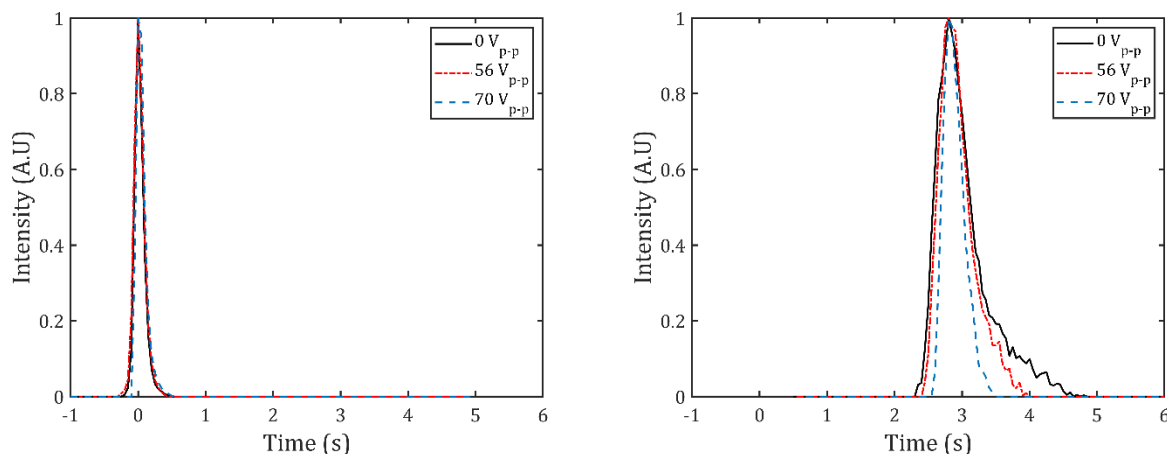


Figure 2: Normalized intensity profiles of the injected plugs at different actuation voltages at the injection point (left) and 5 mm downstream (right). The shown intensity profiles were measured at an average velocity of 1.8 mm/s.

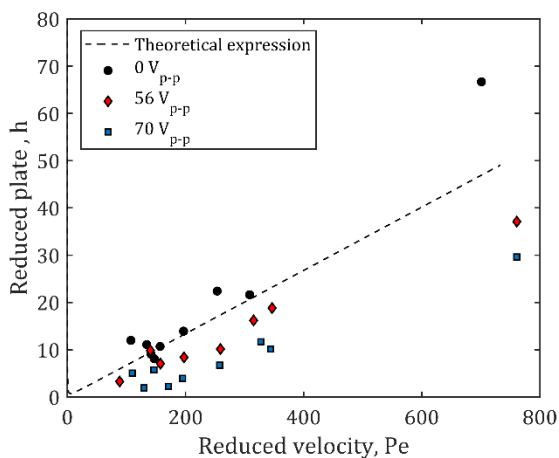


Figure 3: Effect of acoustic streaming in terms of reduced plate heights as a function of reduced velocity. Dispersion is reduced by a factor of 1.5 and 2.2 for an actuation of 56 V_{p-p} and 70 V_{p-p} respectively.

Conclusion

In this contribution the long range lateral vortex flow of acoustic streaming is used to reduce Taylor-Aris dispersion by more than a factor of two. This is of particular importance in chromatographic separations of complex matrices, which are out of the reach for the current analytical separations, or in reactors that require a precise control of the residence time.

References

- [1] Aris, R. *Proc. R. Soc. London A* **235**, 67–77 (1956).
- [2] Stroock, A. D. *et al. Science*. **295**, 647–651 (2002).
- [3] Nivedita, N., Ligrani, P. & Papautsky, I. *Sci. Rep.* **7**, 44072 (2017).
- [4] Hajiani, P. & Larachi, F. *Chem. Eng. J.* **203**, 492–498 (2012).
- [5] Zhao, H. & Bau, H. H. *Anal. Chem.* **79**, 7792–7798 (2007).
- [6] Gelin, P., Sardan, Ö., Hellemans, K., Maes, D. & De Malsche, W. *Chem. Eng. J.* **369**, 370–375 (2019).
- [7] Poppe, H. *J. Chromatogr. A* **948**, 3–17 (2002).

Two-dimensional MXenes Exfoliated and Spin-coated using Surface Acoustic Wave for Gas Sensing

Zerong Chen¹, Ran Tao¹, and JingTing Luo^{1*}

¹Shenzhen Key Laboratory of Advanced Thin Films and Applications, Shenzhen university, Shen Zhen, China
E-mail: 1800211017@email.szu.edu.cn

Introduction

In recent decades, two-dimensional (2D) materials have been demonstrated to have significant potential on the detection of disease-related biomarkers as gas sensors [1]–[2]. To synthesize atomically thin 2D materials from their bulk-form, many exfoliating methods were developed, such as mechanical exfoliation [3], ultrasonic exfoliation [4] and surface acoustic wave (SAW) liquid phase exfoliation [5]. Among them, SAW-based liquid phase exfoliation is a cutting-edge method to obtain high yield suspensions of 2D materials nanoflakes [6]. However, a key challenge hindering the further application of 2D materials as the functional layer of gas sensors is to form large-scale uniformly tiled monolayer using the exfoliated nanoflakes on application devices. In this work, we designed an integrated exfoliating-coating system for the synthesis and deposition of 2D materials. Surface acoustic wave microcentrifugation (SAWM) system was prepared for exfoliating layered bulk MXenes, together with *in situ* acoustic streaming coating process to form a sensitive layer on the target area of SAW gas sensors. The study proves the potential and feasibility of using SAWM system for lab-on-a-chip applications.

Principle of structure design

As schematically shown in Fig. 1a, four SAW devices based on 128° YX LiNbO₃ are integrated to form a SAWM system, where the gold interdigital transducers are prepared by conventional lift-off process. The PDMS reservoir is bonded to the center of the surface after the plasma treatment. In the SAWM system, the electric field effect and mechanical shear force were coupled to produce a suspension of MXenes nanoflakes by exfoliation from the layered bulk powder (Fig. 1b). Mono-layer MXenes nanoflakes stream on the upper layer of the liquid during the exfoliating process and are easy to adhere to the hydrophilic surface of the SAW gas sensor placed inversely above the PDMS reservoir (Fig. 1c). Using this acoustic streaming coating method, we can obtain gas sensors with sensitive areas coated by uniform monolayer of MXenes that is composed of nanoflakes (Fig. 1d).

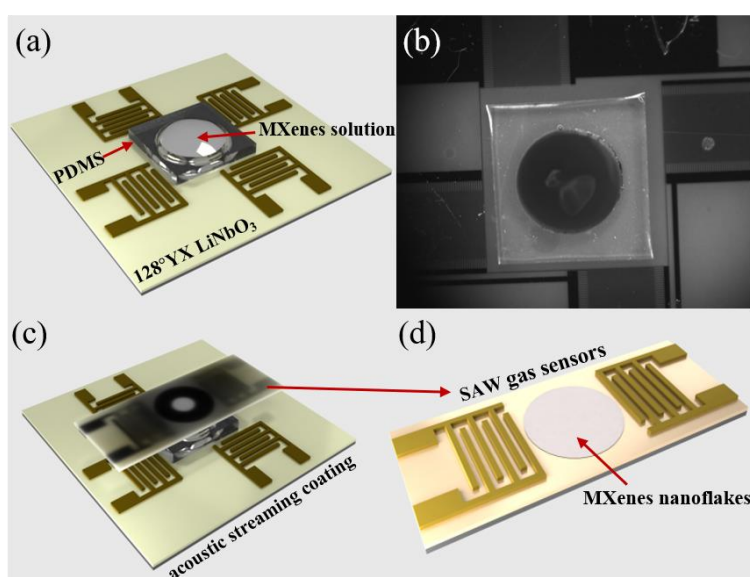


Figure 1: (a) Schematic illustration of SAWM system with a PDMS reservoir bonded to the central functional area. (b) Experimental set-up of SAWM system in operation. (c) Schemes of SAW gas sensors placed inversely on the PDMS reservoir for acoustic streaming coating. (d) SAW gas sensor with thin layer of MXenes after coating.

Materials characterization

The reflection spectrum (S_{11}) of the SAW devices was measured by a vector network analyser, giving a center frequency of ~ 18.18 MHz as shown in Fig. 2d. Fig. 2b and 2c show the SEM images of the layered bulk MXenes and the uniformly deposited 2D MXenes on the gas sensor after the exfoliating and coating driven by the acoustic streaming. In order to investigate and obtain a better insight into the performance of the integrated exfoliating-coating system, the exfoliated MXenes nanoflakes were characterized using atomic force microscope (AFM), Raman spectroscopy and X-ray diffraction (XRD). After acoustic streaming coating, MXenes nanoflakes were coated evenly on the sensitive area of SAW gas sensors and the AFM images were used to measure the surface topography and thickness of the MXenes nanoflakes (see Fig. 2a). Furthermore, for SL- Ti_3C_2 and ML- Ti_3C_2 , the wavenumber difference between the main Raman peaks is shown in Fig. 2e. Because of the exfoliation, all the peaks related to ML- Ti_3C_2 disappeared after exfoliating, except the peak corresponding to the (002) plane in the XRD pattern (see Fig. 2f). The (002) peak is shifted toward the lower angles indicating Ti_3C_2 was exfoliated from the multilayer structure into a single-layer structure.

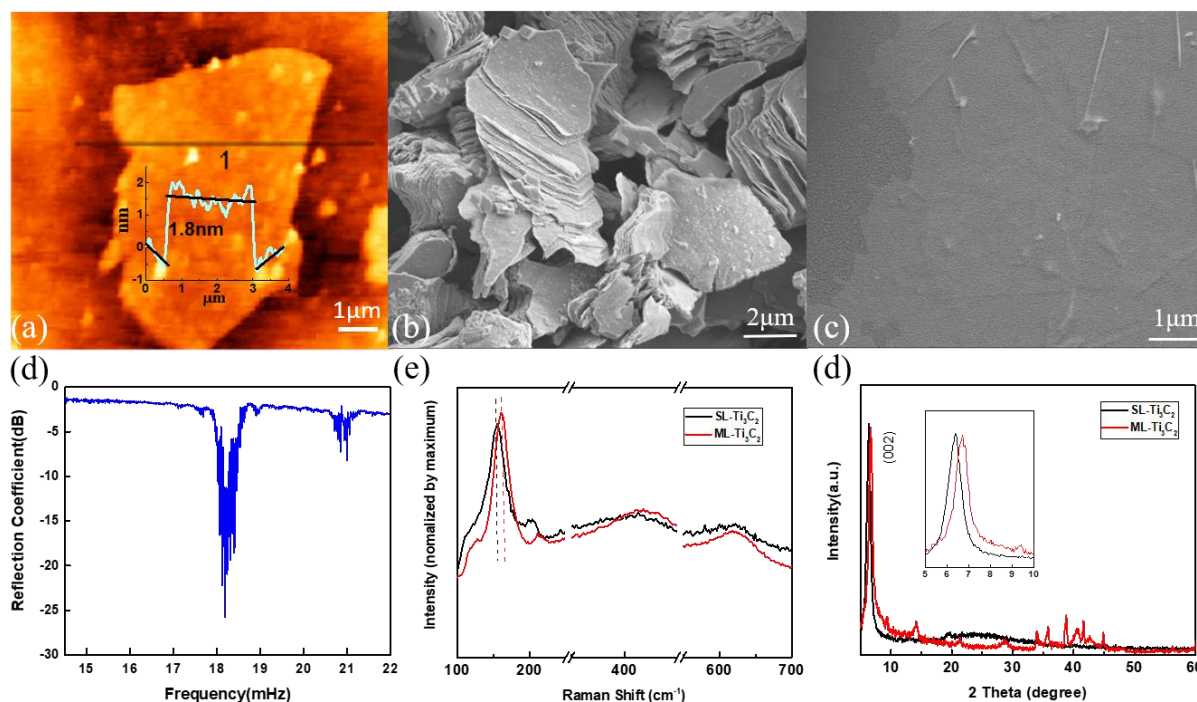


Figure 2: (a) AFM image of monolayer MXenes nanoflakes with their thicknesses measured using the height profile. (b) SEM image of bulk MXenes before exfoliation. (c) SEM image of MXenes nanoflakes coated on the sensitive area of SAW gas sensors after exfoliation and spin-coating of SAWM system. (d) S_{11} spectrum of individual SAW device in SAWM system. (e) Raman spectra of MXenes nanoflakes with 523nm lasers, (f) XRD pattern of delaminated $\text{Ti}_3\text{C}_2\text{Tx}$ film before exfoliating and Ti_3C_2 nanoflakes after exfoliating showing disappearance of other peaks and the shift of (002) plane to lower angles.

Conclusion

An integrated exfoliating-coating SAWM system was developed in our work. We have demonstrated that acoustic streaming could exfoliate lamellar MXenes suspension efficiently by providing a concomitant electric field and mechanical shear force. Meanwhile, the SL- Ti_3C_2 yielded from the exfoliation can be deposited onto the target surface simultaneously due to the acoustic streaming coating effect.

References

- [1] Lu Zhang, Karim Khan, Jifei Zou, Han Zhang, and Yingchun Li. *ADVANCED MATERIALS* **6**, 1901329(2019).
- [2] T. Wang, D. Qi, H. Yang, Z. Liu, M. Wang, W. R. Leow, G. Chen, J. Yu, K. He, H. Cheng, Y.-L. Wu, H. Zhang, X. Chen, *Adv. Mater.* **31**, 1803883(2019).
- [3] Yiqing Sun, Qiong Wu, Gaoquan Shi. *Energy & Environmental Science* **4**, 1113-1132 (2011)
- [4] Chengxue Huo, Zhong Yan, Xiufeng Song, Haibo Zeng. *Materials Science* **60**, 1994–2008 (2015)
- [5] Yu Chen, Chaoliang Tan, Hua Zhang, Lianzhou Wang. *Chemical Society Reviews* **44**, 2681-2701 (2015).
- [6] Md Mohiuddin, Yichao Wang, Ali Zavabeti, Nitu Syed, Robi S. Datta, Heba Ahmed, Torben Daeneke, Salvy P. Russo, Amgad R. Rezk, Leslie Y. Yeo, *CHEMISTRY OF MATERIALS* **30**, 5593-5601 (2018).

A bead-based acoustofluidic platform for time-controlled enzyme reactions in droplets

Zhenhua Liu, Anna Fornell, and Maria Tenje

Dept. Materials Science and Engineering, Science for Life Laboratory, Uppsala University, Uppsala, Sweden
 E-mail: zhenhua.liu@angstrom.uu.se, URL: <http://www.materialvetenskap.uu.se/embla>

Introduction

Bead-based assays, which uses antibodies or other proteins immobilized on microbeads, has been demonstrated in immunoassay applications [1]. Acoustophoresis can be used to manipulate microbeads suspended in single-flow fluids [2] or droplets [3]. Miller *et al.* demonstrated a digital microfluidic device with detection by a plate reader for in-droplet enzymatic assays to study enzyme kinetics [4]. Sjostrom *et al.* integrated a pico-injector on chip to achieve high-throughput assays and they demonstrated the multiplex analysis of enzyme kinetics and inhibition [5]. The enzyme reaction started when the substrate and enzyme were mixed in the droplets and stopped or slowed down when the inhibitor was added into the droplets. However, a challenge with these approaches is to separate the product from the enzyme since they are mixed together in the droplets after the injection step. Here, we present a droplet acoustofluidic platform that enables bead-based enzyme reactions that can be stopped using acoustophoresis.

Methods

Droplets containing substrate are generated on the chip and the enzyme reaction starts when the enzyme-coupled beads are added by the pico-injection (Figure 1). The enzyme-coupled beads are focused in the center of the channel by acoustophoresis and flow into the central channel after the droplet split. The enzyme reaction in the side channels stops once the enzyme-coupled beads are removed. The substrate of 50 μM fluorescein diphosphate (FDP) was chosen as the dispersed phase and converted into fluorescein by catalysis of alkaline phosphatase (ALP). Mineral oil with 2% polyglycerol polyricinoleate was chosen as the continuous phase. The product readout was quantified by measuring the fluorescence intensity. The 5 μm streptavidin-coated polystyrene microbeads were bonded with biotinylated ALP and then washed 3 times by PBS with 1% bovine serum albumin to remove unbonded enzyme. The enzyme-coupled beads were re-suspended in diethanolamine buffer at a concentration of 1 mg/mL before use. The supernatant solution was separated by centrifuging the bead suspension for the control experiment.

A silicon-glass chip with a piezoelectric transducer (2 MHz optimal resonance frequency) was used to generate bulk acoustic standing waves. The fabrication process was the same as in a previous study [6]. A sine wave of 1.81 MHz frequency was supplied by a function generator and amplified to 30 V_{pp} by a power amplifier, and applied over the piezoelectric transducer. A square wave of 5 kHz frequency and 10 V_{pp} amplitude was supplied by the same function generator, and applied on the electrodes for the pico-injection.

The flow rates were controlled by a syringe pump. The flow rates for droplet generation were 2 $\mu\text{L}/\text{min}$ for the oil and 1 $\mu\text{L}/\text{min}$ for the FDP solution. The flow rate for the pico-injector was 0.4 $\mu\text{L}/\text{min}$. The side channel at the split was connected to a syringe in withdrawal mode and the flow rate was 1.5 $\mu\text{L}/\text{min}$. The daughter droplets from the side channel after droplet split were collected on a 24 well plate with arrays of microwells through polyethylene tubing. The fluorescent intensity of the trapped droplets was measured for 1 hour at 10 min in intervals using a fluorescence microscope.

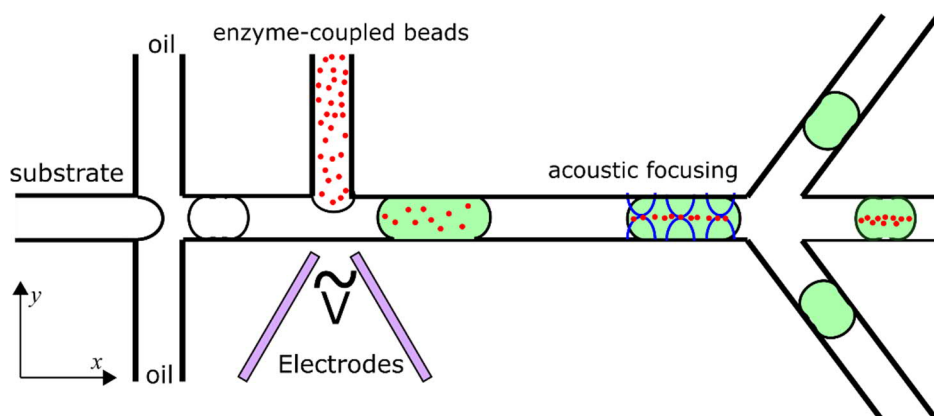


Figure 1: Schematic work flow of. The microfluidic chip contains droplet generation, pico-injection, acoustic focusing and a droplet split.

Results

All flow rates were set constant, and the time when the droplets flowed from the pico-injection to the droplet split was approximately 30s. Droplets were collected for 10 min on a well plate, and the fluorescence intensity was measured every 10 min during 1 hour (Figure 2). When the droplets were split without acoustophoresis, the fluorescence intensity continued to increase over 1 hour after the droplets had been taken off-chip. This is because the enzyme-coupled beads were able to continue to catalyze the reaction. The large standard deviation presents the different reaction time from the pico-injection in each droplet. When the droplets were split with acoustic on, the fluorescence intensity of the droplets did not continue to increase off-chip meaning that the enzymatic reaction was stopped. As a control only supernatant solution was used to generate droplets and then the fluorescence intensity of droplets was also constant over 1 hour. So, the reaction time was precisely limited when droplets flowed from the pico-injection to the droplet split.

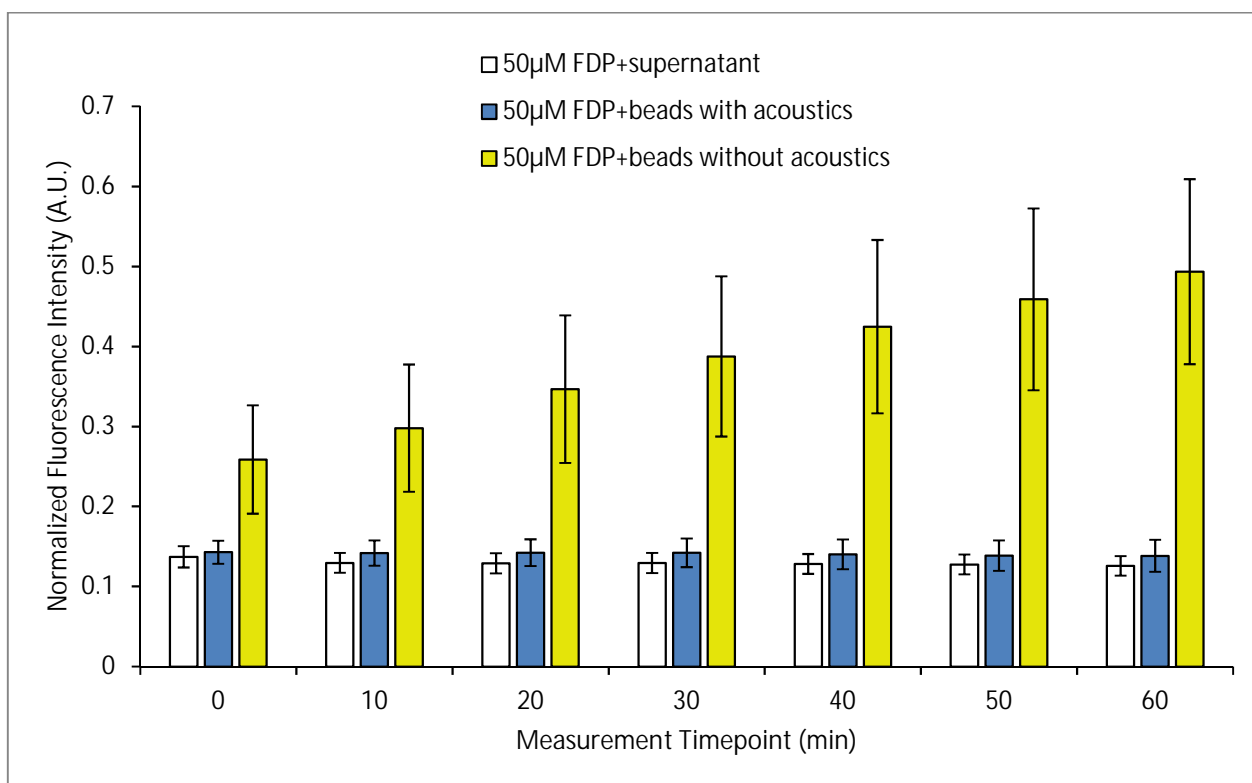


Figure 2: Droplets with substrate were added with supernatant solution and bead suspension by the pico-injection. The beads were focused when the acoustic waves were applied. The collected droplets were collected for 10 min on a well plate and the fluorescence intensity was measured every 10 min during 1 hour. The 0 timepoint means the start of the measurement on the well plate. Error bars stand for the standard deviations.

Conclusion

We have developed a bead-based microfluidic chip where we can start an enzyme reaction by pico-injection and stop the reaction by acoustophoresis. The reaction time in the droplets was controlled and the fluorescence intensity was uniformly distributed in each droplet.

References

- [1] A. H. C. Ng, U. Uddayasankar and A. R. Wheeler, *Analytical and Bioanalytical Chemistry* **397**, 991-1007 (2010).
- [2] A. Lenshof, C. Magnusson and T. Laurell, *Lab on a Chip* **12**, 1210-1223 (2012).
- [3] A. Fornell, J. Nilsson, L. Jonsson, P. K. Periyannan Rajeswari, H. N. Joensson and M. Tenje, *Analytical Chemistry* **87**, 10521-10526 (2015).
- [4] E. M. Miller and A. R. Wheeler, *Analytical Chemistry* **80**, 1614-1619 (2008).
- [5] S. L. Sjostrom, H. N. Joensson and H. A. Svahn, *Lab on a Chip* **13**, 1754-1761 (2013).
- [6] Z. Liu, A. Fornell, L. Barbe, K. Hjort and M. Tenje, *Biomicrofluidics* **13**, 064123 (2019).

Acoustic levitation of *Leishmania* parasites

Abelino Vargas^{1,2}, Diana C. Ochoa¹, Marcela Camacho^{1,2} and Itziar González³

¹ National university of Colombia, Bogotá, Colombia, E-mail: avargasj@unal.edu.co,

² International Physics Center (CIF), Biophysics Laboratory, Bogotá, Colombia.

³ Department of Ultrasounds, ITEFI, CSIC Spanish National Research Council, Madrid (Spain), iciar.gonzalez@csic.es URL: <http://www.itefi.csic.es/en/research-departments/>

Introduction

In this work, we study the behavior of *Leishmania* parasites in their two stages, promastigote and amastigote, exposed to ultrasonic standing waves in a microfluidics. The study was performed in a glass capillary actuated by two faced piezoelectric transducers resonating at 3.7MHz.

Experimental Setup

The microfluidic device consists of a glass capillary with inner square cross section ($200\mu\text{m} \times 200\mu\text{m}$) with a length of 1.2cm, where samples were injected. This device similar to that used by Carreras *et. al.*, in 2015 for the manipulation of blood samples [1], but the single piezoelectric actuator was replaced by two faced transducers resonating at a frequency close to 4 MHz located for a better control of the acoustic pressure patten in the area of interest. (see Figure 1).

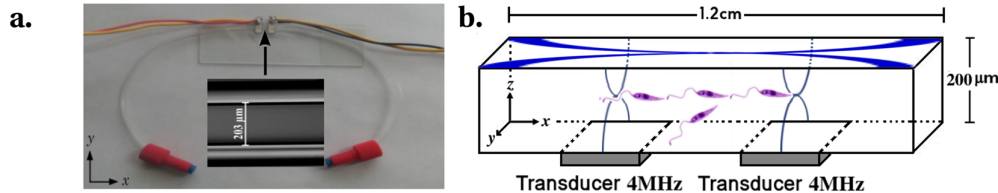


Figure 1: a) Acoustic device; b) Device dimensions and a sketch of the standing waves generated in its within.

Standing waves were driven by a waveform generator set to 10V peak-to-peak at a frequency of 3.7MHz to establish the rectangular mode (1,1,1) inside the device, Figure 1b.

The parasites inside the capillary were filmed by a CCD camera attached to a microscope and controlled by Photron software.

Parasite behavior

In the experiments, different behaviors of the alive parasites in their promastigote (mobile) and amastigote (non-mobile) form were observed when exposed to the acoustic field. They were driven toward the pressure node established along the center of the capillary, where collected and formed aggregates, as shown in Figure 2. However, the trajectories and velocities in this drift motion (thus time of collection) were not the same in promastigotes and amastigotes, due to their different volumes and shapes. In particular, promastigotes described a second order motion with rotation after collected in the center, rotating to orientate their tails aligned along the pressure node (figure 2.a). It is coherent with the direction of the acoustic radiation force, F_R , locating the bodies towards the pressure node while their flagellums were located in the opposite direction.

On the other hand, the acoustophoretic motion in amastigotes, shown Figure 2b, is similar to that one observed in several cells in suspension, such as red blood cells or cancer cells [1,2]. The parasites in this stage have almost spherical shape. These parasites showed a bulk rotation once aggregated around the center of the capillary, which seems to be related to acoustic streaming induced in the microfluidic channel. However, it must be remarked a greater tendency of a bulk rotation motion of the aggregates in amastigotes,

an effect probably associated with the not spherical shape of the parasites at this stage, enhancing the acoustic streaming effects.

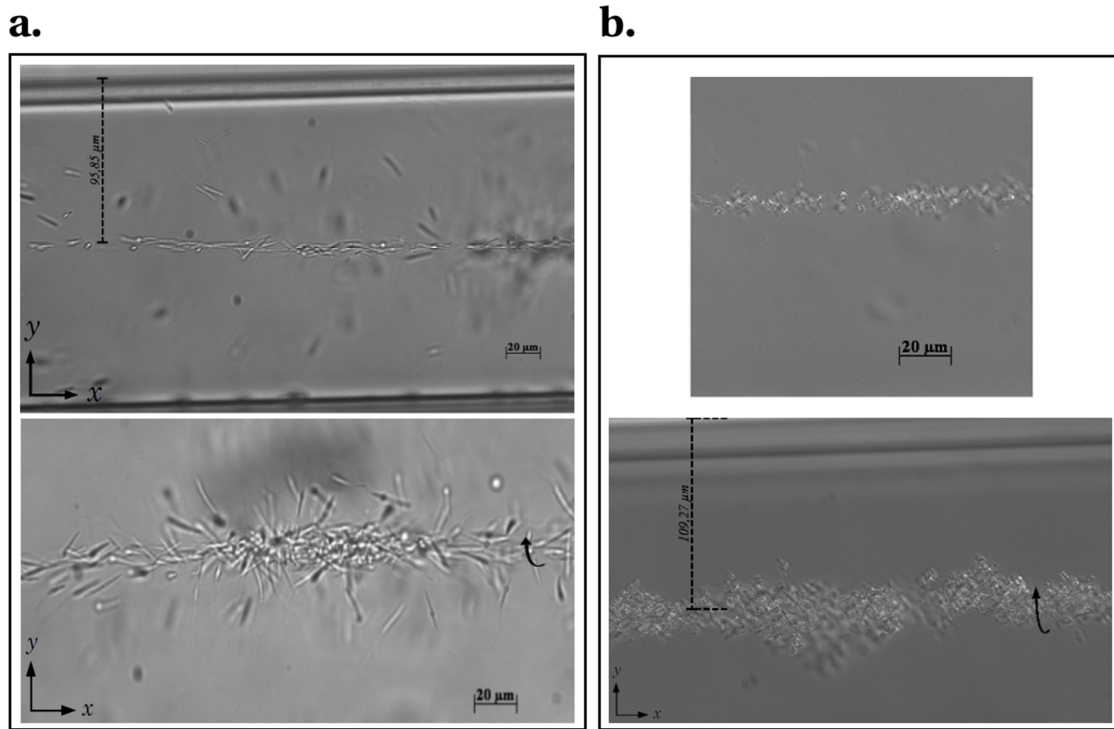


Figure 2: Acoustic levitation of *Leishmania* parasites. Clusters of (a) promastigotes and (b) amastigotes formed in the rectangular device. The black arrows indicate the direction of rotation.

Conclusion

The study of *Leishmania* parasites behavior in the acoustic field would allow the development of the technique to study certain dynamics of parasites and other microorganisms with variable properties along their lives. In addition, in the case of human diseases related to these parasites, the use of acoustic fields can generate new diagnostic and treatment applications, since the parasite and the host cell, change their physical properties when *Leishmania* is phagocytosed by macrophages [3].

References

- [1] P. Carreras, I. González and O. Ahumada. Physics Procedia 70 (2015) 72 – 75. International Congress on Ultrasonics, 2015 ICU Metz.
- [2] I. González, J. Earl, L. J. Fernández, B. Sainz Jr., A. Pinto, R. Monge, S. Alcalá, A. Castillejo, J. L. Soto and A. Carrato. Micromachines 2018, 9, 129.
- [3] M. Hoyos, A. Niño, M. Camargo, J. C. Díaz, S. León and M. Camacho. Journal of Chromatography B, 877 (2009) 3712–3718..

Analysis of a micropillar based quartz crystal microbalance sensor

Siqi Li, Hongwei Sun

Mechanical Engineering, University of Massachusetts Lowell, Lowell, MA, USA
 E-mail: Siqi_Li@student.uml.edu; Hongwei_Sun@uml.edu

Introduction

Quartz crystal microbalance (QCM) is one of the most commonly used acoustic wave sensors due to its simplicity, cost-effectiveness, and high-resolution [1]. However, the relatively low sensitivity of traditional QCM has significantly limited its applications in areas such as protein interaction diagnostics. A new sensing mechanism by coupling the vibrations of quartz crystal microbalance and micropillars (QCM-P) to form a two-degree-of-freedom system was recently discovered and significant sensitivity improvement has been reported [2, 3]. In this paper, an equivalent circuit model combining mechanical vibration of micropillars with electrical impedance analysis was developed to understand the dynamic characteristics of the sensor. The micropillar displacement obtained from the vibration model was integrated into the equivalent circuit model to identify the total impedance of the QCM-P sensor and furthermore, the quality factor (Q-factor) of QCM-P sensors can be predicted. The developed equivalent circuit model is a valuable tool in predicting the dynamic behavior of QCM-P sensors in liquid environment for biosensing applications.

Theory and experimental results

The QCM-P sensor was developed by attaching a micropillar film onto a commercially available QCM substrate, as shown in Fig. 1 (a). The coupled vibration of polymer micropillars and the QCM substrate forms a two-degree-of-freedom resonant vibration system where the QCM substrate can be treated as an equivalent mass-spring unit and the micropillar as a second set of mass-spring unit. The resonance phenomenon occurring between the micropillars and substrate was explored to significantly improve the sensitivity of conventional QCM sensors, thereby making it feasible to detect the mass change on the QCM-P sensor surface at a pg (10-12g) level. For example, when any particles like biomolecules are attached to the surface, the added mass will result in a decrease in the resonant frequency [2]. The Q-factor of the sensor was analyzed using the well-known Krimholtz-Leedom-Matthaei (KLM) model [4]. The total electrical impedance of the QCM-P sensor is given by

$$Z = \frac{1}{j\omega C_0} \left(1 - \frac{K^2 2 \tan \frac{\alpha}{2} - j \frac{Z_L}{Z_0}}{\alpha \left(1 - j \frac{Z_L}{Z_0} \cot \alpha \right)} \right) \quad (1)$$

where C_0 is the static capacitance (4.899 pF) and K is the electromechanical coupling factor (8.8%) for AT-cut quartz crystal plate, α represents the acoustic phase shift of the sensor frequency response [5], and Z_0 is the characteristic impedance of the quartz substrate without loading. The micropillars loading are represented by an acoustic load impedance Z_L .

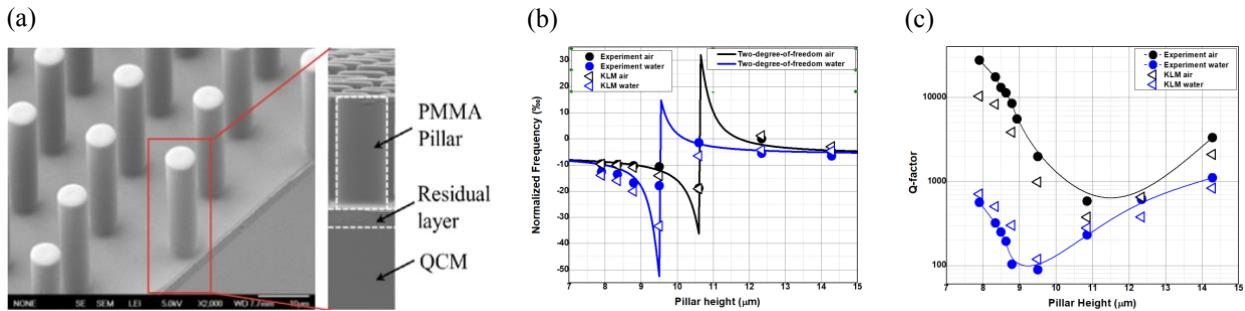


Figure 2: Equivalent circuit model results. (a) SEM images for QCM-P sensor [3]. (b) Frequency response of QCM-P sensor. (c) Q-factor response of QCM-P sensor.

The acoustic load impedance Z_L in equation (1) is defined as the ratio of total shear force ($\hat{\tau}_0$) to the velocity (v_0) at the interface between micropillars and QCM substrate [6].

$$Z_L = -\frac{\hat{\tau}_0}{v_0} = -\frac{N\kappa A G u'(0)}{i\omega u_0} \quad (2)$$

where N is number of micropillars per meter square, κ and G represent the Timoshenko shear coefficient and complex shear modulus of the micropillar respectively, A is the cross-sectional area of the micropillar, and u represents the unknown pillar displacement which will be solved by Euler Bernoulli equation

$$EI \frac{\partial^4 u(z)}{\partial z^4} + \rho_P A \frac{\partial^2 u(z)}{\partial t^2} = \frac{\pi}{4} \rho_L \omega^2 d^2 \Gamma(\omega) u(z) \quad (3)$$

Where E and I represent the young's modulus and inertial of moment of a micropillar, ρ_P is the density of the micropillar, ρ_L is the density of water, ω is the resonance angular frequency of QCM-P system, and $\Gamma(\omega)$ is the well-known hydrodynamic function of pillars with circular cross section [7]. The displacement u is assumed to have the form

$$u(z) = u_0 + \sum_{n=1}^{100} D_n W_n(z) = u_0 \left[1 + \sum_{n=1}^{100} D'_n W_n(z) \right] \quad (4)$$

where u_0 is the initial displacement introduced by QCM, W_n is the free natural deflection [8], n is the n th order of oscillation mode, and z is the coordinate along the pillar height direction. By substituting the equation (4) into equation (3), we have

$$(\omega_{0n}^2 - \omega^2) D'_n \int_0^H [W_n(z)]^2 dz - \omega^2 \int_0^H W_n(z) dz - \frac{\rho_L}{\rho_P} \omega^2 \Gamma(\omega) \left(\int_0^H W_n(z) dz + D'_n \int_0^H [W_n(z)]^2 dz \right) = 0 \quad (5)$$

where D'_n is unknown value that needs to be solved, ω_{0n} is the angular frequency of a free oscillation micropillar, and H is the pillar height. With the help of MATLAB, a discrete matrix result for D'_n , $W_n(z)$, and $u(z)$ can be obtained for each pillar height. Using polynomial fitting of the $u(z)$ as a function of z and back-substituting it to equations (1) and (2), we can calculate the parameters including $u(0)$, $u'(0)$, Z_L and Z . The Q-factor was determined by plotting the conductance ($Re(1/Z)$) vs. frequency curve. The results from equivalent circuit model and two-degree-of-freedom model were compared with experiment data and shown in Fig. 1 (b) and (c).

Conclusion

An equivalent circuit model was developed to predict the Q-factor of QCM-P operating in liquid. The results are in a good agreement with experimental results. It is believed the hydrodynamic loading on the micropillars is the main reason for the low Q-factor values or high-energy dissipation.

Acknowledgment

This work was financially supported by National Science Foundation (NSF ECCS 1916374).

References

- [1] Marx, Kenneth A., *Quartz Crystal Microbalance: A Useful Tool for Studying Thin Polymer Films and Complex Biomolecular Systems at the Solution-Surface Interface*. Biomacromolecules, 2003. 4(5): p. 1099-1120.
- [2] Su, Junwei, Esmailzadeh, Hamed, Zhang, Fang, Yu, Qing, Cernigliaro, George, Xu, Jin, and Sun, Hongwei, *An ultrasensitive micropillar-based quartz crystal microbalance device for real-time measurement of protein immobilization and protein-protein interaction*. Biosensors and Bioelectronics, 2018. 99: p. 325-331.
- [3] Wang, Pengtao, Su, Junwei, Su, Che-Fu, Dai, Wen, Cernigliaro, George, and Sun, Hongwei, *An ultrasensitive quartz crystal microbalance-micropillars based sensor for humidity detection*. Journal of Applied Physics, 2014. 115(22): p. 224501.
- [4] Krimholtz, R., D.A. Leedom, and G.L. Mattheai, *New equivalent circuits for elementary piezoelectric transducers*. Electronics Letters, 1970. 6(13): p. 398-399.
- [5] Jiménez, Y., Otero, M., Arnau, A., *Piezoelectric Transducers and Applications*. 2004, Berlin: Springer.
- [6] Xie, X., et al., *Electromechanical Coupling and Frequency Characteristics of a Quartz Crystal Resonator Covered With Micropillars*. Journal of Vibration and Acoustics, 2019. 141(4): p. 044501-044501-4.
- [7] Elie Sader, J., *Frequency response of cantilever beams immersed in viscous fluids with applications to the atomic force microscope*. Journal of Applied Physics, 1998. 84(1): p. 64-76.
- [8] Weaver, W., S.P. Timoshenko, and D.H. Young, *Vibration Problems in Engineering*. 1990: Wiley.

Sorting of Same-sized Cells in Two-stage Microchannel via Acoustofluidics: A Numerical Analysis

Arash Mahboubidoust¹, Abas Ramiar², and Kurosh Sedighi², and Donya Shahani³

¹Department of Mechanical Engineering, Babol Noshirvani University of Technology, Babol, Iran
E-mail: arashmd538@gmail.com,

²Department of Mechanical Engineering, Babol Noshirvani University of Technology, Babol, Iran

³Department of Mechanical Engineering, Babol Noshirvani University of Technology, Babol, Iran

Introduction

Millions of people around the world die due to cancer and the death toll is rising. However, early prevention and diagnosis can prevent the disease from progressing. Cancer cells released from the tumor that enter the bloodstream are known as circulating tumor cells (CTCs). Detection and analysis of these cells can provide important information to prevent metastasis. Therefore, researchers are trying to find a way to optimally isolate these cancer cells. Nowadays, several methods for the separation of CTCs from blood are used; Microfluidic chips have been widely employed by biological and biomedical researches due to the advantages resulted from the small size of devices, such as short response time, high sensitivity, and low consumption of analytes and reagents. Microfluidic particle and cell separation methods are usually classified into passive separation and active separation. Passive separation makes use of hydrodynamics effects in microchannels, such as inertial forces and biomimetic microstructures. Active separation is accomplished by employing externally induced forces such as dielectric force, magnetic force, optical force, and acoustic force. Unlike other methods, the acoustic seems to be an ideal method to manipulate particles on a micro-scale, since it is gentle, safe, label-free, contactless, and with high accuracy. In this study, OpenFOAM was used to simulate the sheathless focusing and separation of white blood cells (WBCs) from prostate cancer cells (DU145) using standing and traveling surface acoustic waves in two two-stage microchannels. The schematic of both microchannels used in this study is shown in Figure 1. At the first stage of both channels, the cells are focused using standing surface acoustic waves in the middle of the channel. Then, at the second stage, two cell populations are separated in the first channel by standing surface acoustic waves (SSAWs) and in the second channel by traveling surface acoustic waves (TSAWs) with high efficiency. Finally, the simulation results of these two channels were compared and proper voltage and flow rate are specified for each method.

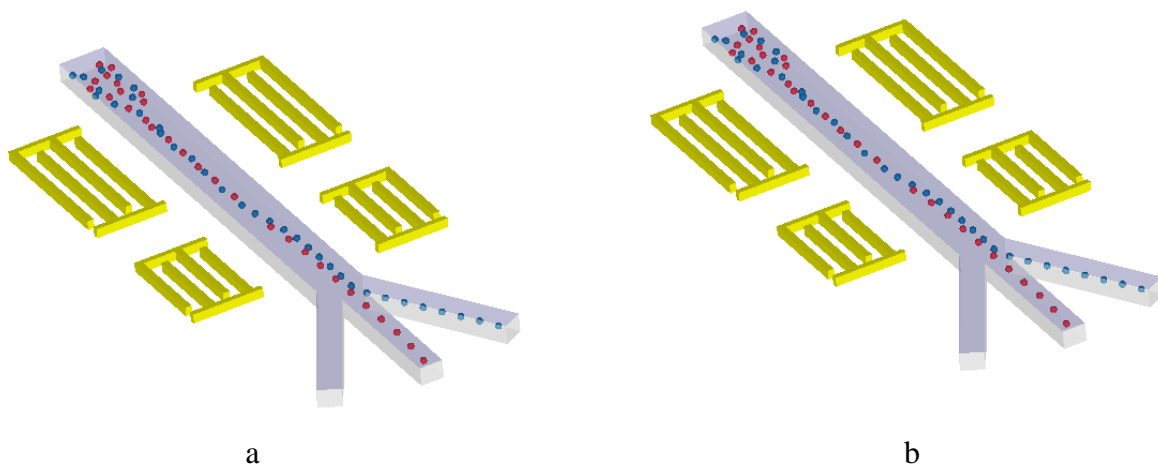


Figure 1: Schematic of microchannels (a) for separation under SSAWs, (b) for separation under TSAWs

Conclusion

We have found some amazing results, which we are looking forward to presenting for the international acoustofluidics community at *Acoustofluidics 2020 Virtual Conference* on 26 - 27 August 2020. These results are:

- For SSAW separation at a flow rate of 7 $\mu\text{L}/\text{min}$ and voltage 9V, the separation efficiency for WBCs is 100% at the lateral outlet and for DU145 is 98.5% at the middle outlet, and the proper separation occurred under SSAW.
- Likewise, at a flow rate of 7 $\mu\text{L}/\text{min}$ and voltage 4V, the separation efficiency for both WBCs and DU145 is 100% at their respective outlets and the proper separation occurred under TSAW.
- As can be seen from the results, at a constant flow rate, the voltage value for separation under TSAWs is lower than one under SSAWs. However, SSAWs have less error than TSAWs, which means that the sensitivity of TSAWs to voltage changes is high.

Analyzing physical fields and particle motions influenced by different descriptions of PDMS in the model of SAW-PDMS acoustofluidics

Zhengyang Ni¹, Xiasheng Guo¹

¹ Key Laboratory of Modern Acoustics (MOE), School of Physics, Nanjing University, Nanjing, China
E-mail: zhengyangni@smail.nju.edu.cn

Introduction

In modelling acoustofluidic chips actuated by surface acoustic waves (SAWs) and using polydimethylsilane (PDMS) as a channel material, reduced models[1,2] are often adopted to describe the acoustic behaviors of PDMS. Here, based on a standing SAW (SSAW) acoustophoresis chip, we compared three different descriptions of a PDMS chamber through finite element (FE) simulations. Specifically, the PDMS domain was considered as an elastic solid material, a non-flow fluid, and a lossy wall, respectively. Comparisons between different models can reveal to what extent the reduced models can impact the accuracies of simulations. More importantly, we then looked into in-chamber physical fields followed by particle tracing results, which might help users of reduced models to understand possible disparities between their observed results and simulations. Through quantitative comparisons and parameter studies, we further show how the side wall played a part, as well as how pressure fields from different models could be roughly scaled to each other.

Simulation Methods

In this work, to clarify the physics in modelling SAW-PDMS chips, three FE models using different descriptions of a PDMS chamber bonded on a standing SAW acoustofluidics chip were compared. The first model (the solid model, model S shown in Fig. 1(c)) was full model, which took the piezoelectric substrate into consideration and allowed the propagation of shear waves in PDMS, except that we set a low-reflecting boundary at the top of the lid. This boundary condition was used to mimic the behaviour of the relatively thin lid to that of a millimeter-thick top layer of real chambers. The second model (the acoustic model, model A shown in Fig. 1(d)) treated PDMS as a non-flowing fluid, which did not support shear waves, but allowed wave leakage at the substrate–PDMS interface. The third model (the impedance model, model I shown in Fig. 1(e)) was similar to that built by Nama *et al*[2].

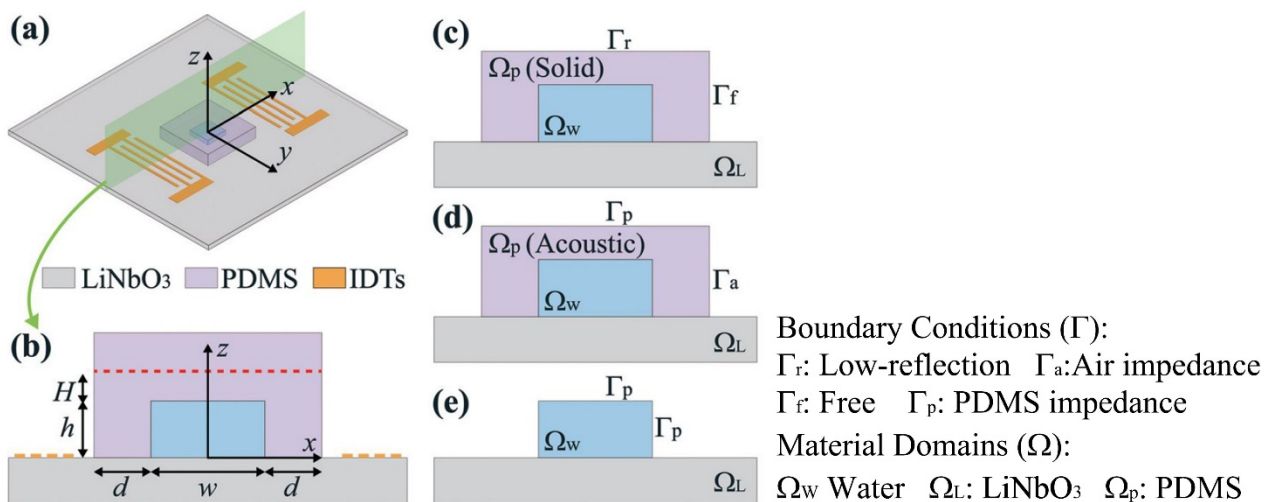


Figure 1: The (a) 3D sketch and (b) 2D x - z cross section of the SAW-PDMS acoustophoretic chip, and the illustrations of (c) model S where PDMS was considered as an elastic solid, (d) model A in which PDMS was treated as fluid, and (e) model I where PDMS was described using impedance boundaries.

Results

The sound field patterns (Fig. 2(a-c)) in all three cases were similar to each other, especially models S and A exhibiting nearly identical performances, while model I showed some disparity at the neighborhood of the

side boundaries. Inside the main area of the chamber, all three models resulted in similar streaming fields (Fig. 2(d-f)), showing six streaming rolls in the bulk. The shear waves that propagated in a solid PDMS wall did not influence the in-chamber pressure fields severely, but induced an observable difference in the acoustic streaming patterns.

In the three models, leakage of acoustic energy into the chamber followed different mechanisms. In Model S and Model A, some of the wave energy was absorbed by PDMS, except that both longitudinal and shear waves suffered from this loss in model S, while only the former needed to be considered in model A. In model I, these energy dissipation mechanisms were absent. After calculating the average pressure amplitude ratios $\Phi^{(S)}$ (between Model S and Model I) and $\Phi^{(A)}$ (between Model A and Model I) with different d/λ_R and f (Fig. 3), we found that the wave attenuation caused by the LiNbO₃-PDMS interface can be characterized by loss per wavelength, and the dispersion of that was approximately a linear function of frequency f , indicating the wave leakage at the interface being the main source of the transmission loss of SAWs.

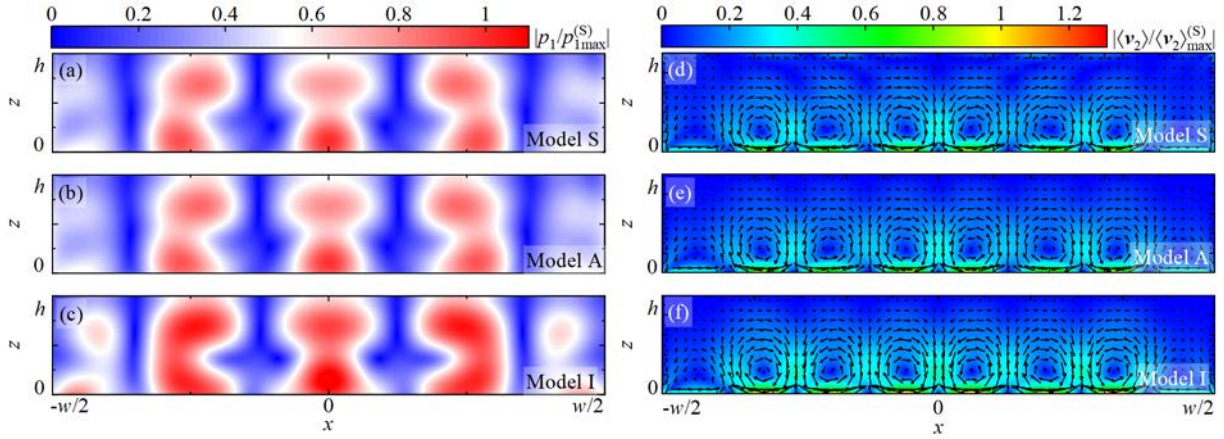


Figure 2: (a-c) Distributions of the acoustic pressure (p_1) amplitude inside the chamber normalized to the maximum value of that in model S, *i.e.*, $|p_1/p_{1\max}^{(S)}|$, corresponding to the results from (a) model S, (b) model A, and (c) model I. (d-f) The AS patterns normalized to the maximum amplitude of that in model S, *i.e.*, $\langle v_2 \rangle / \langle v_2 \rangle_{\max}^{(S)}$, corresponding to the results of (d) model S, (e) model A, and (f) model I. The colored images are the amplitudes; the arrows represent the vector fields. Device parameters: $w = 600 \mu\text{m}$, $h = 100 \mu\text{m}$, $d = 600 \mu\text{m}$, $H = 25 \mu\text{m}$, $f = 13.40 \text{ MHz}$.

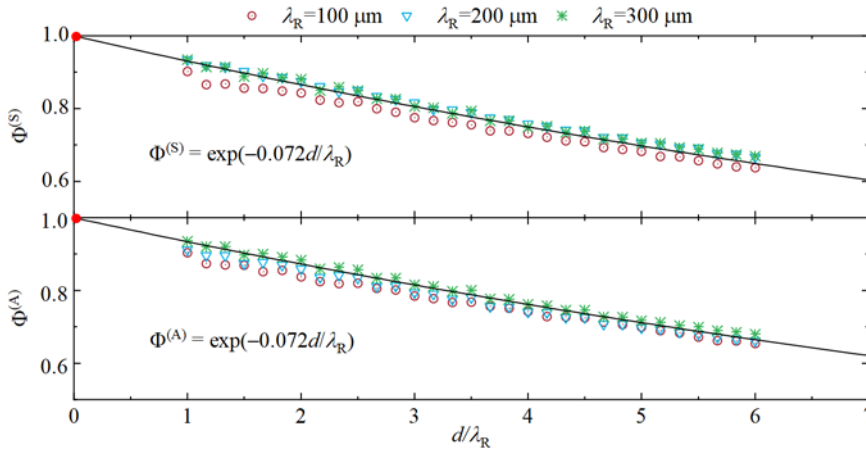


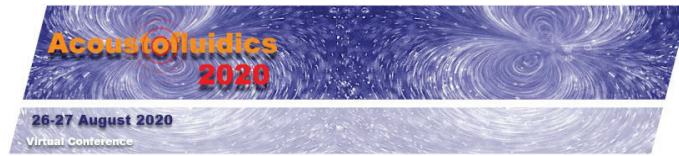
Figure 3: The pressure ratios (a) $\Phi^{(S)}$ (b) $\Phi^{(A)}$ as functions of d/λ_R at working frequencies $f = 13.40$, 26.80 , and 40.20 MHz , corresponding to $\lambda_R = 300$, 200 , and $100 \mu\text{m}$. The black curves are exponential fittings of the simulated data.

Conclusion

The comparisons between models S and A indicate that the prevalent viewpoint that shear waves in PDMS play insignificant roles in the performances of SAW-PDMS chips needs to be carefully reconsidered. Although shear waves carried very low energy and dissipated very fast while propagating in PDMS, they did make a difference to the physical fields especially the AS in the chamber, and thereby influenced the motions of different-sized particles to different extents. The acoustic radiation force can be overestimated when describing PDMS as a lossy wall, especially at the bottom corners of the chamber, which could cause inaccurate predictions of the motion of big particles. The damping effect of substrate-PDMS interfaces mainly originated from the wave leakage into PDMS and followed an exponential law. Based on the damping mechanism, a rough protocol is provided for scaling of pressure fields between different models.

References

- [1] N. R. Skov and H. Bruus *Micromachines* 7, 182 1-14 (2016).
- [2] N. Nama, R. Barnkob et al. *Lab Chip* 15, 2700-2709 (2015).



Defects in a new periodic structure formed by two different side branches

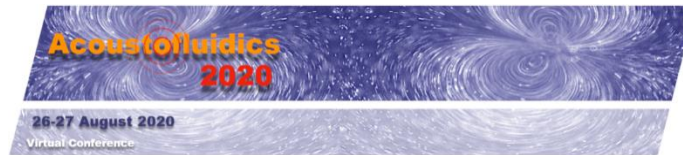
Mohamed El Malki¹

¹LMOEE, Department of Physics, Faculty of Sciences, Mohammed First University, 60000 Oujda, Morocco
E-mail: m.elmalki100@gmail.com

Introduction

We present an original study of the acoustic wave transmission in a new periodic structure with side branches grafted in a waveguide. These resonators have different boundary conditions at their extremities. One of them has a rigid termination, while the other has an open one. The cross-sections of all segments are considered much smaller than the considered wavelength. We limit our study to the case of identical media, without flow, constituting the main tube and the grafted resonators. Because of the periodicity, transmission bands would appear. The proposed structure can be used as an acoustical filter. This theoretical study reveals that, in a periodic structure formed by a high-pass filter and a low-pass filter, the combination of the two resonators can function effectively as a high-frequency wave reflector which can be used to effectively attenuates the generation of sound. When a defective resonator replaces a segment of a rigid/open pipe, localized modes appear inside the forbidden bands. We show that the transmission of these defects modes are very sensitive to the geometrical parameters of the defective resonators. The presence of a defect can also attenuate the whole transmissions inside the pass-bands which produce new bandgaps called a flat band. The numerical results of the transmission spectrum are obtained using the interface response theory and the transfer matrix. The results remain the same. These results can provide a useful way for the design of such a system to achieve a relatively wide noise attenuation band and to track some narrow noise peaks within it. The defective structure can also behaves as a selective filter.

Keywords : acoustic wave transmission, new periodic structure, side branches, acoustical filter, defective resonator, localized modes.



Dynamic coating of one liquid by another by employing the Acoustowetting phenomenon

Avital Reizman¹ and Ofer Manor¹

¹Department of Chemical Engineering, Technion – IIT, Haifa, Israel
E-mail: reizmana@campus.technion.ac.il

Introduction

We investigate the dynamic wetting of one liquid by another under the influence of a 20 MHz, propagating, surface acoustic waves (SAWs) of the Rayleigh type. The dynamics of liquid films, wetting and de-wetting effects, and the transfer of momentum from an acoustic wave to flow, known also as acoustic streaming, have been separately investigated for many years. These different fields of research were recently converged together when the Acoustowetting phenomenon was discovered approximately 10 years ago. Researchers first observed this phenomenon in the coating flows of different types of silicon oil¹⁻³. A following theoretical work, which quantified the acoustic-capillary balance in water, where capillary forces and the friction associated with the motion of the three-phase contact line are formidable, provided the necessary insights to introduce the Acoustowetting effect in water^{4,5}. The phenomenon of Acoustowetting has been further investigated for applications in wetting and de-wetting nano-channels, coating surfaces against the action of gravity, bi-phase microfluidics, and in Landau-Levich type coating problems. Here, we investigate the coating of one liquid by another – a common process in industrial manufacturing and in particular in the manufacturing of polymer-based products. We study a model problem of the dynamic coating of water drops by films of silicon oil under the influence of a propagating MHz-frequency SAW in the solid substrate.

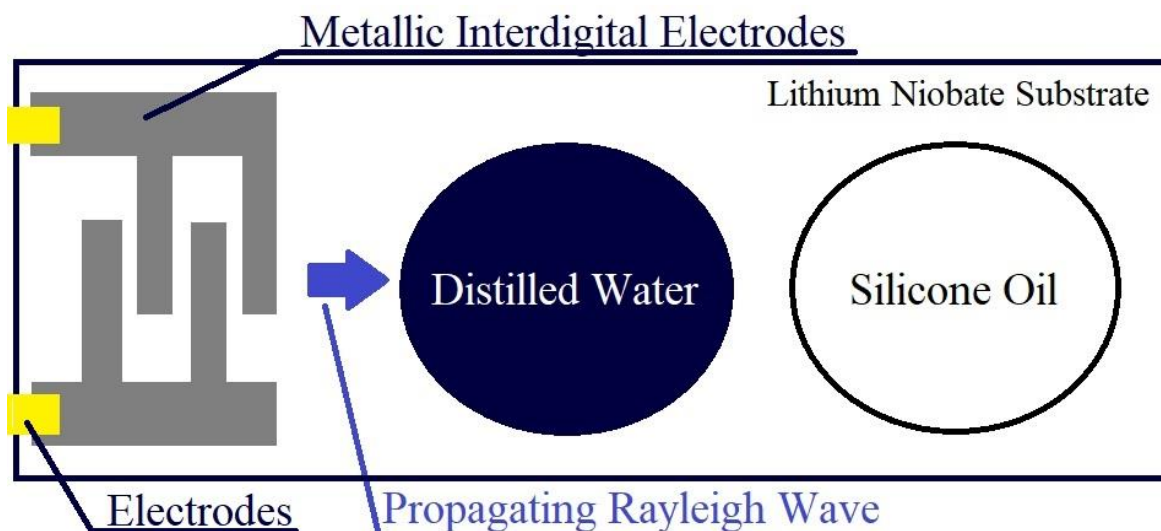


Fig 1: A sketch of a SAW device which supports a deionized water drop and a Silicone Oil film.

Experiment

We position blue-colored deionized water drop and a transparent silicone oil (50 cst) film on an acoustic actuator – a SAW device, as shown in Fig 1. The SAW device is comprised from metallic interdigital electrodes (IDT) which we fabricate atop a piezoelectric lithium niobate substrate (LN). By connecting the device to a signal generator and an amplifier we transmit electrical power to the device. The device converts this power to an electromechanical wave in the form of a propagating Rayleigh wave. The latter is concentrated near the upper surface of the device and hence is referred to as a SAW.

In order to render gravitational contributions to the wetting dynamics marginal, we position the SAW device horizontally and make sure that the thicknesses of the water drop and the oil film are far below the capillary-gravitational length of approximately 1 mm. In the presence of the SAW, we observe that a thin film of silicone oil dynamically wets the substrate opposite the SAW, while the water drop, which experiences formidable capillary resistance to motion, remains in its original position. Eventually the oil film either moves around the water drop, partially covers the drop, or fully covers the drop as function of the thickness of the water drop and the power transmitted to the SAW device. The later scenario mentioned, where the drop is eventually almost fully coated by the oil, is shown in Fig. 2.

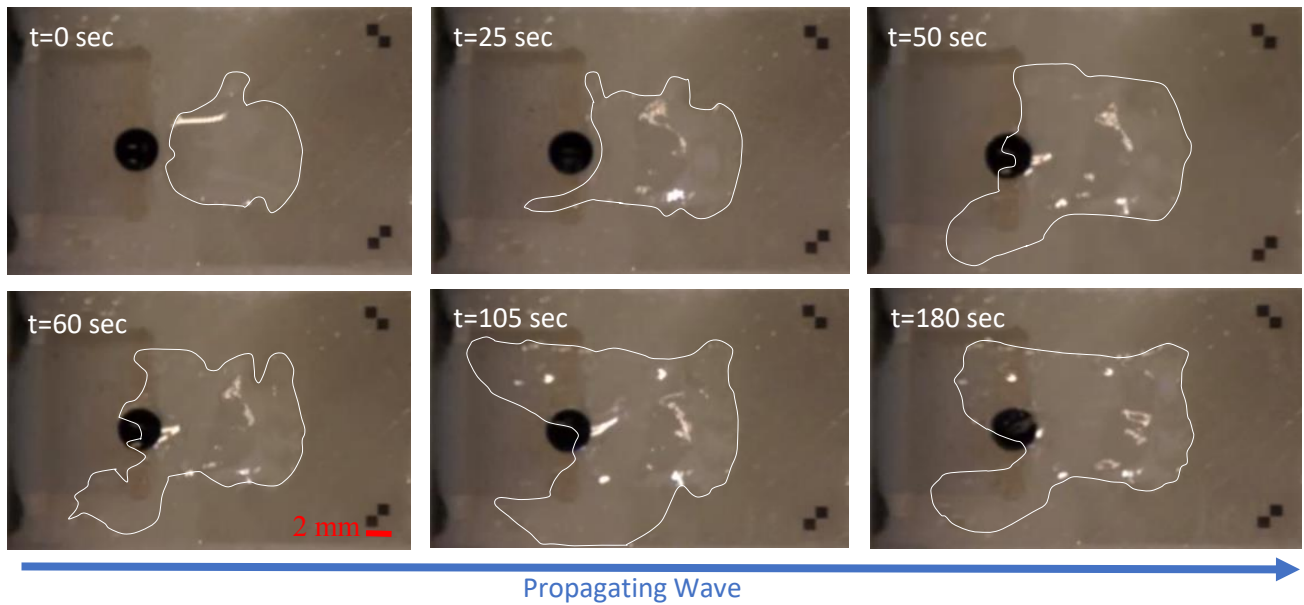


Fig 2: Temporal images of a thin transparent film of silicone oil, which dynamically wets the solid substrate against the propagating SAW to eventually fully coat the blue colored water drop.

Conclusion

In this work we show that it is possible to coat one liquid using another liquid by employing SAWs. As a model problem, we employ a 20 MHz frequency SAW to support the coating of a water drop by a film of silicon oil. We find that the oil film, which dynamically wets the solid substrate under the action of the SAW, may flow around, partially coat, or fully coat the water drop as function of the thickness of the drop and the power transmitted to the SAW device on which the coating process takes place.

References

- [1] A. R. Rezk, O. Manor, J. R. Friend, and L. Y. Yeo, "Unique fingering instabilities and soliton-like wave propagation in thin acoustowetting films," *Nat. Commun.* 3, 1167 (2012).
- [2] A. Rezk, O. Manor, L. Y. Yeo, and J. R. Friend, "Double flow reversal in thin liquid films driven by MHz order surface vibration," *Proc. R. Soc. A* 470, 20130765 (2014).
- [3] O. Manor, A. R. Rezk, L. Y. Yeo, and J. R. Friend, "Dynamics of liquid films exposed to high frequency surface vibration," *Phys. Rev. E* 91, 053015 (2015).
- [4] G. Altshuler and O. Manor, "Partially wetting water films atop propagating substrate vibrations," *Phys. Fluids* 27, 102103(2015).
- [5] G. Altshuler and O. Manor, "Free films of a partially wetting liquid under the influence of a propagating MHz surface acoustic wave", *Phys. Fluids* 28, 072102 (2016)

Modeling of acoustic enhanced electrochemical polishing processes

Johannes Landskron^{1,2}, Sabrina Tietze^{1,2}, Conrad Wolf² and Klaus Stefan Drese^{1,2}

¹Institute of Sensor and Actuator Technology, Coburg University of Applied Sciences and Arts, Am Hofbraeuhaus 1b, 96450 Coburg, Germany

E-mail: isat-info@hs-coburg.de, URL: <https://www.isat-coburg.de/>

²Coburg University of Applied Sciences and Arts, Friedrich-Streib-Straße 1b, 96450 Coburg, Germany

Introduction

It is well known that electrochemical processes can be positively influenced by acoustic waves [1,2]. In previous works, it has been shown that guided plate modes on flat copper electrodes can accelerate electrochemical polishing processes [3,4]. A FEM model describing the essential processes is presented to verify the understanding of the processes and to investigate details not accessible in the experiment. The simulation results are compared with the experimental data for these purposes.

Experimental setup and observations

The experiments were performed on a laboratory scale setup (Figure 1a). The electrolyte was a mixture of water, phosphoric acid and isopropanol. For the electroplating experiments, 0.3 mm thick copper plate electrodes were used. The excitation signals were generated by a sinewave generator combined with an amplifier and a piezo-electric transducer fixed to the top end of the anode. This way standing waves with amplitudes of 30 nm at a frequency of 910 kHz were achieved at room temperature. The cell voltage and the polishing current in the experiment were measured by the power supply. In case of potentiostatic experiments the influence of the acoustic mixing was observed as a step-wise increase of the polishing current in the current-time diagram (Figure 2f) as the excitation was turned on. Furthermore, a deformation of the dark colored boundary layer near the electrode was visible. At the end of the acoustically enhanced polishing process, a periodic surface profile was seen under the optical microscope.

Computational modeling

The FEM model was implemented in COMSOL Multiphysics for a small 2D section of the electrode immersed in the electrolyte (Figure 1b). To avoid a resonator setup a perfectly-matched-layer (PML) was used in the acoustic simulations to allow energy dissipation at the top end of the electrolyte domain. Because of different timescales of the various physical effects, the system was calculated in multiple steps. In the first step the dispersion relations for a narrow section of the electrode covered with the electrolyte were calculated using Floquet boundary conditions. A working point for a non-decoupling wave (QSP mode) was selected from the calculated eigenvalues. In the next steps the scale of the FEM model was adapted to a multiple of the chosen wavelength to implement the periodicity of the small partial model. To calculate the acoustically induced streaming effects in the electrolyte a two-step perturbation approach was used [5]. First, the harmonic parts of sound field related to the motion of the electrode surface were calculated in the frequency domain. Then, based on the perturbation theory the mean acoustic streaming effects were determined from the sound field. In the last step the ion transport in the electrolyte was modeled by convection-diffusion equations including mixing terms caused by the acoustic streaming. The reaction rate was described by a Butler-Volmer equation related to the ion concentration on the electrode surface. The parameters used in this model were taken from experimental data or literature values if they were not determined yet.

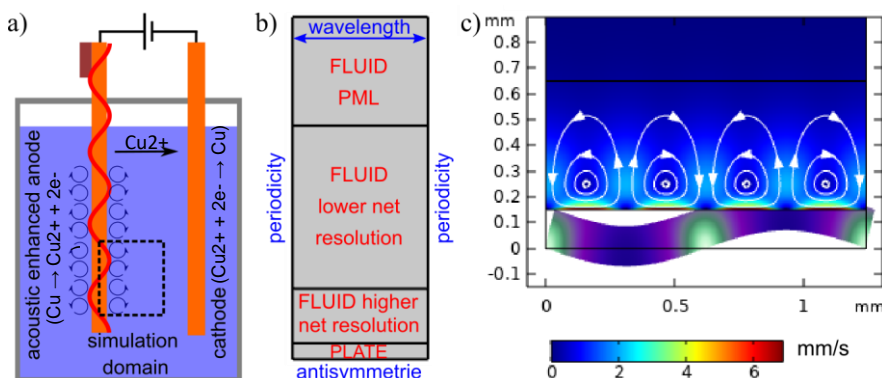


Figure 1:

(a) Sketch of the experimental setup with acoustic introduced streaming caused by a standing wave. The transducer is fixed on the top end of the anode.

(b) Sketch of the geometry used in the COMSOL model including the domains for the anode the electrolyte and the PML.

(c) Calculated streaming pattern caused by a standing wave on the electrode. Four alternating vortex flows are observed per each single wavelength.

Comparison between computational and experimental results

As can be seen in Figure 1c four vortices with alternating flow directions occur per one wavelength section. The flow pattern shows streaming towards the walls in the nodes and away from the walls in the antinodes. These vortices ensure an increased ion exchange between the boundary layer next to the electrode and the electrolyte bulk. Since not all simulation parameters, especially in the electrochemical part of the model, could be determined, results are compared qualitatively only. The streaming pattern leads to alternating ion concentrations along the electrode, with two peaks per wavelength (Figure 2a). Likewise, in the experiment, two profile peaks per wavelength can be observed in the electrolyte (Figure 2b). Based on the simulation results, the optical effects in the experiment can be attributed to the local ion concentrations caused by the acoustic mixing, not to the streaming itself. Furthermore, these varying ion concentrations also cause local variations in current density along the electrode via the Butler-Volmer equation (Figure 2c). The mean value of this current is higher than without streaming. Faraday's law of electrolysis couples the local removal rate with the local current density. Consequently, the local removal rate also varies, resulting in a periodic surface pattern seen after the experiment (Figure 2d). Finally, the transient simulation of the overall current shows the same effects as the experiment did (Figure 2e-f). From the beginning of the measurement, the current decreases rapidly caused of the depletion of the involved chemical species. By switching on the acoustic induced mixing the current is reset to a higher level resulting in a reduction of the electrical resistance of the electrolyte.

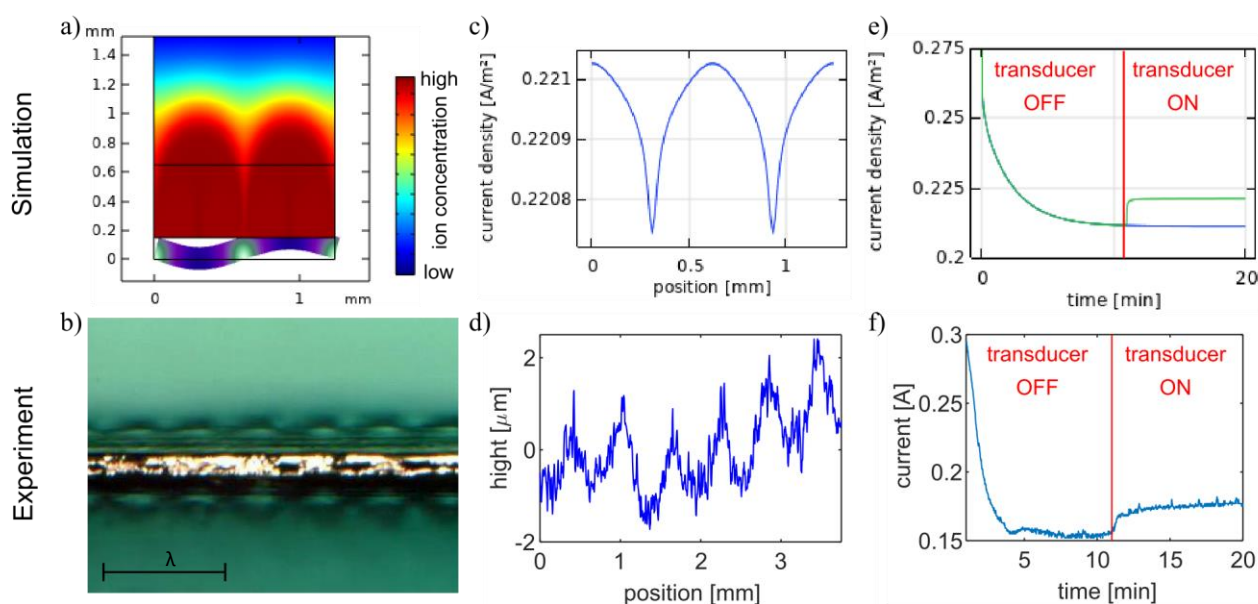


Figure 2:

Calculated local variations in the ion concentration profile (a) at the electrode and corresponding variation of optical properties under the microscope (b). Local variations in the current distributions (c) explain the wavy electrode surface (d) after the polishing process and prove the standing wave theory. Both in the simulation (e) and in the experiment (f), an increase in the total current, caused by the activation of the acoustic support, is observed.

Conclusion

The results from the developed FEM model correlate well with the experimental data in multiple aspects. The model will help to understand and predict the interaction and influence of different parameters e.g. excitation frequency, excitation amplitude and electrolyte concentrations on electrochemical processes. This will allow enhancing not only electrochemical polishing but also other diffusion-limited electrochemical processes. Further experiments will support detailed validation and improvement of the model (e.g. by evaluating the streaming pattern using a PIV measurement and determining the open parameters for the simulation by electrochemical measurements). The improved model will help us to investigate additional aspects like acoustic mixing and ion depletion on structured electrodes in future.

References

- [1] T. Mason, J. Lorimer, D. Walton. *Ultrasonics* **28**(5), 333–337, 1990.
- [2] J. Kaufmann, M. Desmulliez, Y. Tian, D. Price, M. Hughes, N. Strusevich, C. Bailey, C. Liu, D. Hutt, *Microsyst Technol* **15**(8), pp. 1245–1254, 2009.
- [3] S. Tietze, J. Schlemmer, G. Lindner. *Procs. 89231B, SPIE Micro+Nano Materials, Devices, and Applications*, Melbourne, Australia, 8 - 11 December 2013
- [4] S. Tietze, M. Reißerweber, J. Schlemmer, G. Lindner. *Procs. pp. 1039 – 1042, ICU*, Metz, France, 10 – 14 May 2015
- [5] P. Muller, R. Barnkob, M. Jensen, H. Bruus. *Lab on a Chip* **12**, 4617 – 4627, 2012

This work was supported by the “Technologie Allianz Oberfranken (TAO)” and by the European Fund of Regional Development (EFRE) within the project “InnoTerm”.

A multi-channel programable amplifier for high voltage high frequency transducer excitation

Hiep X. Cao^{1,2}, Han-sol Lee^{1,2}, Daewon Jung², Byungjeon Kang², Jong-Oh Park^{1,2}, Chang-Sei Kim^{1,2}

¹Department of Mechanical Engineering, Chonnam National University, Gwangju 61186, Korea
E-mail: hiep.caoxuan@gmail.com

²Korea Institute of Medical Microrobotics, Gwangju 61186, Korea

Introduction

Acoustic techniques are becoming very popular in trapping and manipulating particle recently. In those techniques, it required the amplifier with multi-channel for driving transducers at high voltage high frequency. In this study, we design and fabricate the compact and economical multi-channel programable amplifier for high voltage and high frequency transducer to researcher in laboratory. The 16 channels were programmed independently to generate bipolar square wave in continuous mode at a frequency of 1MHz, and amplitude up to 200 Vpp to drive 16 1-MHz piezoelectric transducers. The amplifier is easy to increase the number of channels by adding more diver board. The purpose of this study was to investigate the performance of trapping micro particle (300 μm) with 16 transducers in the water.

System Design

A block diagram of the proposed multi-channel programable amplifier for high voltage and high frequency transducer is shown in Figure 1. The transducer is driven at high-voltage bipolar square wave in continuous mode. The bipolar voltage shows many advantages for driving high voltage, high frequency transducer. First, the bipolar voltage pulse has lower unwanted DC and a low-frequency component that can decrease the leakage current compared to its unipolar counterpart. Second, bipolar voltage is peak-to-peak voltage can be twice the voltage age rating of the coaxial cable connecting the amplifier and the transducer [1]. So, the size and cost of the cable can be substantially reduced. This amplifier was designed with 16 channels.

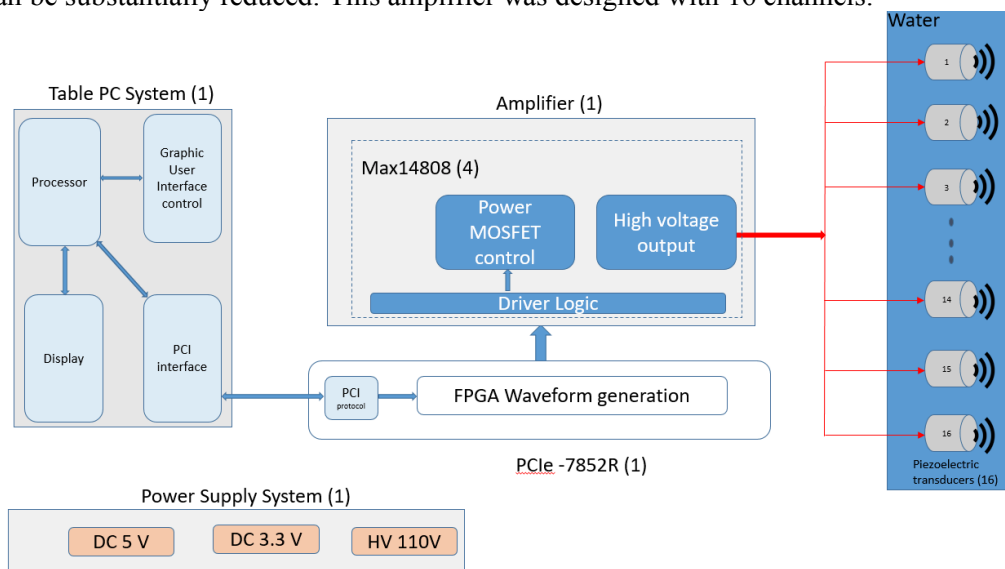


Figure 1: A block diagram of the 16 channels programable amplifier for high voltage high frequency transducer

The system have been mainly designed into 4 subsystems; (1) the table PC subsystem for user control the amplifier parameter like amplitude, frequency, time delay for each channel independently, (2) the microcontroller used the Labview FPGA card PCIe-7852R for generated square wave control at 3.3V, to control bipolar voltage, we use two control signal to control the output signal. One control signal will control the positive part, and another is control negative of bipolar output voltage. (3) For amplifying the voltage from 3.3V to $\pm 100\text{V}$ in continuous mode, the amplifier used four MAX14808 boards. Each board will control give four $\pm 100\text{V}$ output signals. (4) Power supply subsystem supply DC 5V, DC 3.3V and bipolar voltage from

$\pm 5V$ to $\pm 100V$. All the cable in the system is designed in considering of acoustic impedance. we use the RG316 flexible Coax Cable.

System fabrication

Micocontroller

The Labview FPGA card is inserted in computer, the control interface is programed on Labview FPGA 2017. The control signal connected to the amplifier board by SHC68 (Texas instrument) cable.

Amplifier

The amplifier was designed as 4 modules, each module has 4 output signals. The SMA connecter was soldered into the board and was connected to transducer by SMA-BNC cable.

Cooling devices:

Cooling devices consists copper heatsink and fan for MAX14808 IC. There are four MAXIM 14808, the system used four coopers heatsink and four fans. Heat sink was taped on IC, and fan was designed as one layer above the board. It makes the system more compact and replacement.

The bipolar power supply:

The bipolar power supply was supplied by other bipolar power system in the laboratory.

System validation and Experiment

Validation

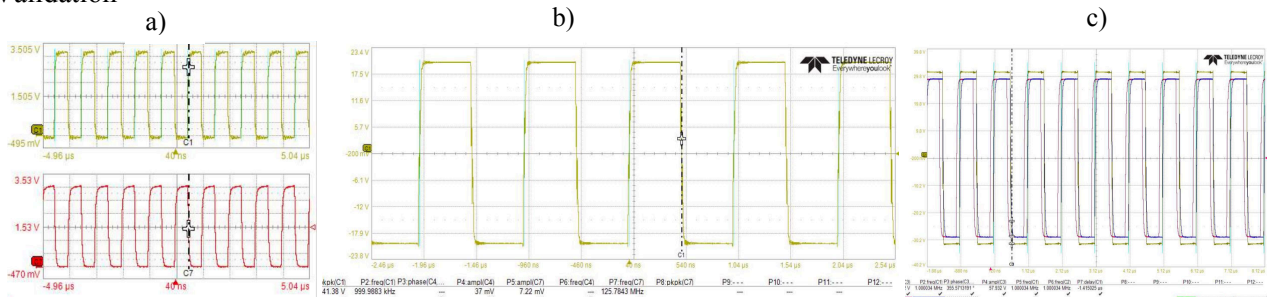


Figure 2: the control signal and the output signal

- (a) Two control signals were generated by labview FPGA card at 1 MHz. (b) the one output signal was generated at 60 Vpp and 1 MHz from two control signal in Fig 2.a (c) multi-channel output signal at 60 Vpp were generated.

Experiment

Briefly, we show results for a twin trap[2] generated by flat type with 16 transducers operate at 60 Vpp and 1 MHz. The particle is scaffold with 300 μm diameter can be trap in the water. The transducer is 1C10I (japan probe) with resonant frequency at 1MHz

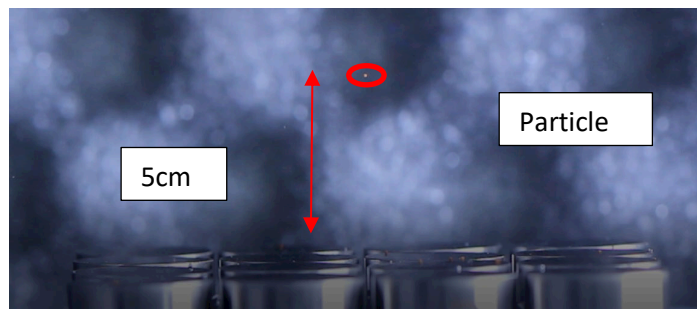
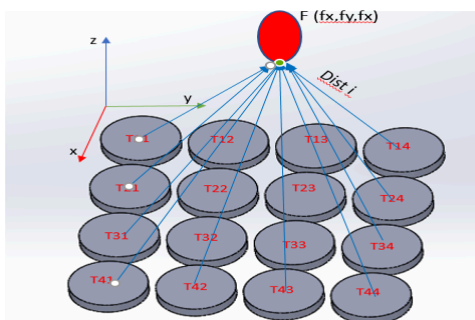


Figure 3: The result of experiment (a) the arrangement of 16 transducers [3]. (b) the position of particle at trap point.

Conclusion

In this work, we success develop a multi-channel programable amplifier for high voltage high frequency transducer excitation. The experiment result shown that the amplifier can drive 16 transducers independently to generate a trap. This amplifier will be applied to our research in trapping and manipulating particle.

Acknowledgment

This research was supported by a grant of the Korea Health Technology Development R&D Project through the Korea Health Industry Development Institute (KHIDI), funded by the Ministry of Health & Welfare, Republic of Korea (grant number: HI19C0642).

References

- [1] S.C Tang, G.T Clement. IEEE transactions on ultrasonics, ferroelectrics, and frequency control **54**, 1772 (2007).
- [2] A. Marzo, S.A. Seah, B.W. Drinkwater, D.R. Sahoo, B. Long, and S. Subramanian, Nat. Commun. **6**, 8661 (2015)
- [3] C.X Hiep. *Procs. pp. 261, KSPE 2019 autumn conference*, Changwon, 30. October - 1 November 2019.

Acoustophoretic manipulation of particles in impedance mismatched systems

Amal Nath¹, and Ashis K. Sen¹

¹Department of Mechanical Engineering, Indian Institute of Technology Madras, Chennai, India
 E-mail: me17d008@smail.iitm.ac.in, URL: <http://www.ashislab.in>

Introduction

Acoustic relocation is observed when an inhomogeneous fluid system is subjected to an acoustic standing wave inside a microchannel [1]. For a symmetric trifurcated system exhibiting negative acoustic impedance mismatch, i.e. when the stream with higher acoustic impedance through the side inlets, the higher impedance side stream is relocated to the center. If the side stream is a dilute suspension, the particles are also dragged along with the convected side stream. In this experimental study, we look at the behavior of low-impedance dilute suspensions infused through the central inlet under acoustic relocation. Here, as the relocation process initiates, the relocating suspension drags the particles to the sides against a competing acoustophoretic force field. Depending on the final configuration of particles, a phase diagram is developed outlining the different regimes observed which provide guidelines in developing cell sorters or medium exchange devices.

Methodology

A silicon based acoustofluidic chip with trifurcated inlet-outlet channel of length $L = 2$ cm, width $W = 400 \mu\text{m}$ and height $H = 300 \mu\text{m}$ is used in experiments. A piezoceramic transducer is attached to the bottom of the channel and actuated with an amplified sinusoidal signal at resonant frequency of 2.02 MHz. An inverted microscope was used along with a high speed camera to visualize the flow. Dilute suspensions of monodispersed polystyrene beads with suspending fluid I (DI + 9% iodixanol concentration) is infused through the center using syringe pump. The higher impedance stream (DI + 18% iodixanol concentration) enters the channel through the side inlets.

Analysis of results

First, the time required for relocation (τ_{rel}) at different flow rates, energy densities are found out as described in Fig. 1. Based on a previous scaling for relocation speed u_{ac} [2], we arrive at an analytical expression for relocation time:

$$u_{ac} = \frac{E_{ac}\hat{\rho}l}{\eta} \quad \tau_{rel} = \frac{W/3}{u_{ac}} \quad (1)$$

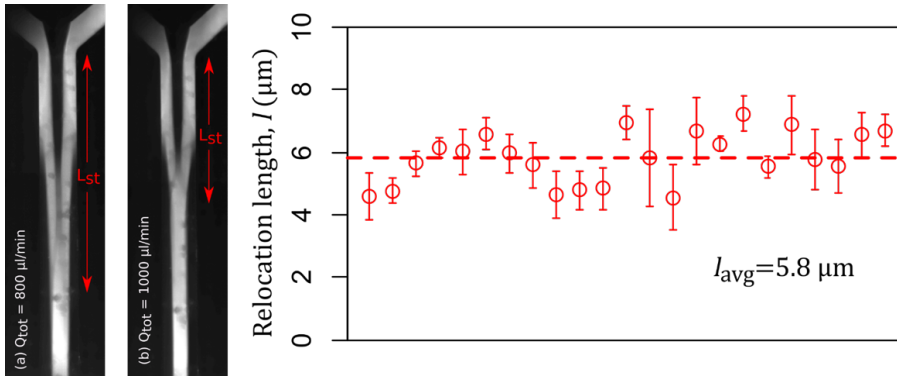


Figure 1: Fluorescent dye Rhodamine-B is added to the side streams to track the flow pattern while particle-free lower impedance stream is infused through the center. The relocation time is computed by scanning the fluorescent profile at different downstream lengths from the inlet. Beyond L_{st} , the length required to achieve stable configuration, the width of the relocated high-impedance stream in the fluorescent profile does not change. The relocation time is then defined as $\tau_{rel} = L_{st}/u_0$, where u_0 is the average inlet flow velocity.

Here, E_{ac} , $\hat{\rho}$ and η refer to the acoustic energy density, the normalized density difference between the streams and the average viscosity respectively. The average value of relocation length scale $l = 5.8 \mu\text{m}$ in Eq. 1 is obtained from experiments.

In the next set of experiments, monodispersed fluorescent polystyrene particles of different sizes are introduced in the central inlet in separate experiments and their trajectories under the combined effect of acoustic relocation and migration are observed. The particle sizes studied are $a = 1 - 15 \mu\text{m}$, the total flow rates are in the range $Q = 15 - 200 \mu\text{l}/\text{min}$ and acoustic energy densities were varied from $E_{ac} = 4 - 113 \text{ J}/\text{m}^3$. It is seen that generally for smaller-sized particles relocation-induced drag force dominates over the acoustophoretic force and are transported along with the relocating stream to the sides. Larger sized-particles are driven back to the new central stream. Based on the location of the fluorescent particle band at the outlet, three different regimes were observed as outlined in Fig. 2. The different regimes are generalized in terms of non-dimensional parameters relating to the residence

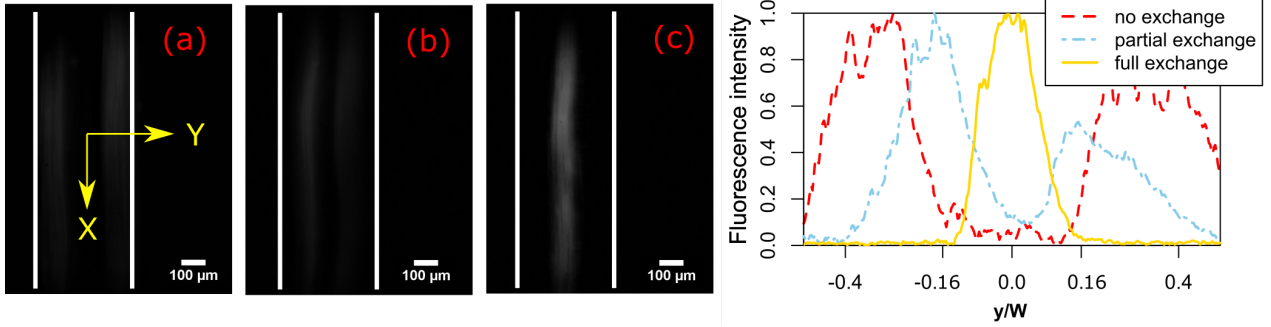


Figure 2: For $2 \mu\text{m}$ sized particles at a total flow rate of $Q_{tot} = 80 \mu\text{l}/\text{min}$, we observe three distinct regimes: (a) at $E_{ac} = 31 \text{ J}/\text{m}^3$, zero medium exchange where the particles remain in the original stream; (b) at $E_{ac} = 67 \text{ J}/\text{m}^3$, partial exchange of the suspending medium where the particles are distributed across both streams; and (c) at $E_{ac} = 113 \text{ J}/\text{m}^3$, full exchange where the particles are in the new central stream.

time in the channel $\tau_{res} = L/u_0$, the relocation time (obtained from Eq. 1 with the calculated length scale l) and the acoustophoretic migration time $\tau_{ac} =$ and is shown in Fig. 3.

$$\frac{\tau_{res}}{\tau_{rel}} = \frac{L}{u_0} \times \frac{E_{ac}\hat{\rho}l}{\eta W/3}; \quad \frac{\tau_{res}}{\tau_{ac}} = \frac{L}{u_0} \times \frac{2\phi a^2 k E_{ac}}{3\eta u_0} \quad (2)$$

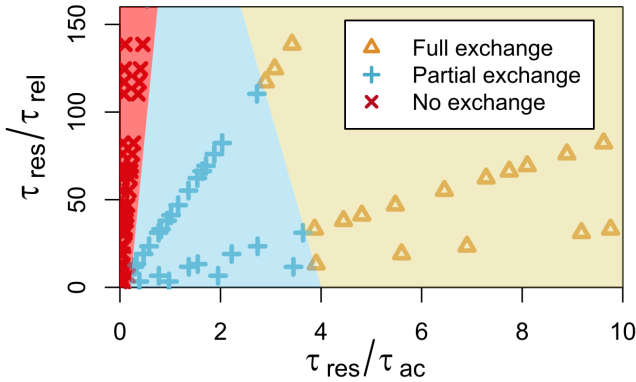


Figure 3: For large values of acoustophoretic time τ_{ac} , the particles remain in the original stream (red region) relocated to the sides irrespective of how quick the relocation proceeds. We see that the partial exchange to full exchange transition is dependent on the relocation time τ_{rel} . As the relocation proceeds faster, we see that particles with lower acoustic mobility, i.e. lower values of τ_{ac} are able to be fully transported into the new medium.

Conclusion

The different particle regimes under the combined effect of acoustic relocation and migration is characterized. The phase diagram provides some guidelines on designing devices to sort bidisperse particle suspensions or cell sorters. Although the phase diagram is developed for a fixed concentration difference between the streams ($\Delta c = 9\%$), similar trends can be extrapolated for other concentrations, once the limits of each regime are obtained.

References

- [1] S. Deshmukh, Z. Brzozka, T. Laurell and P. Augustsson. Lab Chip **14**, 3394-3400 (2014).
- [2] J. Karlsen and H. Bruus. Phys. Rev. Applied **7**, 1-10 (2017).

Control of a Bulk Acoustic Wave micro-channel through frequency shifting and its application to cell reconcentration

Ludovic Bellebon^{1,2}, Deborah François², Mauricio Hoyos¹ and Jean-Luc Aider¹

¹PMMH Laboratory, ESPCI Paris - PSL, Paris, France

E-mail: ludovic.bellebon@espci.fr

²Aenitis Technologies, Paris, France

Introduction

Tuning the acoustic frequency of a Bulk Acoustic Wave (BAW) resonator is the first step before using any acoustofluidics setup, precisely because the Acoustic Radiation Force (ARF) is supposed to be maximum if the resonance condition ($\lambda_{ac} = 2.h$, with h the height of the cavity and λ_{ac} the acoustic wavelength) is satisfied. If this condition is theoretically simple, it is much more difficult to find the right acoustic frequency when dealing with an actual experimental setup where multiple imperfect boundary conditions have to be dealt with, from the transducer to the reflector and through the transmitter and fluid layer. Many studies have been devoted to this issue, searching for a possible simple method to find the optimal frequency based on electric measurements, admittance or impedance measurements [1-3].

In this study we are interested in using the acoustic frequency as a way to control some of the main characteristics of an acoustofluidics cavity or micro-channel. Indeed, it was shown by Dron & Aider [4] that it is possible to move the axial position of the levitation plane z_{foc} along the entire height of a micro-channel just by shifting the acoustic frequency over a wide range of acoustic frequency centered on the optimal frequency of the transducer (from 1.6 to 2.8 MHz). In this experimental work we go further and show that this phenomenon is robust and can be used to control the position of acoustic focusing as well as the axial acoustic focusing velocity of particles. Finally this approach is applied successfully to various biological cells for cell-reconcentration applications.

Height and axial velocity depending the frequency

Using microscopy, we measured the evolution of the axial position of the levitation plane as a function of the

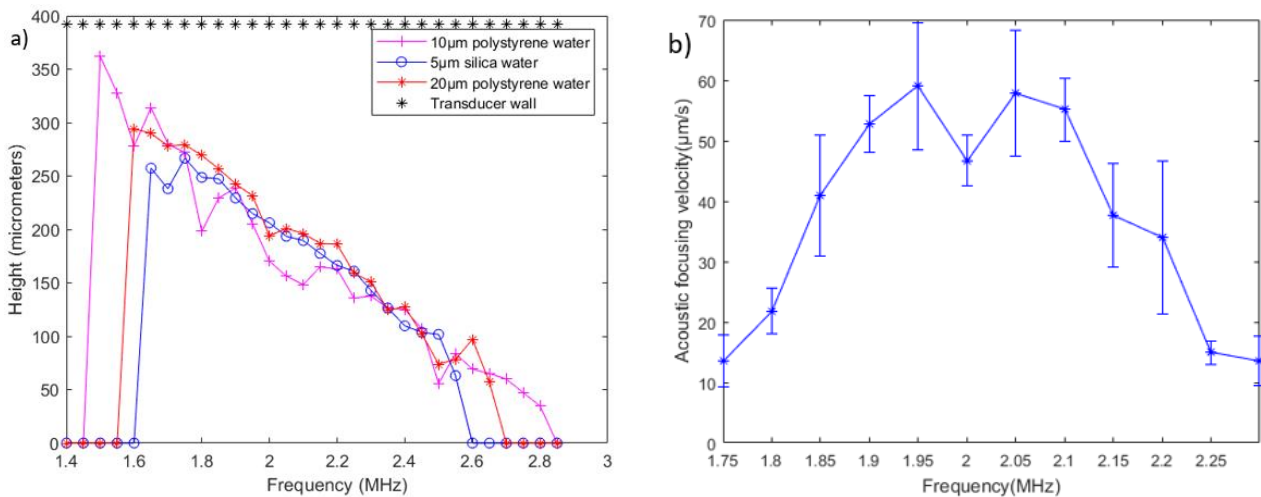


Figure 1: a) Position of 10µm, 20µm polystyrene and 5µm silica particles in micro-channel depending the frequency. Transducer is placed on the upper part of the channel. As we increase the frequency, particles are moving to the opposite wall of the transducer. b) Evolution of the focusing velocity of 5µm silica particles. Two peaks around the resonant frequency are observed while the velocity decreases as we are getting away from it.

acoustic frequency for different types and sizes of particles (10µm and 20µm polystyrene particles and 5µm silica). The channel height is $h = 400\mu\text{m}$, which corresponds to an optimal resonant frequency $F_{ac} = 1.9\text{MHz}$. As shown on Fig. 1, the axial location of the levitation plane can be moved nearly over the full height of the

channel, depending on the type of particles, over a wide range of acoustic frequencies, from 1.4MHz to 2.8MHz. The first observation is that z_{foc} decreases as the frequency increases. For low frequencies, the levitation plane is close to the transmitter wall and as we increase the frequency, it moves toward the opposite wall of the transducer. It is important to notice that the levitation planes are stable, i.e. the particles can be kept in levitation for each position.

To go further, it is important to measure the axial focusing velocity v_{foc} as a function of the acoustic frequency, in order to assess the yield of the system, as it is directly correlated to the magnitude of the ARF. We measure v_{foc} using the defocusing technique as presented in [5]. Two peaks of maximal velocities are observed around the resonant frequency (Fig. 1b). This velocity decreases for higher or lower frequencies; nevertheless the velocity is close to its maximum value over a relatively broad range of frequency (0.2MHz).

Knowing the frequency dependency of these two parameters it is possible to use it to optimize either separation or reconcentration processes.

Application to cell reconcentration

In order to validate these results in an actual acoustofluidics reconcentration setup, we apply this approach to various cells, illustrated here on Non Parenchymal Cells (NPC). We vary f_{ac} from 1.9MHz to 2.5MHz for a given flow rate of 1.5mL/min and a given voltage of 20V. Samples are collected in three different outlets of the micro-channel: one outlet is close to the transmitter wall, another collect the fluid at the mid-height of the channel while the third collect samples close to the reflector wall (opposite outlet). The result is shown on Fig. 2. We succeed to collect most of the cells in different outlets depending on the frequency. Most of the cells were collected in the adjacent outlet for 1.9MHz, in the central outlet for 2.1MHz and in the opposite outlet for 2.5MHz, in agreement with the frequency evolution shown in Fig. 1.

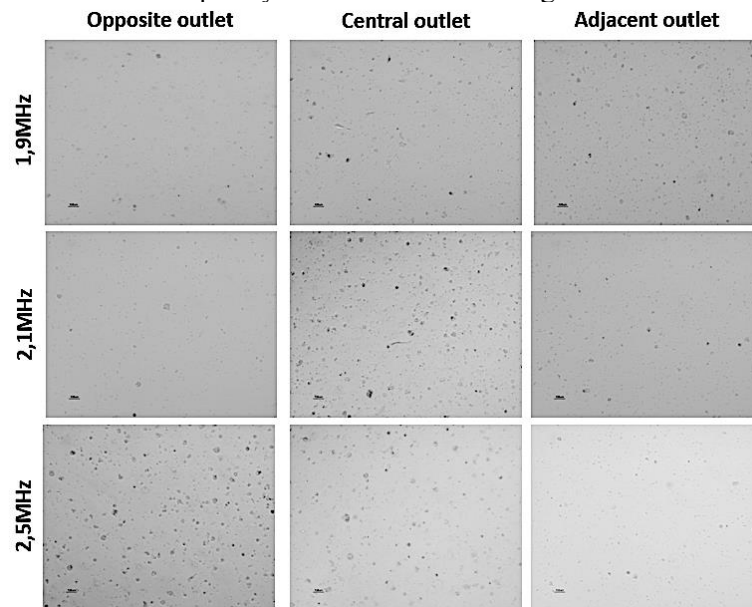


Figure 2: Pictures of samples of NPC cells in the different outlets after their passage in the BAW micro-channel for a given flow rate (1.5mL/min) and voltage (20V). Depending on the acoustic frequency the concentration of cells is increased in the adjacent outlet (1.9 MHz), central outlet (2.1 MHz) or opposite outlet (2.5 MHz).

Conclusion

In this experimental study, we demonstrate that it is possible to control some of the main properties of a broadband bulk acoustic wave micro-channel just through the proper choice of the acoustic frequency. We show that it is possible to control the axial position of the acoustic levitation plane as well as the focusing velocities of particles by tuning the acoustic frequency and we apply it successfully to a reconcentration process of NPC cells.

References

- [1] J. Dual, et al., *Lab on a Chip* 12.5 (2012): 852-862.
- [2] B. Hammarström, et al., " *Lab on a Chip* 14.5 (2014): 1005-1013.
- [3] V. Vitali, et al. *Nature Scientific Reports* 9, 19081 (2019).
- [4] O. Dron & J.-L. Aider. *Ultrasonics* 12, 4617-4627 (2013).
- [5] O. Dron & J.-L. Aider. *European Physics Letters* 97.4: 44011 (2012).

Dispensing and manipulation of femtolitre droplets by inkjet nozzle

Dege Li¹, Bingfang Huang¹, Yi Cao¹, Chao Zheng¹, Yonghong Liu¹, Yanzhen Zhang*^{1, 2}

¹College of Mechanical and Electrical Engineering, China University of Petroleum (East China), Qingdao, China

E-mail: zhangyanzhen@upc.edu.cn

²Swinburne University of Technology, Melbourne, Australia

Introduction

In recent years, the demand for dispensing and manipulation of picoliter, femtoliter and attoliter droplets is increasing in many scientific fields. Many approaches, including electrical, magnetic, optical, thermal and acoustic methods, have been proposed for this need. However, few of them are competent for both droplets dispensing and manipulation, simultaneously. For instance, as a non-contact method, acoustic wave has been successfully utilized as a means for droplets manipulation. Acoustic wave, usually the surface acoustic wave, can realize the particle focusing, separating, alignment, directing and patterning [1], and also can be used to actuate bulk fluid [2, 3]. Acoustic tweezers based on circular, slanted finger interdigital transducers were proposed for dynamic manipulation of micro-objects [4]. Furthermore, the surface acoustic waves can also be used for non-contact manipulation in the biological field [5] due to its superior performance. The sound wave propagates in the liquid phase, and the liquid is driven by the sound wave to form a water wave with a specific flow direction and waveform, which in turn drives the particles or micro droplets in the microfluidic system to move to achieve specific manipulation.

Here, inspired by the mechanism of the acoustic wave acting on the droplet, we propose a novel method that can realize the ultra-fine droplet generation and manipulation by a conventional commercial inkjet nozzle itself in an immiscible liquid phase. It no longer depends on the external acoustic wave, and the droplet can be manipulated by the mechanical wave generated by the nozzle itself.

Generation of the ultra-fine droplets

Firstly, here we confirmed that droplets much smaller than the orifice can be actively generated using a normal inkjet nozzle (MJ-AT-01-60 μm) purchased from MicroFab (USA). As shown in Fig. 1a and 1b, the piezoelectric actuator nozzle is controlled by a precise 3D positioner. And the head of the nozzle is partially immersed into another immiscible liquid phase. The microscope was connected to a high speed camera (Fastcam NOVA S12, Japan) to record the droplet generation and motion process. Different from the normal

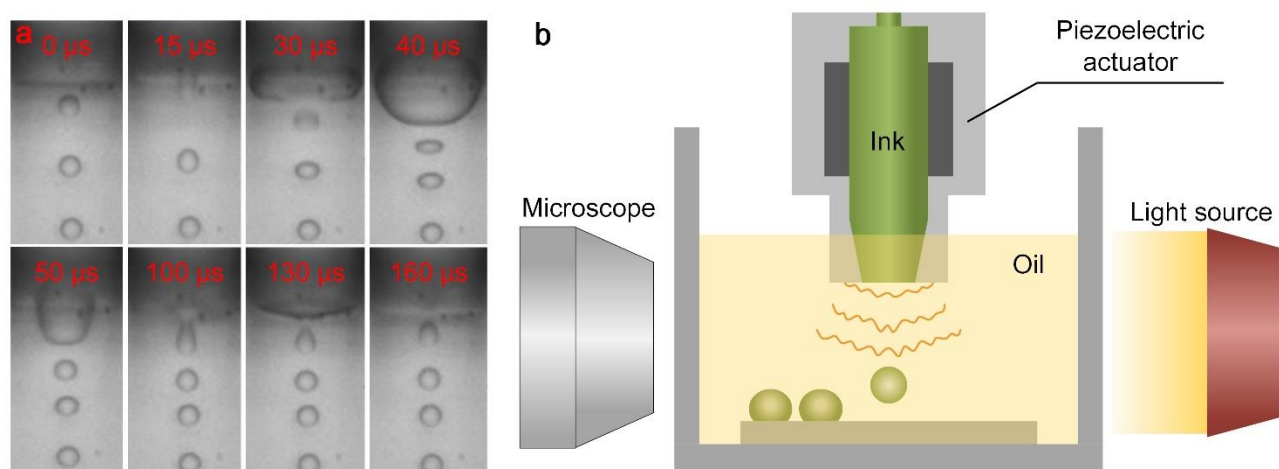


Figure 1: High speed images indicating the generation mechanism, schematic diagram illustrating the generation and manipulation mechanism and the experimental setup (not to scale). (a) The high speed images displaying the droplet generation process using conventional inkjet nozzle with diameter of 60 μm . (b) Schematic diagram of the experimental device and manipulation of the droplets.

operation, here the ink will be extruded out of the orifice and then sucked back in an immiscible liquid phase,

such as water in oil (Fig. 1a). With the combination action of the viscosity force, interfacial tension and inertial force, droplets several dozen times smaller than the orifice can be dispensed. Droplets with volume ranging from femtoliter to picolitre can be obtained by adjusting the voltage and time settings.

Manipulation of the droplets

Due to the ultra-small size of the droplet and the density difference, the gravity effect can be neglected. The free movement of the droplet is quite slow considering the buoyancy and viscous forces. Therefore, droplet manipulation must be realized by introducing external force. Inspired by the manipulation mechanism of the acoustic field and the droplet generation principle, here we let the nozzle itself generate the corresponding driving wave after dispensing the droplet. As shown in Fig. 2a, the first pulse T1 with high voltage and long duration is utilized to dispense the droplet. After the first extrusion and suction, the generated droplet will stay still near the nozzle, as shown in the first panel of Fig. 2b.

Considering the extruding and sucking action can cause fluctuations in the surrounding fluid medium, the high frequency and low amplitude pulses T₂, T₃, and T_n are applied to the piezoelectric nozzle to induce the directional movement of droplets, like the acoustic field. The extrusion process will bring a positive impact to the droplet due to the constraint of the nozzle, and the forward wave will carry the droplet moving together. The transportation mechanism is illustrated by the left inset panel in Fig. 2a. Then in the sucking back phase, the extruded liquid will be sucked back into the nozzle, and the position occupied by the extruded liquid medium will be supplemented by the incompatible medium nearby (see the right inset panel of Fig. 2a). Consequently, the flow rate becomes extremely small compared to the extrusion process. Therefore, for the droplets that have been pushed forward, the impact of the flow field during the suction process can be neglected. After the suction process being completed, the droplet basically stays in place and remains still. The whole process is illustrated by the series of panels in Fig. 2b, which are arranged in chronological order. In this way, we can transport the generated droplets to the destination step by step without using external equipment such as acoustic emission devices, high voltage DC power supply or laser source and etc.

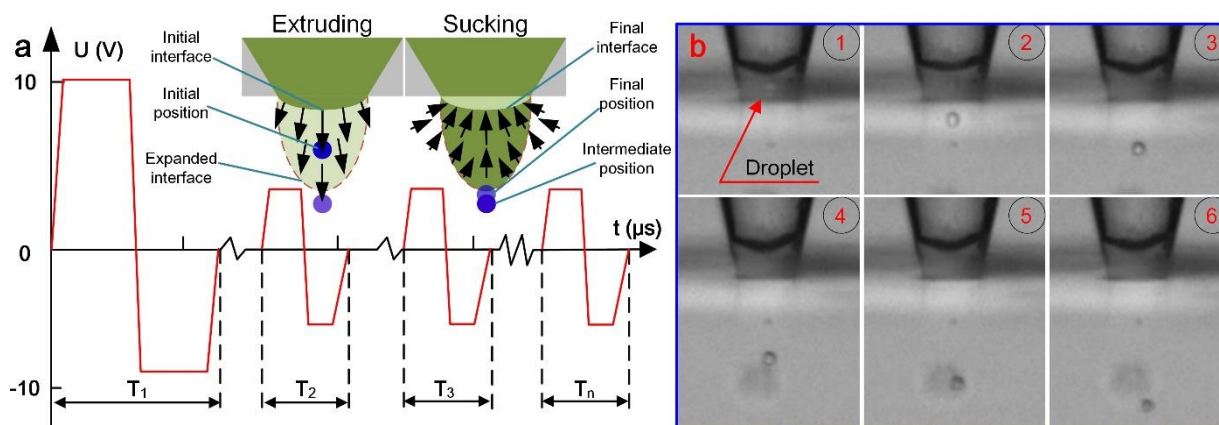


Figure 2: (a) Schematic diagram of generation and manipulation pulse waveform and flow field of extrusion and suction mode. (b) Movement manipulation process in chronological order.

Conclusion

Here we proposed a novel method for generating the ultra-fine droplets just using a conventional inkjet nozzle in another immiscible liquid phase, whose volume can vary from femtoliter to picoliter by adjusting the relative voltage and time settings. Then inspired by the mechanism of acoustic manipulation, we realized the self-control of the microfluidic system. After the generation of the droplet, a series of gentle pulses will be applied to the piezoelectric inkjet nozzle to induce a conveying waveform to transport the droplet to the destination. We have found some amazing results as mentioned above, which we are looking forward to presenting for the international acoustofluidics community at *Acoustofluidics 2020 Virtual Conference* on 26 - 27 August 2020.

References

- [1] Y. Zhou, Z. Ma, Y. Ai, *RSC ADV* 9, 31186 (2019).
- [2] G. Destgeer, H. J. Sung, *LAB CHIP* 15, 2722 (2015).
- [3] Z. Wang, J. Zhe, *LAB CHIP* 11, 1280 (2011).
- [4] P. Kang, Z. Tian, S. Yang, W. Yu, H. Zhu, H. Bachman, S. Zhao, P. Zhang, Z. Wang, R. Zhong, T. J. Huang, *LAB CHIP* 20, 987 (2020).
- [5] J. Zhang, S. Yang, C. Chen, J. H. Hartman, P. Huang, L. Wang, Z. Tian, P. Zhang, D. Faulkenberry, J. N. Meyer, T. J. Huang, *LAB CHIP* 19, 984 (2019).

Robotic microfingers: acoustic assembly and magnetic manipulation

Xiaolong Lu^{1,2}, Hui Shen¹ and Ying Wei¹

¹State Key Laboratory of Mechanics and Control of Mechanical Structures, Nanjing University of Aeronautics and Astronautics, Nanjing 210016, Jiangsu, China

E-mail: xllu@is.mpg.de

²Micro, Nano and Molecular Systems Group, Max Planck Institute for Intelligent Systems, Heisenbergstr. 3, 70569 Stuttgart, Germany

Introduction

Controllable assembly of complex structures from simple micro- and nanoparticles is of great importance for manufacturing micro and nanomachines [1]. Those assemblies have attracted extensive attention owing to their considerable promise in catalysis, chemical or biosensing, cell biology, and tissue engineering. In recent years, external physical fields have been developed as attractive strategies for accurate assembly of the particle components over a large area, demonstrating a combination of high productivity and facile operability [2]. Here, we present an attractive chain-like robotic microfinger assembled from dispersed microparticles based on local acoustic fields and manipulated by magnetic field. With the localized acoustic propulsion forces [3] generated around arrays of V-shape micropillars enclosed in a micro-manipulation chip, microparticles nearby are trapped and attached to the narrow opening ends of micropillars and then assemble to a chain-like structure. Experimental results basically confirm the compatibility of the acoustic assembling method with magnetic fields for manipulating robotic microfingers. Such an assembly method with high efficiency and controllability to microparticles offers new alternatives for manufacturing micromachines for biological engineering, lab-on-chip architectures and micro factories, etc.

Working principles

The acoustic micro-manipulation chip comprises one piezoelectric transducer and one glass substrate, as illustrated in Figure 1a. One piezoelectric (PZT) plate with 0.5 mm thickness is utilized as the transducer and bonded with the 0.5 mm rectangular substrate ($25 \times 15 \text{ mm}^2$) by the epoxy resin. Driven by a power amplifier coupled with a signal generator, the piezoelectric transducer could excite the vibration of glass substrate, thereby activating the organized assembly for microparticles around the micropillars. Arrays of V-shape-like micropillars (see Figure 1a inset) fabricated on top of the micro-manipulation chip are made of photoresist SU-8 by ultraviolet (UV) photolithography and covered with one 100 nm layer of SiO_2 by physical deposition. Each side of the V-shape-like pillar is $1.4 \times 10 \times 60 \mu\text{m}^3$ (height \times width \times length) and the V-shape angle is 40° , with $30 \mu\text{m}$ and $75 \mu\text{m}$ width for the narrow and wide opening ends, respectively.

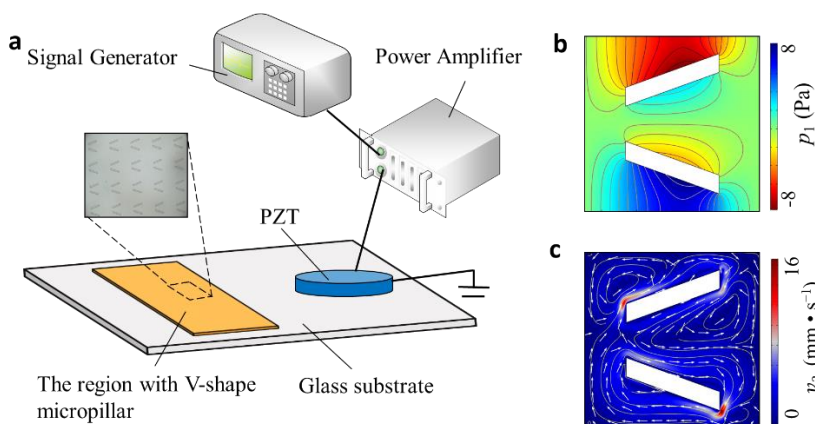


Figure 1: Micro-manipulation chip for acoustic assembly. (a) Schematic diagram showing the configuration of the assembling platform and arrays of V-shape-like micropillars. (b) First order acoustic pressure distribution. (c) Second order acoustic streaming distribution.

Figure 1 b&c illustrates the calculated pressure distribution of first order acoustic field and velocity distribution of second order acoustic streaming when the microstructure oscillates around a clockwise elliptical trajectory. According to the contour lines in Figure 1b, the first order acoustic pressure is nearly symmetrical to both sides of V-shape pillars and decreases to a minimal value ($\sim 0 \text{ Pa}$) at the ends of each side. The remarkable change of the pressure gradient along each side of pillar indicates that particles could be trapped by strong acoustic radiation force at the end of the micropillars. The calculated second-order

acoustic streaming in Figure 1c displays dual clockwise rolls around sides of the V-shape micropillar, accompanied by several small counter clockwise rolls. The enhancement of closed-loop acoustic streaming around the sides of micropillar could provide sufficient propulsion force for driving microparticles to move towards the end parts of the micropillar for organized assembly. Numerical simulation results basically explain the mechanism of how to utilize the micropillar's vibration-induced local enhanced acoustic field for the organized assembly of microparticles.

Results and discussion

Driven by the ultrasound power system, the micro-manipulation chip was tested for assembling polystyrene (PS) particles, which exhibit a high motion uniformity in a wide range of different size scales in aqueous solution. The profiles of Figure 2a indicate that the multiple 10 μm microparticles can be assembled to a long chain from the initial dispersed elements after trapping. The strong acoustic streaming force and radiation force acting on the particles maintain their organized assembling structures. Multiple microparticle elements assembled to form a straight chain around a pillar hold accurately linear position. It is observed from Figure 2b that the length of chain is proportional to the time and the length of five-particle formed chain in 13.5 s is approximately 50 μm .

The image sequences demonstrated in Figure 2c display the chain-like flexible robotic fingers assembled from magnetic PS microspheres (5 μm) in the presence of both ultrasound and magnetic fields. The simultaneous application of the magnetic fields (while the ultrasound power is on) provides a net magnetization that enables on-demand alignment and reversible guidance to the flexible fingers. The alternating magnetic field gives rise to the motion of the finger to be periodically reoriented. Originally, the magnetic polystyrene microspheres are assembled to a chain-like finger pointing to the left direction, solely achieved by applying the acoustic field (Figure 2b-1). Then, the flexible finger gradually swings to the right side, after counter-clockwise rotating the magnetic field (Figure 2b-2–5). Moreover, the swing motion can be reversed by clockwise rotating the applied magnetic field (Figure 2b-6–9). These results clearly indicate that functional microsystems acoustically assembled from magnetic elements could dynamically reorient or transform into different structures by tuning the external magnetic field.

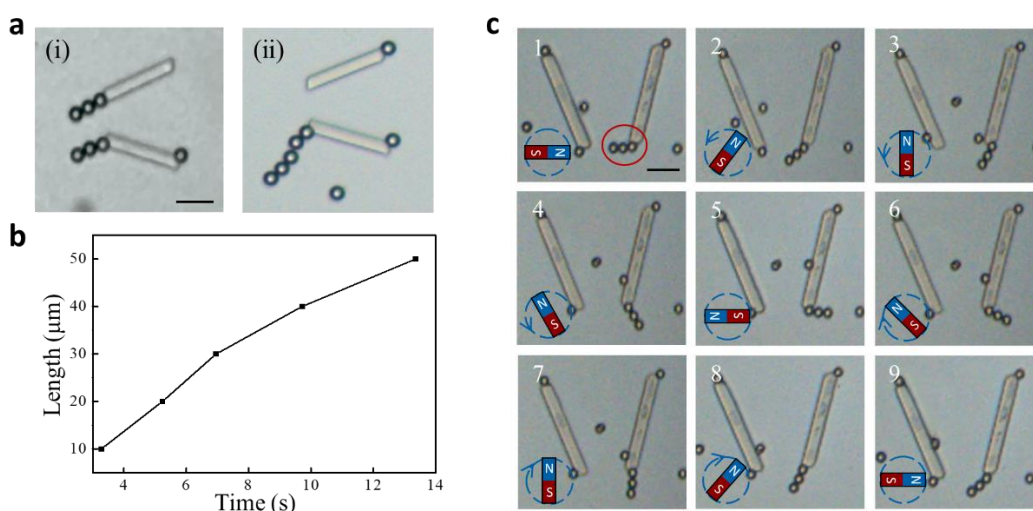


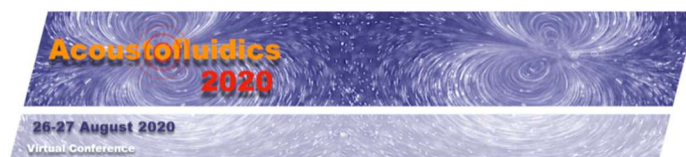
Figure 2: Acoustic assembly and magnetic control of robotic fingers. (a) Chains assembly of particles trapped by the end of the V-shape micropillar. (b) Dependence of the length of particle chain upon the operating time. (c) Magnetically controlled swing motion of a flexible finger acoustically assembled from 5 μm magnetic particles.

Conclusion

In general, we developed a strategy to utilize local acoustic fields near the microstructures for organized assembly of microspheres to obtain functional microsystems, for example, flexible chains that can serve as robotic arms or fingers. Combined with the modulation of external magnetic fields, one flexible chain acoustically assembled from magnetic microparticles could serve as a robotic finger with tunable orientations.

References

- [1] C.R. Kagan, E. Lifshitz, E.H. Sargent, D.V. Talapin. *Science* **353**, aac5523 (2016).
- [2] X. Lu, K. Zhao, W. Liu, D. Yang, H. Shen, H. Peng, X. Guo, J. Li, J. Wang. *ACS Nano* **13**, 11443-11452 (2019).
- [3] P.B. Muller, R. Barnkob, M.J.H. Jensen, H. Bruus. *Lab. Chip* **12**, 4617–4627 (2012).



Washing Electroporated Cells Using Surface Acoustic Wave (SAW)

Fangda Wu¹, Mao Mao², Fan Yuan², Ming Hong Shen³, and Xin Yang¹

¹ Department of Electrical and Electronic Engineering, School of Engineering, Cardiff University, UK CF24 3AA

E-mail: WuF6@cardiff.ac.uk

²Department of Biomedical Engineering, School of Engineering, Duke University, NC 27708-0281, USA

³Preclinical Studies of Renal Tumours Group, Division of Cancer and Genetics, School of Medicine, Cardiff University, Cardiff CF14 4XN, UK

Introduction

Electrotransfection is a nonviral technique for exogenous molecules delivery in both in-vitro and in-vivo¹. It is commonly used for DNA, RNA and proteins delivery²⁻⁸, and cancer gene therapy^{9,10}. Electrotransfection is applying pulsed electric fields on cells to attract the molecules of interest around the cells¹¹, and allowing for intracellular transport of materials¹². Electrotransfection is a relatively simple gene delivery method only using modified plasmid DNA (pDNA) solution for transfection without other chemicals¹. However, it is noted that electrotransfection has low transfection efficiency¹³ and cell viability¹¹, due to the unprotected pDNA degraded by nucleases¹⁴⁻¹⁸ and the metal ions generated from the metal electrodes. These ions will cause many biological macromolecules to precipitate from solutions so that the available amount of pDNAs will be reduced for cell transfection^{19,20}. Acoustic-based microfluidic technique is an emerging technique to manipulate biological cells with the advantage of preserving original cellular structure and states^{21,22}. Such devices have been applied in manipulating biological particles such as circulating tumour cells (CTCs)^{21,23,24}, bacteria²⁵⁻²⁷, and inflammatory cells²⁸. This study presents a acoustofluidic devices to effectively wash cells after electrotransfection to enhance transfection efficiency and cell viabilities.

Mechanism of SAW cell washing

A tilt-angle standing surface acoustic wave (SSAW) device²⁹ was employed to switch cell medium as the schematic shown in Fig. 1a. A pair of interdigital transducers (IDTs) produce SSAW forming a series of pressure nodes (PNs) along the propagation. A polydimethylsiloxane (PDMS)-made microchannel with three inlets and two outlets is placed between the IDTs with an angle of 15 degrees. The width of the microchannel is four times as the SSAW wavelength, which allows eight PNs to form inside the microchannel. A sample of microparticles in Medium 1 is introduced to the middle inlet, and two sheath flows containing Medium 2 are introduced to the side inlets for controlling the position and width of the sample inside the microchannel. The microparticles are attracted by acoustic radiation force produced by SSAW and trapped along the PNs after entering the acoustic field, while Medium 1 remains its dynamic flow pattern due to the two sheath flows. By optimising the outlets, microparticles trapped on the PNs are migrated to the Outlet 1 entering Medium 2, while Medium 1 flows on its original course and enters Outlet 2. The microparticles are removed from the old medium and join the new medium after SSAW actuation. The Device made by photolithography patterning with metal electrodes on a lithium niobate (LiNbO₃) piezoelectric substrate. The PDMS microchannel was bonded by plasma treatment. Steel and Tygon tubings are connected with the microchannel at the inlets and outlets.

Switching medium of polystyrene microspheres

The set flow rates of the three inlets allow the recovery rate of the 15 μm microspheres to achieve 100% when SAW applied. The recovery rate was defined as the ratio of the number of the microparticles pumped through inlet 2 to the number of the microparticles collected from outlet 1. Fig. 1b shows the outlet area when SAW is applied. It is noted that the blue pigment was dispended due to the streaming effect produced by SAW. 100% of 15 μm microspheres were driven by the acoustic radiation force and removed from the sample toward Outlet 1. The exerted acoustic radiation force is proportional to the input power for producing SAW. A higher input power allows faster particle migration inside the SAW field resulting in a higher recovery rate. To investigate the relationship between the recovery rate and the input power using the aforementioned flow rates, the input power was increased from 0.5 W to 1.3 W, as shown in Fig. 1c, the recovery rate increased from 92.1% to 100%.

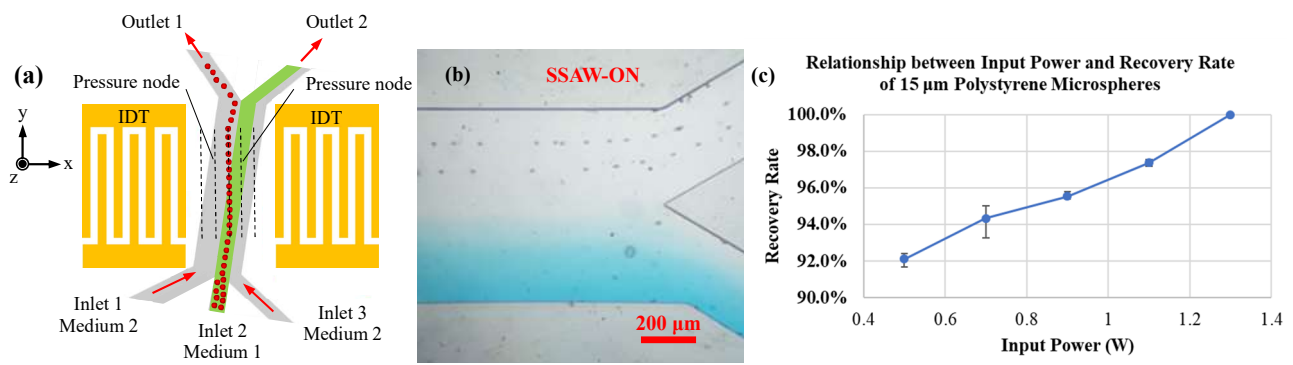


Figure 1: (a) Schematic of the standing surface wave (SSAW) device integrating two interdigitated transducers (IDTs) and a microfluidic channel (b) The 15 μm polystyrene microspheres were washed from the original medium when SSAW was on. (c) Relationship between input power and recovery rate of 15 μm polystyrene microspheres.

Switching medium of cells after electrotransfection

With the experience of polystyrene beads test, the input power of 4 W and the flowrate (upper, middle sample and lower inlets were 12 μl/min, 3 μl/min and 6 μl/min, respectively) were used. As shown in Fig. 2a, where SSAW is off, all the mouse embryonic fibroblast (MEF) cells are remained flowing at the bottom and collected by the lower outlet. When SSAW is on (Fig. 2b), the MEF cells are driven by the PN and leave the original medium to be collected by the upper outlet. The electrotransfection efficiency (eTE) percentage is the main characters to justify electrotransfection efficiency. Furthermore, the eTE percentage in washed group and control group were 43.8% and 18.4%, respectively. In addition, the viability of collected cells after switching media (94.5%) was significantly higher than the control group (34.3%).

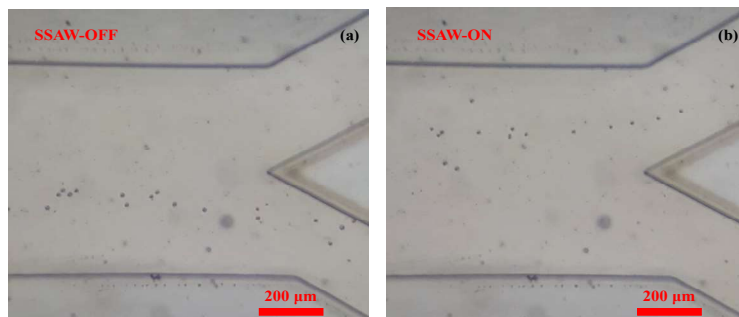


Figure 2: MEF cells were collected by the lower outlets when SSAW was off. (b) MEF cells were collected by the upper outlets when SSAW was on.

Conclusion

SAW cell washing shows a significant increase of both pDNA transfection efficiency and cells viability after electroporation. The SAW washing has the potential to be an automated and efficient medium switching system to condition the medium of the samples after electrotransfection. we are looking forward to presenting for the international acoustofluidics community at *Acoustofluidics 2020 Virtual Conference*.

References

- L. D. Cervia and F. Yuan, *Molecular Pharmaceutics*, 2018, **15**, 3617-3624.
- D. B. T. Cox, R. J. Platt and F. J. N. m. Zhang, 2015, **21**, 121.
- P. I. Thakore, A. M. D'ippolito, L. Song, A. Safi, N. K. Shivakumar, A. M. Kabadi, T. E. Reddy, G. E. Crawford and C. A. J. N. m. Gersbach, 2015, **12**, 1143.
- D. Balboa, J. Weltner, S. Eurola, R. Trokovic, K. Wartiovaara and T. J. S. c. r. Otonkoski, 2015, **5**, 448-459.
- M. C. Latella, M. T. Di Salvo, F. Cocchiarella, D. Benati, G. Grisendi, A. Comitato, V. Marigo and A. J. M. T.-N. A. Recchia, 2016, **5**, e389.
- I. Maggio and M. A. J. T. i. b. Goncalves, 2015, **33**, 280-291.
- W. Qin, S. L. Dion, P. M. Kutny, Y. Zhang, A. W. Cheng, N. L. Jillette, A. Malhotra, A. M. Geurts, Y.-G. Chen and H. J. G. Wang, 2015, **200**, 423-430.
- K. Schumann, S. Lin, E. Boyer, D. R. Simeonov, M. Subramaniam, R. E. Gate, G. E. Haliburton, J. Y. Chun, J. A. Bluestone and J. A. J. P. o. t. N. A. o. S. Doudna, 2015, **112**, 10437-10442.
- K. Okita, Y. Matsumura, Y. Sato, A. Okada, A. Morizane, S. Okamoto, H. Hong, M. Nakagawa, K. Tanabe and K.-i. J. N. m. Tezuka, 2011, **8**, 409.
- R. Heller and L. C. Heller, in *Advances in genetics*, Elsevier, 2015, vol. 89, pp. 235-262.
- J. W. Henshaw and F. J. J. o. p. s. Yuan, 2008, **97**, 691-711.
- J. J. A. P. S. Gehl, 2003, **177**, 437-447.
- A. G. Pakhomov, D. Miklavcic and M. S. Markov, *Advanced electroporation techniques in biology and medicine*, CRC Press, 2010.
- D. Lechardeur, K. J. Sohn, M. Haardt, P. B. Joshi, M. Monck, R. W. Graham, B. Beatty, J. Squire, H. O'Brodovich and G. L. Lukacs, *Gene therapy*, 1999, **6**, 482-497.
- K. Crook, G. McLachlan, B. J. Stevenson and D. J. Porteous, *Gene therapy*, 1996, **3**, 834-839.
- N. Cifani, L. Chronopoulou, B. Pompili, A. Di Martino, F. Bordi, S. Sennato, E. G. Di Domenico, C. Palocci and F. Ascenzioni, *Biotechnol Lett*, 2015, **37**, 557-565.
- M. F. Bureau, S. Naimi, R. Torero Ibad, J. Seguin, C. Georger, E. Arnould, L. Maton, F. Blanche, P. Delaere and D. Scherman, *Biochim Biophys Acta*, 2004, **1676**, 138-148.